FINAL REPORT PROJECT A–1863

HARDENED ARRAY DESIGN AND ANALYSIS

By

J. A. FULLER AND T. S. TAYLOR

Sponsored by

BALLISTIC MISSILE DEFENSE
ADVANCED TECHNOLOGY CENTER
RADAR DIRECTORATE (ATC–R)
P. O. BOX 1500
HUNTSVILLE, ALABAMA 35807

CONTRACT DASG60–76–C–0070
AMENDMENT NO. P00009

29 July 1980 through 28 July 1981

GEORGIA INSTITUTE OF TECHNOLOGY
A Unit of the University System of Georgia
Engineering Experiment Station
Atlanta, Georgia 30332

REPORT DOCUMENTATION PAGE

READ INSTRUCTIONS BEFORE COMPLETING FORM

1. REPORT NUMBER	2. GOVT ACCESSION NO. / 3. RECIPIENT'S CATALOG NUMBER
4. TITLE (and Subtitle): HARDENED ARRAY DESIGN AND ANALYSIS	5. TYPE OF REPORT & PERIOD COVERED: Final Report, 29 July 1980-28 July 1981
	6. PERFORMING ORG. REPORT NUMBER: A-1863-5-82
7. AUTHOR(s): J. A. Fuller, T. S. Taylor	8. CONTRACT OR GRANT NUMBER(s): DASG60-76-C-0070, Amendment No. P0009
9. PERFORMING ORGANIZATION NAME AND ADDRESS: Engineering Experiment Station, Georgia Institute of Technology, Atlanta, Georgia 30332	10. PROGRAM ELEMENT, PROJECT, TASK AREA & WORK UNIT NUMBERS: 6.33.04.A
11. CONTROLLING OFFICE NAME AND ADDRESS: Ballistic Missile Defense, Advanced Technology Center (ATC-R), P.O.Box 1500, Huntsville, Alabama 35807	12. REPORT DATE: May 1982
	13. NUMBER OF PAGES: xiv + 199
14. MONITORING AGENCY NAME & ADDRESS (if different from Controlling Office)	15. SECURITY CLASS. (of this report): Unclassified
	15a. DECLASSIFICATION/DOWNGRADING SCHEDULE

16. DISTRIBUTION STATEMENT (of this Report)

Distribution limited to U.S. Government agencies only
Test and Evaluation, 14 May 1980.
Other requests for this document must be referred to
Ballistic Missile Defense Advanced Technology Center, ATTN. ATC-R
P.O. Box 1500; Huntsville, Alabama 35807

17. DISTRIBUTION STATEMENT (of the abstract entered in Block 20, if different from Report)

18. SUPPLEMENTARY NOTES

BMDATC Project Engineer: Fan King (ATC-R)

19. KEY WORDS (Continue on reverse side if necessary and identify by block number)

Phased-Array Antennas
Microstrip Antenna Elements
Hardened Phased Arrays
Phased-Array Simulators
Dielectric Measurements
High-Temperature Testing

20. ABSTRACT (Continue on reverse side if necessary and identify by block number)

This report describes work performed at the Georgia Tech Engineering Experiment Station (EES) to develop phased-array antenna technology for ballistic missile defense (BMD) radar applications. Ground-based and interceptor-based radars are of interest, and in both cases the heating rates in the operational environment are recognized as a major factor in

the antenna design problem. Ground-based antennas must be able to survive the radiant heat of nearby nuclear explosions, and interceptor antennas must function on hypersonic missiles, where both aerodynamic and radiant heating occur. All of the work on this research program has concerned the development and evaluation of concepts for phased arrays that can survive and operate under severe heating conditions. Part of the work has been directed toward the development of a new type of radiating element for hardened arrays, part has been the development of methods to test hardened arrays and high-temperature components, and part has been to assist other BMD contractors with related analysis and testing problems.

The general objectives of this research program are (1) to determine the suitability and potential capabilities of microstrip phased-array elements for BMD applications in ground-based and interceptor-based radar antennas, and (2) to develop and apply methods for testing antenna components in high-temperature environments. The principal concerns with the microstrip element are how mutual coupling may affect its performance in a large, dense array and whether adequate performance can be maintained, when the array face is covered with a protective dielectric layer. The primary measure of performance is the beam-scan range that can be achieved. This is essentially controlled by mutual coupling effects, which are very sensitive to element spacing and to the presence of a dielectric covering.

A capability to utilize multielement phased-array simulator technology was established, and an extensive set of parametric experiments were conducted with microstrip elements. This is the first data of its kind to become available on microstrip elements. The important variable parameters were the size of the array lattice, relative to the size of the element, and the thickness of the cover layer, relative to the thickness of the substrate. The results suggest that microstrip elements could have potential for providing a reasonable scan range over, perhaps, a five percent frequency bandwidth, when the covering dielectric is not much thicker than the substrate. However, there is not yet enough data to make this a well-founded conclusion. The approach to this investigation has yielded good data, and the work is being continued.

GEORGIA INSTITUTE OF TECHNOLOGY
Engineering Experiment Station
Atlanta, Georgia 30332

TECHNICAL REPORT

Project A-1863

HARDENED ARRAY DESIGN AND ANALYSIS

By

J. A. Fuller and T. S. Taylor

Contract No. DASG60-76-C-0070
Amendment No. P0009

May 1982

Prepared for

BALLISTIC MISSILE DEFENSE ADVANCED TECHNOLOGY CENTER
Radar Directorate (ATC-R)
P.O. Box 1500
Huntsville, Alabama 35807

PREFACE

The research discussed in this report was performed at the Engineering Experiment Station (EES), Georgia Institute of Technology, for the Ballistic Missile Defense Advanced Technology Center (BMDATC), under Contract No. DASG60-76-C-0070. Technical direction was exercised through the BMDATC Radar Directorate by the Project Engineer, Mr. Fan King. The work was performed by personnel in the Electromagnetic Effectiveness Division of the EES Electronics and Computer Systems Laboratory. Dr. James A. Fuller was the EES Project Director. This report covers work which was performed from 29 July 1980 through 28 July 1981, under Contract Amendment No. P0009.

The authors would like to acknowledge the support provided by several other members of the Engineering Experiment Station, including Mr. F. L. Cain, Dr. C. E. Ryan, Jr., Dr. R. L. Moore, and Mr. J. D. Walton. The authors also express their appreciation to Mr. W. H. Warden for his assistance with the measurements, computer calculations, and figure preparation, and to Ms. B. E. Gonzalez for preparation of this manuscript.

Respectfully submitted,

James A. Fuller
Project Director

Approved:

Charles E. Ryan, Jr.
Chief,
EM Effectiveness Division

TABLE OF CONTENTS

LIST OF FIGURES

LIST OF FIGURES (continued)

LIST OF FIGURES (continued)

LIST OF FIGURES (continued)

LIST OF TABLES

SECTION I
INTRODUCTION AND SUMMARY

This report describes work performed at the Georgia Tech Engineering Experiment Station (EES) to develop phased-array antenna technology for ballistic missile defense (BMD) radar applications. Ground-based and interceptor-based radars are of interest, and in both cases the heating rates in the operational environment are recognized as a major factor in the antenna design problem. Ground-based antennas must be able to survive the radiant heat of nearby nuclear explosions, and interceptor antennas must function on hypersonic missiles, where both aerodynamic and radiant heating occur. All of the work on this research program has concerned the development and evaluation of concepts for phased arrays that can survive and operate under severe heating conditions. Part of the work has been directed toward the development of a new type of radiating element for hardened arrays, part has been the development of methods to test hardened arrays and high-temperature components, and part has been to assist other BMD contractors with related analysis and testing problems. In terms of immediate impact on the overall BMD program, these tasks are probably listed in reverse order of importance. The major contributions and results in each area are discussed in this report.

A. Background

For five years Georgia Tech has conducted research on hardened phased array technology for the Radar Directorate of the Ballistic Missile Defense Advanced Technology Center (BMDATC). A substantial portion of the earlier work concerned dipole arrays [1,2], which are most appropriate for relatively low frequency (VHF/UHF) radars. Calculations and small scale experiments showed that a planar array of dipole elements could be successfully hardened by embedding the face of the array in a dielectric layer. The primary concern was whether an adequate beam-scan range could be achieved with the elements in a thick dielectric layer. A general theoretical analysis and a design-oriented computer program were developed and utilized to generate design guidelines for such a dipole array.

A need to identify and test refractory dielectric materials evolved from the work on dipole arrays and from the work of several other BMDATC

contractors on microwave arrays of waveguide elements. Through this contract and related ones with the Army Materials and Mechanics Research Center (AMMRC), Georgia Tech conducted numerous tests in the CNRS 1,000 kW Solar Furnace at Odeillo, France [3,4]. Most of this work was directed toward components for ground-based radars, but it included some tests of window materials for interceptor seekers. In the process, Georgia Tech became familiar with projected requirements for high-temperature microwave tests and developed improved procedures and capabilities.

As the technical feasibility of a very hard ground-based radar antenna became established, BMDATC placed more emphasis on technology to lower costs and on technology suitable for a millimeter-wave (mmW) interceptor seeker antenna. In recent work, Georgia Tech has addressed this need with research on the microstrip patch element. The microstrip element is basically a metallic patch of approximately half-wavelength dimensions that is plated on an electrically thin dielectric substrate over a ground plane. Because its cost is relatively low, and because it is unusually thin for an antenna, the microstrip element is a popular choice for airframe applications. Array applications have been very limited (e.g., low density fixed-beam arrays or small frequency-scanned linear arrays), but the element seems to have potential for large, dense, scanning arrays. The photo-etching or plating methods used to fabricate the elements are a relatively economical way to obtain the good dimensional tolerances required for mmW phased arrays, and use of these methods could make the element more compatible for integration with microwave-integrated-circuit (MIC) modules. The application of microstrip elements in arrays has been limited by the small demand for large arrays and by the total absence of knowledge about the properties of the element in an array environment. Work sponsored by BMDATC at Georgia Tech and at the Polytechnic Institute of New York is developing the technical base needed to make use of these elements.

B. Objectives

The general objectives of this research program are (1) to determine the suitability and potential capabilities of microstrip phased-array elements for BMD applications in ground-based and interceptor-based radar antennas, and (2) to develop and apply methods for testing antenna

components in high-temperature environments. The principal concerns with the microstrip element are how mutual coupling may affect its performance in a large, dense array and whether adequate performance can be maintained, when the array face is covered with a protective dielectric layer. The primary measure of performance is the beam-scan range that can be achieved. This is essentially controlled by mutual coupling effects, which are very sensitive to element spacing and to the presence of a dielectric covering.

A theoretical study of microstrip phased-array elements is in progress for BMDATC at the Polytechnic Institute of New York, and this parallel work at Georgia Tech is intended to be primarily experimental. In particular, methods based on the multielement phased-array simulator are to be developed and applied. The development of simulator technology is important in its own right, because it can be used for high-temperature tests of elements and subarrays. The tests could be very practical with a well collimated radiant heat source, such as a laser, and the exact simulation of the array environment would provide a much better electrical test than is achieved in a solar furnace. The simulator could also be conveniently heated in a conventional furnace.

C. Accomplishments

A capability to utilize multielement phased-array simulator technology was established, and an extensive set of parametric experiments were conducted with microstrip elements. This is the first data of its kind to become available on microstrip elements. The important variable parameters were the size of the array lattice, relative to the size of the element, and the thickness of the cover layer, relative to the thickness of the substrate. The data presented on this subject represents over 50,000 separate phase and amplitude measurements of element-to-element coupling at microwave frequencies, and several times this number were completed while developing the procedures. It is clear that computer-controlled data processing was necessary, and that required additional development. The results suggest that microstrip elements could have potential for providing a reasonable scan range over, perhaps, a five percent frequency bandwidth, when the covering dielectric is not much thicker than the substrate. However, there is not yet enough data to make this a well-founded

conclusion. The approach to this investigation has yielded good data, and the work is being continued.

This report is organized according to three categories of tasks that have been undertaken during the work. Section II summarizes two peripheral tasks in which Georgia Tech assisted other BMD contractors with design efforts. In one case, a computer program available at Georgia Tech was used to evaluate the sensitivity of waveguide phased-array elements to the configuration of a protective dielectric window. In the other case, a series of microwave tests were conducted in a thermal simulator to determine what effect the flashlamps might have on antenna measurements. Section III discusses work to develop techniques for testing antennas and component materials. This includes methods for high-temperature dielectric measurements, the multielement array-simulator technology, and methods for mmW measurements, such as the six-port network analyzer. Section IV describes the experimental investigation of microstrip array elements and summarizes the results. Supporting discussions and data for various sections are contained in Appendices A through H.

SECTION II
DESIGN SUPPORT

As one of the tasks of this research program, Georgia Tech has supported other BMDATC contractors in their efforts to design, develop, and test antennas and related systems. Two of these support activities are reviewed in this section. The first concerns a series of microwave tests that were conducted for Science Applications, Inc. (SAI), to evaluate a flashlamp-based thermal simulator for possible use in antenna testing. The second activity concerns a series of phased-array calculations that were performed for Malibu Research Associates (MRA) to assist with the design of an array element. Both activities utilized capabilities that were developed at Georgia Tech during previous work for BMDATC. The results are only summarized in this report; complete data packages were delivered to SAI [5] and MRA [6], respectively, and copies were provided to BMDATC.

A. Thermal Simulator Tests

Under Contract No. DNA001-80-0322 with the Defense Nuclear Agency (DNA) and BMDATC, SAI is developing a xenon flashlamp facility to simulate the intense radiant heat of a nuclear explosion. Design projections indicate that the flashlamp simulator should produce significantly more flux than is obtained in the French CNRS 1,000 kW Solar Furnace, and there is interest in using the simulator to test BMD antenna components. Georgia Tech was asked to determine what effect the flashlamps would have on microwave tests of the type that have been conducted in the French solar furnace [7].

The configuration of the thermal simulator is shown in Figure 2-1. The simulator consists of a 12-inch long, rectangular aluminum "light-pipe," which has highly polished interior surfaces, and a bank of xenon flashlamps, which are located at the upper end of the pipe. In normal operation, the upper end is capped with a polished aluminum plate, and test samples are placed in the opening at the lower end. For these microwave tests, the end-plate was removed to allow microwave transmission through the region occupied by lamps. Only one lamp was operated during these tests.

A diagram of the microwave equipment configuration is provided in Figure 2-2. This is essentially the same configuration that has been used

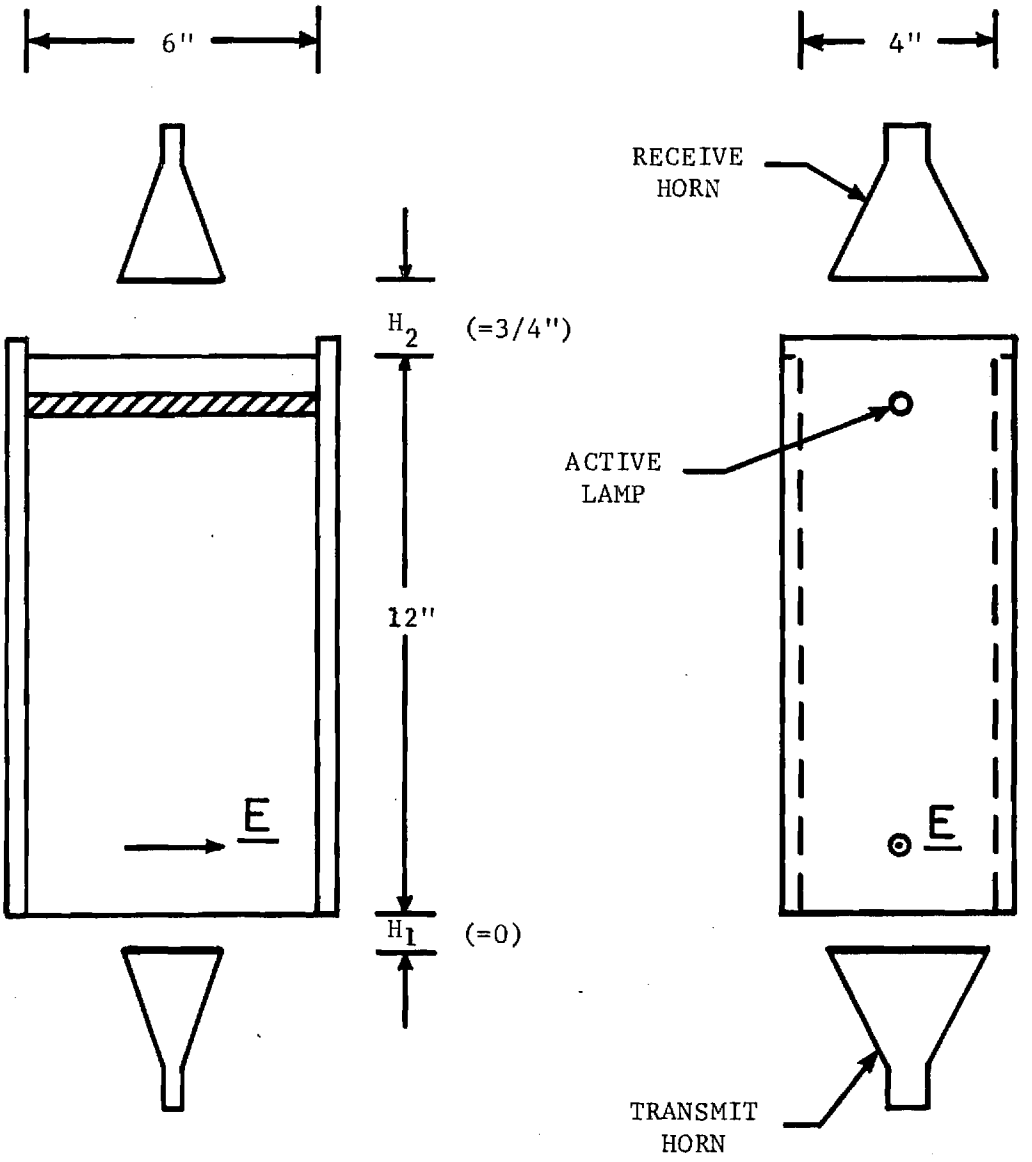

Figure 2-1. Configuration of thermal simulator for microwave tests. (Note: Reflecting end-plate is removed from upper end of light pipe.)
H_1 = 0" for tests 1-23
H_1 = 5/8" for tests 24-26
H_2 = 3/4"

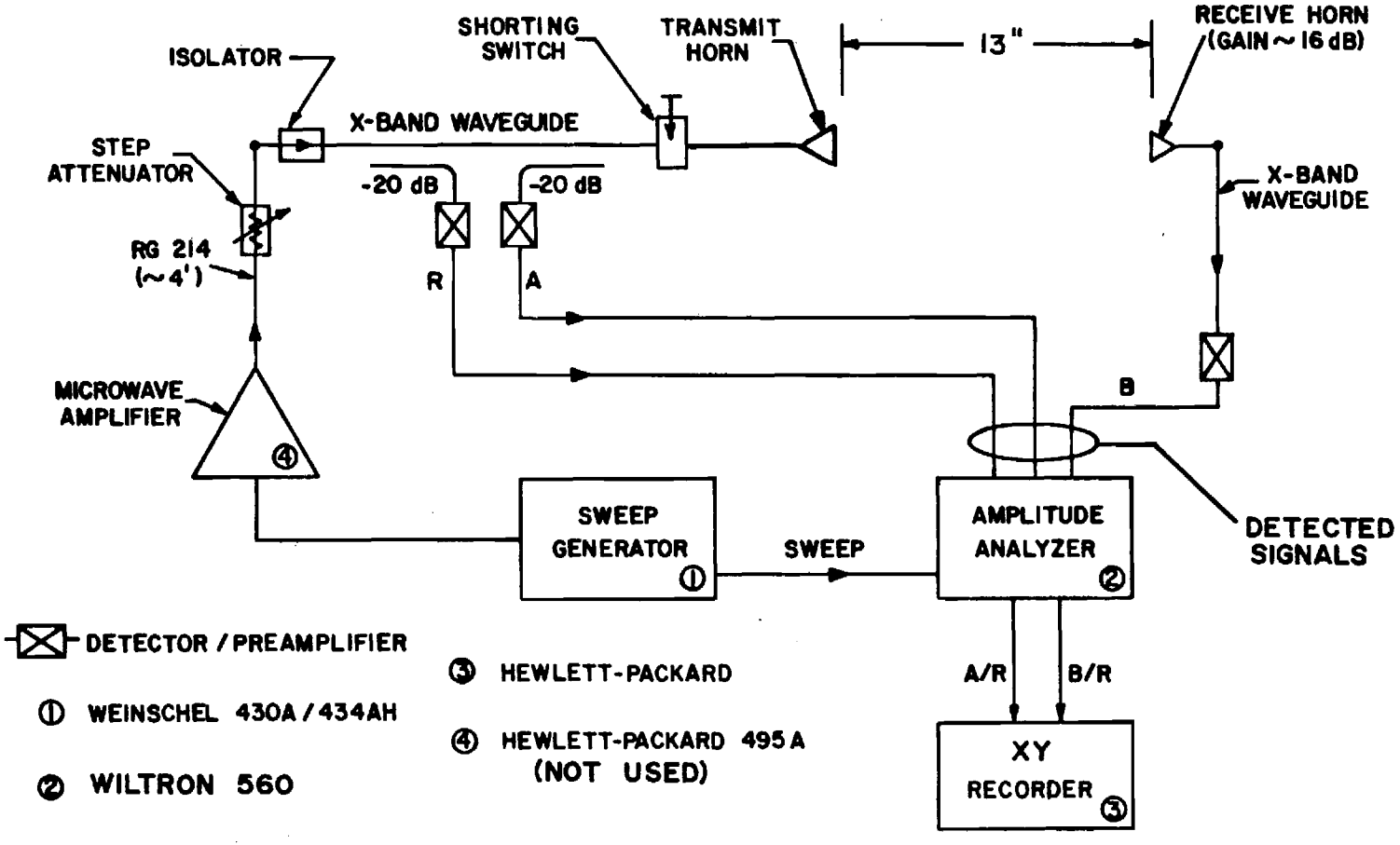

Figure 2-2. Microwave equipment configuration used to evaluate flashlamp effects in the SAI thermal simulator.

in the solar furnace tests [3]. The main difference is that in the flashlamp simulator, event times are measured in milliseconds, and the electronic data storage provided by the analyzer is necessary; for the solar furnace tests, a stripchart recorder is adequate. A photograph of the equipment is shown in Figure 2-3.

Figure 2-4 shows a typical set of data. The recordings numbered 5 and 6 show reference reflection and transmission levels, respectively, when the flashlamp is completely extinguished, and recordings 7 and 8 show how the levels change when the lamp is fired. The changes result from ionization of the gas in the tube; the ionized gas is apparently very lossy at X-band frequencies, as is clearly indicated by the large decrease in both transmitted and reflected signals, during the period of the flash.

The fact that the flashing lamps cause a significant change in the microwave configuration (i.e., a change in some of the reflecting boundaries) means that the simulator could be difficult to use for antenna tests. There will be a problem in determining with certainty whether measured changes are caused by changes in the hot antenna or by the lamps in the simulator.

As a possible method for isolating the flashlamps from the microwave environment, SAI suggested that the lamps could be placed behind a window that would function as a high-pass filter; the window would be optically transparent but would be opaque to microwaves. A saltwater-filled double-paned glass window was tried and found to be very effective for isolating the flashlamp from the microwave channel. Optical transparency was not evaluated but was contended to be quite good.

At the completion of the Phase I development effort, SAI will have the capability to fire a bank of lamps in the rectangular light-pipe. Development beyond Phase I, to achieve the desired nuclear effect simulation, will require a larger facility with a different configuration of flashlamps, and Georgia Tech was invited to suggest configurations that are compatible with microwave tests.

Our recommendation is illustrated in Figure 2-5. A large number of lamps can be contained in the circular configuration, and the filter (e.g., a water-filled window) should provide adequate isolation between the flashing lamps and the microwave channel. The angle β must be adjusted to

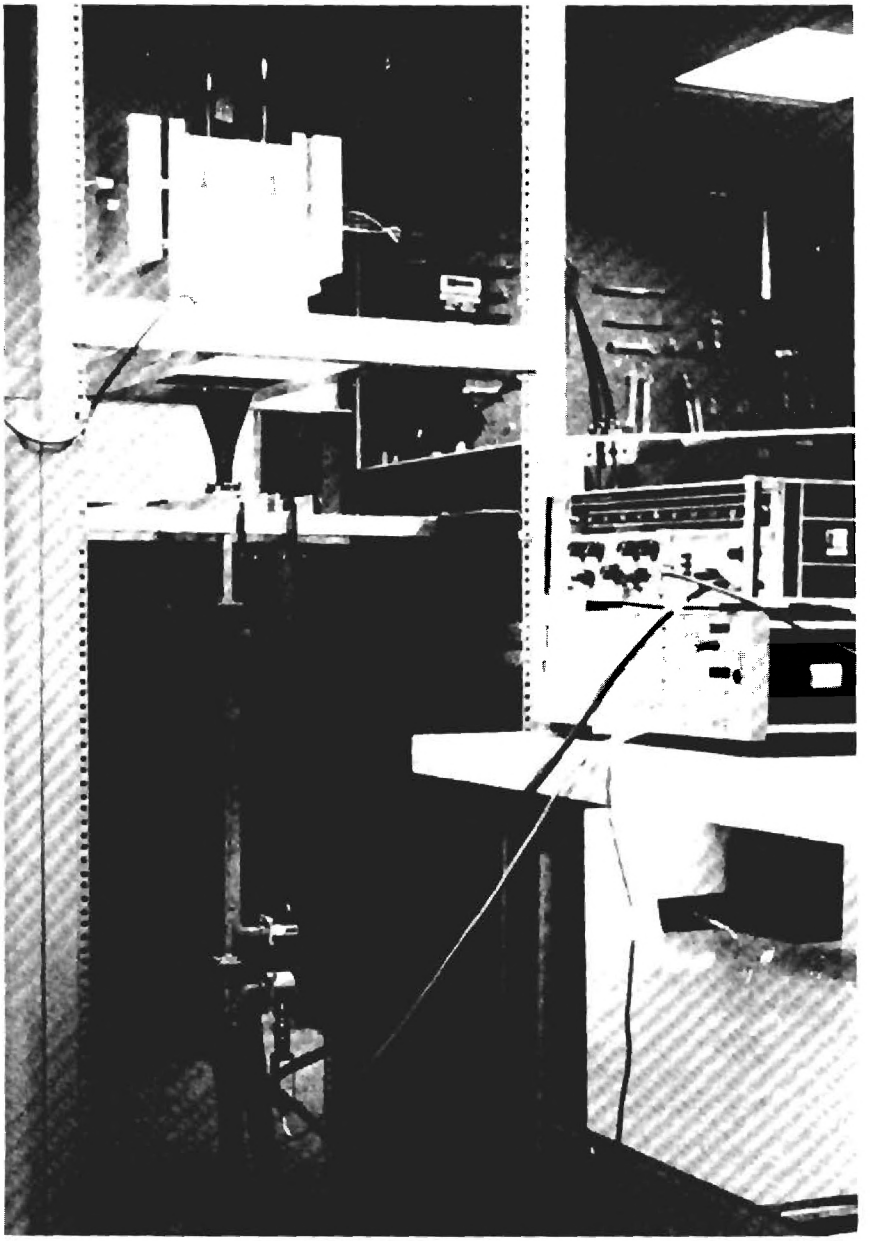

Figure 2-3. Photograph of microwave equipment. in thermal simulator.

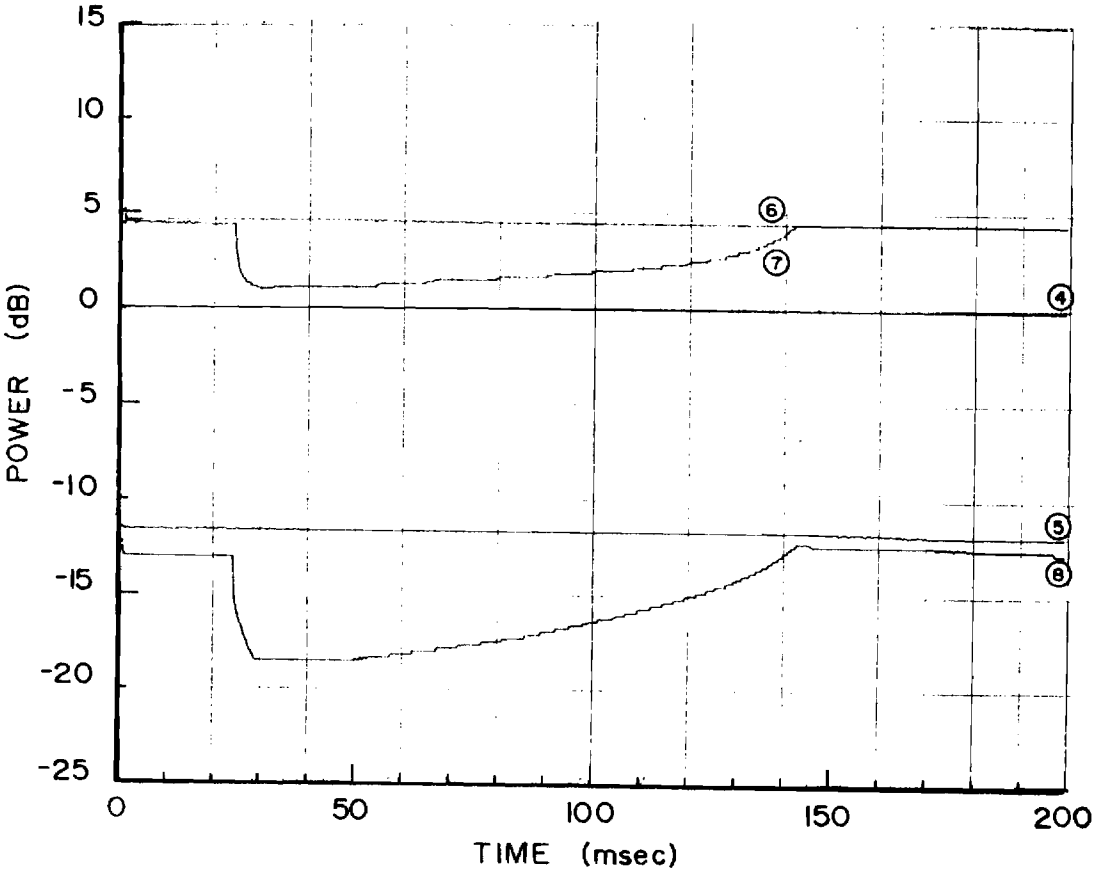

Figure 2-4. 5 recordings of 10 GH_z reflected and transmitted signals during a single flash discharge (Energy = 6.2kJ, visible pulse length ≈ 20ms).
Curve No. 4 - Reflection from waveguide short.
Curve No. 5 - Reflection from simulator with lamp off
Curve No. 6 - Transmission through simulator with lamp off.
Curve No. 7 - Transmission through simulator with lamp ignited.
Curve No. 8 - Reflection simulator with lamp ignited.

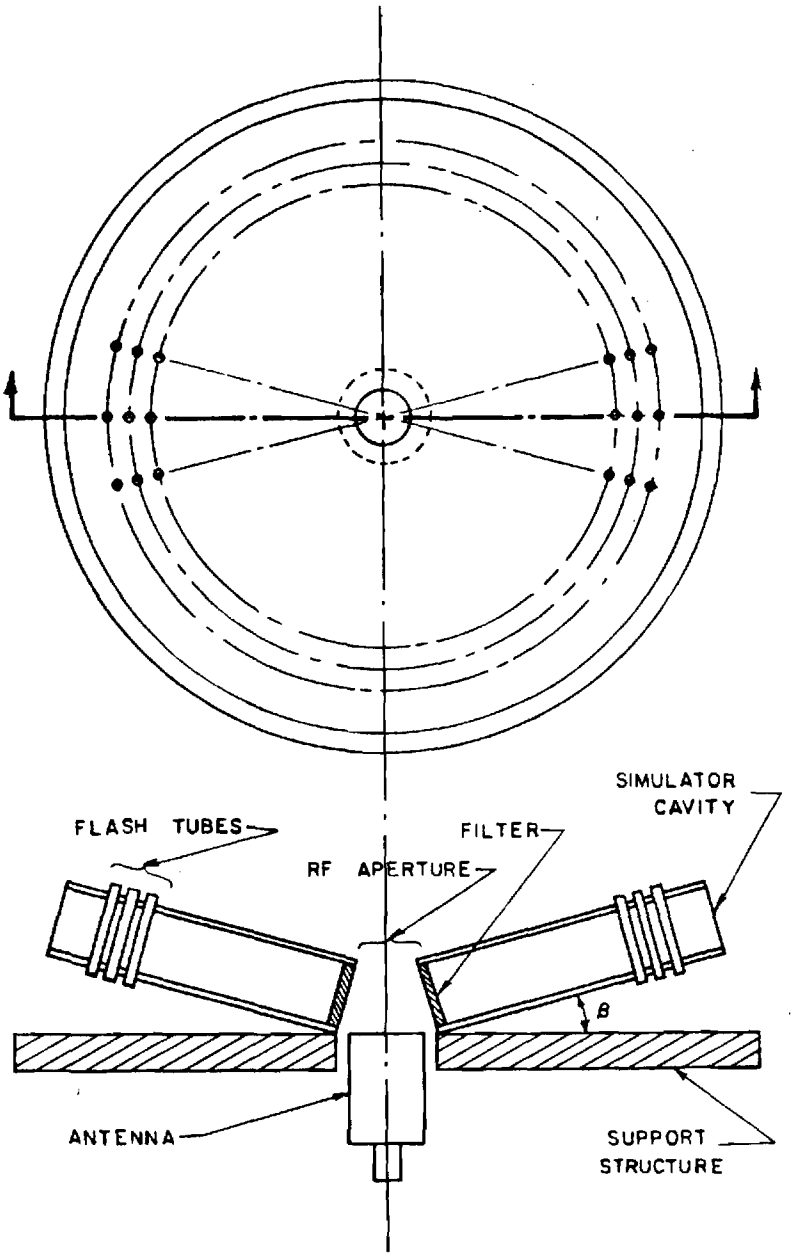

Figure 2-5. Suggested configuration for thermal simulator.

compromise the thermal efficiency and the size of the RF aperture. The thermal efficiency of this configuration is reduced by the oblique, indirect illumination of the test aperture (i.e., the antenna face), because the "light-pipe" concept does not provide collimation, or focusing, beyond the exit aperture.

If the filter is as good as the preliminary tests indicated, the antenna test capabilities of this configuration are probably adequate to detect major heat-induced changes in performance, and that has been the primary objective of the solar furnace tests. It is unlikely that tests conducted in the French solar furnace could be duplicated, because the RF environment is quite different. In the solar furnace, the antenna radiates into free space through an insulated aperture in a ground plane (e.g., as in Figure 2-5, with the simulator removed), while here, the antenna radiates through the conical section formed by the filter. The proper way to use this facility would be simply to compare reflection and transmission measurements before, during, and after heating, just as has been done in the solar furnace. In general, the French solar furnace offers a better (i.e., cleaner) RF test environment, with the possibility for sampling the radiation pattern at several points, while the flashlamp simulator offers the possibility for producing significantly higher thermal flux.

B. Phased-Array Calculations

Under Contract No.DASG60-80-C-0095, Honeywell, Inc., and MRA, the antenna subcontractor, are developing phased-array antennas for potential application on BMD interceptor vehicles. In the course of their work, questions arose about the effect of a dielectric window. For the configuration being considered at that time, the array lattice was large enough to admit grating lobes, the window was electrically thick, and the spacing between the array aperture and the window was electrically large. Georgia Tech assisted MRA by conducting a series of theoretical calculations to evaluate variations of the basic configuration. These calculations were made using a generalized model for large arrays of waveguide elements, which was developed at Lincoln Laboratory [8]. Georgia Tech had adapted the computer code to run on computers at Georgia Tech and at BMDATC during previous work.

Figure 2-6 shows the geometrical parameters used in the array

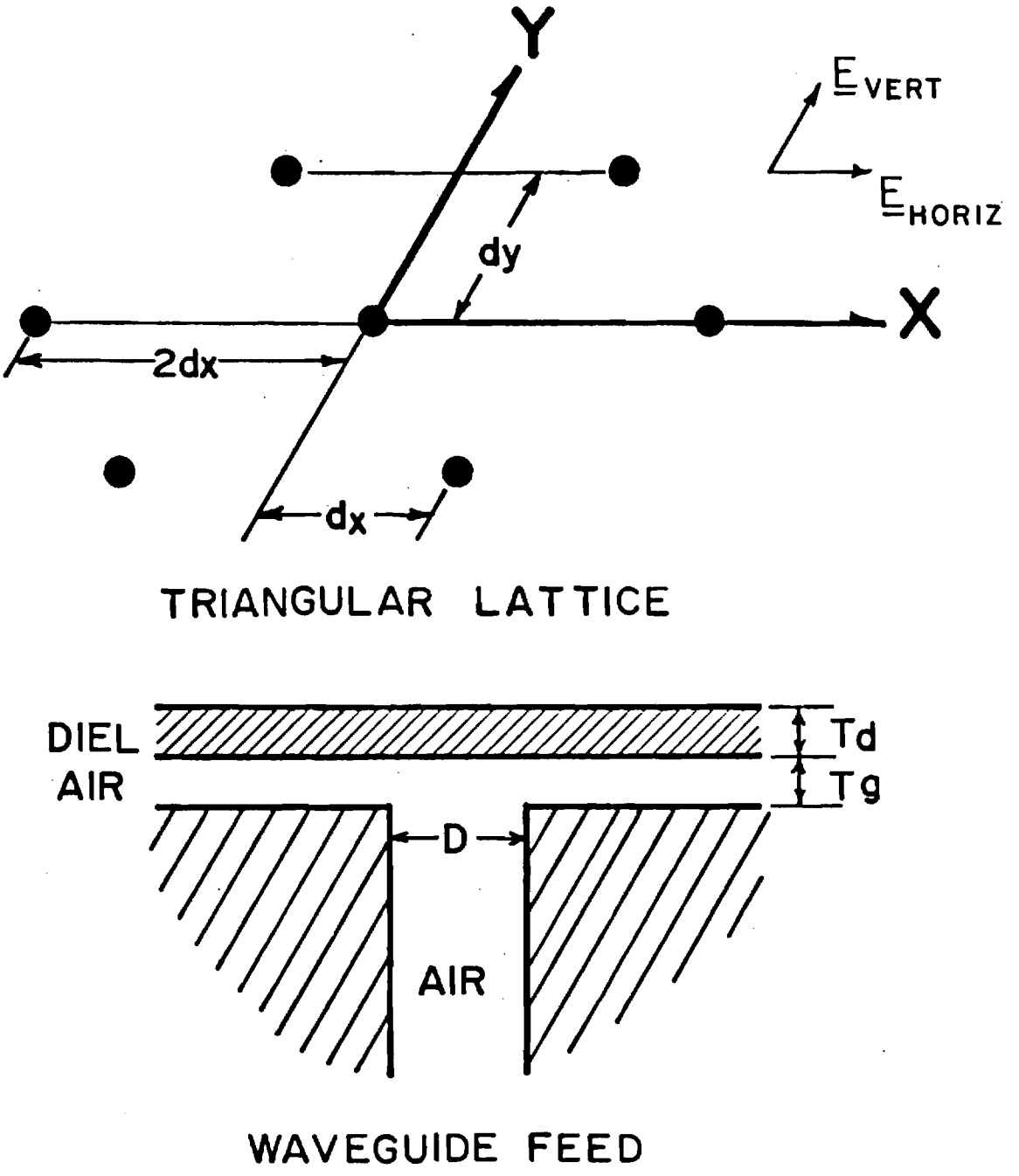

Figure 2-6. Geometrical parameters used in array calculations.

calculations. The nominal values for the baseline configuration were d_x/λ_o = 0.513, d_y/λ_o = 0.909, D/λ_o = 0.739, T_g/λ_o = 1.186, and T_d/λ_o = 0.371, where λ_o is the free-space wavelength, and the dielectric constant of the layer is K = 8.5. A grating lobe diagram for the baseline configuration is shown in Figure 2-7, and it is clear that a pair of grating lobes appear, when the main lobe is scanned beyond θ = 8 degrees in the ϕ = 0 plane.

When Georgia Tech undertook the array calculations, MRA was in the process of designing an element to suppress the grating lobes. During the work, major changes were made in the lattice and in the element. As much as possible, the changes were modelled by calculations; but the computer code was not capable of modelling the final configuration, which employed two elements per phase shifter, and there was not time for development of a new code. Data are included here for the baseline configuration, as a typical example of the modelling capability. At least ten different configurations were analyzed during this effort [6].

Figures 2-8(a) and (b) show the percentage of radiated power that is lost in the grating lobes, as a function of the main lobe scan angle, for horizontal and vertical polarizations, respectively, when there is no dielectric layer. Figure 2-9 shows the power lost, when the dielectric is present. These curves are strictly valid only for an infinite array, where the lobes become delta-functions and sidelobes do not exist. However, they provide a useful guideline for estimating how the power divides between the principal lobe and the grating lobes. More than half the available power can go into the grating lobes, when they are closer to broadside than the principal lobe, because this baseline element favors broadside radiation over wide-angle radiation.

Figures 2-10 and 2-11 show Smith chart plots of the active impedance of the baseline element, without and with a dielectric layer over the array, respectively. The active impedance varies with the beam scan angle, strictly as a result of mutual coupling, and the primary concern about the thick dielectric layer is its effect on mutual coupling. Therefore, the active impedance is useful for estimating sensitivity to the dielectric. (Actualy, most aspects of array performance can be calculated easily, if

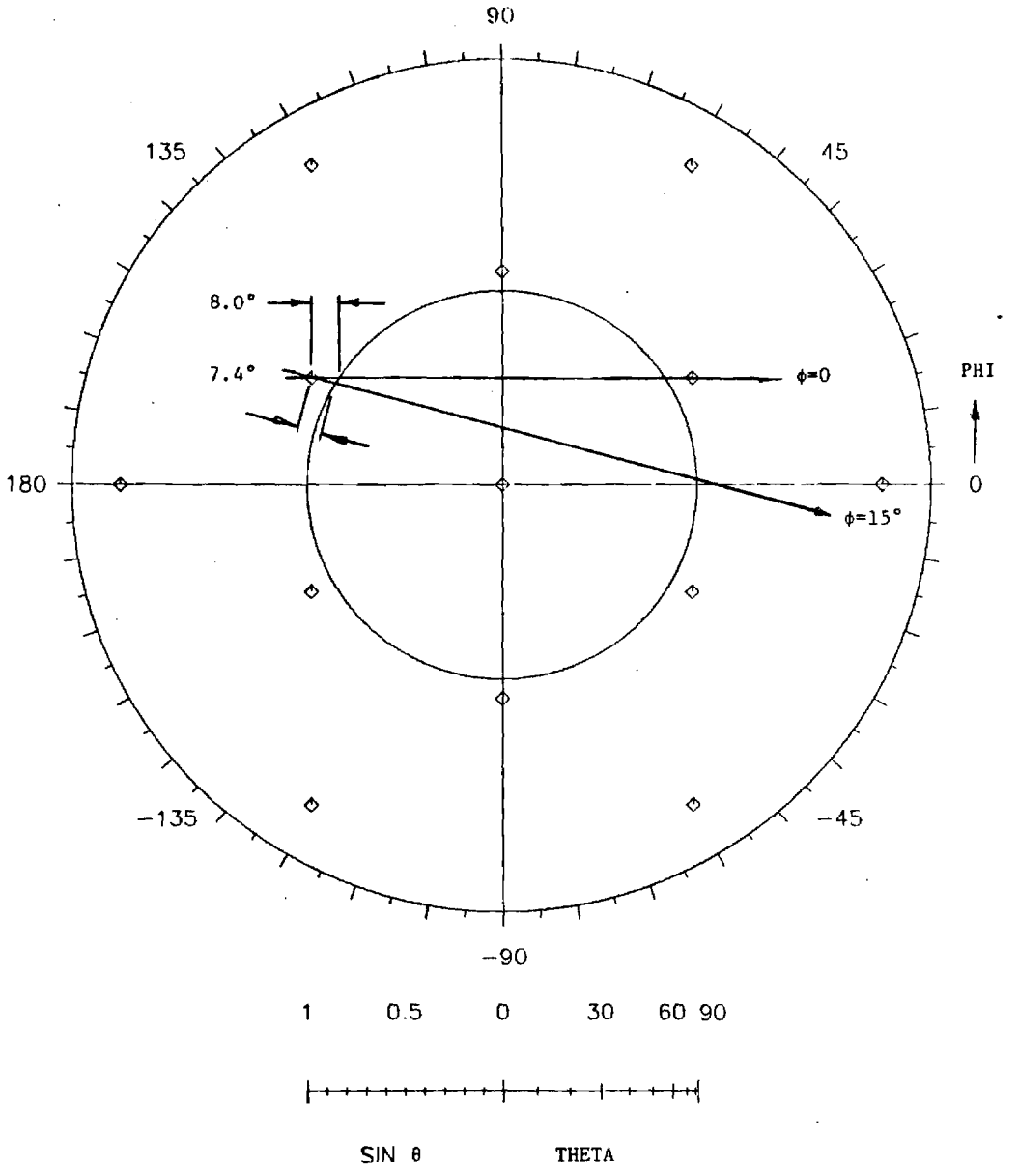

Figure 2-7. Grating lobe diagram for baseline configuration.

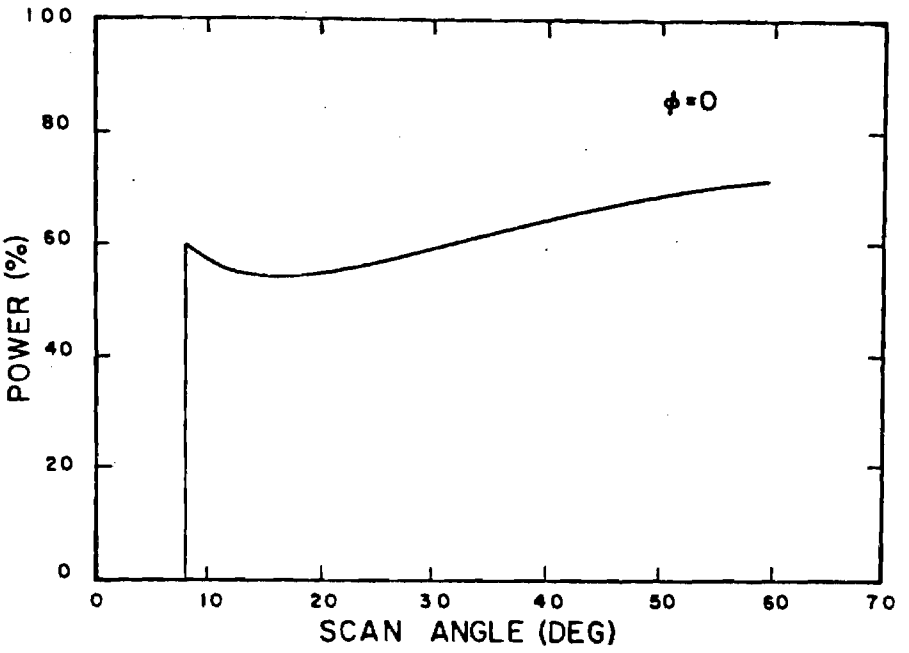

(a) Horizontal Polarization

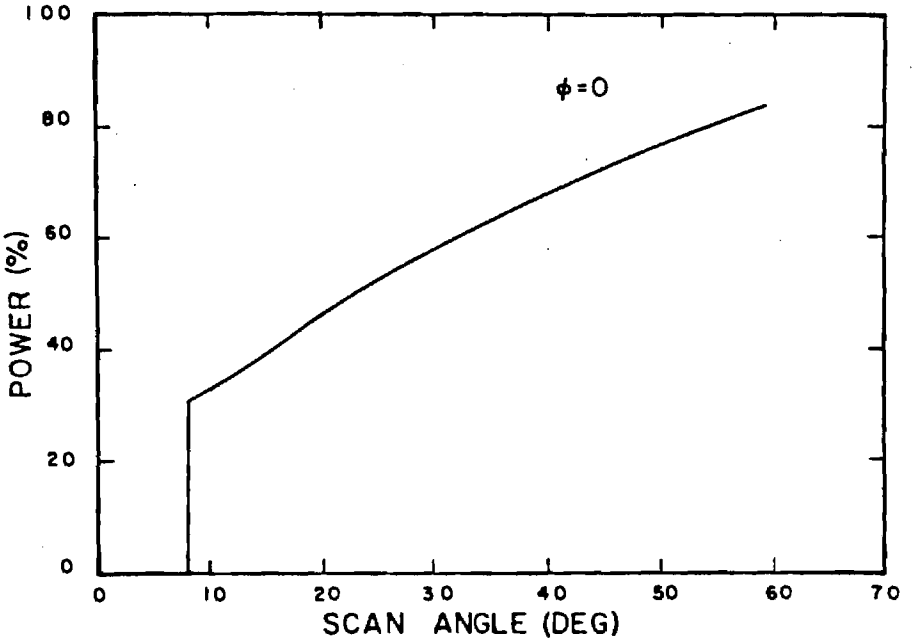

(b) Vertical Polarization

Figure 2-8. Power lost through grating lobe radiation, with no dielectric layer.

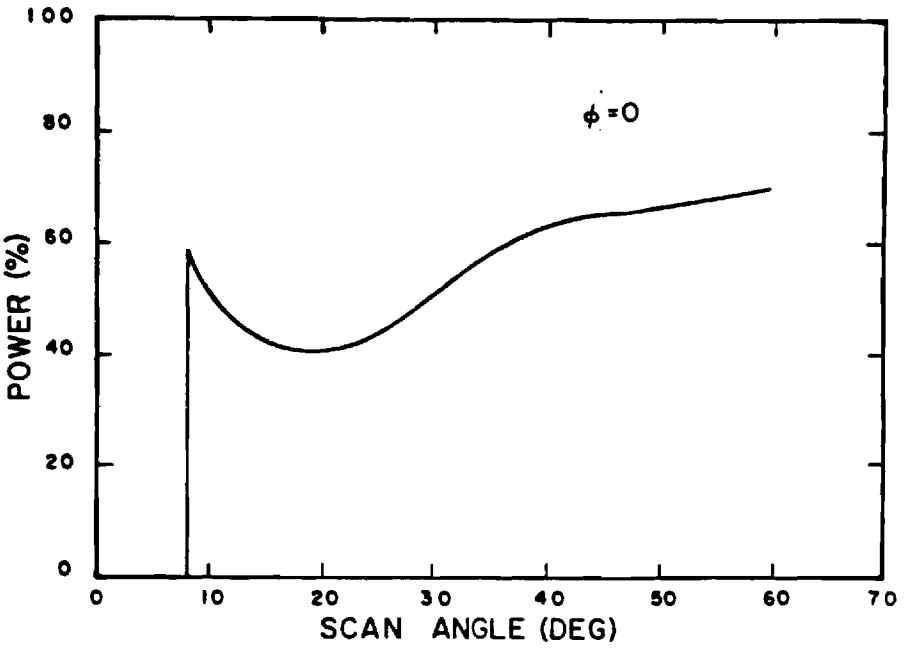

(a) Horizontal Polarization

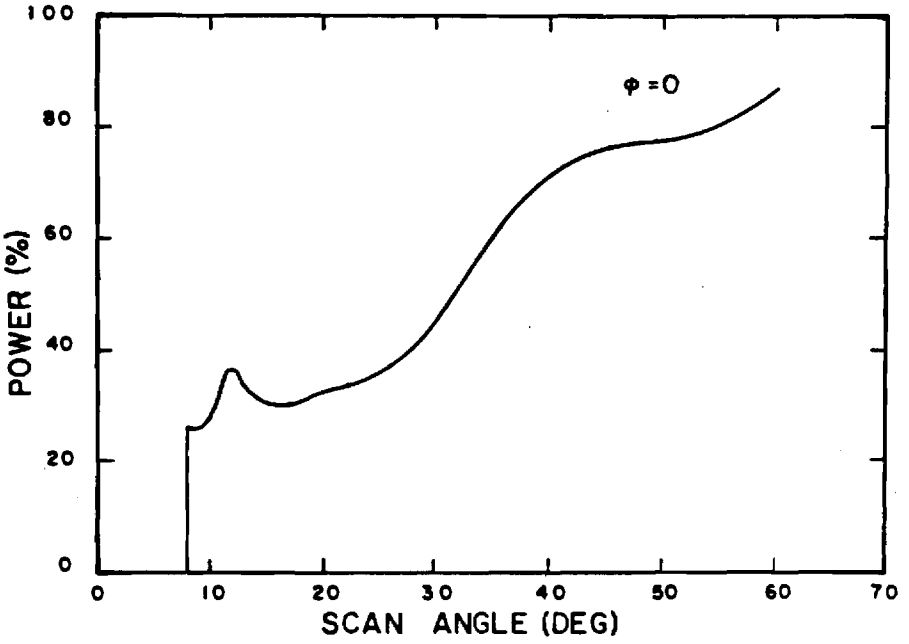

(b) Vertical Polarization

Figure 2-9. Power lost through grating lobe radiation, with dielectric layer.

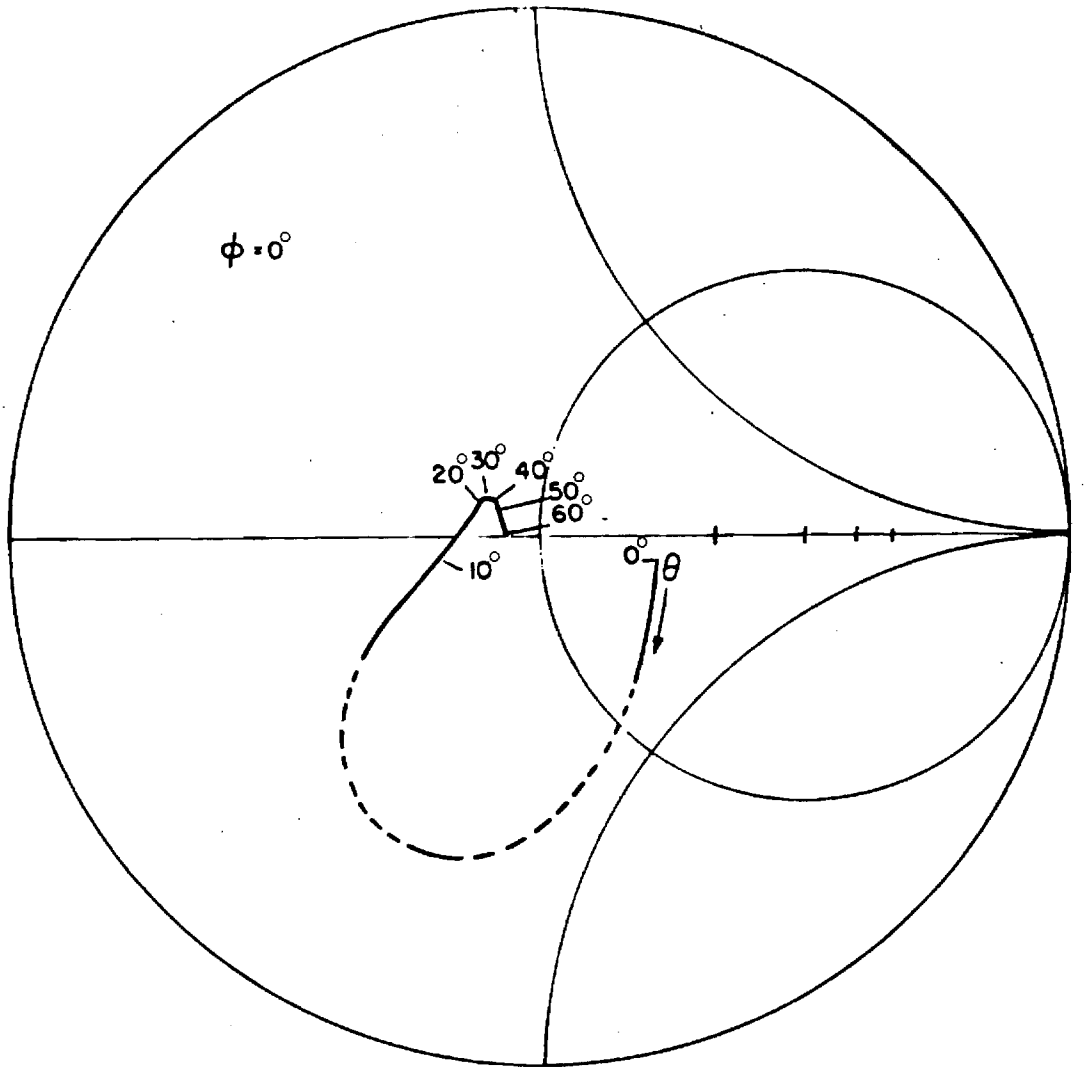

Figure 2-10. Active impedance for infinite planar array, with no dielectric layer (horizontal polarization).

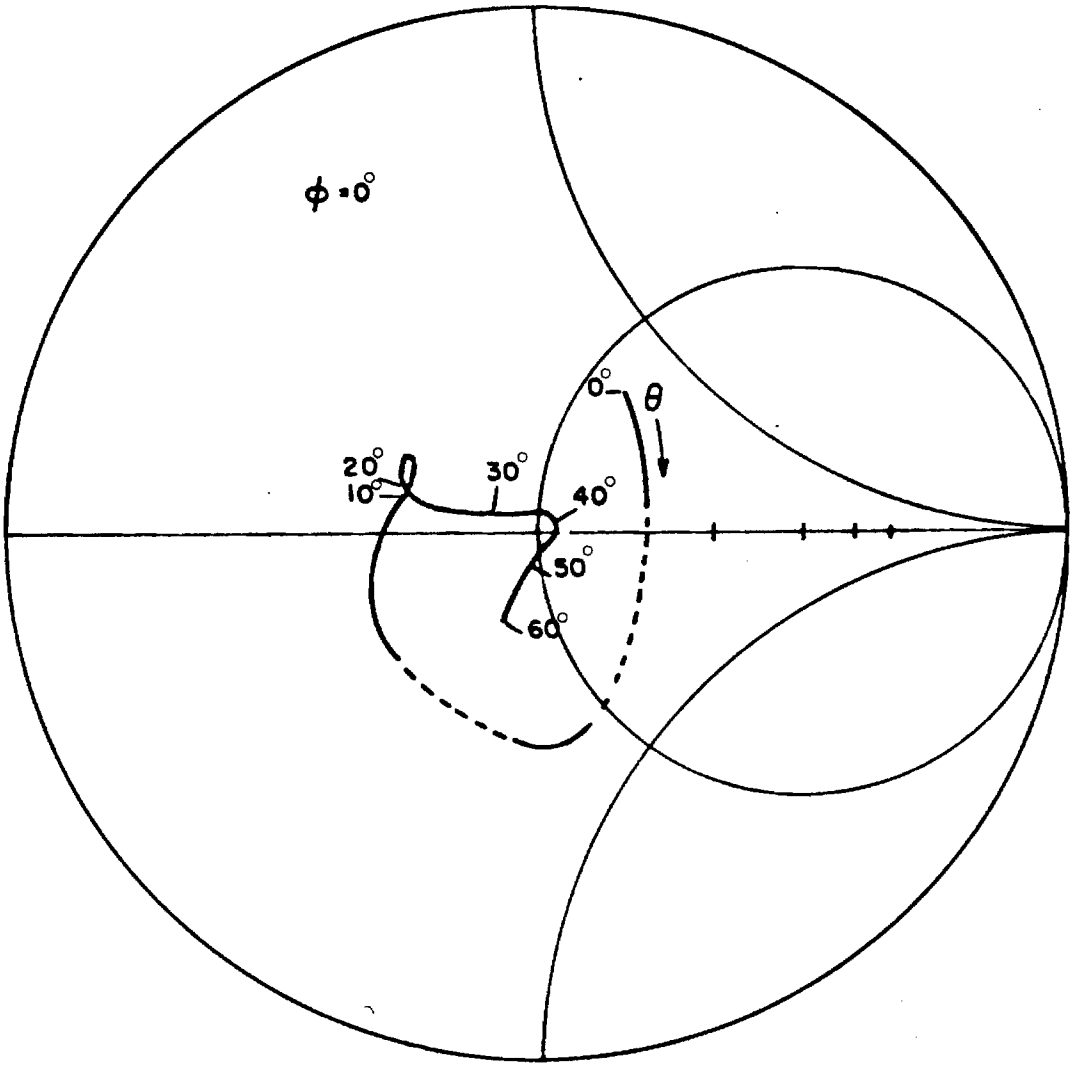

Figure 2-11. Active impedance for infinite planar array, with dielectric layer (horizontal polarization).

the active impedance is known.) In this example, the dielectric has relatively little effect on the impedance. The effect is small, because most of the coupling occurs near the array face, and the dielectric layer is spaced away from the face by a reasonable distance.

Although the final configuration has not been analyzed, these results suggest that the dielectric layer should be of secondary importance in the design of the antenna. In other words, the dielectric should behave more like a separate radome than like an integral part of the antenna.

SECTION III
TECHNIQUES DEVELOPMENT

During this research program, several microwave measurement techniques have been developed, or at least investigated, for possible use in the evaluation of hardened phased-array antennas and components. This section includes discussions of work on high-temperature dielectric measurements, multielement phased-array simulators, and six-port network analyzers. Associated technical discussions and theoretical analyses are contained in Appendices A through D.

A. Dielectric Measurements

There is a continuing need to characterize the high-temperature behavior of dielectric materials for use in BMD antennas. Ground-based phased arrays must survive the intense radiant heat of nuclear explosions, and interceptor-based antennas must survive the aerodynamic heating caused by hypersonic velocities. In both cases, exposed surfaces may reach temperatures in the range of 1,000°C to 2,000°C. The face of either antenna may be formed by dielectric-plugged waveguide elements or by a continuous dielectric window, and the antenna performance may be quite sensitive to heat-induced changes in dielectric properties of the window.

The radiant thermal environment can be simulated in a large solar furnace, and the CNRS 1,000 kW furnace at Odeillo, France, has been used for this purpose [3,4]. Subsection III. A.1 presents the results of solar furnace tests to evaluate a selection of refractory cements. Such material has been used previously in nuclear-hardened communications antennas [9,10], and in previous work on the present program, it has been suggested as a candidate for the face of large, low-frequency (UHF) dipole arrays [1,2]. The tests revealed that the cement melts rather quickly; they also showed that the molten cement is electrically opaque.

The solar furnace tests have been useful primarily in screening components for electrical and structural survival of heating cycles. The basic microwave test is a simple insertion measurement, which does not yield enough information to determine, for example, the dielectric constant and loss tangent of a material being tested. The two dielectric measurement techniques discussed in Subsections III. A.2 and III. A.3 have

been investigated as potentially useful supplements to the solar furnace tests. These particular methods were selected, because they are compatible with the circular-disk samples that are used in the solar furnace.

1. Refractory Cements

Refractory cement was identified in the early phases of this research program as a candidate for encapsulating the face of a physically large dipole array [1,2]. As part of the current phase of this program, samples of five types of cement were prepared and included in solar furnace tests. The tests were actually conducted under a separate, but related, research program, which is discussed in detail elsewhere [3,4]. This subsection gives the results of the cement tests, with only a brief summary of the test procedure.

The tests were conducted in the French CNRS 1,000 kW Solar Furnace. A photograph of the paraboloidal concentrator and the Focal Building is shown in Figure 3-1(a), and the test area in the front of the Focal Building is shown in Figures 3-1(b). The facility normally produces a thermal flux of 200 to 300 cal/cm^2-sec on a two-inch diameter sample placed at the focal point, which is the center of the concentric rings in Figure 3-1(b). The outer aluminum panels are water-cooled, pneumatically-actuated shutters that slide on horizontal tracks in front of the test sample at the focal point. Heating is initiated by opening the shutters, and it is terminated either by closing the shutters or by dropping the sixty-three heliostats that illuminate the concentrator. (The heliostats are out of view, to the right, in Figure 3-1(a).)

The microwave tests consist of measurements of reflection from and transmission through a disk-shaped sample placed at the focal point of the furnace. The sample is held directly over the one-inch square aperture of an X-band horn by a slip-cast fused silica guard ring, as shown in Figure 3-2(a). The horn is excited through a reflectometer, to measure the incident and reflected signals, as shown in Figure 3-2(b). The signal transmitted through the sample is measured by a receiving horn that is placed four feet in front of the focal point, inside the foil-shielded vertical column shown in Figure 3-1(b). A schematic diagram of the microwave equipment configuration is provided in Figure 3-3.

The test procedure for a sample material normally involves the

(a) Concentrator and Focal Building.

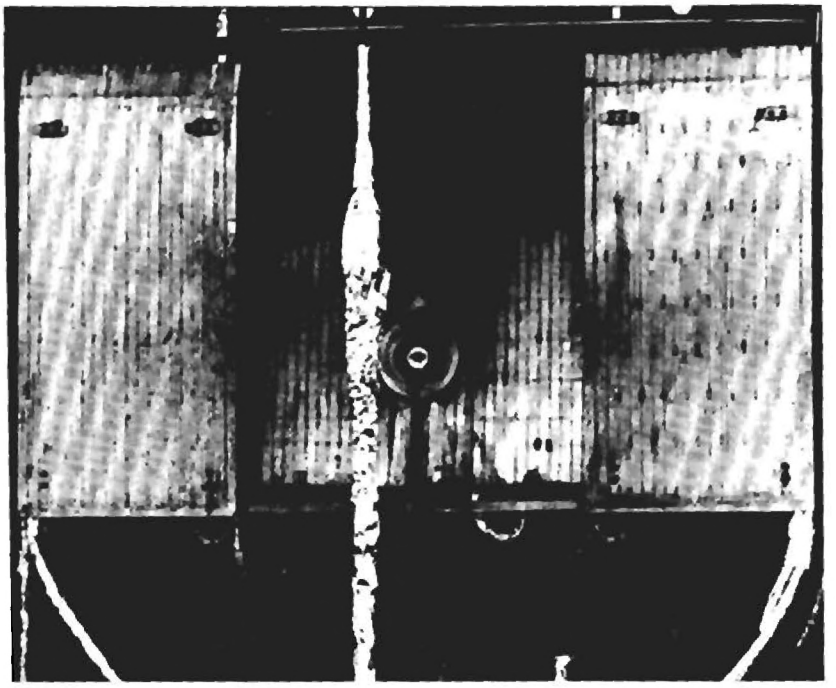

(b) Test area at front of Focal Building.

Figure 3-1. Photographs of the CNRS 1,000 kW Solar Furnace at Odeillo, France.

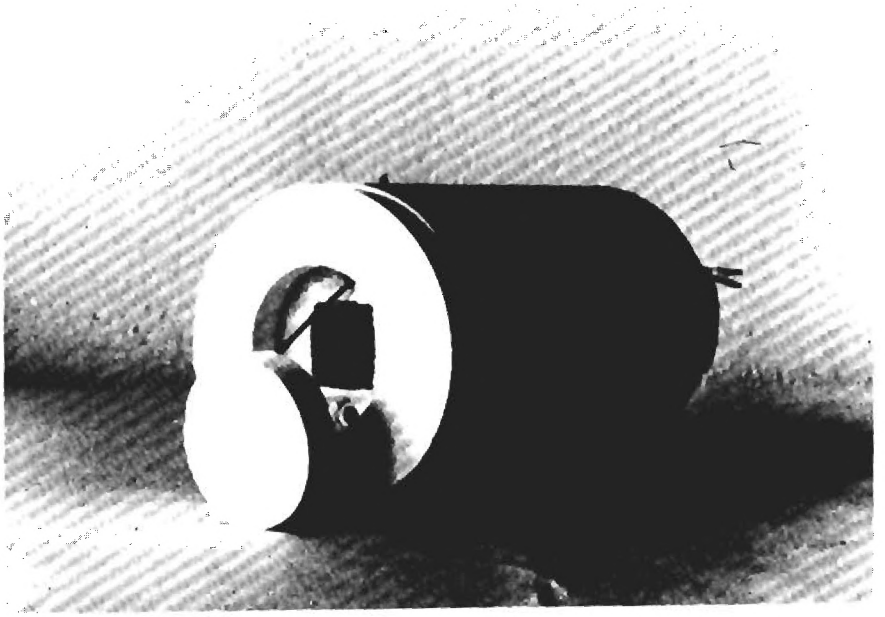

(a) Sample holder and horn aperture.

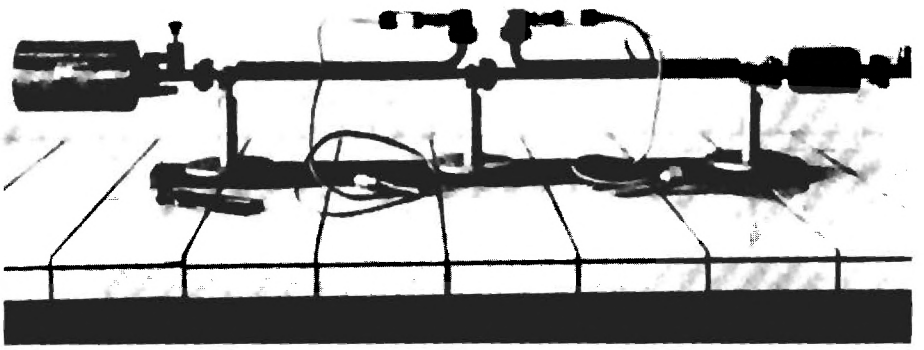

(b) Sample holder and waveguide reflectometer.

Figure 3-2. Photographs of microwave equipment for solar furnace tests.

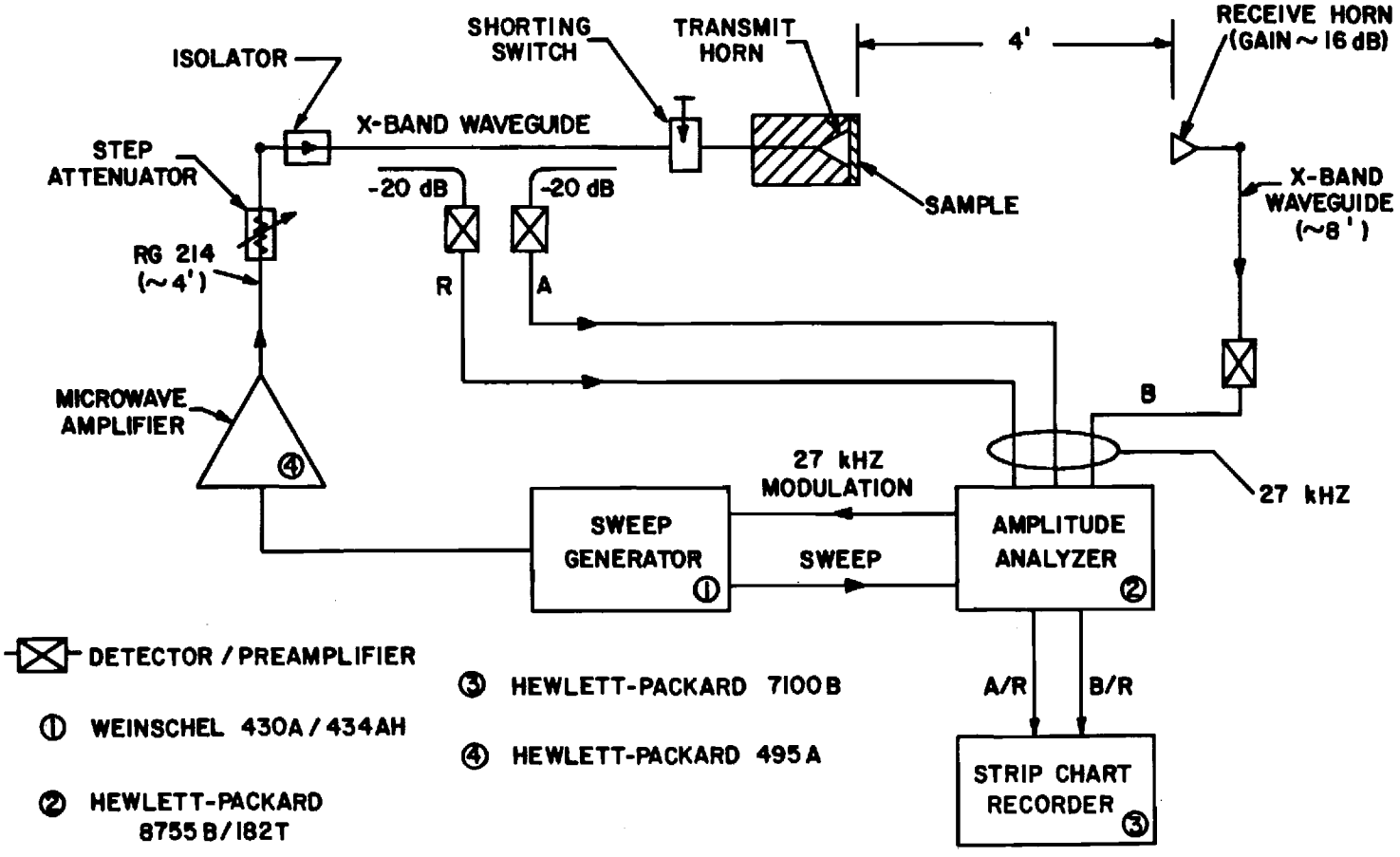

Figure 3-3. Diagram of microwave equipment for solar furnace tests.

recording of microwave reflection and transmission signal levels before, during, and after the heating period. Before and after heating, swept-frequency recordings are made, which show the signal variation over a nominal range of 8 to 12 GHz. During heating, continuous wave (CW) recordings are made at a fixed frequency of 10 GHz, to show the signal variation as a function of heating time. For microwave tests, heating is terminated by dropping the heliostats, and the CW recording is continued during a short period while the sample cools. Temperatures are measured by a chromel-alumel thermocouple, which is cemented to the back side of the sample, and by two pyrometers with bandpass filters at 0.65 and 5.6 microns, which view the front side of the sample. Motion pictures are recorded on color film.

The test results presented here are for five types of castable cement. Included are two brands of refractory aluminum oxide (Kaiser Puritab and A. P. Green Mizzon 3000) and three mixtures of Portland cement (white Portland with fused silica aggregate, white Portland with sand, and grey Portland with sand). Although the Portland mixtures are not highly refractory, they were included because they can be made very white and, therefore, relatively reflective to the radiant heat. The Kaiser Puritab has been used to encapsulate hardened communications antennas [9 , 10], but in that application the selection was based primarily on low-loss dielectric properties, and there was no data available on thermal survivability.

Post-test photographs of the Kaiser Puritab and the white Portland with fused silica are shown in Figure 3-4, and these are typical of all cement samples tested. In all cases, melting began within two seconds after the start of heating, and the molten material flowed like water. The Kaiser Puritab survived slightly longer than the other materials.

Figures 3-5 through 3-9 show the CW microwave recordings for the five cement samples, during the heating and cooling period. In all cases, microwave transmission through the sample is completely attenuated, when the surface becomes molten, and the transmission returns as soon as the heat is removed and the surface solidifies. In the first case, that of Figure 3-5, the heat was stopped by closing the shutters, and the recovery of transmission cannot be seen; but for the remaining cases, the heat was stopped by dropping the heliostats. Because these tests clearly show that

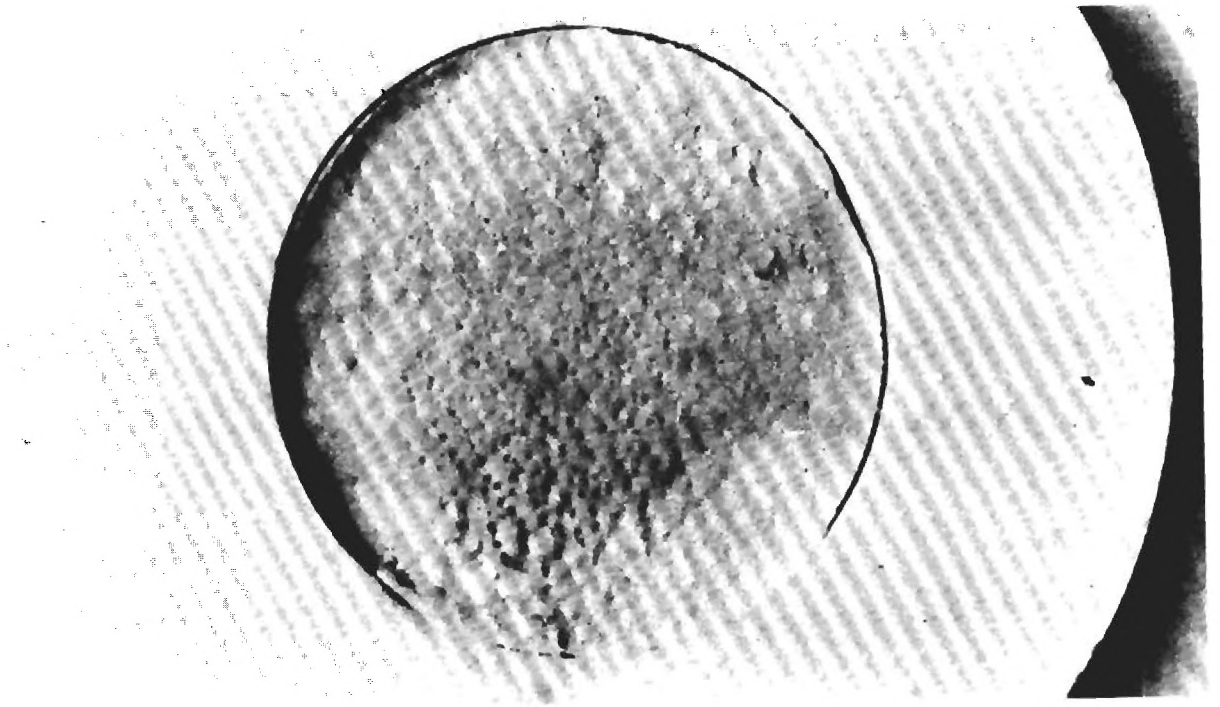

(a) Aluminum Oxide
(Kaiser Puritab)

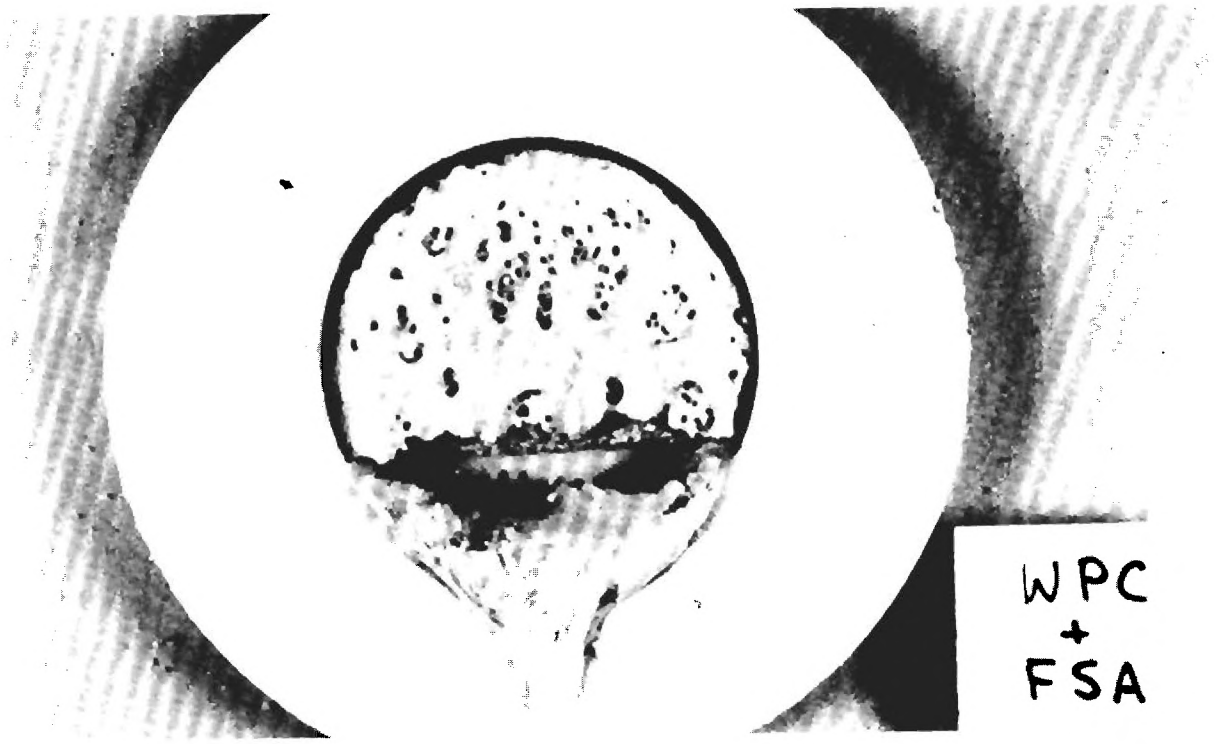

(b) White Portland Cement
with fused silica aggregate

Figure 3-4. Photographs of cement samples after test.

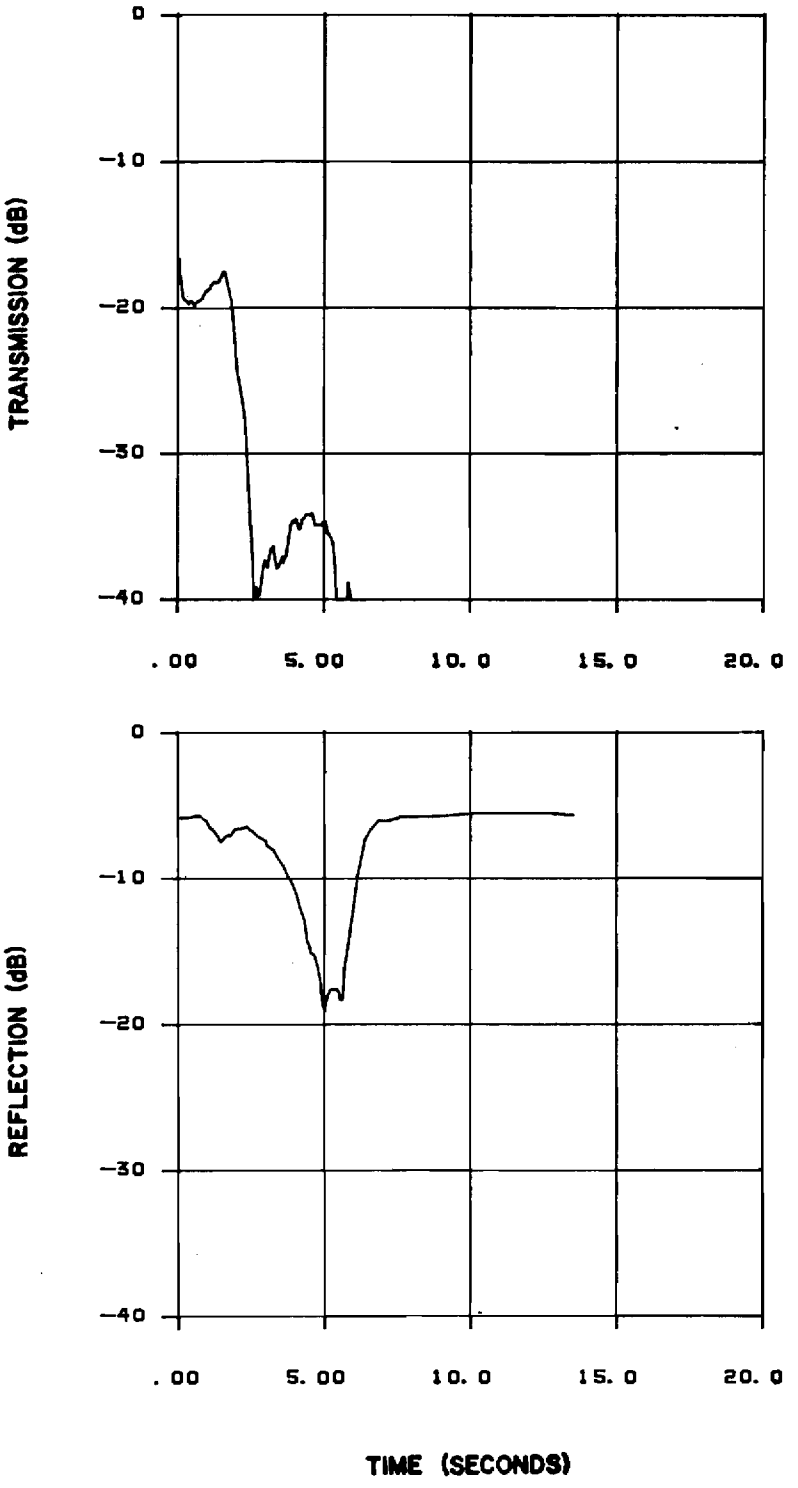

Figure 3-5. CW microwave data
Castable Aluminum Oxide
(Kaiser Puritab, 2" dia. x ½" thk.)
Incident Flux = 247 cal/cm^2

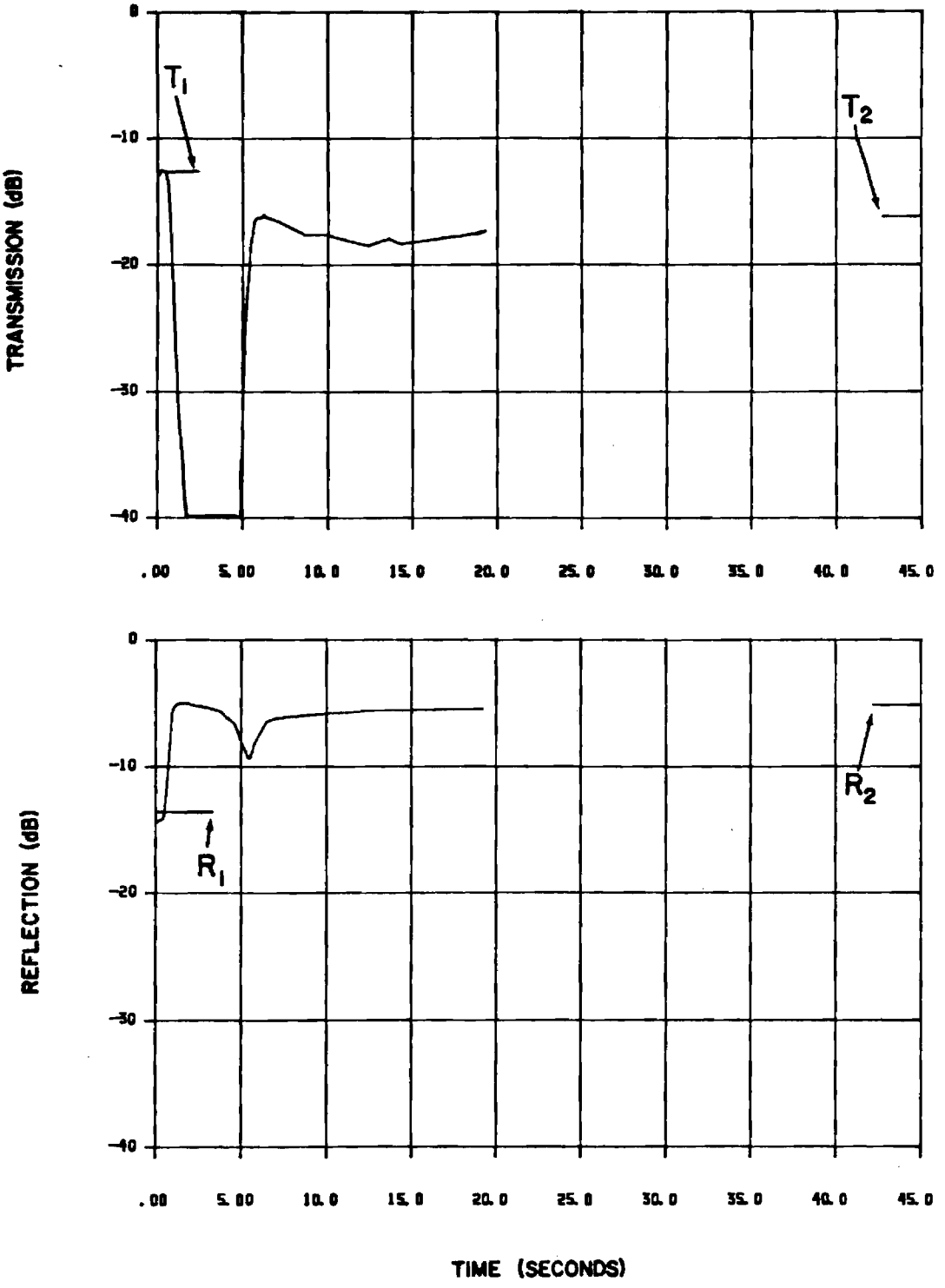

Figure 3-6. CW microwave data
Castable Aluminum Oxide
(A. P. Green Mizzou 3000, 2" dia. x ½" thk.)
Incident Flux = 222 cal/cm^2

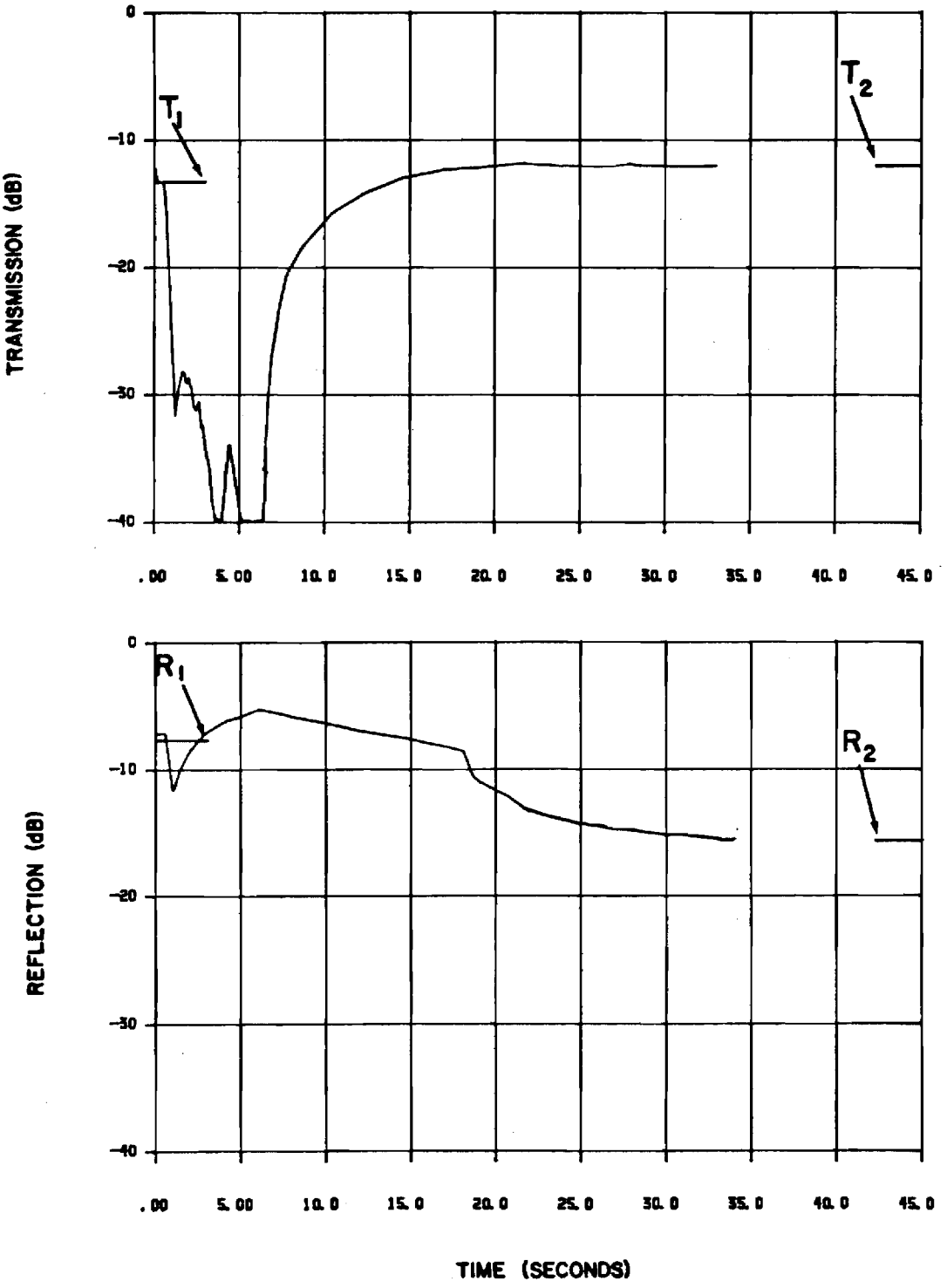

Figure 3-7. CW microwave data
White Portland cement/fused silica aggregate
(2" dia. x ½" thk.)
Incident Flux = 224 cal/cm^2

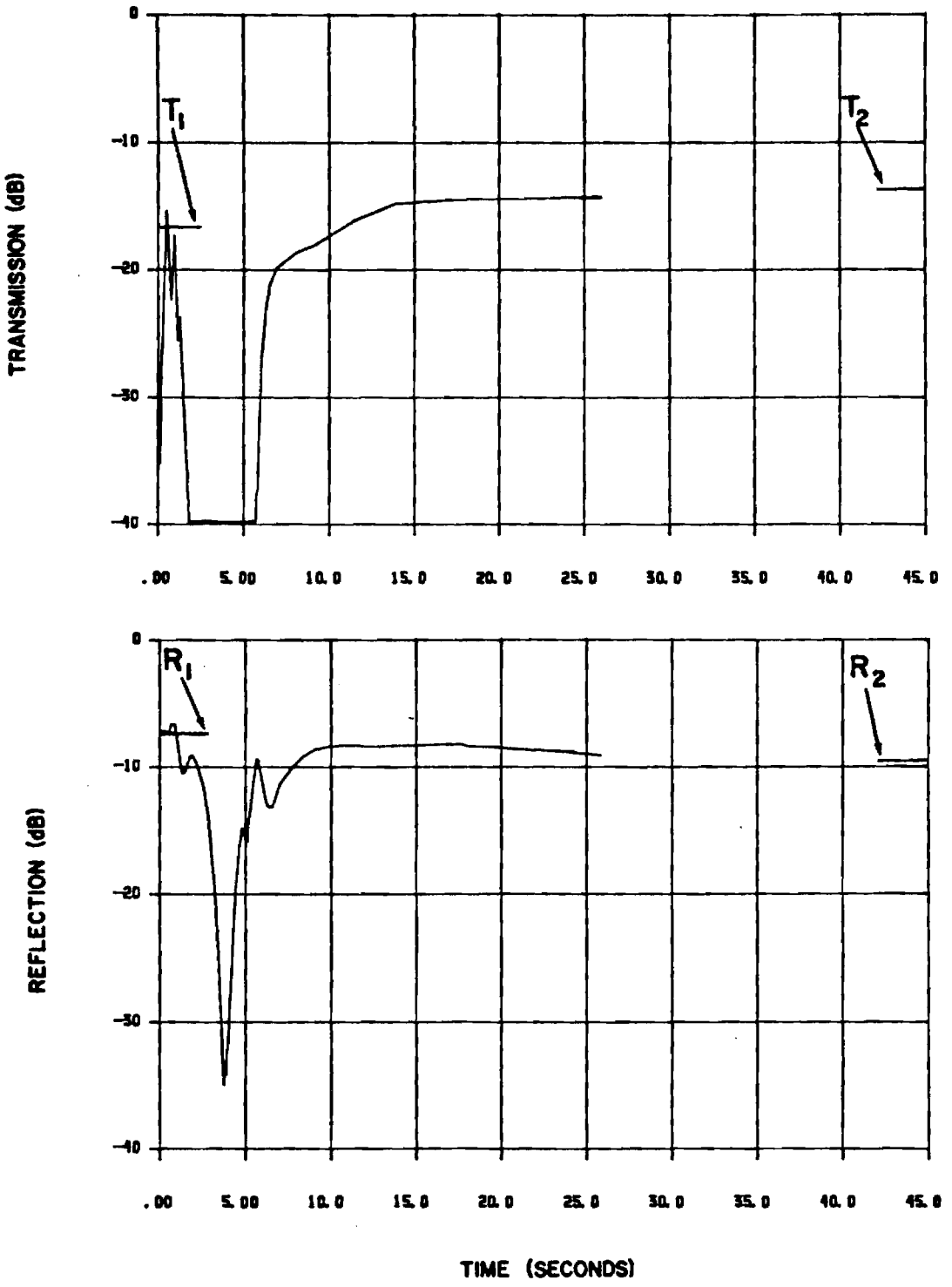

Figure 3-8. CW microwave data
White Portland cement/sand
(2" dia. x ½" thk.)
Incident Flux = 224 cal/cm^2

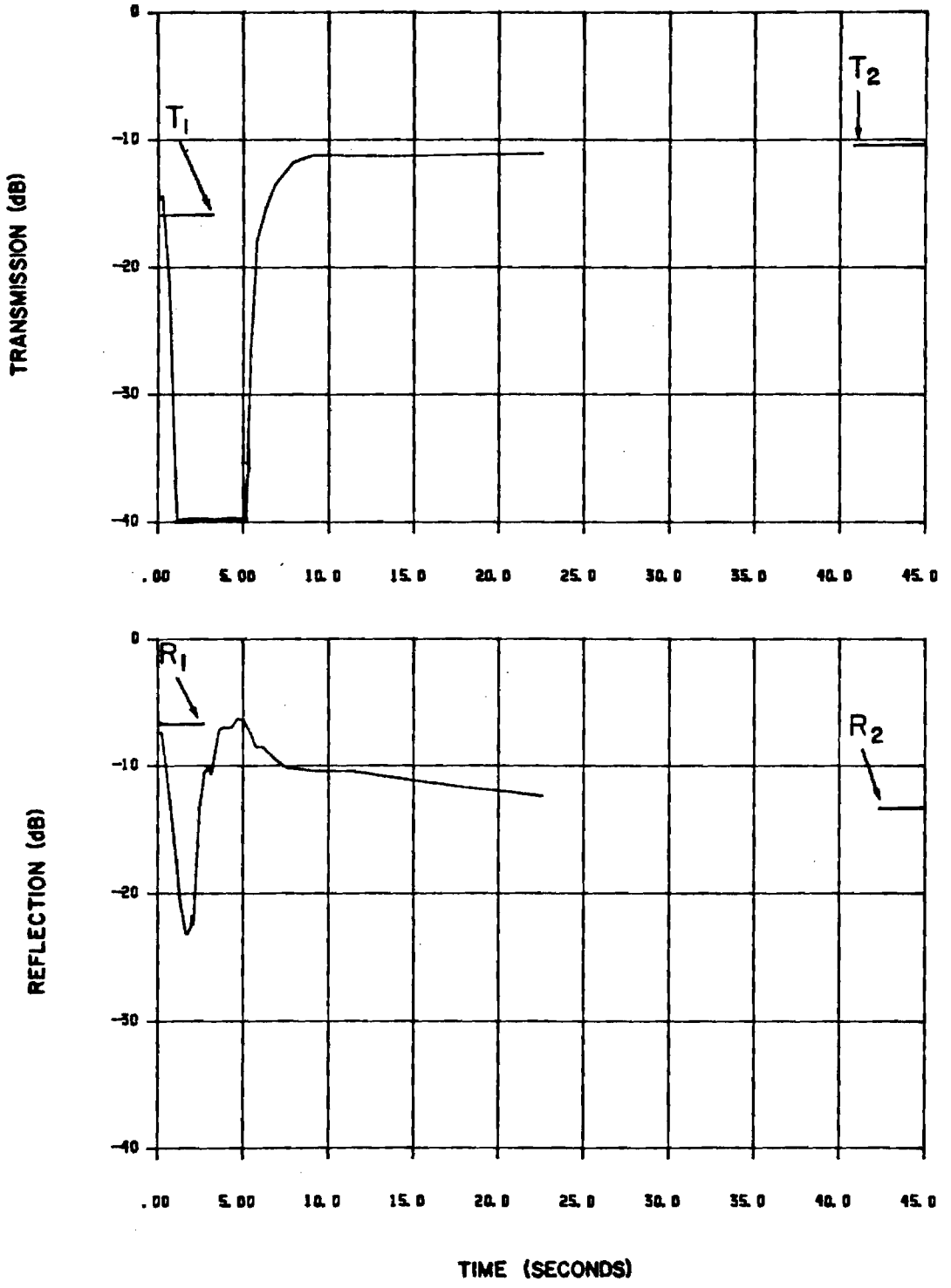

Figure 3-9. CW microwave data
Portland cement/sand
(2" dia. x ½" thk.)
Incident Flux = 223 cal/cm^2

all the cements fail at high heating rates, the swept-frequency data are not included here. The additional data will be presented in a separate report on the solar furnace test program [4].

Aluminum oxide-based refractory cement has good structural integrity, good dielectric properties (dielectric constant K = 5.89 and loss tangent tan d = 0.015 at room temperature), and a relatively high melting point (T_{melt} = 3,000°C). If the color were white, rather than grey, it might survive in the radiant environment. If interest in this material should develop (e.g., for large antenna structures), it would be worthwhile to consider coating the surface with a thin white layer of plasma-sprayed aluminum oxide. Materials and fabrication costs for such a configuration could be kept relatively low.

2. Solar Furnace Resonator

The measurement described in the preceeding subsection is useful for evaluating survivability of antenna components in an intense radiant environment, but it does not provide a direct measurement of high-temperature dielectric properties. The basic requirement for a dielectric measurement system is that the test configuration must be suitable for the development of an accurate theoretical model. Usually, either the entire configuration represents an exactly solvable electromagnetic boundary-value problem, or else insertion of a material sample causes a small, measurable perturbation from a known state. This subsection considers an example of a perturbation method, and the following subsection considers a method based on an exact boundary-value problem. To configure a solvable boundary-value problem, it is usually necessary to enclose the material sample in a metallic (highly conductive) holder. However, at temperatures above 1,000°C, most metals will oxidize, soften, melt, or react with the sample under test. This subsection outlines a perturbation method that allows the sample to be held in free space, at the focal point of a small solar furnace.

As part of work under a related materials test program [4], a small solar furnace at Georgia Tech is being configured for high-temperature measurements of absorbtivity at visible wavelengths, and this work on dielectric measurements was undertaken to determine whether the same furnace could be used for high-temperature dielectric measurements. The

conclusions are (1) heat-induced changes in dielectric constant can be measured with reasonably good accuracy; (2) absolute values for dielectric constants can be estimated without supplementary information; and (3) losses in low-loss dielectrics cannot be measured, at least, not without more work.

The small solar furnace is based on a 60-inch paraboloidal searchlight mirror, which is illuminated by a sun-tracking heliostat. An illustration is provided in Figure 3-10. Because the searchlight mirror is formed by silver on copper, it can also function as a collimating mirror for microwaves. When a microwave feed (e.g., a point source) is placed at the focal point, the searchlight mirror forms plane waves that are directed toward the heliostat. Introduction of a properly polarized, wire-grid ground plane, as shown, causes the plane waves to be returned to the feed at the focal point. The feed will scatter a portion of the returned energy, and a microwave resonator is formed whenever the scattered field is in phase with the directly radiated field. The relative phases can be adjusted by moving the ground plane or by changing the frequency, so a resonance can always be obtained. The resonance is also very sensitive to the insertion of a dielectric sample at the focal point. If the wire grid is designed properly, it will pass light from the heliostat with little blockage, and it will reflect nearly all of the microwave energy [11]. Therefore, a high quality (Q) microwave resonator can be formed without serious degradation of the solar heating capability.

The solar furnace resonator is no more suited to theoretical analysis than is the test configuration used in the French solar furnace; but as a resonator that can be repeatably reconfigured, it can function as a dielectric measurement instrument, when it is calibrated by a set of known dielectric samples, and it is well suited for measuring the change in an initially known dielectric constant, as the sample is heated. The basic concept for calibrating an arbitrary resonator for dielectric measurements, using a set of known materials, is defined as a standard test procedure under ASTM Standard Method C [12]. The concept is also discussed in electromagnetics texts [13].

The solar furnace resonator was simulated using a 36-inch reflector with a 10-inch focal length. A solid brass sheet was used for the ground

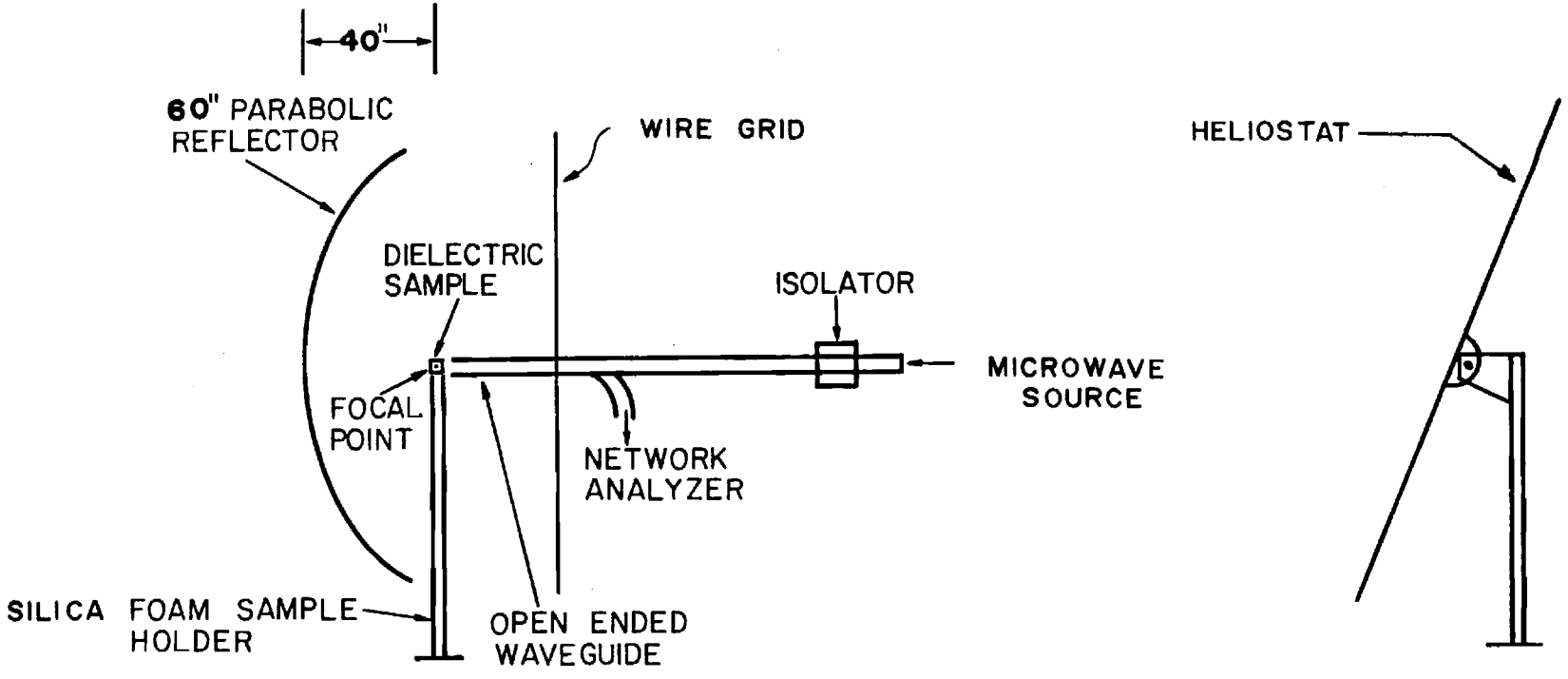

Figure 3-10. Solar furnace resonator with parabolic concentrator wire-grid,ground plane, and open ended waveguide feed.

plane, to save the cost of fabricating a grid structure. After several iterations, which are described in Appendix A, a configuration was discovered that produced repeatable resonances, and the dielectric constants shown in Table 3-1 were measured. In these cases, a single calibration standard, Plexiglas, was used. This material has a dielectric constant K = 2.59, and it is apparent that the error for other materials increases with the deviation of the test material from the standard. The useful range for dielectric measurements can be increased by calibrating the system with several standard materials that bracket the properties of the material under test, as prescribed in the ASTM Standard.

To measure dielectric loss with this resonator is difficult, because losses in the metal surfaces and losses due to scattering or leakage are greater than the dielectric loss. Although such a measurement may be feasible, it was judged to be beyond the scope of the preliminary investigation described here.

This test procedure was not pursued beyond an initial investigation for two reasons. First, with the very white ceramics that have been of most interest in this work, a solar furnace does not produce temperatures much above 1,000°C; and second, at temperatures below 1,000°C, better results can be obtained using metallic sample holders. This resonator could operate at higher temperatures, but another type of heating (e.g., convective, conductive, or inductive) would be required to reach the required temperatures.

3. Parallel-Plate Resonator

A microwave resonator can be formed, when a disk-shaped dielectric sample is placed between parallel metallic plates [16, 17]. This resonator can be used for precise dielectric measurements, and it is of particular interest in this work for at least two reasons. First, the resonator can accept the same disk-shaped samples that are to be tested in the French solar furnace; the faces of a circular disk must be parallel, but otherwise, there is no requirement that the sample be machined to fit a constrained volume. Second, the open resonator is better suited for high-temperature tests than a closed waveguide or cavity; the test volume is determined by the sample volume, and there is no requirement to account for differential thermal expansion between the sample and the sample holder.

TABLE 3-1

Dielectric Constants Measured with a Simulated Solar Furnace Resonator*

Material	Dielectric Constant (K) Referenced (**)	Measured	Difference (%)
Polyethelene	2.25 (1)	2.35	+4.4
Rexolite 1422	2.54 (1)	2.54	0.0
Nylon	3.00 (1)	2.96	-1.3
Silica (SCFS)	3.46 (2)	3.14	-7.6
Stycast	4.0 (3)	3.49	-12.7

*Calibrated with Plexiglas, K = 2.59.

** (1) [14]
(2) [15]
(3) Manufacturer's Data

A preliminary design for a parallel-plate resonator was developed and tested. The configuation is illustrated in Figures 3-11 and 3-12. The sample is placed between parallel metallic plates, one of which forms the top wall of a standard (WR-90) rectangular waveguide. With dimensions and frequency adjusted properly, a TE_{011} mode will resonate in the sample, and only the evanescent fields of that mode will exist outside the sample. The theoretical analysis of this resonator is provided in Appendices B and C. The mode can be excited by coupling a source through a slot to the evanescent region of the resonator. A transmission resonator is formed by similarly coupling a detector through another slot. Because here the two slots are cut in the top wall of the same waveguide, it is necessary to block direct transmission through the waveguide by the insertion of a waveguide short. The strength of the slot coupling is determined by the size of the slot and by the offset of the slot from the waveguide centerline. With the top wall attached to the waveguide by screws, as shown in Figure 3-12, the coupling can be adjusted by sliding the slotted wall across the waveguide. The upper plate of the resonator is supported by the dielectric sample.

Preliminary experiments showed that a variety of samples had resonances near the frequencies that were predicted by the analytical model. The samples tested had dielectric constants in the range of 2.25 for polyethelene to 4.0 for stycast. Several of the samples had reasonably high Q values (500-1000). If the samples were displaced in the cavity slightly, there was a minimal effect on the resonance frequency, as is shown in Figure 3-13. However, at non-resonant frequencies the slot-to-slot coupling was stronger than desired. Also, there were some very sharp and deep anti-resonances. These seemed to be caused by the interaction of the energy passing down the waveguide through the slot and the energy that was reflected off the shorting wall. These anti-resonances occurred just below or just above the resonant frequency and distorted the resonance curves. These anti-resonances were removed by placing a piece of absorber against the waveguide shorts. The improvement is evident in Figure 3-14.

Further investigation of the preliminary design showed that there was some leakage of the microwave energy through cracks arounds the top wall of the waveguide. Therefore, the wall was soldered in a position of optimum

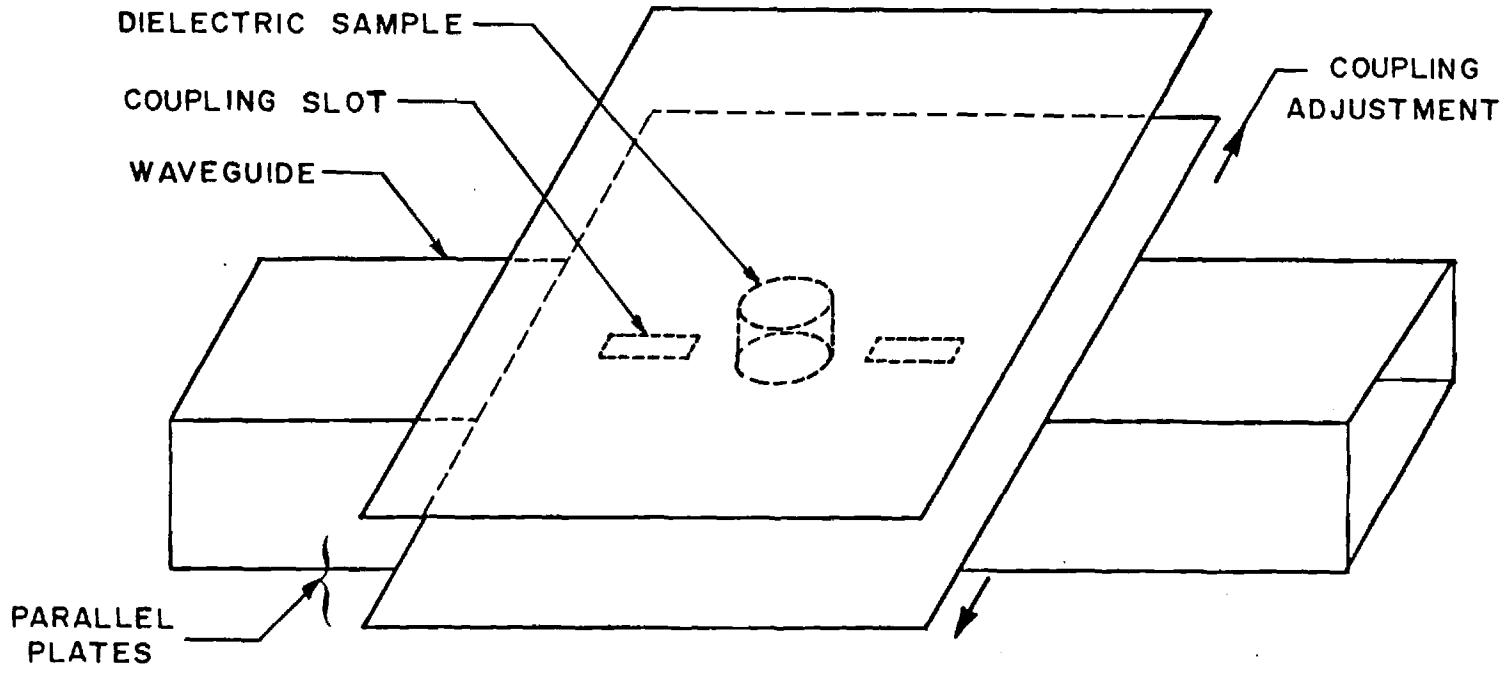

Figure 3-11. Cavity resonator with dielectric sample and top plate in place. Horizontal displacement of slots changes the coupling into the cavity.

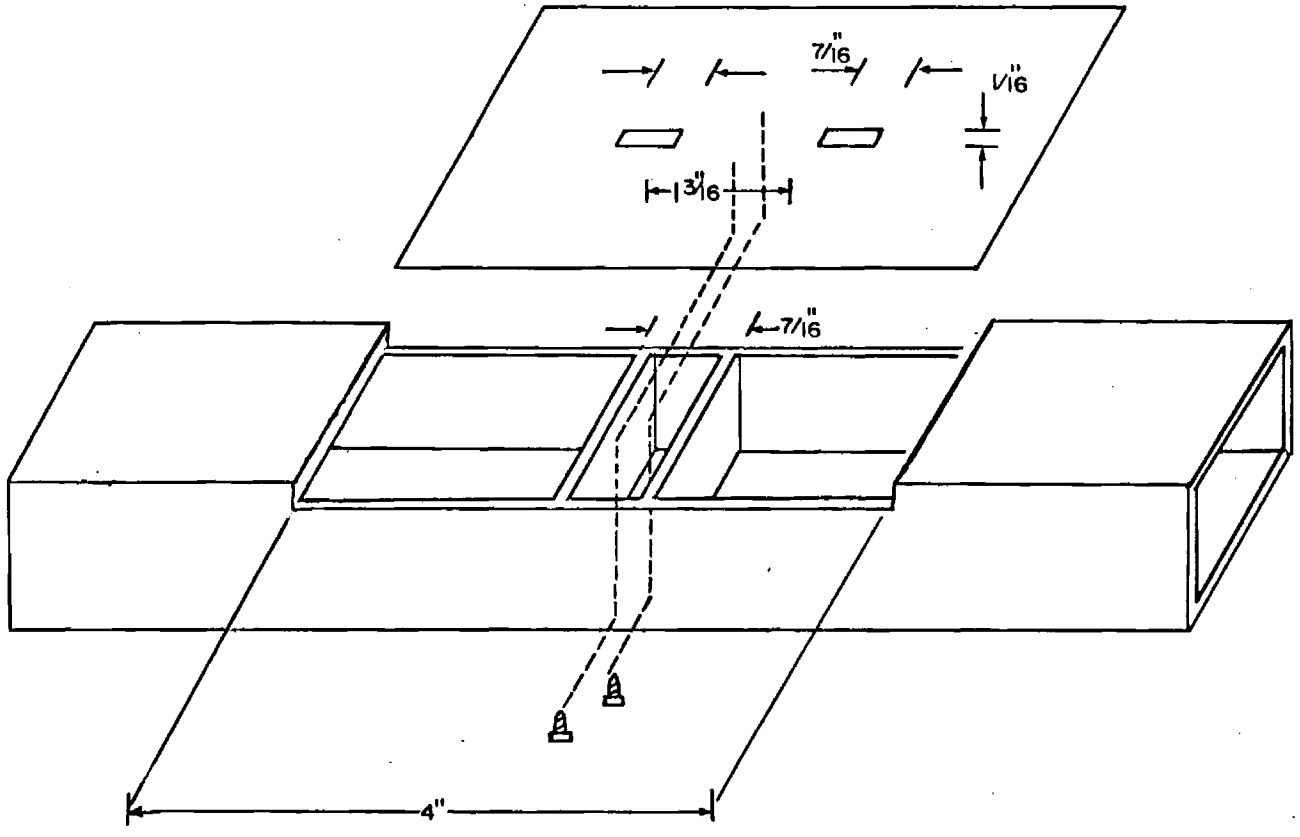

Figure 3-12. Exploded view of bottom plate of the cavity resonator.

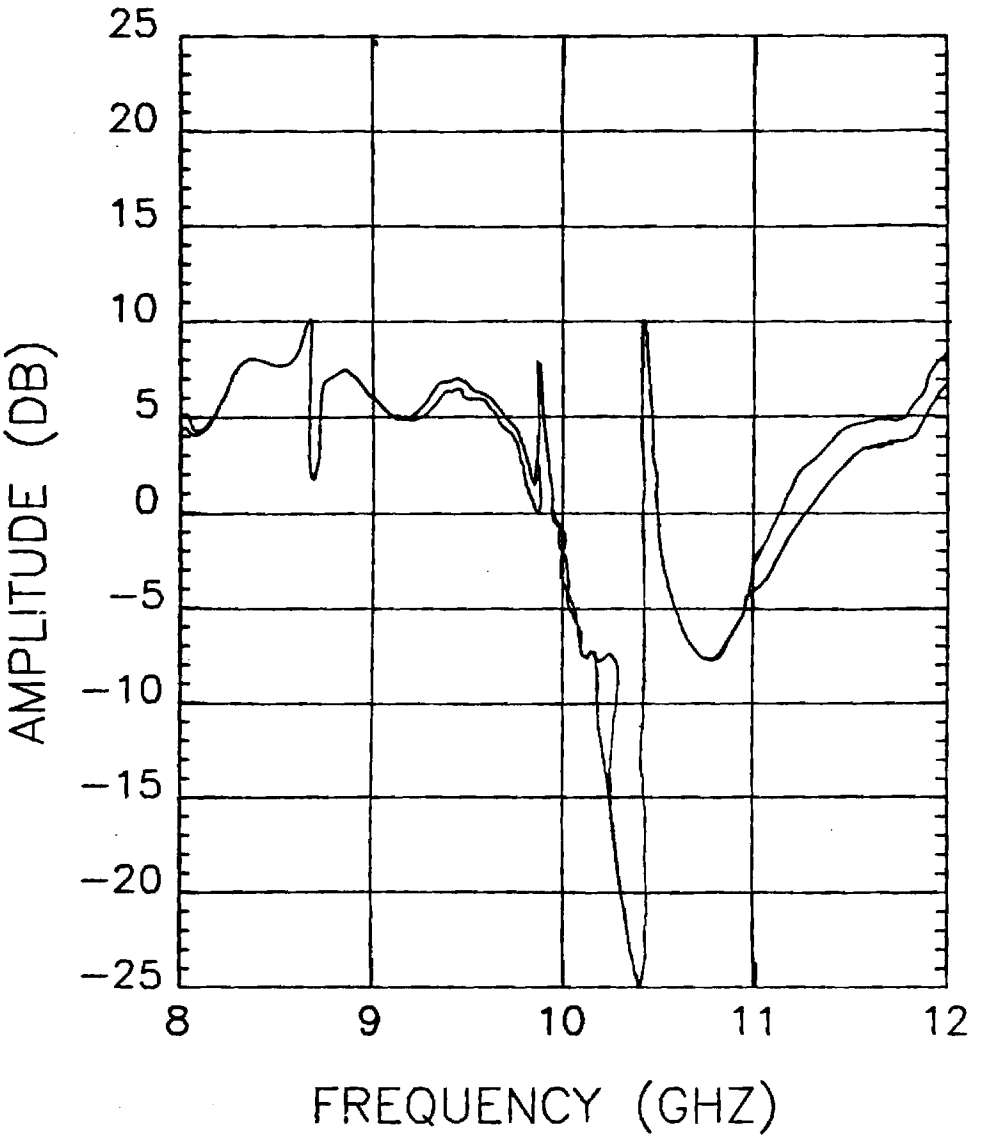

Figure 3-13. Swept-frequency plot for a cylindrical Rexolite sample in two positions in the resonant cavity.

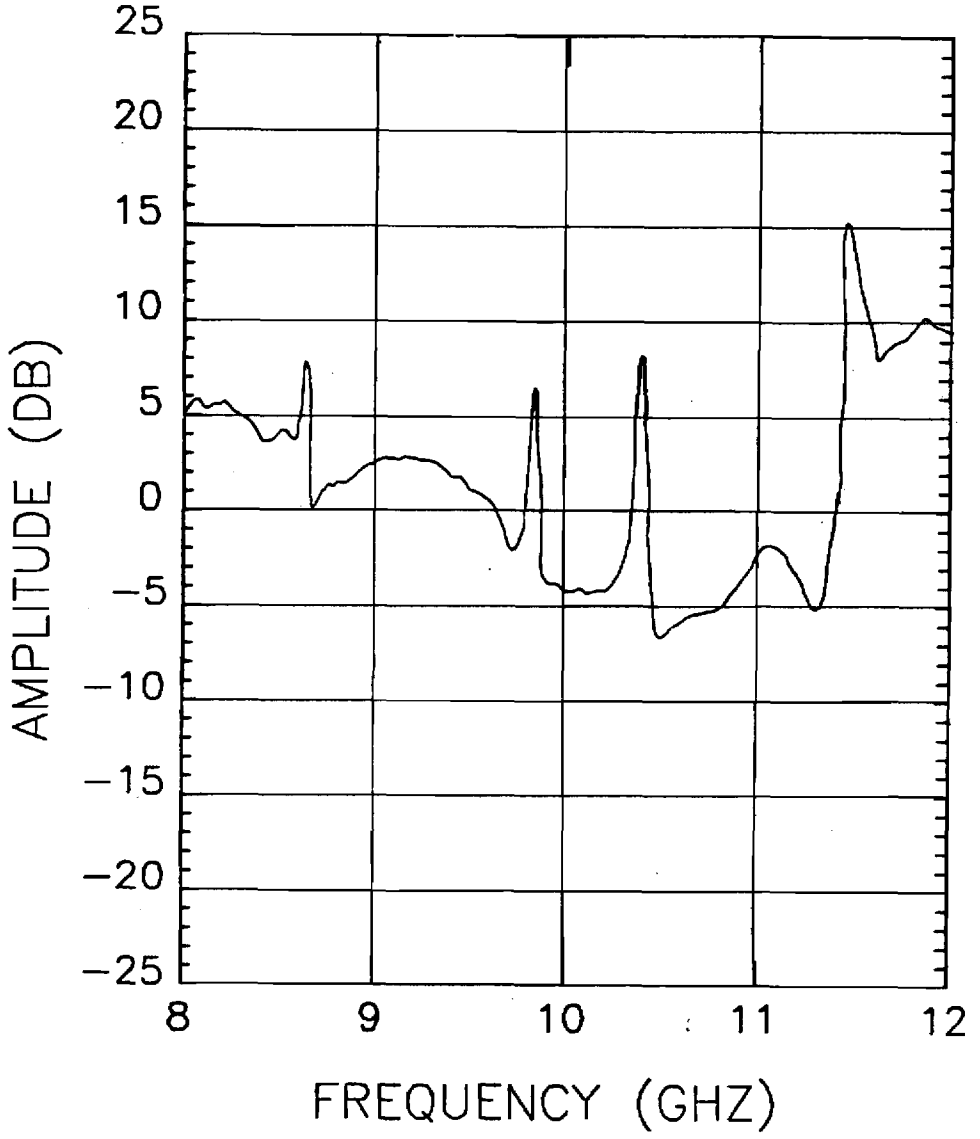

Figure 3-14. Swept-frequency plot for a cylindrical Rexolite sample in resonant cavity, with absorber placed against the shorts.

coupling. The solder reduced the leakage to zero and all of the samples produced well defined resonances with no anti-resonances. Sample data is shown in Figure 3-15. A summary of the measurement data is given in Table 3-2. The dielectric constants and loss tangents were calculated and then compared to known values and previous measurements. This data is presented in Table 3-3.

Although a high-temperature version of this resonator was not implemented, the concept that was demonstrated is very suitable. For temperatures to about 1,000°C, the sample holder could be made of copper, probably as an electroformed unit. For temperatures to about 1,500°C, nickel could be used, and for higher temperatures, a refractory metal such as tantalum could be used. Any of these metals should be held in an inert atmosphere, such as nitrogen or argon, to prevent oxidation at high temperatures. Platinum could be used in air at temperatures close to 1,500°C, if material costs were not a consideration.

In the course of this work, Georgia Tech learned that a high-temperature sample holder had been developed for the Air Force by the Aerospace Corporation and that it possibly could be transferred to Georgia Tech for use on BMD programs [18]. The sample holder is a circular waveguide made from tantalum tubing. It is held in a vacuum chamber, and it can be heated by electron bombardment to temperatures exceeding 2,000°C. An investigation was started to evaluate the equipment and to determine how to transfer it to Georgia Tech. The actual transferral of property will occur under a subsequent contractual effort, and it appears the equipment will be quite useful.

B. Phased-Array Simulators

The design process for elements of large phased-array antennas must some way take into account the effect of mutual coupling between elements. The relative phasing of the coupling between pairs of elements varies with the main-beam scan angle, so even where coupling between pairs of elements may seem to be small, coherent contributions from many elements can be very large. Therefore, an element may behave quite differently in a large array environment than it does in isolation. The difficulty in the design process is to approximate the large array environment, without actual fabrication of several hundred elements for each preliminary design iteration.

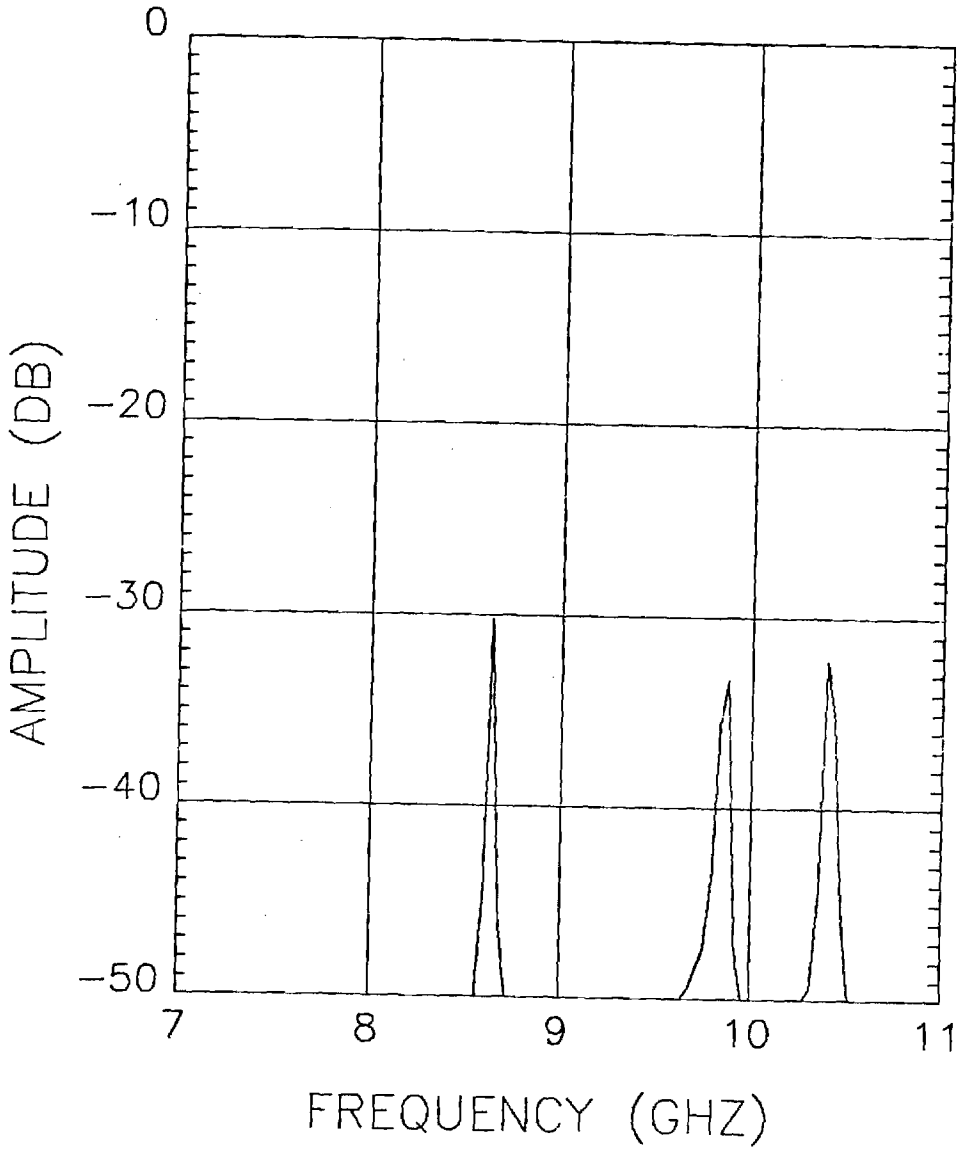

Figure 3-15. Swept-frequency plot for a cylindrical Rexolite sample, with absorber placed against the shorts, and with the top wall soldered to the waveguide.

TABLE 3-2

MEASUREMENT DATA FOR CYLINDRICAL SAMPLES

Material	Resonant Frequency (GHz)	Quality Factor
Polyethylene	10.334	1725
Polystyrene	9.929	1100
Rexolite 1422	9.883	1000
Lexan	9.685	125
Nylon 66	9.679	175
Plexiglas-1	9.560	190
Plexiglas-2	9.758	190
Silica	8.824	1100
Stycast	7.972	600

TABLE 3-3

DIELECTRIC PARAMETERS OF KNOWN MATERIALS

Material	Source*	Frequency GHz	Dielectric Constant	Loss Tangent
Polyethylene	1a	10.0	2.24	.0007
	2	10.3	2.33	.0004
	3	9.5	2.43	.0006
	4	9.0	2.44	.0059
Polystyrene	1a	10.0	2.54	.0004
	2	9.9	2.55	.0007
	3	9.5	2.62	.0008
	4	9.0	2.57	.0012
Plexiglas	1a	10.0	2.59	.0067
Plexiglas-1	2	9.7	2.66	.0043
Plexiglas-2	2	9.6	2.78	.0043
	3	9.5	2.74	.0085
	4	9.0	2.67	.0076
Rexolite 1422	1a	10.0	2.54	.0005
	2	9.9	2.58	.0008
Lexan	1b	3.0	2.77	.0052
	2	9.7	2.70	.0066
Nylon	1a	3.0	2.84-3.03	.0128
	2	9.7	2.71	.0045
Silica	1b	8.5	3.46	.0010
	2	8.8	3.31	.0007

* 1a: Tables of dielectric properties [14]
  1b: Tables of dielectric properties [15]
  2 : Cylindrical cavity measurements
  3 : Slotted line measurements
  4 : Network analyzer measurements

The waveguide simulator is one of the most useful experimental tools available for the development of phased-array elements [19,20]. The mutual coupling effects in an infinite array can be exactly duplicated with a finite subarray in a simulator, provided the elements satisfy certain symmetry requirements. The simulation is strictly valid only for a discrete set of scan angles, and the number of available angles is approximately equal to the number of elements in the subarray. Most work with simulators has been conducted with very small subarrays (one to three elements), for the purpose of matching the element at one scan angle, or to validate a theoretical model at one scan angle. The scan angle can be varied slightly by changing the frequency, and it has been demonstrated that the phased-array "blindness" effect can be exhibited in a simulator [21].

The possibility of using a larger, multielement simulator to study array elements at a number of scan angles has been recognized for some time [22]. The symmetry requirements for the existence of a valid waveguide simulator were shown to be requirements for the existence of a variational integral equation for the active admittance of the element. Larger simulators became practical after the explicit demonstration that the required data consists of the coupling coefficients between the elements in the simulator [23] and, especially, after the development of the microwave automatic network analyzer (ANA). For elements that are not amenable to theoretical and numerical analysis, the multielement simulator is a powerful design tool. The simulator can provide exact active impedance data at enough scan angles to permit a reasonable attempt at interpolation over the entire scan range.

The following subsections outline the analytical basis for the multielement simulator and describe equipment that has been assembled to perform measurements. The application of this technique to microstrip-array elements is discussed in Section IV.

1. Analytical Model

The basic idea behind the phased-array simulator is that conducting ground planes can be used to image a few regularly spaced elements so that they appear to form an infinite array of elements in a

periodic lattice. The element and lattice must satisfy certain symmetry conditions in order for the imaged configuration to provide boundary conditions that are equivalent to the infinite array. If these conditions are met, then at a finite, discrete set of scan angles, the active-element reflection coefficient (or impedance) for an element in the infinite array can be calculated from measurements of the coupling between elements in the imaged configuration.

The geometry for a general periodic array lattice is shown in Figure 3-16. The lattice is triangular, and the elements are indicated by circles. The triangular lattice an be interpreted as a superposition of two rectangular lattices, each of which has element spacings a and b, and which are offset by x=a/2, y=b/2. A rectangular lattice can be formed by deleting either of the two rectangular lattices in the composite. The symmetry requirements for existence of a rectangular simulator are that the boundary conditions for the array structure be invariant under the following operations [22]

(a) reflection in the (x,z)-plane,
(b) reflection in the (y,z)-plane, and
(c) 180 degree rotation around the z-axis.

If these conditions are satisfied, an imaging simulator can be formed by conducting planes that coincide with symmetry planes and are parallel with the z-axis. The blackened elements in Figure 3-16 can be contained inside a rectangular simulator with cross-sectional dimensions A by B.

The symmetry requirements imply that the element polarization must be linear and parallel with one of the simulator walls (i.e., horizontal, E_x, or vertical, E_y). A one-port element must conform to one of these cases, and a two-port element that produces two orthogonal polarizations must be excited to generate one of these cases. Results obtained with the two linear polarizations of a two-port element can be combined to yield the reflection coefficient for arbitrary polarizations [24].

The symmetry requirements also imply that the infinite array can be excited in such a way that null planes (tangential E=0) form where simulator walls are desired. In such a case, insertion of conducting planes along the null planes creates no disturbance of the field, and the elements contained within the simulator cross-section excite a single mode

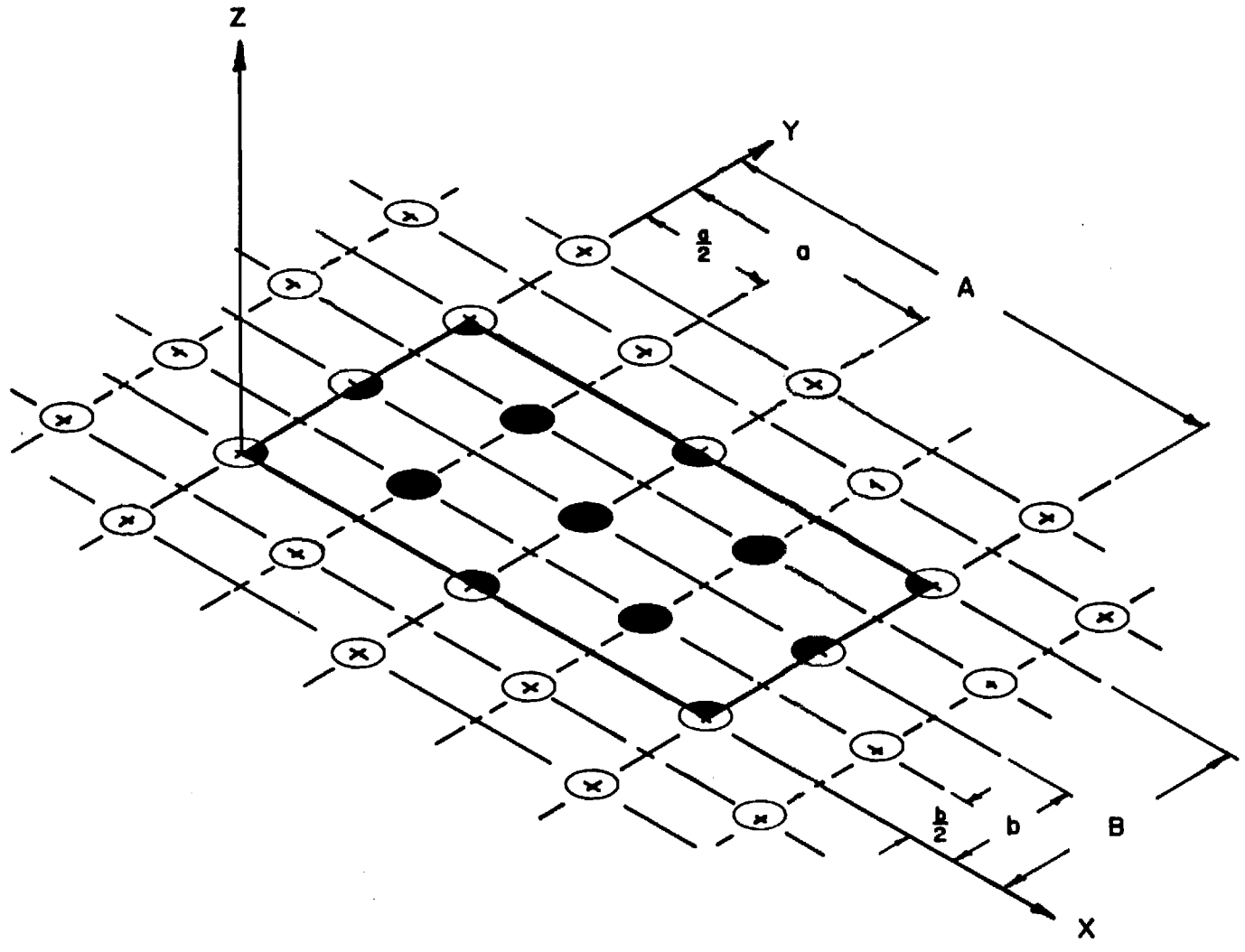

Figure 3-16. Array geometry for simulator analysis.

in the simulator waveguide. It is well known that rectangular waveguide modes can be represented by a superposition of four symmetrically diverging plane waves, and it follows that the required excitation for the infinite array is the superposition of four symmetrically diverging beams. Symmetry ensures that each beam has the same reflection coefficient. The point to be demonstrated is the connection between coupling measurements in the simulator and the active reflection coefficient in the infinite array.

To form a single beam at an angle (θ_o,ϕ_o), the elements of the infinite array are phased so that the excitation of the (u,v)-th element is

$$a_{uv} = \exp\ (j\ U\ K_x + j\ V\ K_y) \quad , \tag{3-1}$$

where

$$K_x = k_x a = k_o a \sin\theta_o \cos\phi_o, \tag{3-2a}$$
$$K_y = k_y b = k_o b \sin\theta_o \sin\phi_o, \tag{3-2b}$$

with free-space phase constant k_o. Depending on which of the two offset rectangular lattices, R_o or R_1, contains the element,

$$U = u, \quad V = v, \qquad \text{(Lattice } R_o\text{)}$$

or

$$U = u + \tfrac{1}{2}, V = v + \tfrac{1}{2}, \qquad \text{(Lattice } R_1\text{)},$$

where u and v are integers that identify lattice points, and R_o denotes the lattice with an element at the origin. If $S^{mn,uv}$ is the coupling coefficient (i.e., scattering parameter) between element (u,v,) and the (m,n)-th element in lattice R_o, and $S^{pq,uv}$ is the coupling from the (p,q)-th element in lattice R_1, the reflected signal at (u,v) is

$$\begin{aligned} b_{uv} &= R^{uv}(K_x,K_y)a_{uv} \\ &= \sum_{mn} S^{mn,uv} \exp(j\ m\ K_x + j\ n\ K_y) \\ &+ \sum_{pq} S^{pq,uv} \exp(j\ (p+\tfrac{1}{2})K_x + j(q+\tfrac{1}{2})K_y), \end{aligned} \tag{3-3}$$

where R_a^{uv} is the active reflection coefficient. Note that R_a^{uv} is the reflection coefficient at (u,v) when the entire array is excited, while $S^{mn,uv}$ is the coupling coefficient from (m,n) to (u,v), when only (m,n) is excited. Both coefficients include contributions from all propagating and evanescent modes that are excited.

Equation (3-3) states that R_a^{uv} can be computed as the Fourier transform of the element-to-element coupling coefficients. It is clear that R_a^{uv} is a periodic function of K_x and K_y, with period 2π in each variable. Array periodicity implies that R_a^{uv} must be the same for every element, and (u,v) could just as well be taken as (0,0). Lorentz reciprocity implies that

$$S^{mn,uv} = S^{uv,mn}, \tag{3-4}$$

and this fact can be used to show [25,p.55] that the reflection coefficient has reflection symmetry within a scan plane,

$$R_a^{uv}(K_x,K_y) = R_a^{uv}(-K_x,-K_y) . \tag{3-5}$$

If the array structure satisfies the previously discussed symmetry conditions, it can also be shown that

$$\begin{aligned} R_a^{uv}(K_x,K_y) &= R_a^{uv}(-K_x,K_y) \\ &= R^{uv}(K_x,-K_y). \end{aligned} \tag{3-6}$$

Under these conditions, the active reflection coefficient is the same at the four beam positions,

$$(\theta,\phi) = \begin{cases} (\theta_o,\phi_o) \\ (\theta_o,-\phi_o) \\ (\theta_o,\pi+\phi_o) \\ (\theta_o,\pi-\phi_o) \end{cases} \tag{3-7}$$

In particular, $R_a^{uv}(K_x,K_y)$ is the total reflection coefficient, when the four beams are excited simultaneously by superposition of the four aperture excitations.

To create null planes on the simulator walls, the four beams are adjusted to synthesize a waveguide mode for the rectangular guide with dimensions A by B. The phase increments are chosen to be

$$K_x = \frac{k\pi a}{A}, \quad K_y = \frac{\ell\pi b}{B} , \tag{3-8}$$

where k and ℓ are non-negative integers. This phasing places a beam at $(\theta_{k\ell}, \phi_{k\ell})$, where

$$\sin \theta_{k\ell} = \left[\left(\frac{k\pi}{k_o A}\right)^2 + \left(\frac{\ell\pi}{k_o B}\right)^2 \right]^{1/2} , \tag{3-9a}$$

and

$$\tan \phi_{k\ell} = \frac{\ell A}{kB} . \tag{3-9b}$$

The amplitudes of the four beams are made equal, and the signs are selected according to the polarization of the array element, relative to the simulator waveguide. With the coordinate system shown in Figure 3-16, the transverse field components of all $TE_{k\ell}$ and $TM_{k\ell}$ waveguide modes in the AxB simulator cross-section have the following form:

$$E_x = (E^{TE}_{k\ell} k_y - E^{TM}_{k\ell} k_x) \cos(k_x x) \sin(k_y y), \tag{3-10a}$$

$$E_y = (-E^{TE}_{k\ell} k_x - E^{TM}_{k\ell} k_y) \sin(k_x x) \cos(k_y y), \tag{3-10b}$$

where

$$k_x = \frac{k\pi}{A}, \quad k_y = \frac{\ell\pi}{B} . \tag{3-11}$$

A "beam" of an infinite array can be represented as a continuous spectrum of plane waves that is weighted by a delta-function at the beam scan-angle. In this case, the beam defined by Equation (3-8) is a single plane wave, polarized TE or TM (to the z-axis), with Cartesian components given by

$$E_i(K_x,K_y) = E_{oi} \exp(j\, k_x x + j\, k_y y - j\, k_z z), \qquad (3\text{-}12)$$

where $K_x = k_x a$, $K_y = k_y a$, and

and $$k_z = (k_o - k_x - k_y)^{1/2} \qquad (3\text{-}13)$$

To synthesize a waveguide mode, four beams are combined to give the transverse field distribution specified by Equation (3-10). For x-polarized elements, the required linear combination is

$$\begin{aligned} E^s_x(K_x,K_y) &= [\, E_x(K_x,K_y) - E_x(-K_x, -K_y)\,] \\ &\quad - [\, E_x(K_x,-K_y) - E_x(-K_x,K_y)\,] \\ &= j4E_{oi} \cos(k_x x) \sin(k_y y) \exp(-jk_z z), \end{aligned} \qquad (3\text{-}14a)$$

and for y-polarized elements,

$$\begin{aligned} E^s_y(K_x,K_y) &= [\, E_y(K_x,K_y) - E_y(-K_x,-K_y)\,] \\ &\quad + [\, E_y(K_x,-K_y) - E_y(-K_x,K_y)\,] \\ &= j4E_{oi} \sin(k_x x) \cos(k_y y) \exp(-jk_z z). \end{aligned} \qquad (3\text{-}14b)$$

The array fields represented by E_i^s have null planes at x = 0, $\pm A$, ..., and at y = 0, $\pm B$, ..., so the insertion of conducting walls to form a simulator waveguide does not disturb the array fields. The AxB simulator cross-section indicated in Figure 3-16 contains MxN unit cells (axb) of each of the two offset lattices, R_o and R_1, where

$$M = A/a \ , \qquad N = B/b \ . \tag{3-15}$$

By including fractional elements in the summation, the total number of elements inside the simulator is 2* (MxN). Because the insertion of the simulator walls does not affect the active reflection coefficient R_a^{uv} (K_x,K_y), and because the walls prevent coupling between interior and exterior elements, it is apparent that the summations in Equation (3-3) must be equivalent to sums over interior elements and their images in the conducting walls.

The summations in Equation (3-3) can be grouped into sums over successive, adjacent regions AxB by defining

$$m = m' + m'' \ M \ , \qquad n = n' + n'' \ N, \tag{3-15a}$$

and

$$p = p' + p'' \ M \ , \qquad q = q' + q'' \ N, \tag{3-15b}$$

where

$$\begin{aligned} m' &= 0, 1, \ldots , M \ , \\ n' &= 0, 1, \ldots , N \ , \\ p' &= 0, 1, \ldots , M-1, \\ q' &= 0, 1, \ldots , N-1, \end{aligned}$$

and

$$m'', n'', p'', q'' = 0, \pm 1, \ldots \ .$$

With K_x and K_y as specified in Equation (3-8), the result is

$$\begin{aligned} & R_a^{uv} (K_x,K_y) \exp (j UK_x + j VK_y) \\ &= \sum_{m'} \sum_{n'} \exp (jm'K_x + jn' K_y) \ S_g^{m'n', uv} \\ & \sum_{p'} \sum_{q'} \exp(j(p'+\tfrac{1}{2})K_x + j(q'+\tfrac{1}{2})K_y) S^{p'q',uv}, \end{aligned} \tag{3-16}$$

where

$$S_g^{m'n',uv} = \sum_{m''} \sum_{n''} S^{mn,uv} (-1)^{km'' + \ell n''} h(\tfrac{m'}{M}) h(\tfrac{n'}{N}) \qquad (3\text{-}17a)$$

$$S_g^{p'q',uv} = \sum_{p''} \sum_{q''} S^{pq,uv} (-1)^{kp'' + \ell q''} , \qquad (3\text{-}17b)$$

with $h(x) = \frac{1}{2}$ for $x = 0$ or 1, and $h(x) = 1$, otherwise.

The S_g coefficients represent the sum of coupling coefficients from element (u,v) to all elements spaced with period x=A, y=B from element (m',n') or (p',q'). The elements (u,v,), (m',n'), and (p',q') are assumed to lie inside the simulator, and all other elements in each summation lie outside the simulator. All of the "outside" elements (m,n) are images of (m',n') or of a symmetrically located element inside the simulator (and similarly for the elements (p,q)).

It is possible to rearrange the summations in Equation (3-16) to exhibit explicitly the coupling from element (u,v) to (m',n') (or to (p',q')) and all of its images. To do so, it is necessary to apply the four-beam excitation of Equation (3-14), but the result has the same form as obtained directly from Equation (3-16); i.e.,

$$R_a^{uv} (\tfrac{k\pi}{M}, \tfrac{\ell\pi}{N}) \begin{matrix}\cos\\ \sin\end{matrix} (\tfrac{k\pi}{M} U) \begin{matrix}\sin\\ \cos\end{matrix} (\tfrac{\ell\pi}{N} V)$$

$$= \sum_{m'=0}^{M} \sum_{n'=0}^{N} \begin{matrix}\cos\\ \sin\end{matrix} (\tfrac{k\pi m'}{M}) \begin{matrix}\sin\\ \cos\end{matrix} (\tfrac{\ell\pi n'}{N}) S_g^{m'n',uv}$$

$$\sum_{n'=0}^{M-1} \sum_{q'=0}^{N-1} \begin{matrix}\cos\\ \sin\end{matrix} (\tfrac{k\pi}{M} (p'+1/2)) \begin{matrix}\sin\\ \cos\end{matrix} (\tfrac{\ell\pi}{N} (q'+1/2)) S_g^{p'q',uv},$$

(3-18)

where the upper (or lower) sinusoid is selected for x- (or y) element polarization.

The factors S_g are, therefore, the coupling coefficients between pairs of elements, when they are surrounded by a simulator waveguide. These coefficients can be measured directly with a microwave network analyzer, by sequential measurements between any element (u,v) and all others , (m',n') and (p',q'). The active reflection coefficient at the scan angles given by Equation (3-9) can then be calculated using Equation (3-16) or (3-18). It may be noted that the reflection can, in principle, be computed even for evanescent grating lobes. This is because the coupling measurement includes contributions from evanescent waveguide modes. However, it is not likely that such low order contributions can be measured with great precision.

2. Instrumentation

The measurement of coupling between elements in a multielement simulator requires high accuracy and a capability to process a large volume of data. The task is reasonably practical with a microwave automatic network analyzer (ANA) that is equipped to transfer data to a large computer. Over the past several years, Georgia Tech has developed a system for this work. The system is patterned after the Hewlett-Packard HP-8409 (A/B) system [26]; but all the software was developed at Georgia Tech, and the use of a phased-locked or synthesized microwave source gives the system capabilities that lie between the A and B models of Hewlett-Packard. This system has a capability to transfer measured data by telephone line to a large mainframe computer (CDC Cyber 170), and this is absolutely necessary for processing simulator data.

A block diagram of the ANA is shown in Figure 3-17. The microwave source may be either the Watkins-Johnson synthesizer shown or a sweep-oscillator (HP 8620C) that is phased-locked at discrete frequencies by an EIP 578 Source-Locking Counter. The test set consists basically of couplers that sample incident, reflected, and transmitted signals for a one- or two-port device under test (DUT). The network analyzer measures the amplitude and phase of the reflected or transmitted signal, relative to the incident signal. Normally, amplitude is measured on the rectangular display, and phase is measured on the polar display. The small computer controls the instruments and records data through the IEEE-488 bus interconnections.

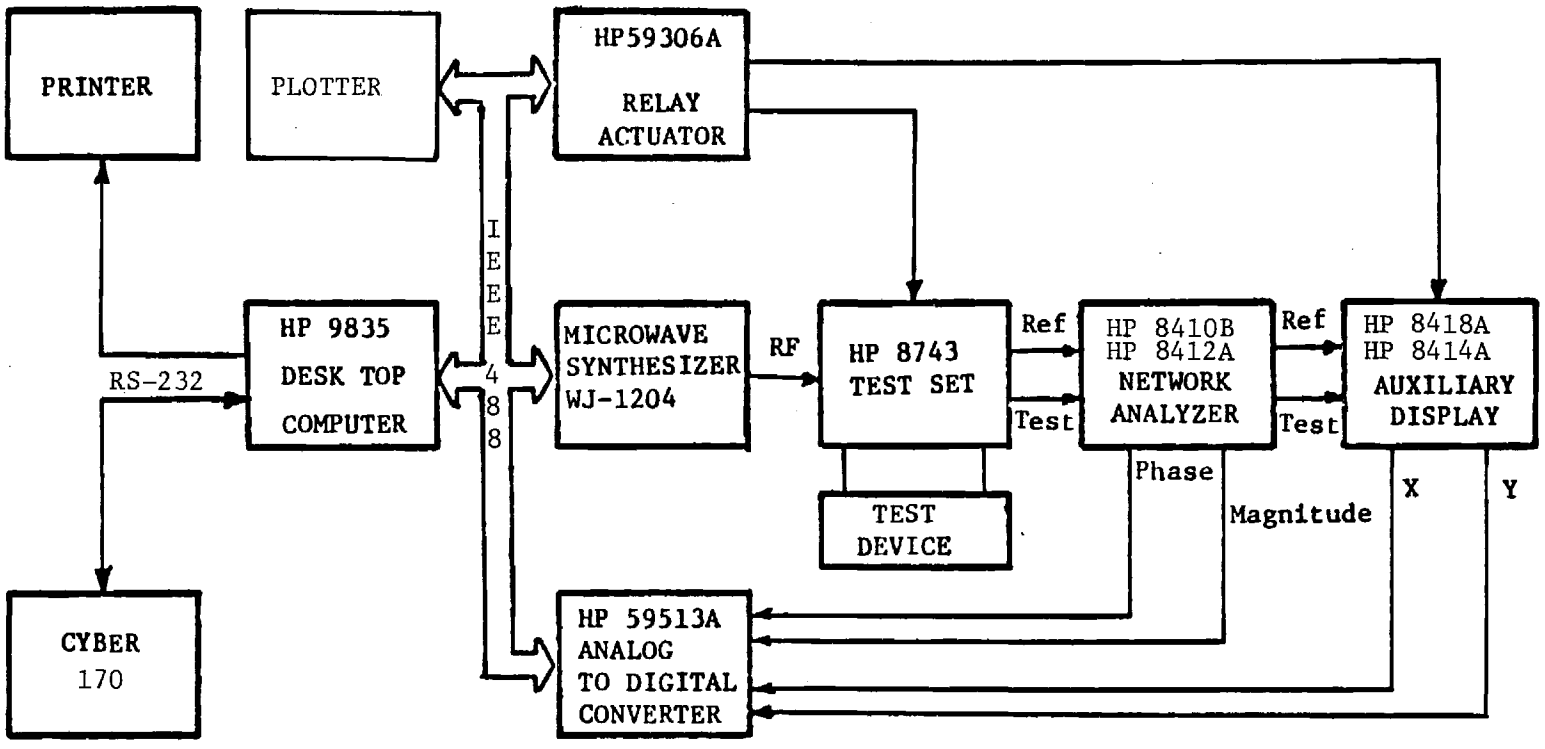

Figure 3-17. Equipment diagram of automatic network analyzer.

The importance of the automated system is that extensive calibration and error-correction are practical. Random errors caused by electrical noise, temperature changes, or imperfect transmission line connections cannot be systematically eliminated, but they can be reduced by averaging large numbers of measurements and by good operating practice. However, analyzer measurements made through coupler networks contain significant systematic errors that can be measured and eliminated. These errors are usually identified as directivity, source-port mismatch, and frequency-tracking errors in reflection measurements, and as leakage, load-port mismatch, and frequency-tracking errors in transmission measurements. These are six errors for a forward-path measurement through a two-port DUT, and there are six similar errors for the reverse-path measurement; therefore, the standard error-correction model is sometimes identified as a "twelve-term" model [26].

Although it has been the subject of a large number of papers [27, 28], the basic error model for an ANA is relatively simple. A diagram is shown in Figure 3-18. It is assumed that the analyzer measures reflections from the DUT, looking through an unknown two-port $\underline{\underline{S}}^r$. Similarly, it measures transmissions through the DUT, at the output of an unknown three-port $\underline{\underline{S}}^t$, where the third port allows for leakage around the DUT. It is assumed that the analyzer can make accurate measurements of the two ratios,

$$M^r = b_1^r / a_1^r \tag{3-19a}$$

and

$$M^t = b_2^t / a_1^r \quad . \tag{3-19b}$$

By substituting several known networks for the DUT, the parameters of the scattering matrixes $\underline{\underline{S}}^r$ and $\underline{\underline{S}}^t$ can be measured. Then, the reflection and transmission coefficients for the DUT can be calculated from measurements M^r and M^t.

The calibration process illustrated in Figure 3-18 is usually used in the Georgia Tech system. The first three loads (short, offset short, and matched load) are used to measure $\underline{\underline{S}}^r$.

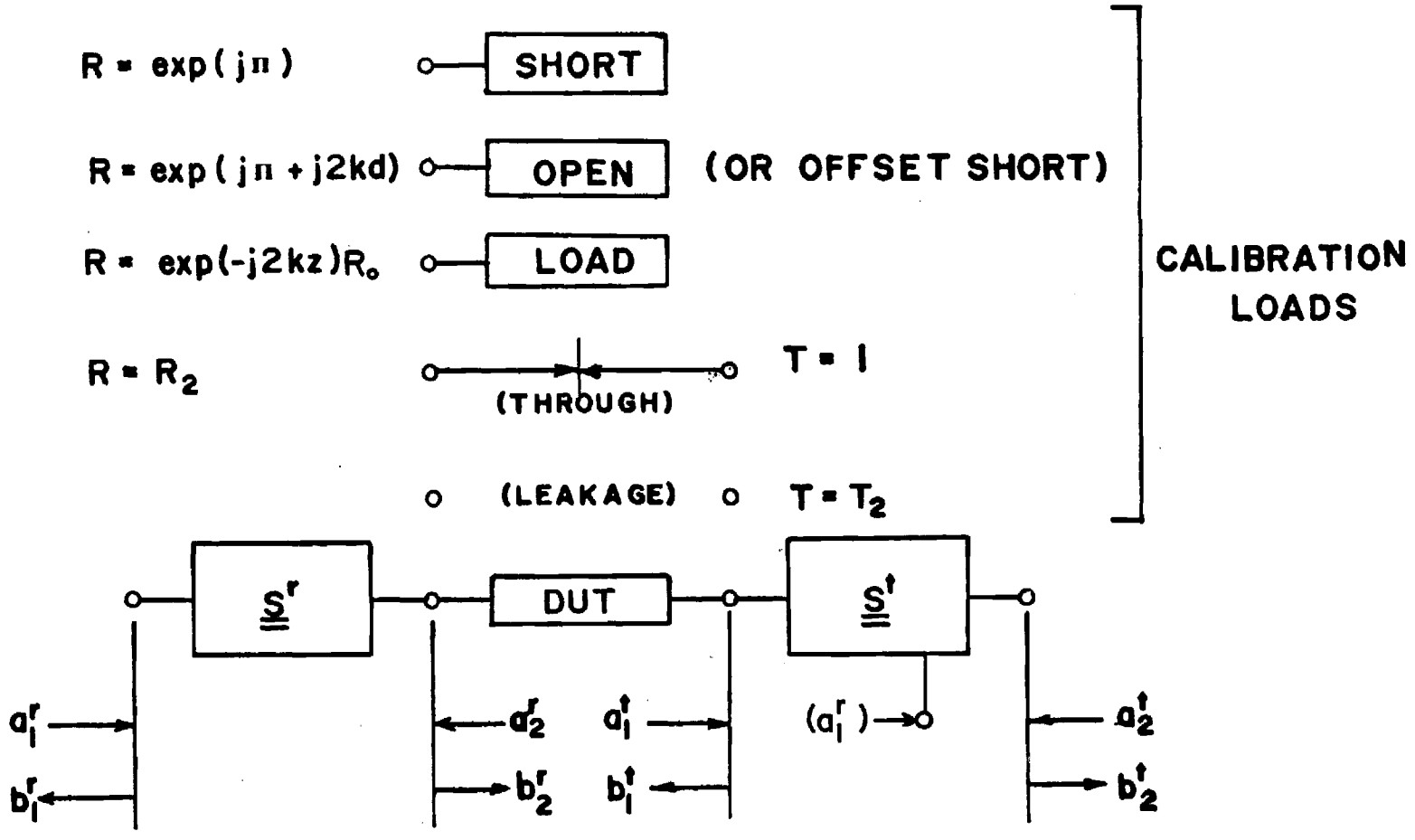

Figure 3-18. Diagram of calibration model for automatic network analyzer. Equipment has capability to measure b_1^r/a_1^r and b_2^t/a_1^r, with $a_2^t=0$. Values for $\underline{\underline{S}}^r$ and $\underline{\underline{S}}^t$ are determined from measurements of calibration loads.

The terminal relations are

$$b_1^r = S_{11}^r a_1^r + S_{12}^r a_2^r \quad , \tag{3-20a}$$

$$b_2^r = S_{21}^r a_1^r + S_{22}^r a_2^r \quad . \tag{3-20b}$$

With a perfect termination, $a_2^r = 0$, and S_{11} is measured directly,

$$M_o^r = b_1^r/a_1^r = S_{11}^r \quad . \tag{3-21}$$

This gives the effective directivity of the couplers, adapters, and connectors in the test set. The perfect termination is simulated by a sliding load. The phase of the load reflection changes as the load slides, and the load reflection adds vectorially to the constant phasor S_{11}. The locus of M^r in the complex reflection plane is a circle, as shown in Figure 3-19, and from at least three measurements of M^r, the center of the circle is located. This procedure allows the contribution from the imperfect load to be removed.

Two additional calibrations are required to specify $\underline{\underline{S}}^r$. A short placed at a distance d from the reference plane has a reflection coefficient

$$R = \exp(j\pi + j2k_g d), \tag{3-22}$$

where k_g is the propagation constant. The two additional measurements M_1^r and M_2^r are made with two different offset shorts R_1 and R_2, with the results

$$M_i^r = S_{11}^r + \frac{R_i S_{12}^r S_{21}^r}{1 - R_i S_{22}^r} \quad , \; i = 1,2. \tag{3-23}$$

Since R_1, R_2, and S_{11} are known, Equations (3-23) can be solved to obtain

$$S_{22}^r = \frac{R_1(S_{11}^r - M_2^r) - R_2(S_{11}^r - M_1^r)}{R_1 R_2 (M_2^r - M_1^r)} \quad , \tag{3-24a}$$

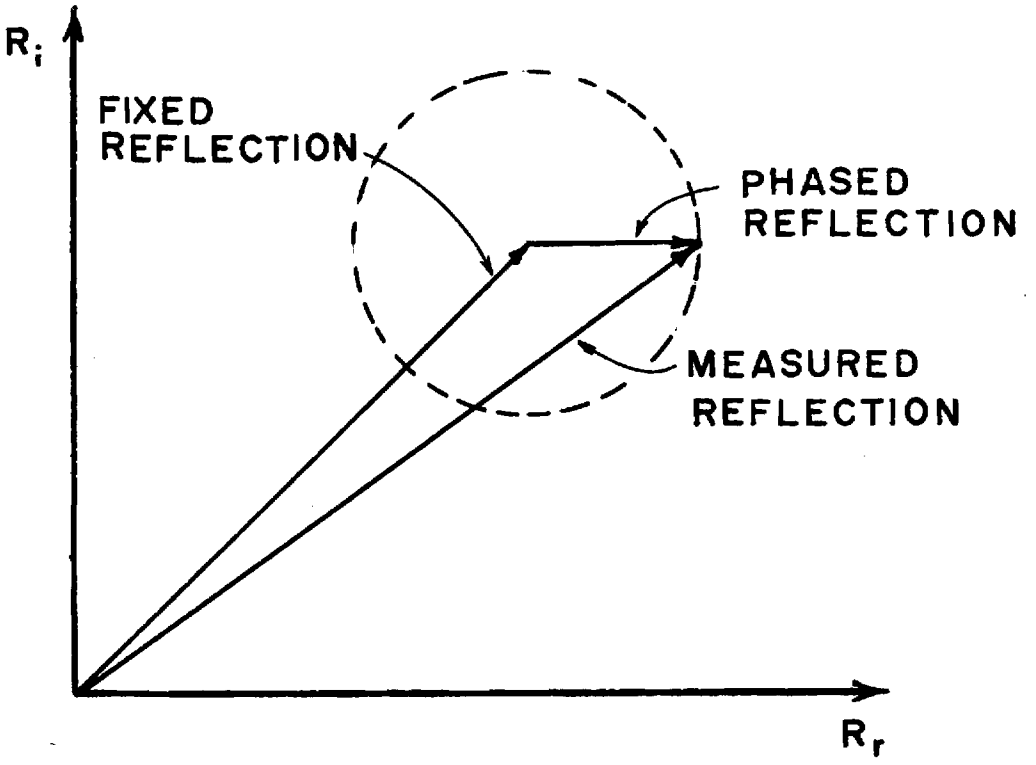

Figure 3-19. Vector sum of measured reflections from a sliding load used to calculate the actual effective directivity.

and

$$S_{12}^r S_{21}^r = \frac{(R_2-R_1)(S_{11}^r-M_1^r)(S_{11}^r-M_2^r)}{R_1R_2(M_2^r-M_1^r)} , \qquad (3\text{-}24b)$$

Then the error-corrected reflection coefficient for any DUT is

$$R_{DUT} = \frac{M^r - S_{11}^r}{S_{12}^r S_{21}^r + S_{22}^r (M^r-S_{11}^r)} , \qquad (3\text{-}25)$$

where M^r is the measured quantity.

To measure the parameters of $\underline{\underline{S}}^t$, leakage is measured, when the primary channel is opened by removing the DUT. Then, reflection from $\underline{\underline{S}}^t$ and transmission through $\underline{\underline{S}}^t$ are measured, when the output of $\underline{\underline{S}}^r$ is joined to the input of $\underline{\underline{S}}^t$. The terminal relations for $\underline{\underline{S}}^t$ are

$$b_1^t = S_{11}^t a_1^t + S_{12}^t a_2^t + S_{13}^t a_1^r , \qquad (3\text{-}26a)$$

$$b_2^t = S_{21}^t a_1^t + S_{22}^t a_2^t + S_{23}^t a_1^r , \qquad (3\text{-}26b)$$

where the third terms represent leakage around the DUT, and it is generally assumed that $S_{13}^t = 0$. It is also assumed that $a_2^t = 0$.

With the primary channel opened (and with the ports terminated), $a_1^t = a_2^t = 0$, and the leakage is measured directly,

$$M_o^t = b_2^t/a_1^r = S_{23}^t . \qquad (3\text{-}27)$$

With $\underline{\underline{S}}^t$ connected directly to $\underline{\underline{S}}^r$, the reflection from $\underline{\underline{S}}^t$ can be measured to obtain

$$R_t = b_1^t / a_1^t = S_{11}^t \quad , \tag{3-28}$$

where Equation (3-25) is used to calculate R_t. Then the transmission through $\underline{\underline{S}}^t$ is measured,

$$M_2^t = b_2^t / a_1^t$$

$$= S_{23}^t + \frac{S_{21}^r \, S_{21}^t}{1 - S_{22}^r S_{11}^t} \tag{3-29}$$

to obtain the product

$$S_{21}^r S_{21}^t = (M_2^t - S_{23}^t)(1 - S_{22}^r S_{11}^t) \quad , \tag{3-30}$$

where S_{22}^r, S_{11}^t, and S_{23}^t are known. The error-corrected transmission coefficient for any DUT is

$$T_{DUT} = \frac{(M^t - S_{23}^t)(1 - S_{22}^r R_{DUT})}{S_{21}^r S_{21}^t} \tag{3-31}$$

where M^t is measured and R_{DUT} is given by Equation (3-25).

To summarize these results, it is noted that the calibration process requires at least six phasor measurements at each frequency of interest. To simulate a perfect termination for M_o^r, two to five additional measurements are needed. Then the DUT is inserted for at least two additional measurements. For one DUT and one frequency, at least ten phasor measurements must be recorded and processed. Additional devices can be measured without recalibration. This operation is not practical without automation, but it is reasonably efficient with the system that has been configured.

C. Six-Port Network Analyzer

Some concepts for BMD interceptors require millimeter-wave (mmW) phased-array seeker antennas. The frequency range would most likely lie in Ka-band (26 to 40 GHz) or in the center portion of W-band (say, 90 to 100 GHz). Because the conventional microwave network analyzer (ANA) does not

operate above 18 GHz, there is a clear need for similar mmW instrumentation. One possibility is to modify the ANA by addition of an external stage of frequency down-conversion. Such equipment is available, but it is fairly expensive, and the sensitivity is obviously reduced. For several recent years, the six-port network analyzer has received serious consideration as a relatively inexpensive instrument for mmW applications [29, 30]. The economy of this instrument results from its use of amplitude-only sensors, such as detectors or thermistors, so that no frequency-conversion (receiver) circuitry is required.

The six-port analyzer was examined for possible development as a test instrument to be used in future work on mmW phased arrays for BMD systems. A description of the six-port network and details of the study are presented in Appendix D. The conclusions are that the equipment can be economical, and with great attention to detail, the accuracy can be as good or better than that of a microwave ANA. However, the sensitivity and dynamic range can be marginal, and to achieve high accuracy may require the use of extremely precise power sensors (which are not routinely available or inexpensive).

Further investigation of possibilities for a mmW network analyzer suggested that a conventional Scientific-Atlanta phase/amplitude antenna measurement receiver could provide the basis for an extremely sensitive network analyzer with great dynamic range. These receivers are nominally rated for operation through 100 GHz, and they achieve stability through local oscillators that are phase-locked to the RF signal. The phase of the test channel is measured with respect to a second, reference channel, to which the local oscillator is locked. The equivalent of the "Reflection/Transmission Test Set" used with the microwave ANA can be assembled from high-directivity waveguide couplers. A number of receivers are available at Georgia Tech, and this approach seemed to be more attractive than implementation of a six-port.

What decisively led to a final recommendation to implement a receiver-based mmW network analyzer was the recent introduction by Scientific-Atlanta of highly-stable, external down-converter for use with its receivers. The primary internal local oscillator in the receivers operates between 1 and 4 GHz, and the high harmonics required for mmW conversion

lead to high conversion loss. The new equipment (S/A Model 1784/1785) provides a stable (phase-locked), first-stage local oscillator near 11 GHz. Georgia Tech is currently procurring all the equipment necessary to implement a receiver-based mmW network analyzer that can operate from 18 GHz to 160 GHz. A block diagram of the system is provided in Figure 3-20. The receiver will be interfaced with a small computer, and the error-correction capabilities discussed for the microwave ANA will be available. We believe this system will provide better capabilities than would a six-port system.

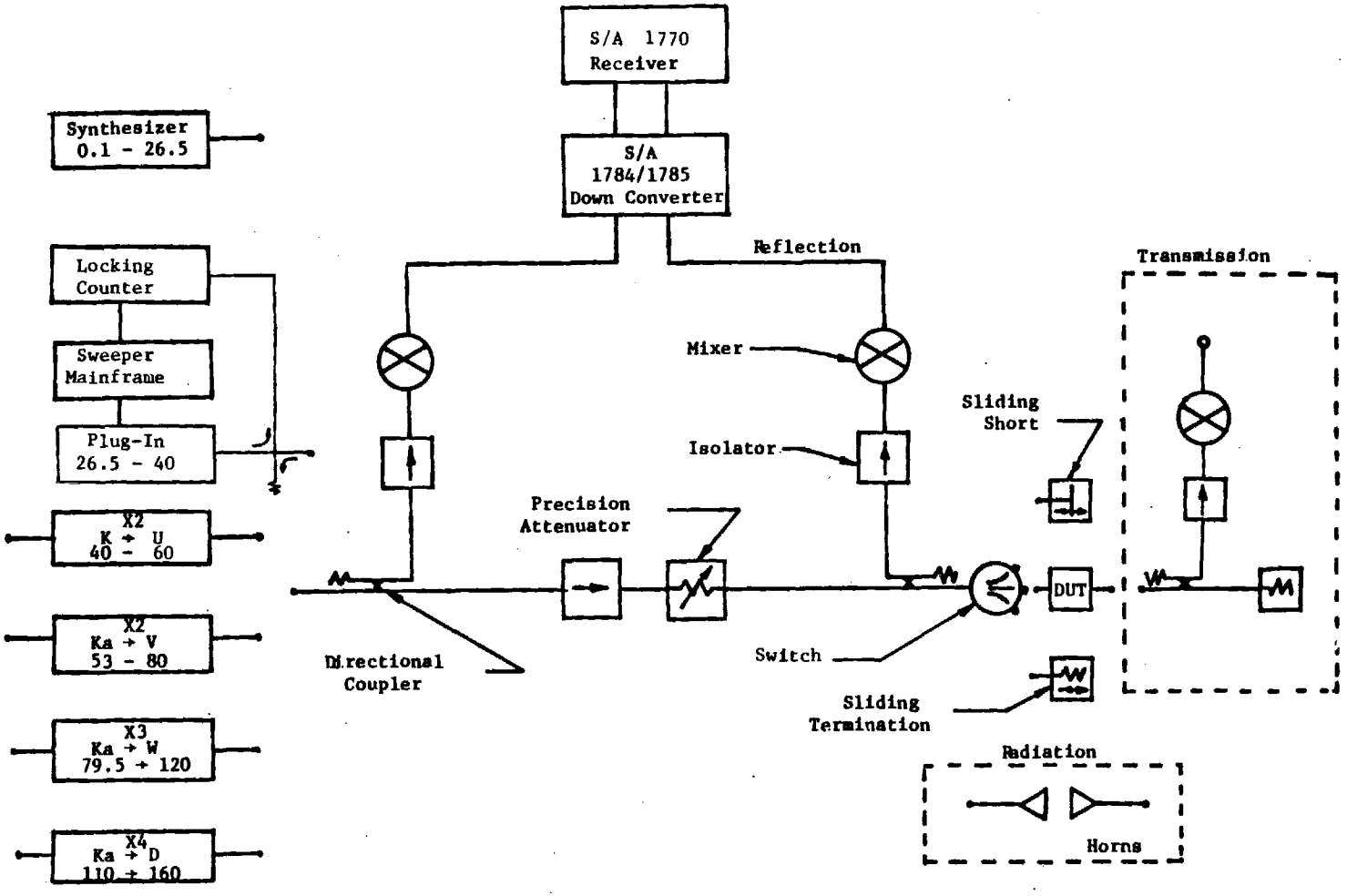

Figure 3-20. Receiver-based millimeter-wave network analyzer.

SECTION IV
MICROSTRIP ELEMENT INVESTIGATION

The microstrip antenna element consists of a metallic patch with dimensions on the order of one-half wavelength, which is plated on an electrically thin dielectric substrate that covers a metallic ground plane. For about ten years, the element has been recognized as an important antenna, primarily because of its suitability for conformal applications on airframes [31,32,33], and developments over this period are reviewed in a recent special conference [34], a special journal issue [35], and one of several books [36]. Although the element has been used in a number of arrays, none of the arrays fall in the category of large, electronically steerable radar antennas with wide-angle coverage. The microstrip arrays that have been developed are primarily either fixed-beam arrays with a lower density of elements than would be needed for a scanning-beam antenna, or very rudimentary frequency-scanned linear arrays that do not yet approach the capabilities required of a large radar antenna. From a theoretical viewpoint, the isolated microstrip element is fairly well understood [37], but only one thorough study of mutual coupling effects in a dense array has been completed [38,39], and that work deals only with passive elements in a reflectarray application. Several efforts on the array problem, inlcuding the one reported here, are in progress.

Microstrip arrays are of interest for BMD applications in both ground-based and interceptor-based radar antennas. Typical frequency ranges for these applications are X-band and Ka-band, respectively. Because large subarrays of elements may be photo-etched or plated in one operation, the good mechanical tolerances required in large arrays can be achieved at a relatively low cost. Great mechanical strength can be achieved, if the antenna is formed by a thin dielectric layer on a massive ground plane. Microstrip arrays are well suited for missile applications, because the thin dielectric substrate can readily conform to curved surfaces and because it has potential for being light in weight.

For both BMD applications, microstrip arrays will require substantial thermal protection. The paper-thin metallic patches on a (thermally) insulating substrate clearly could not survive temperatures exceeding

1,000°C. Therefore, it is necessary to place the array under a window or radome made of a refractory dielectric material. If the window is spaced well away from the array face, it may distort the radiation pattern and cause beam-pointing errors, but it will generally have only a second-order effect on the array capabilities, as determined by mutual coupling effects. However, such an approach raises the problem of supporting the window or radome, when it may be exposed to severe mechanical loads caused by weapon blast and/or aerodynamic pressure. A more attractive approach is to place the window or radome directly against the array face, so that it may be supported by the array ground plane. Such an approach requires that the window be included in the array design process, because the over-lying dielectric layer directly affects mutual coupling and, in general, must be expected to reduce the achievable beam-scan and frequency ranges.

Previous investigations [1,2] have shown that dipole arrays can operate under a relatively thick layer, if the element spacing is reduced appropriately. This section reports an experimental investigation, based on multielement simulator tests, to determine whether the same principle holds for dielectric-covered microstrip arrays. The data available at this time indicates that a thin over-lying layer may be tolerated with no decrease in element spacing.

The process of drawing firm conclusions from the data is complicated by the fact that the elements are resonant, and every change in a design parameter changes the resonant frequency. Subjective judgements are required to decide what data to compare at which frequencies. At this point, an important result of the work is that the effect on the resonant frequency has been established for a variable thickness over-lying dielectric layer and for variable element spacing in the array lattice. A dielectric layer can lower the resonant frequency by at least ten percent, and close spacing in the lattice can increase the resonant frequency by ten to fifteen percent above that expected for the isolated element. These results have not been available previously, and they will be useful in planning future experimental work.

Four parametrically scaled microstrip subarrays were fabricated and tested in a multielement phased-array simulator. The following subsections describe the selection of design parameters and present results at the

nominal resonant frequency. The reduced data is presented as Smith Chart plots of the active impedance at discrete scan angles. Complete data for a broad frequency range is presented for each of the four designs in Appendices E through H.

A. Design Parameters

All of the tests were conducted in a rectangular waveguide simulator with inside dimensions H = 2.271, W = 3.934, L = 22 inches, and all of the microstrip subarrays were required to fit exactly into the 2.271 by 3.934 inch opening at one end of the simulator. The subarrays were bonded to a brass end-plate, which bolted into the end of the simulator. A drawing of an end-plate with a typical subarray is shown in Figure 4-1. The cross-sectional dimensions of the simulator are appropriate for imaging an equilateral triangular lattice with sides ℓ = H/N inches, where N = 1,2,..., and the four tested arrays had this form. Rectangular lattices were not considered.

All of the subarrays were photo-etched on a copper-clad Rexolite 1422 substrate. This is a rigid plastic with dielectric constant K = 2.54 and loss tangent tan δ = 0.0005 at 10 GHz. A substrate of thickness t_s = 1/16 inch was used for all four subarrays. Preliminary tests were conducted with teflon-fiberglass substrates, but that material had a tendency to warp and it was very difficult to bond to the brass plate or to over-lying layers. The rigidity of the Rexolite reduced warpage, and a Rexolite adhesive was available that was claimed to have the same dielectric properties as the substrate.

All of the subarrays had circular elements that were excited by probes formed by the extended center pins of SMA connectors. The connectors were soldered into carefully located holes in the brass end-plates, and the center-pins acted as alignment pins to locate the etched substrate on the end-plate. Preliminary tests were conducted to investigate the significance of the probe offset p, measured vertically from the center of the element, as shown in Figure 4-1. The vertical offset causes the element to be vertically polarized. The offset has a major effect on the driving point impedance; for example, the element acts as a short circuit when the probe is attached at the center (p = 0). In the preliminary tests, the best impedance match was observed with the probe attached to the

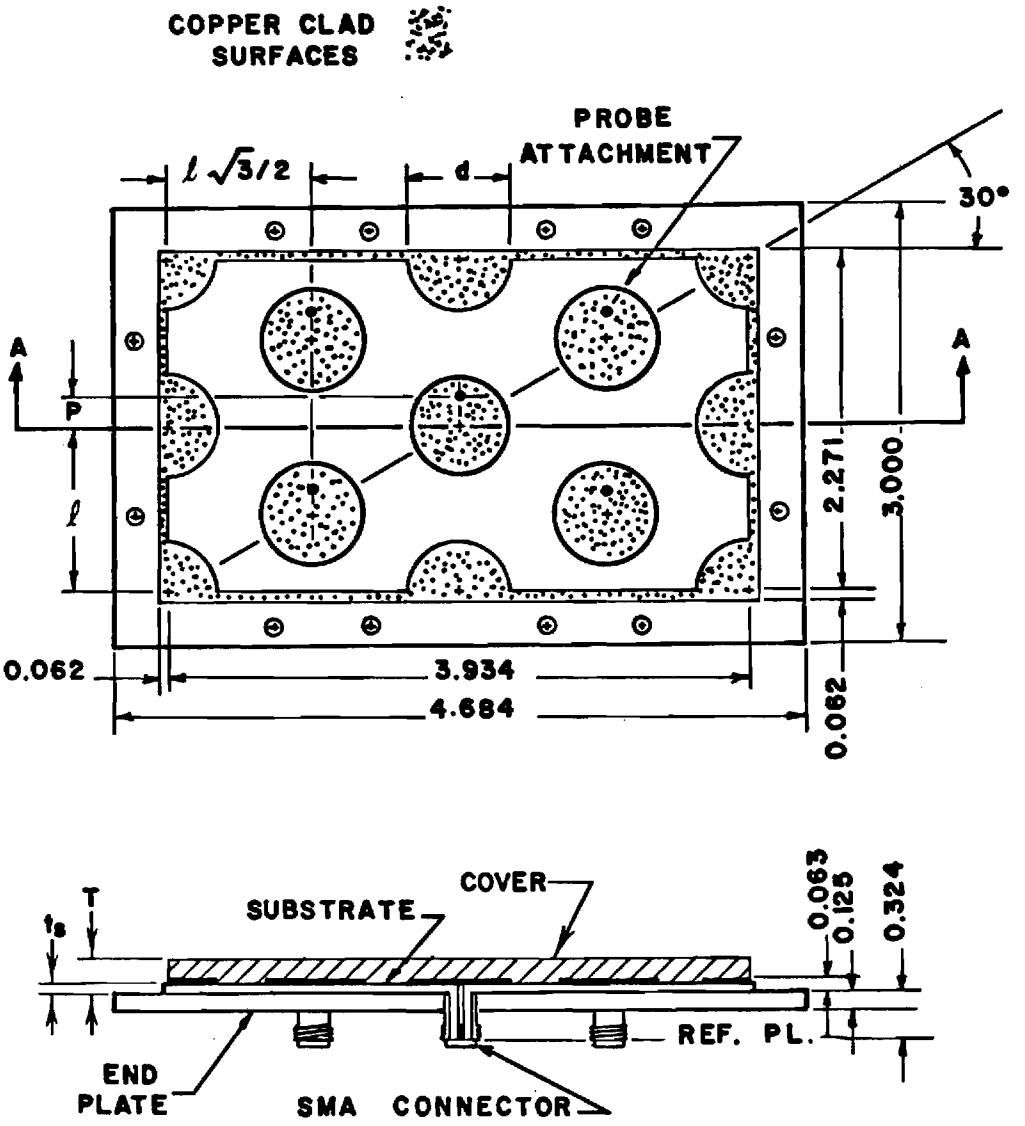

Figure 4-1. Drawing of typical subarray used in simulator tests. Feed probes are provided only for whole elements.

top edge of the element (p = d/2, where d is the element diameter). To limit the number of parameters to be investigated, it was decided to set p = d/2 for all four simulators. This approach assumes that the impedance adjustment provided by the probe offset is not strongly sensitive to other array parameters, such as the thickness of any over-lying dielectric layer and the size of the lattice. However, it is likely that the optimum probe offset is sensitive to the E-plane scan angle, and a need for further work on the optimum probe offset can be anticipated.

The two parameters considered as variables in this study are the thickness of the over-lying dielectric layer, as measured by the ratio t_s/T, and the size of the array lattice, as measured by the ratio d/ℓ. As shown in Figure 4-1, T is the combined thickness of the dielectric substrate and the cover layer; when the cover is removed, $t_s/T = 1$, and as the cover thickness increases, t_s/T approaches zero. When $t_s/T = 0$, the elements are embedded in a homogeneous dielectric half-space. Data has been obtained for t_s/T = 0.20, 0.33, 0.50, and 1.00. The ratio d/ℓ is called the "fill-factor", because it indicates the degree to which the elements fill the area associated with a unit cell of the array. The elements exactly touch, when $d/\ell = 1$. Data has been obtained for d/ℓ = 0.6, 0.8, and 0.9.

To conduct all the tests in a single simulator waveguide, changes in the lattice size must be constrained to discrete steps, $\ell = H/N$, to achieve imaging. Two simulators had a lattice size $\ell = H/2$, and the other two had size $\ell = H/3$. In the first case, there are whole elements, four half-elements and four quarter-elements; in the second case, there are thirteen whole elements, eight half-elements, and four quarter-elements. The fill-factor is adjusted to achieve intermediate values by changing the element diameter, which changes the resonant frequency. The nominal resonant frequency of an isolated circular microstrip element with no cover layer is defined to be [37]

$$f_o = \frac{c_o x'_{11}}{\pi d\sqrt{K}} \quad , \qquad (4\text{-}1)$$

where c_o is the free-space phase velocity, and x'_{11} is the first zero of the differentiated Bessel function, $J'_1(x)$. (This is the cutoff frequency of the TE_{11}-mode in a dielectric-filled circular waveguide of diameter d.) Various more sophisticated models are available for the isolated microstrip element, but the effects of the array environment and any dielectric cover are more important than higher order corrections to Equation (4-1), and the simple model provides an adequate estimate for designing an experiment. A complete description of the four simulators is provided in Table 4-1.

As indicated in Figure 4-1, only the whole elements in each simulator have feed probes. Those fractional elements centered on the E-plane (side) walls have their feed probes perfectly short-circuited, and it is theoretically correct to omit the probes. However, the elements centered on the H-plane wall are imaged symmetrically; the probes are not shorted, and by a strict interpretation, they should be included. One loss in omitting the probes is the ability to completely sample the distribution of higher order modes in the wavegude; another possible loss is that those elements are not loaded properly, which could have some effect on the mutual coupling environment.

Another imperfection in these simulators is that the feed is not a balanced structure, and, therefore, the element does not strictly satisfy the requirement for reflection symmetry about the H-plane (horizontal) bisector. A two-point (push-pull) feed for each element would be unnecessarily complex for an actual array element, because it would not be expected to change the performance of the element. Within the simulator, the two-point feed should not be absolutely necessary, provided the current distribution on the <u>outer</u> surface of the patch-element has the proper symmetry; and the highly resonant nature of the element should tend to force such a condition. Symmetry could be further impoved, without using a balanced feed, by shorting the center of each element to the ground plane through a pin. Such a pin would tend to short-circuit those modes that have the incorrect symmetry in the "cavity" region between the patch and the ground plane.

For reference, Table 4-2 shows the cutoff frequencies below 12 GHz for all TE_{mn} and TM_{mn} modes in the simulator waveguide. As discussed in Section III.B.1, each mode represents a distinct beam position that can

TABLE 4-1

ARRAY SIMULATOR PARAMETERS

Number	d/ℓ	d(in.)	f_o(GHz)	ℓ (in.)	ℓ/λ_o	t_s(in.)	t_s/λ_o	t_s/T
1	0.6	.681	6.373	1.136	0.613	0.063	0.034	1.00,0.50, 0.33,0.20
2	0.8	0.606	7.162	0.757	0.459	0.063	0.038	1.00,0.50
3	0.9	0.681	6.373	0.757	0.409	0.063	0.034	1.00,0.50
4	0.9	1.022	4.246	1.136	0.409	0.063	0.023	1.00,0.50

TABLE 4-2

CUTOFF FREQUENCIES FOR TE_{mn} AND TM_{mn} MODES IN ARRAY SIMULATOR WAVEGUIDE*

Frequency	Mode Index mn and Scan Plane ϕ (deg)				
(GHz)	n=0	n=1	n=2	n=3	n=4
1.500	10(0)				
2.598		01(90.0)			
3.000	20(0)	11(60.0)			
3.969		21(40.9)			
4.500	30(0)				
5.196		31(30.0)	02(90.0)		
5.408			12(73.9)		
6.000	40(0)		22(60.0)		
6.538		41(23.4)			
6.874			32(49.1)		
7.500	50(0)				
7.794				03(90.0)	
7.937		51(19.1)	42(40.9)	13(79.1)	
8.352				23(69.0)	
9.000	60(0)			33(60.0)	
9.124			52(34.7)		
9.368		61(16.1)			
9.836				43(52.4)	
10.392			62(30.0)		04(90.0)
10.500	70(0)				14(81.8)
10.817		71(13.9)		53(46.1)	24(73.9)
11.325					34(66.6)
11.715			72(26.3)		
11.906				63(40.9)	
12.000	80(0)				44(60.0)

*Waveguide cross-sectional dimensions are 2.271 x 3.934 inches. Modes are defined transverse to the axial direction and are designated TE_{mo}, TE_{on}, TE_{mn}, and TM_{mn}, with m = 1,2,...; n = 1,2,... .

be simulated. In this simulator the scan plane is the angle ϕ measured from the H-plane (broad) wall. As the frequency increases above a modal cutoff, the simulated beam scans from the plane of the array face (θ = 90°) to broadside (θ = 0°), but it remains in the scan plane associated with that particular mode. The scan angles can be calculated from Equation (3-9). For each possible mode in each simulator, plots of the scan angle as a function of frequency are provided in Appendices E through H. At any one frequency, a number of modes may exist in the simulator, and the active reflection coefficient or active impedance at the same number of beam angles can be calculated from measured coupling data. The following subsection presents such data for each simulator at the nominal resonant frequency of each element.

B. Test Results

The results presented in this subsection are extracted from the more extensive data contained in Appendices E through H. The data selected here allows a comparison of the scan capability for each of the four basic simulator designs at their respective nominal resonant frequencies. The data consists of Smith Chart plots of the active impedance for each design at a number of simulated scan angles. On the plots, the scan angles are identified by the mode index of the corresponding simulator waveguide mode, and the actual scan angles are specified in an associated table.

The scan capabilities of different designs can be ranked according to how tightly the impedances are grouped on the Smith Chart. If the impedances for a range of scan angles are grouped tightly, but are not near the center of the chart, it is reasonable to assume that the whole group of points can be moved to the center by a single impedance-matching operation (e.g., a transformer). On the other hand, if the impedances are spread widely over the chart, it is not possible to design a single network that will provide a good match at all the scan angles. As indicated in Figure 4-1, the electrical reference plane for all the data presented is taken at the mating face of the SMA connector. This face is located 0.324 inches to the rear of the microstrip ground plane, through a teflon-filled coaxial transmission-line section. In some cases, interpretation of the data is facilitated by transforming the reference plane to the ground plane.

1. Simulator No. 1

The parameters for Simulator No. 1 are summarized in Figure 4-2, and active impedances at f_o = 6.4 GHz are plotted in Figure 4-3 for cover layer thicknesses $T-t_s$ = 0, 1/16, 1/8, and 1/4 inch. At this frequency, the simulator has the symmetry and polarization needed to excite six modes, which correspond to the six scan angles given with Figure 4-2. At these angles, the impedances are fairly well grouped, except for the thickest, 1/4-inch cover layer. However, a firm conclusion cannot be based on this data, because, as will be shown later, the optimum frequency is not f_o for any of these cases, and it changes (decreases) as the thickness of the cover layer increases.

2. Simulator No. 2.

Parameters for Simulator No. 2 are given in Figure 4-4, and active impedances at f_o = 7.0 GHz are plotted in Figure 4-5 for cover thicknesses $T-t_s$ = 0 and 1/16 inch. This simulator has thirteen whole elements and can excite eleven modes, which correspond to the scan angles given with Figure 4-4. This array has a higher fill-factor than does Simulator No. 1 (d/ℓ = 0.8, compared with d/ℓ = 0.6), and based on experience with dipole arrays, it is expected to be more tolerant of a cover layer than No. 1. The 1/16-inch layer is apparently not thick enough to prove or disprove such a contention. The layer clearly spreads the impedances, when the beam is scanned closer to the E-plane (i.e., the 12, 22, and 32 modes), but these angles were not available with the few elements contained in Simulator No. 1.

3. Simulator No. 3

Parameters for Simulator No. 3 are given in Figure 4-6, and active impedances at f_o = 6.4 GHz are plotted in Figure 4-7 for cover thickness $T-t_s$ = 0 and 1/16 inch. This simulator has thirteen whole elements and can excite nine modes, which correspond to the scan angles given with Figure 4-6. The array has a fill-factor d/ℓ = 0.9, and it was expected to be more tolerant of a cover layer than Nos. 1 and 2. However, it is clear that the cover causes the impedances to spread considerably more than in the previous case. This may indicate that a smaller fill-factor is better, but is seems more likely that the anomaly results from making comparisons at non-optimum frequencies.

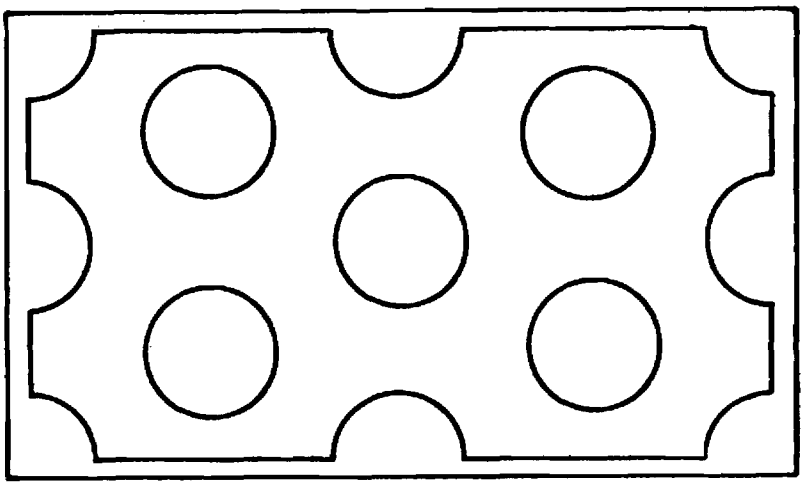

Figure 4-2. Sketch of subarray for Simulator No. 1.
Nominal frequency: f_o = 6.373 GHz
Element diameter: d = 0.681 in.
Lattice size: ℓ = 1.136 in.
= 0.613 λ_o
Fill-factor: d/ℓ = 0.6

SCAN ANGLES FOR WAVEGUIDE MODES IN SIMULATOR NO. 1 AT f_o = 6.4 GHz

MODE	THETA	PHI
10	13.6	0.0
20	28.0	0.0
30	44.7	0.0
11	28.0	60.0
21	38.3	40.9
31	54.3	30.0

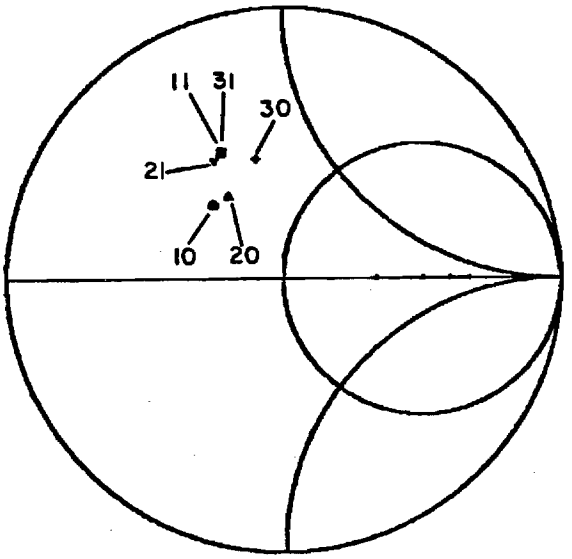

(a) No layer

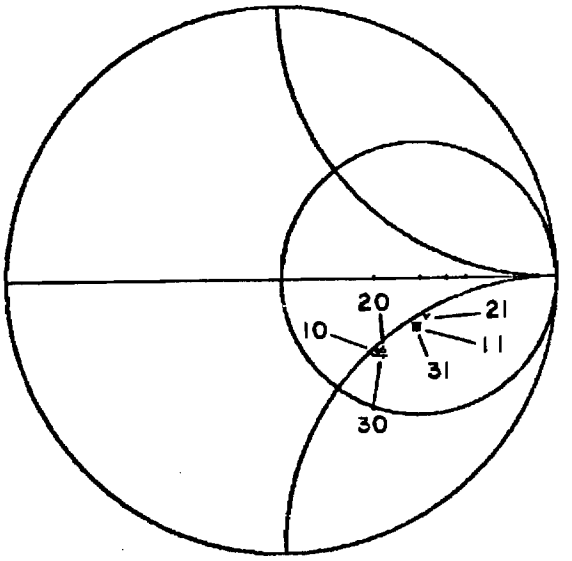

(c) 1/8" Rexolite layer

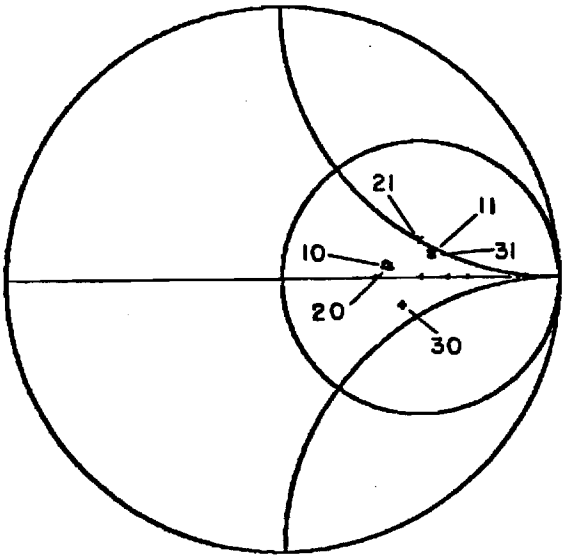

(b) 1/16" Rexolite layer

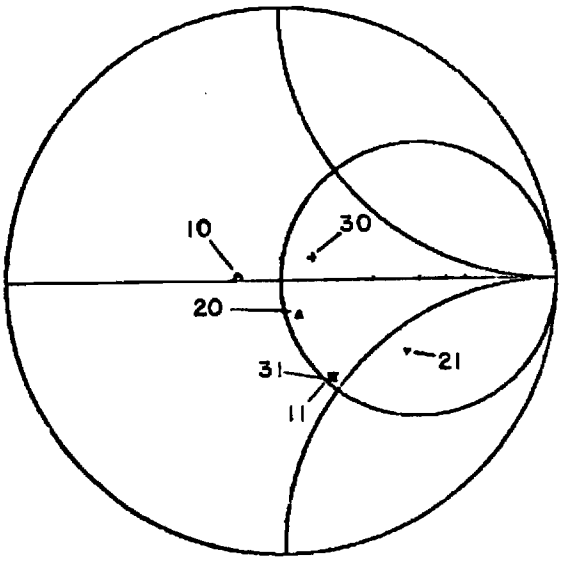

(d) 1/4" Rexolite layer

Figure 4-3. Smith Chart impedance plots for waveguide modes in Simulator No. 1 at f_o = 6.4 GHz.

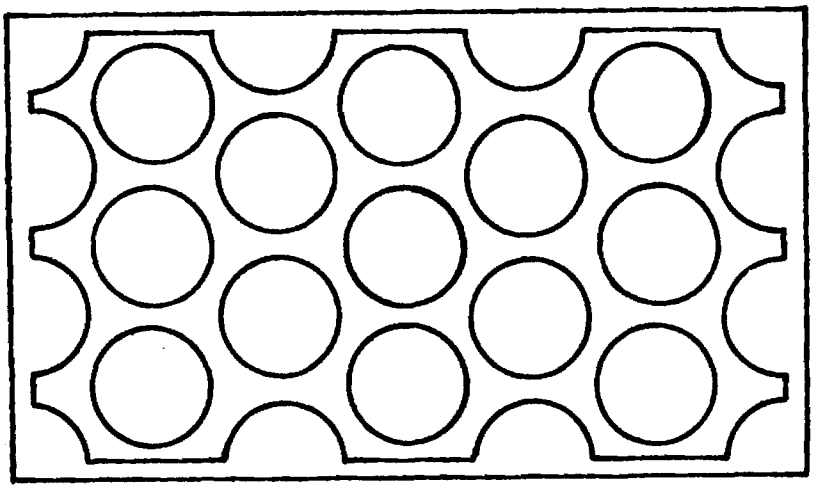

Figure 4-4. Sketch of subarray for Simulator No. 2.
Nominal frequency: f_o = 7.162 GHz
Element diameter: d^o = 0.606 in.
Lattice size: ℓ = 0.757 in.
= 0.459 λ_o
Fill-factor: d/ℓ = 0.8

SCAN ANGLES FOR WAVEGUIDE MODES IN SIMULATOR NO. 2 AT f_o = 7.0 GHz

MODE	THETA	PHI
10	12.4	0.0
20	25.4	0.0
30	40.0	0.0
40	59.1	0.0
11	25.4	60.0
21	34.6	40.9
31	48.0	30.0
41	69.2	23.4
12	50.7	73.9
22	59.1	60.0
32	79.4	49.1

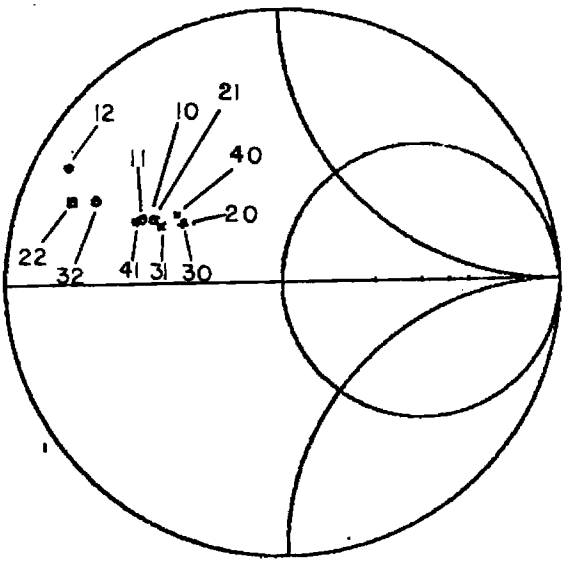

(a) No layer

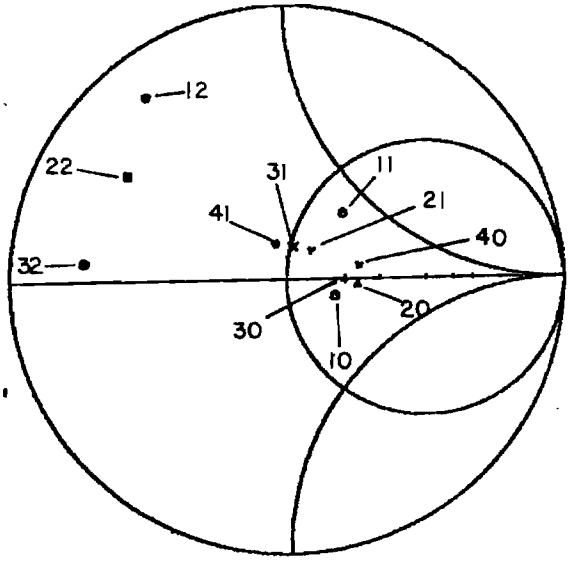

(b) 1/16" Rexolite layer

Figure 4-5. Smith Chart impedance plots for waveguide modes in Simulator No. 2 at f_o = 7.0 GHz.

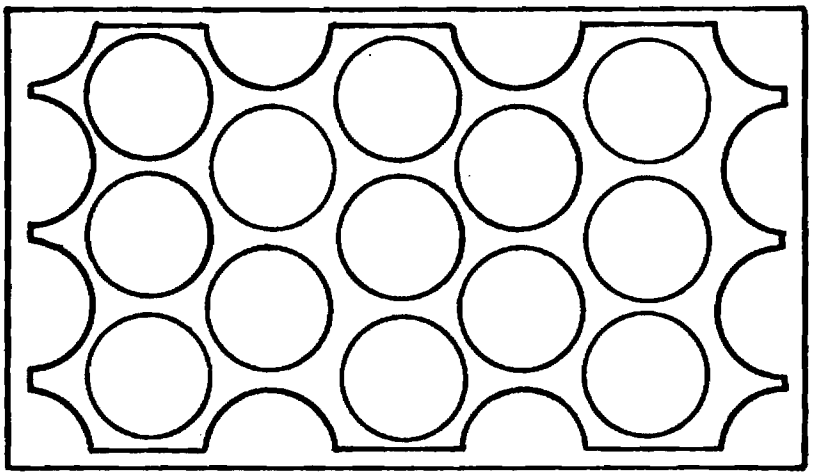

Figure 4-6. Sketch of subarray for Simulator No. 3.
Nominal frequency: f_o = 6.373 GHz
Element diameter: d^o = 0.681 in.
Lattice size: ℓ = 0.757 in.
= 0.409 λ_o
Fill-factor: d/ℓ = 0.9

SCAN ANGLES FOR WAVEGUIDE MODES IN SIMULATOR NO. 3 AT f_o = 6.4 GHz

MODE	THETA	PHI
10	13.6	0.0
20	28.0	0.0
30	44.7	0.0
40	69.8	0.0
11	28.0	60.0
21	38.4	40.9
31	54.4	30.0
12	57.8	73.9
22	69.8	60.0

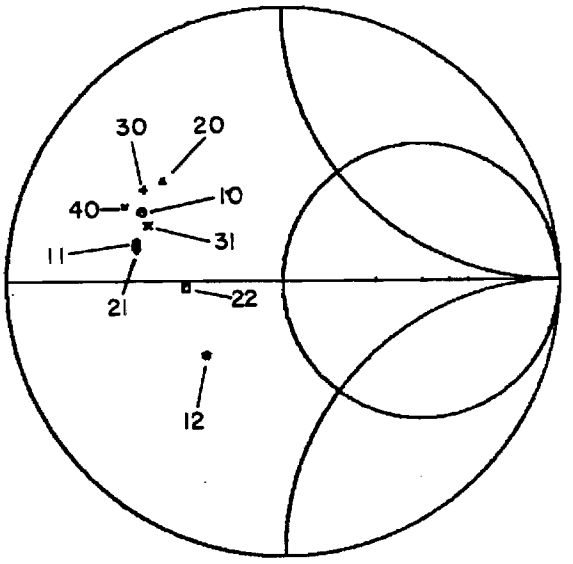

(a) No layer

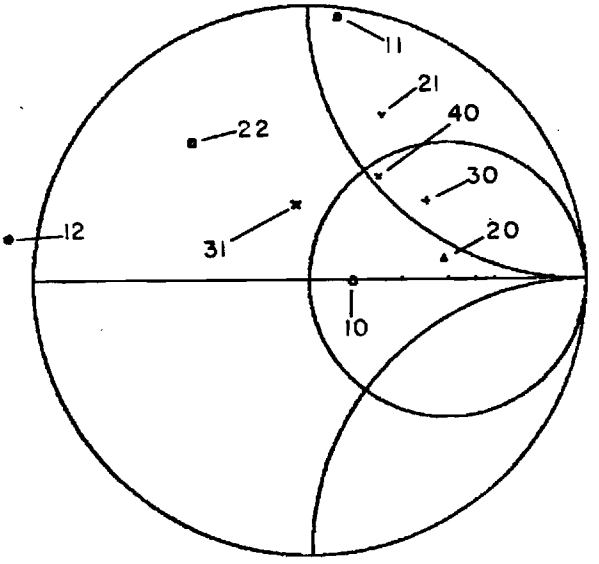

(b) 1/16" Rexolite layer

Figure 4-7. Smith Chart impedance plots for waveguide modes in Simulator No. 3 at f_o = 6.4 GHz.

4. Simulator No. 4,

Parameters for Simulator No. 4 are given in Figure 4-8, and active impedances at f_o = 4.2 GHz are plotted in Figure 4-9 for cover thicknesses $t-t_s$ = 0 and 1/16 inch. This simulator has five whole elements and can excite four modes, which correspond to the scan angles given with Figure 4-8. These scan angles are farther from broadside than for the same modes at the higher frequencies used for the first three simulators. Also, the fill-factor d/ℓ = 0.9 is relatively high, which, it turns out, means that the actual resonant frequency is substantially different from the nominal value f_o. The element is not matched well with or without a cover layer, and there is little difference in the quality of the two cases. There is some evidence in the more complete data in Appendix H that the termination in the simulator was not good enough. The termination was made from four-inch thick, stratified foam absorber (Emerson Cumming AN-79), and this may not have been thick enough for operation below 5 or 6 GHz.

5. Resonant Frequencies

The active impedances for each mode are plotted as functions of frequency in Appendices E through H. The data presented above was extracted to show the impedance as a function of scan angle at one frequency (i.e., at the nominal frequency f_o). An examination of the more complete data shows that the microstrip elements generally do not resonate at f_o, when they are in the array environment or when they are covered by a dielectric layer. The observed resonant frequencies f for each simulator are plotted in Figure 4-10. It is clear that the array environment raises the resonant frequency above the nominal value f_o, for the isolated element. Also, the dielectric cover layer lowers the resonant frequency. Therefore, to compare several array designs properly, it is first necessary to determine the optimum frequency range for each design. The data in the Appendices suggests that an operating bandwidth of more than about five percent may be very difficult to achieve.

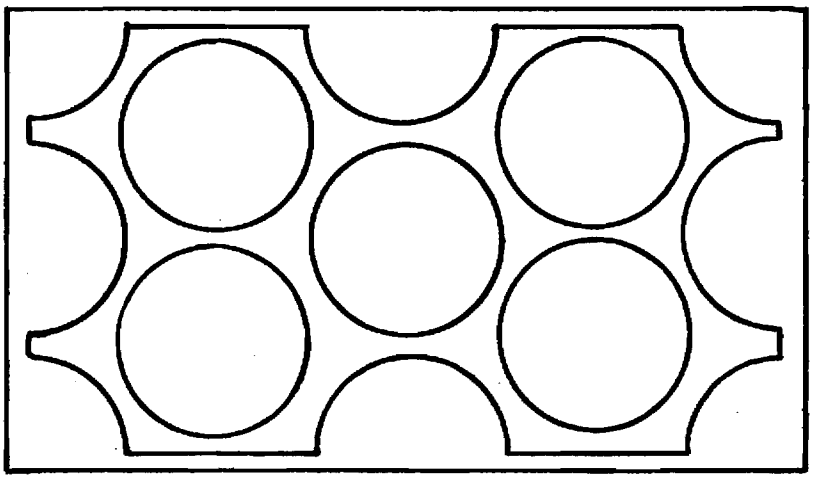

Figure 4-8. Sketch of subarray for Simulator No. 4.
Nominal frequency: f_o = 4.246 GHz
Element diameter: d^o = 1.022 in.
Lattice size: ℓ = 1.136 in.
= 0.409 λ_o
Fill-factor: d/ℓ = 0.9

SCAN ANGLES FOR WAVEGUIDE MODES IN SIMULATOR NO. 4 AT f_o = 4.2 GHz

MODE	THETA	PHI
10	20.9	0.0
20	45.6	0.0
11	45.6	60.0
21	71.0	40.9

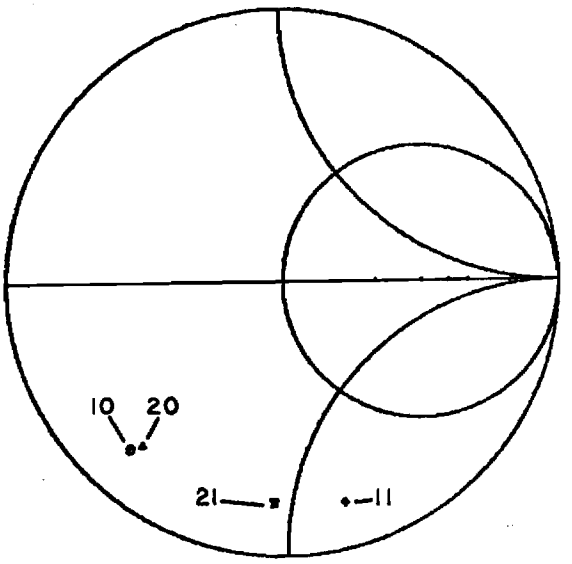

(a) No layer

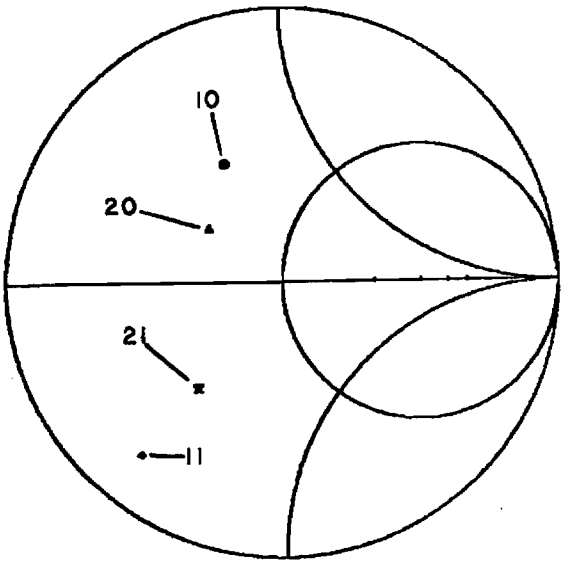

(b) 1/16" Rexolite layer

Figure 4-9. Smith Chart impedance plots for waveguide modes in Simulator No. 4 at f_o = 4.2 GHz.

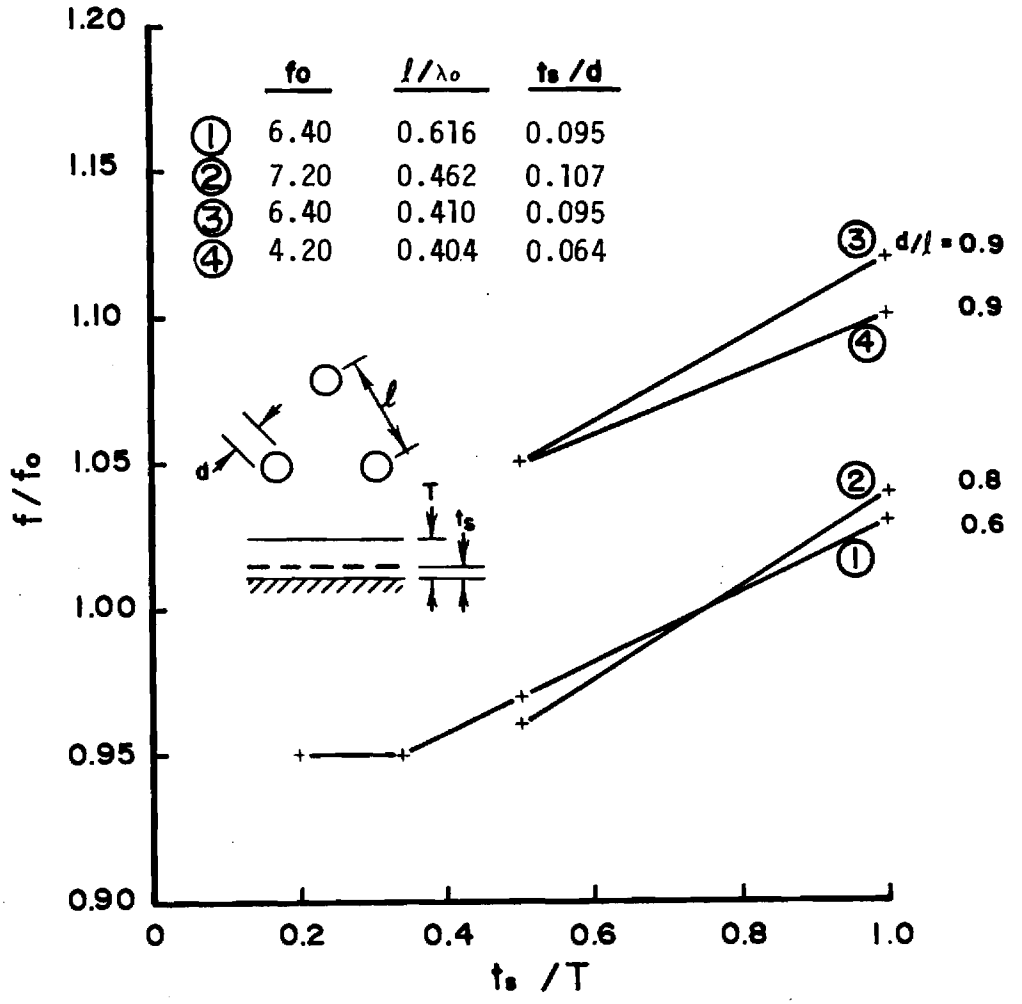

Figure 4-10. Change in apparent resonant frequency for microstrip elements in large arrays, covered by a dielectric layer of thickness $T-t_s$.

SECTION V
CONCLUSIONS AND RECOMMENDATIONS

The work discussed in this report has addressed several important problems associated with hardened phased-array antennas for BMD radar applications. The primary environmental threat considered has been the intense heat caused by nuclear explosions or by hypersonic aerodynamic friction. Over the five-year period of the contract, relevant BMD array technology has included dipole, waveguide, and microstrip elements, but microstrip elements have been the main new subject for the phase reported here. Throughout the program, the goal has been to identify array configurations that can maintain an acceptable beam-scan range, when the array face is protected by a refractory dielectric window or radome. As a result, Georgia Tech has developed analytical models, test methods, and a knowledge of materials that have directly supported phased-array development undertaken by the Ballistic Missile Defense Advanced Technology Center (BMDATC) and its industrial contractors.

The work discussed in Section II includes analytical calculations to evaluate the sensitivity of a planar waveguide array to a thick planar window and experimental measurements to evaluate the sensitivity of a microwave antenna measurement to flashing xenon lamps in a thermal simulator. The following conclusions were reached:

(1) The thick window does not have a major effect on the performance of the array of waveguide elements. The gap between the aperture of the array and the window is large enough that evanescent Floquet modes do not couple through the window, and the window has a second order effect on mutual coupling.

(2) Although a planar window does not dominate the coupling behavior, it is expected that a planar or curved window will cause boresight angle and slope errors as the beam is scanned, just as can happen with any radome.

(3) The available analytical model for waveguide arrays is not suitable for configurations that employ two or more elements for each phase shifter. A new model is needed to investigate the division of power between the main lobe and any grating lobes in such cases.

(4) The flashing xenon lamps in the thermal simulator had a pronounced effect on microwave measurements, and without further development, the simulator could not be used for electrical tests of antennas.

(5) A clear, saltwater filter could form an effective electrical barrier between a microwave test zone and the flashlamps in the simulator.

The work discussed in Section III includes the development of techniques for dielectric measurements and for phased array measurements. The following conclusions were reached:

(1) Refractory cements cannot survive the heating rates anticipated for ground-based radars. Previous applications of these materials apparently did not emphasize thermal survivability.

(2) Georgia Tech is assembling test equipment that can make X-band dielectric measurements at temperatures approaching 2,000°C. BMDATC has requested that the Air Force transfer the high-temperature components from the Aerospace Corporation to Georgia Tech.

(3) The parallel-plate resonator, which was implemented for dielectric measurements of disk-shaped samples, is precise and useful. The latitude allowed in sample sizes makes the method attractive for high-temperature testing.

(4) The multielement simulator, which was implemented to study microstrip elements, is a practical experimental tool for testing array elements. The five to twenty-five elements in a typical simulator represent a reasonable fabrication requirement, and this number is not enough to construct a convincing "small" array. The simulator eliminates the need for a feed network.

(5) The instrumentation and software developed at Georgia Tech to process the simulator data are satisfactory and should be useful in future work.

(6) A current procurement by Georgia Tech of millimeter-wave (mmW) sources, reflectometers, and receivers will establish a network analyzer capability in all bands though 170 GHz. This will permit dielectric measurements, array simulator measurements, and other antenna measurements of the type discussed in this report, but at mmW frequencies. This receiver-based system appears to offer better dynamic range, sensitivity, and accuracy than would six-port network analyzers.

The work discussed in Section IV concerns the general characteristics and suitability of microstrip elements for hardened BMD arrays. The following conclusions were reached:

(1) Microstrip elements are basically resonant elements, whether they are isolated or arrayed.

(2) The typical environment for a scanning array may cause the resonant frequency to be ten or fifteen percent higher than for the isolated element.

(3) A dielectric layer placed over the array element may lower the resonant frequency by ten to twenty percent.

(4) The probe-fed element seems to scan better in the H-plane than in the E-plane. The active impedance varies more as the beam is scanned toward the E-plane. (It is not possible to simulate an exact E-plane scan.) A scan of 60^{o} in the H-plane and a five percent bandwidth appear to be reasonable expectations.

(5) The data available at this time suggests that a cover layer with the same thickness as the substrate does not degrade the performance.

(6) The data available suggests that increasing the density of elements does not improve the scan performance of a dielectric covered array. This is contrary to expectations, but a conclusion is premature.

(7) The probe-fed element is readily fabricated for X-band dimensions, but for mmW dimensions, the attachment of a coaxial probe is undesirable and is probably impractical. The advantages of etched fabrication are lost, unless feed couplings can be made with the same ease and precision. The element could be well-suited for use with microwave-integrated-circuit (MIC) modules.

(8) For microstrip elements to be attractive in mmW arrays, non-contacting couplings to feed lines will be needed. This will probably mean that the elements in a subarray will be fed by series couplings from a single, short stripline or microstrip transmission line. The losses in mmW stripline are too great to permit long series feeds.

Although the role for microstrip elements in large scanning arrays is not entirely clear, there are good reasons to recommend that investigations be continued until the capabilities and limitations of the array element are better established. In several ways, the microstrip element is to the

microwave array what the dipole is to the VHF/UHF array. Both can be lightweight, compared with waveguide, both can be driven directly from coaxial lines, and both are resonant. The compatibility with coaxial line, the probable compatibility with MIC modules, low-cost fabrication, and conformal shape requirements are likely to cause continued interest in microstrip elements. More work is needed to establish scan limitations, bandwidth limitations, and better methods for coupling to feeds. The data obtained during this program is the first of its type to become available. More data is needed before firm conclusions can be formed, and ultimately, a theoretical model will be needed to provide the basis for a design procedure.

REFERENCES

1. J. A. Fuller and R. L. Moore, "Hardened Phased Array Feasibility Assessment," Technical Report, Contract DASG60-76-C-0070, Georgia Institute of Technology: Project A-1863, July 1977.

2. J. A. Fuller and R. L. Moore, "Hardened Phased Array Feasibility Assessment," Technical Report, Contract DASG60-76-C-0070, Amend. P00001, Georgia Institute of Technology: Project A-1863, October 1978.

3. J. D. Walton, et al, "Materials for Hardened Phased Array Antennas," Final Report, Contract No. DAAG46-79-C-0038, Georgia Institute of Technology: Project A-2360, April 1980.

4. J. D. Walton, et al, "Materials Development for Hardened Antennas - Phase II," Contract No. DAAG46-81-C-0015, Georgia Institute of Technology: Project A-2684, Work in Progress, 1982.

5. J. A. Fuller and T. S. Taylor, Trip Report for travel to Science Applications, Inc., McLean, VA, on 21 January 1981; submitted to BMDATC as attachment to Letter Progress Report No. 6, Contract No. DASG60-76-C-0070, April 1981.

6. J. A. Fuller, Letter to Dr. Louis Rondinelli, Malibu Research Associates, Santa Monica, CA, (Copy to Mr. Fan King, BMDATC), 7 April 1981.

7. J. A. Fuller, Trip Report for travel to Science Applications, Inc., McLean VA, on 18 December 1980, submitted to BMDATC as attachment to Letter Progress Report No. 5, Contract No. DASG60-76-C-0070, April 1981.

8. K. E. Lazdowski and H. J. Stalzer, Jr., "CWGARR -- A Program to Analyze an Infinite Periodic Array of Circular Waveguide Aperture Radiators," Technical Memorandum, MIT Lincoln Laboratory, 9 August 1978.

9. R. G. FitzGerrell, "SAMSO Antenna Measurements: Boeing Prototype Annular Slot," Technical Report, Institute for Telecommunication Sciences, U.S. Dept. of Commerce, Boulder, CO, April 1972.

10. L. L. Haidle, J. E. Partch, and R. G. FitzGerrell, "Encapsulant for Buried UHF Antennas," Electronic Letters, Vol. 7, 1971.

11. N. Marcuvitz, Waveguide Handbook, McGraw-Hill: New York, pp. 280-285, 1951.

12. American Society for Testing and Materials, "Standard Test Methods for Complex Permittivity of Solid Electrical Insulating Materials at Microwave Frequencies and Temperatures to 1,650°C," ANSI/ASTM D 2520-80, 1980.

13. R. F. Harrington, Time-Harmonic Fields and Waves, McGraw-Hill: New York, Chapter 7, 1961.

14. A. R. Von Hippel, Dielectric Materials and Applications, MIT Press: Cambridge, MA, 1954.

15. W. B. Westphal, "Dielectric Constant and Loss Data," Technical Report, No. AFML-TR-74-250, Part III, Contract No. F33615-77-C-5063, Massachusetts Institute of Technology, June 1980.

16. W. E. Courtney, "Analysis and Evaluation of a Method of Measuring the Complex Permittivity and Permeability of Microwave Insulators," IEEE Trans. Microwave Theory and Techniques, Vol. MTT-18, pp. 476-485, August 1970.

17. W. E. Courtney, "Complex Permittivity of GaAs and CdTe at Microwave Frequencies," IEEE Trans. Microwave Theory and Techniques, Vol. MTT-25, pp. 697-701, August 1977.

18. Private Communications: Mr. Fan King, Ballistic Missile Defense Advanced Technology Center; Dr. William T. Messick, Naval Surface Weapons Center (White Oak); Dr. Gordon Stewart, Aerospace Corporation.

19. P. W. Hannan and M. A. Balfour, "Simulation of a Phased-Array Antenna in Waveguide," IEEE Trans. Antennas and Propagation, Vol. AP-13, p. 342-353, May 1965.

20. H. A. Wheeler, "A Survey of the Simulator Technique for Designing a Radiating Element," in Phased Array Antennas, Artech House: Dedham, MA, pp. 132-148, 1972.

21. S. S. Gregorwich, A. Hessel, and G. H. Knittel, "A Waveguide Simulator Study of a Blindness Effect in a Phased Array," Microwave Jour., Vol. 14, pp. 37-41, Sept. 1971.

22. V. Galindo and C. P. Wu, "Integral Equations and Variational Expressions for Arbitrary Scanning of Regular Infinite Arrays," IEEE Trans. Antennas and Propagation, Vol. AP-14, pp. 392-394, May 1966.

23. J. J. Gustincic, "The Determination of Active Array Impedance with Multielement Simulators," IEEE Trans. Antennas and Propagation, Vol. AP-20, p. 589-595, Sept. 1972.

24. A. G. Derneryd, "Multielement Phased Array Waveguide Simulator for Circular Polarization," IEEE Trans. Antennas and Propagation, Vol. AP-24, pp. 480-483, July 1976.

25. N. Amitay, V. Galindo, and C. P. Wu, Theory and Analysis of Phased Array Antennas, Wiley-Interscience: New York, 1972.

26. Hewlett-Packard Staff, "Automating the HP 8410B Microwave Network Analyzer," Hewlett-Packard Application Note 221A, 1979.

27. S. F. Adam, "Automatic Microwave Network Measurements," Proc. IEEE, Vol. 66, pp. 384-391, April 1978.

28. S. Rehnmark, "On the Calibration of Automatic Network Analyzer Systems," IEEE Trans. Microwave Theory Tech., Vol. MTT-22, pp. 457-458, April 1974.

29. G. F. Engen, "The Six-Port Reflectometer: An Alternative Network Analyzer," IEEE Trans. Microwave Theory Tech., Vol. MTT-25, pp. 1075-1083, December 1977.

30. G. F. Engen, "Advances in Microwave Measurement Science," Proc. IEEE, Vol. 66, pp. 374-383, April 1978.

31. J. Q. Howell, "Microstrip Antennas," IEEE 1972 Int. Symp. Antennas and Propagation, Symposium Digest, p. 177, Dec. 1972.

32. R. E. Munson, "Conformal Microstrip Antennas and Microstrip Phased Arrays," IEEE Trans. Antennas and Propagation, Vol. AP-22, pp. 74-78, Jan. 1974.

33. J. Q. Howell, "Microstrip Antennas," IEEE Trans. Antennas and Propagation, Vol. AP-23, pp. 90-93, Jan. 1975.

34. K. R. Carver, ed., Proc. Workshop Printed Circuit Antenna Tech., New Mexico State Univ., Las Cruces, October 1979.

35. D. C. Chang, ed., "Special Issue on Microstrip Antenna Technology," IEEE Trans. Antennas and Propagation, Vol. AP-29, Jan. 1981.

36. J. R. James, P.S. Hall, and C. Wood, Microstrip Antenna Theory and Design, Peter Peregrinus Ltd.: Stevenage, UK, 1981.

37. Y.T. Lo, D. Solomon, and W. F. Richards, "Theory and Experiment on Microstrip Antennas," IEEE Trans. Antennas and Propagation, Vol. AP-27, pp. 137-145, March 1979.

38. J. P. Montgomery, "Scattering by an Infinite Periodic Array of Microstrip Elements," IEEE Trans. Antennas and Propagation, Vol. AP-26, pp. 851-854.

39. F. L. Opp and J. P. Montgomery, "Microstrip Reflectarray Antenna Program," Final Report, Air Force No. RADC-TR-77-296, Texas Instruments, Inc., Aug. 1977.

APPENDIX A

DIELECTRIC MEASUREMENTS IN A SOLAR FURNACE RESONATOR

7 January 1981

TECHNICAL MEMORANDUM

TO: Project File A-2684, A-1863

FROM: T. S. Taylor

SUBJECT: Measuring Dielectric Constant of Samples in a Solar Oven Using a Free Space Resonator

To solve the problem of measuring dielectric properties while they are being heated in a solar furnace, a free space resonator has been developed. A resonance is set up in free space by using a flat metal ground plane and a metal parabolic solar reflector. By monitoring the change in frequency at which there is a resonance the dielectric properties can be calculated.

Three different setups have been used so far with increased success with each new setup. The first setup is shown in Figure 1. By changing the position of the sliding short, the path length in the waveguide could be changed and hence the frequency at which resonance occurred. The system was tested by moving the sliding short, by inserting different dielectrics, and of course, by moving the horn relative to the parabolic reflector. The sliding short could be moved through one waveguide wavelength. By using the change in path length, the waveguide wavelength could be calculated within 4%. When the dielectric samples were inserted into the field, the resonance pattern did change; however, it was difficult to know exactly how the pattern changed. The main factors were that the Q of the system was too low and the dielectric samples were too large. When the horn was close to the focal point, the Q of the system was approximately 600 to 800. The quality factor Q is defined by

$$Q = \frac{fo}{BW_{3dB}} \qquad (1)$$

where fo is the resonant frequency and BW is the 3 dB bandwidth. The second setup was much like the first except for the fact that the 22" diameter parabolic reflector was replaced with a 36" diameter parabolic reflector. The Q factor increased to about 800 to 1000, but it was still not consistently high enough.

The third setup as shown in Figure 2 placed the resonance totally in the free space between the parabolic reflector and the ground plane. This was accomplished by placing an iris on the horn so that when the horn was near the focal point the microwave energy would be reflected off of the iris. It was found that a capacitive iris on a small horn and open ended waveguide worked quite well. Quality factors of about 2000 to 4000 could be obtained with this system.

Small circular (dia = 1", thickness = ½") dielectric samples were placed at the focal point of the parabolic reflector and the horn was placed just behind the dielectric samples. The change in the resonant pattern was easily recognized and it was possible to calculate the dielectric constant for a dielectric sample. The dielectric constant for any sample is given by ε_s , where

$$\varepsilon_s + \Delta\varepsilon = \varepsilon_o \left(1 + \frac{\Delta f}{f} \frac{\tau}{\Delta\tau} \frac{1}{C}\right) \qquad (2)$$

where ε_o = dielectric constant of free space

$\Delta\tau$ = perturbed volume in the resonant cavity

τ = total volume of the resonant cavity

f = resonant frequency with the dielectric sample in place

Δf = change in resonant frequency when the sample was inserted

$\Delta\varepsilon$ = change in dielectric of the perturbed volume

C = cavity constant.

The cavity constant can be calculated by using Equation 2 and a known dielectric since the constant only depends on the geometry of the resonant cavity. The cavity constant was calculated using open ended waveguide over a frequenccy range of 9 to 10 GHz and a dielectric sample of plexiglass. The dielectric constants for five different samples were then calculated as shown in Table II.

cc: JAF, JDW, SHB, JNH

TABLE I

Calculation of Cavity Constant, C, using Plexiglass (ϵ_s = 2.6) Over a Frequency Range of 9.0 to 10.0 GHz

Dielectric	Frequency (GHz)				Change in Frequency (GHz)						Cavity Constants			
	f_1	f_2	f_3	f_4	Δf_1	Δf_2	Δf_3	Δf_4	ϵ	$\Delta\epsilon$	C_1	C_2	C_3	C_4
Air	9.125	9.370	9.620	9.860					1.0					
Plexiglass	9.040	9.275	9.525	9.765	.085	.095	.095	.095	2.6	1.6	44.0	48.0	46.7	45.6

TABLE II

Calculation of Dielectric Constant using Cavity Constants C_1, C_2, C_3, C_4 for a Frequency Range of 9.0 to 10.0 GHz

	Air	Polyethelene	Rexolite	Nylon	Silica	Stycast
f_1	9.125	9.060	9.045	9.020	9.005	8.980
f_2	9.370	9.290	9.280	9.250	9.240	9.220
f_3	9.620	9.540	9.530	9.505	9.495	9.480
f_4	9.860	9.780	9.760	9.745	9.735	9.715
Δf_1		.065	.080	.105	.120	.145
Δf_2		.080	.090	.120	.130	.150
Δf_3		.080	.090	.115	.125	.140
Δf_4		.080	.100	.115	.125	.145
$\Delta\varepsilon_1$		1.25	1.50	1.97	2.23	2.70
$\Delta\varepsilon_2$		1.38	1.50	2.02	2.16	2.50
$\Delta\varepsilon_3$		1.38	1.50	1.93	2.08	2.33
$\Delta\varepsilon_4$		1.38	1.67	1.93	2.07	2.41
$\bar{\Delta\varepsilon}$		1.35	1.54	1.96	2.14	2.49
$\bar{\varepsilon}$		2.35	2.54	2.96	3.14	3.49
known ε		2.25	2.54	3.00	3.4	4.00
Diff		4.4%	0%	-1.3%	-7.6%	-12.7

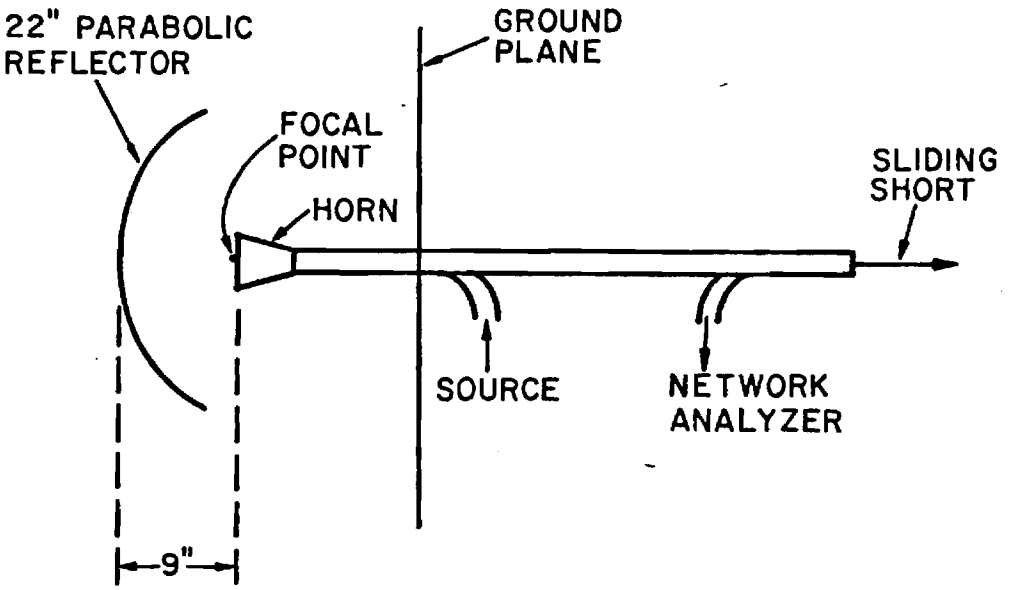

Figure 1. Free space resonator with parabolic reflector, ground plane, horn, and sliding short.

APPENDIX B

DIELECTRIC CONSTANT MEASUREMENTS IN A PARALLEL-PLATE RESONATOR

Georgia Institute of Technology
ENGINEERING EXPERIMENT STATION
ATLANTA, GEORGIA 30332

13 May 1981

TECHNICAL MEMORANDUM

TO: Project File A-1863

FROM: T. S. Taylor

SUBJECT: Computer Analysis for Measurement of the Dielectric Constant of a Cylindrical Sample in a Parallel Plate Cavity Resonator

Courtney [1,2] has described an accurate method for measuring the dielectric constant and loss tangent for a cylindrical sample in a parallel plate cavity resonator. In this method, a cylindrical sample is placed between two highly conductive plates. Probes are then placed close to the sample. The electric and magnetic fields outside the dielectric decay very rapidly since they are below the cutoff frequency. The modes that propagate in the dielectric are given by the following characteristic equation

$$\alpha J_o(\alpha)/J_1(\alpha) = -\beta K_o(\beta)/K_1(\beta) \tag{1}$$

where $J_o(\alpha)$, $J_1(\alpha)$ are Bessel functions of the first level

$K_o(\beta)$, $K_1(\beta)$ are Bessel functions of the second kind

and

$$\alpha = \frac{\pi D}{\lambda_o}\left[\varepsilon - \left(\frac{\ell\lambda_o}{2L}\right)^2\right]^{1/2} \tag{2}$$

$$\beta = \frac{\pi D}{\lambda_o}\left[\left(\frac{\ell\lambda_o}{2L}\right)^2 - 1\right]^{1/2} \tag{3}$$

Thus, for a cylindrical sample of diameter, D, and height L, only the resonant frequency for the TE_{01} mode needs to be measured to calculate

the dielectric constant. The free space wavelength, λ_o, is calculated from the measured resonant frequency, and then β can be calculated using Equation 3. Once β is known, Equation (1) can be solved by using an iterative method. Newton's method provides a method for quick convergence. For this method let

$$f(\alpha) = \alpha J_o(\alpha)/J_1(\alpha) - F(\beta) = 0 \qquad (4)$$

where $F(\beta) = \beta K_o(\beta)/K_1(\beta)$

The solution to Equation (4) is then given by

$$\alpha_{n+1} = \alpha_n - \frac{f(\alpha_n)}{f'(\alpha_{n+1})} \qquad (5)$$

It can be shown that

$$f'(\alpha) = -\alpha(J_o(\alpha)/J_1(\alpha))^2 + 2J_o(\alpha)/J_1(\alpha) - \alpha$$

After α_{n+1} is calculated to the desired accuracy, the dielectric constant, ε, can be calculated from Equation (2).

A computer program has been written to calculate the dielectric constant for any sample given the sample size, and the measured resonant frequency; and the following preliminary conclusions can be made.

1. The iteration by Newton's Method provides for quick convergence.

2. There are many possible values of α that will satisfy Equation (1). The first root, $\ell = 1$, is the root of interest. The first root must be in the region of $J_1 > 0$ and $J_o < 0$. Therefore, must have a value between 2.4 and 3.9.

3. Not all sample sizes will provide a resonant frequency in X-band. For the standard sample size resonance will occur for the following dielectric constants.

Dia = 1"	L = ½"	ε = 4.0 to 1.7
Dia = 2"	L = ½"	ε = 2.7 to 1.2

If the height of the sample is decreased, measurements can be made for samples with higher dielectric constants.

Dia = 1"	L = ¼"	ε = 11.1 to 5.3
Dia = 2"	L = ¼"	ε = 9.4 to 4.5

Figures 1, 2, and 3 show how the resonant frequency of the TE_{01} mode varies with the dielectric constant for different sample sizes. As can be seen from the graphs, the thinner samples will yield a more accurate value for the dielectric constant for any measured resonant frequency, since the slope decrease with sample thickness. The larger the ratio of the diameter to the height, the more the separation between the modes. This is very desirable since the mode of interest, TE_{01}, is identified by being the second mode. This mode also remains stationary when the small air gap above the sample is used, while all the neighboring modes will move in frequency.

TST:bg

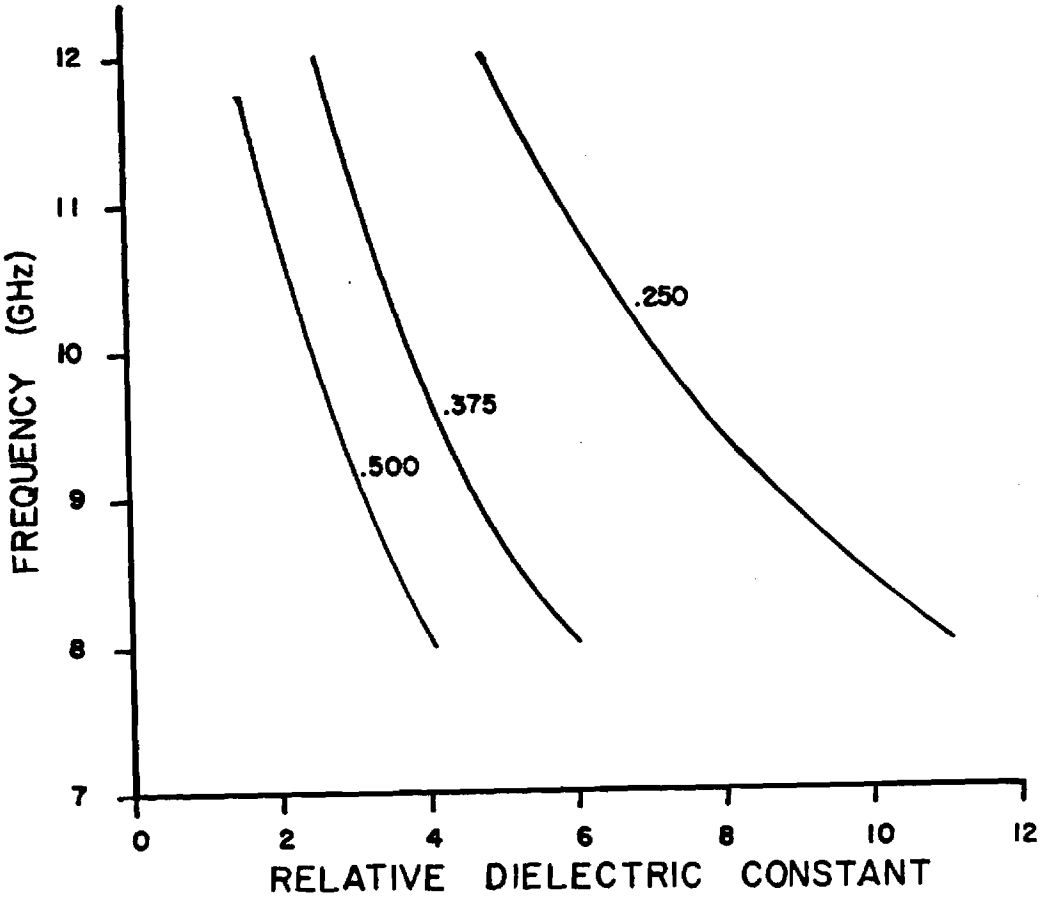

Figure 1. Frequency of TE_{01} mode in a cylindrical sample vs. the relative dielectric constant.
Diameter = 1.0 in.
Thickness = Parameter (in.)

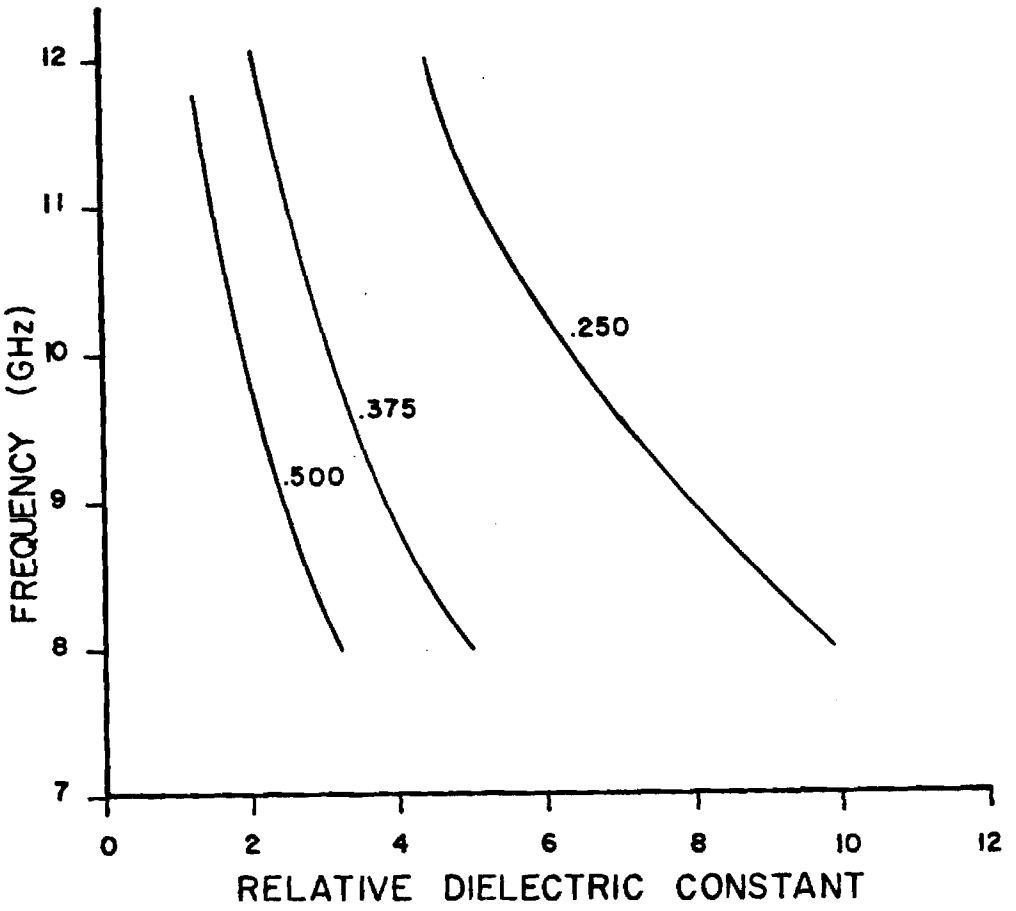

Figure 2. Frequency of TE_{01} mode in a cylindrical sample vs. the relative dielectric constant.
Diameter = 1.5 in.
Thickness = Parameter (in.)

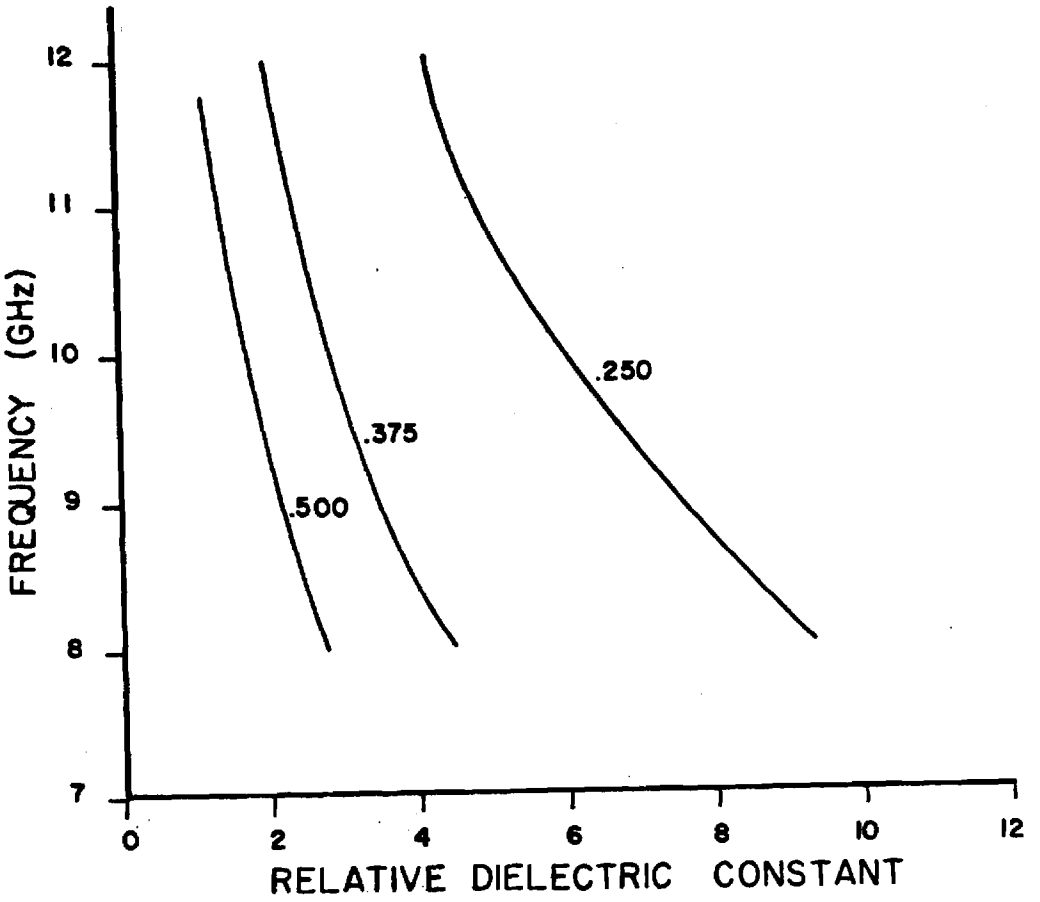

Figure 3. Frequency of TE_{01} mode in a cylindrical sample vs. the relative dielectric constant.
Diameter = 2.0 in.
Thickness = Parameter (in.)

REFERENCES

1. W. E. Courtney, "Analysis and Evaluation of a Method of Measuring the Complex Permittivity and Permeability of Microwave Insulators," IEEE Trans. Microwave Theory and Techniques, Vol. MIT-18, pp. 476-485, August 1970.

2. W. E. Courtney, "Complex Permittivity of GaAs and CdTe at Microwave Frequencies," IEEE Trans. Microwave Theory and Techniques, Vol. MIT-25, pp. 697-701, August 1977.

APPENDIX C

DIELECTRIC LOSS MEASUREMENTS IN A PARALLEL-PLATE RESONATOR

Georgia Institute of Technology
ENGINEERING EXPERIMENT STATION
ATLANTA, GEORGIA 30332

27 May 1981

TECHNICAL MEMORANDUM

TO: Project File A-1863

FROM: T. S. Taylor

SUBJECT: Analysis for Measurement of the Loss Tangent of a Cylindrical Sample in a Parallel Plate Cavity Resonator

Courtney [1,2] has described an accurate method for measuring the dielectric constant and loss tangent for a cylindrical sample in a parallel plate cavity resonator as discussed in a previous memo. In this memo, in Section I, the theory behind the stated characteristic equation will be investigated for complex dielectric constants. In Section II the measurement of the Q factor of the cavity wll be discussed. An analysis of the effect of measurement error will be discussed in Section III.

I. Theory of Cylindrical Cavity Resonators

The characteristic equation for the propagating modes in a cylindrical sample that is placed in a cavity resonator can be obtained from the scalar Helmhotz equation. This Helmhotz equation written for a cylindrical coordinate system is given by

$$\frac{1}{\rho}\frac{\partial}{\partial\rho}\left(\rho\frac{\partial\psi}{\partial\rho}\right)+\frac{1}{\rho^2}\frac{\partial^2\psi}{\partial\phi^2}+\frac{\partial^2\psi}{\partial z^2}+k^2\psi=0 \qquad (1)$$

This is solved using the method of separation of variables where

$$\psi = R(\rho)\Phi(\phi)Z(z) \qquad (2)$$

Substitution and division yields

$$\frac{1}{R}\frac{d^2R}{d\rho^2}+\frac{1}{\rho R}\frac{dR}{d\rho}+\frac{1}{\rho^2\Phi}\frac{d^2\Phi}{d\phi^2}+\frac{1}{Z}\frac{d^2Z}{dz^2}+k^2=0 \qquad (3)$$

In the standard fashion, Equation (3) can then be separated into three separate equations:

$$\frac{d^2Z}{dz^2} + k_z^2 Z = 0 \qquad (4a)$$

$$\frac{d^2\Phi}{d\phi^2} + n^2\Phi = 0 \qquad (4b)$$

$$\rho \frac{d}{d\rho}\left(\rho\frac{dR}{d\rho}\right) + [(k_\rho\rho)^2 - n^2] R = 0 \qquad (4c)$$

To solve this set of equations, the boundary conditions must be considered. The problem can be considered to have two regions-- the region inside the dielectric sample (region 1), and the region outside the sample (region 2). The sample is assumed to be a low loss dielectric with a complex dielectric constant, κ; radius, a; and height, L. The wavenumber is

$$k = k_o \kappa \qquad (5a)$$

where $$k_o = \omega \sqrt{\mu_o \varepsilon_o} \quad , \qquad (5b)$$

$$\kappa = \varepsilon_r(1 - j\tan\delta) \quad , \qquad (5c)$$

ε_r is the relative dielectric constant, and $\tan\delta$ is the loss tangent.

The boundary conditions that must be met are: $Z(0) = Z(L)=0$, and the tangential fields inside the sample must be equal to the fields outside the sample at $\rho = a$.

When the first boundary condition is applied to Equation (4a), the only solution is

$$Z(z) = A\sin k_z z$$

where $$k_z = \frac{\ell\pi}{L} \text{ for } \ell = 1,2,3...$$

Since there is ϕ symmetry, the lowest order solution (n=0) can be chosen for Equation (4b). Equation (4c) is then the zeroth order Bessel equation. Therefore, the scalar-wavefunction that corresponds to the solution in region 1 is

$$\psi_1(\rho,\phi,z) = A\, J_o(k_1\rho)\sin k_z z \qquad (6)$$

where $k^2 = k_I^2 + k_z^2$

and therefore $k_1^2 = \omega^2\mu_o\varepsilon_o\,\kappa - (\frac{\ell\pi}{L})^2$

In region 2, outside the dielectric sample, the modes are evanescent and therefore the solution to Equation (4c) is a modified Bessel function. The solution to Equation (1), in region 2, is

$$\psi_2(\rho, \phi, z) = AK_o(k_2\rho)\sin k_z z \qquad (7)$$

where $k_o^2 = (ik_2)^2 + k_z^2$

and therefore $k_2^2 = (\frac{\ell\pi}{L})^2 - \omega^2\mu_o\varepsilon_o$

The boundary condition of continuity at ρ=a yields the characteristic equation

$$\alpha\,\frac{J_o(\alpha)}{J_1(\alpha)} = -\,\beta\,\frac{K_o(\beta)}{K_1(\beta)} \qquad (8)$$

where $\alpha = ak_1 = \frac{\pi D}{\lambda}\,[\varepsilon_r(1 - j\tan\delta) - (\frac{\ell\lambda}{2L})^2]^{1/2}$ (9)

$$\beta = ak_2 = \frac{\pi D}{\lambda}\,[\,(\frac{\ell\lambda}{2L})^2 - 1\,]^{1/2} \qquad (10)$$

where D = 2a, the diameter of the sample

The relative dielectric constant and loss tangent can then be calculated by first solving Equation (10) for β . Using this β the right hand side of Equation (8) can be determined. Equation (8) is then solved for α by an interative method and the complex dielectric constant is determined from Equation (9).

Although the above solution takes the loss in the dielectric sample into account, it assumes that the walls of the cavity are perfect conductors. This problem is minimized by using only TE modes in the sample. To accurately take all of the losses into account, the above solution must be perturbed by the losses in the walls. This perturbation is valid for low loss dielectrics and highly conductive walls.

To take the wall losses into account, the Q of the cavity must be determined. The unloaded Q of the resonant structure, Q_o, is given by

$$\frac{1}{Q_o} = \frac{1}{Q_{wall}} + \frac{1}{Q_{cav}} \tag{11}$$

where $$Q_{wall} = \frac{\omega(U_{cav} + U_{space})}{W_{wall}}$$

$$Q_{cav} = \frac{\omega(U_{cav} + U_{space})}{W_{cav}}$$

and therefore, $$Q_o = \frac{\omega(U_{cav} + U_{space})}{W_{wall} + W_{cav}} \tag{12}$$

The total energy stored in the resonant cavity is $U_{cav} + U_{space}$ where

$$U_{cav} = \int_{cav} \frac{\epsilon_o \epsilon_r}{2} |E_1|^2 \, d\tau \tag{13}$$

$$U_{space} = \int_{space} \frac{\epsilon_o}{2} |E_2|^2 \, d\tau \tag{14}$$

where $$E_1 = i_\phi \, k_1 A \, J_1(k_1 \rho) \sin k_z z$$

$$E_2 = i_\phi \, k_2 A \, K_1(k_2 \rho) \sin k_z z$$

The energy losses occur in the walls, W_{wall}, and in the cavity, W_{cav}.

$$W_{wall} = R_S \int_{Wall} |H_z \times i_z|^2 \, ds \tag{15}$$

$$W_{cav} = \frac{wk\tan\delta}{2} \int_{cav} |E_1|^2 \, d\tau \qquad (16)$$

where $R_S = \left(\frac{\pi f \mu_o}{\sigma}\right)^{1/2}$

σ = the conductivity of walls

$$H_z = \frac{-jAk_2}{\omega\mu_o} [i_\rho k_z K_1(k_2\rho) \cos k_z Z + i_z k_2 K_o(k_2\rho) \sin k_z Z]$$

Equations (13-16) can be solved to obtain the loss tangent, where

$$\tan\delta = \frac{1}{Q_o}\left[1 + \frac{1}{\varepsilon_r} F(\alpha)\, G(\beta)\right] - \frac{\ell^2 R_s}{2\pi f^3 \mu^2 \varepsilon_o \varepsilon_r L^3}\left[1 + F(\alpha)G(\beta)\right]$$

where $F(\alpha) = \dfrac{|J_1(\alpha)|^2}{|J_1(\alpha)|^2 - J_o(\alpha)J_2(\alpha)}$

$$G(\beta) = \frac{K_o(\beta)K_2(\beta) - K_1^2(\beta)}{K_1(\beta)}$$

II. Measurements

To find the relative dielectric constant and loss tangent of a cylindrical sample, three quantities must be known. The conductivity of the plates must be either taken from reference tables or calculated using a sample with a well known relative dielectric constant and loss tangent. The resonant frequency of the loaded cavity can be measured directly. The third quantity, the unloaded Q of the cavity, Q_o, must also be determined. It, of course, cannot be measured directly since it represents the Q of the cavity without the loading of the transmission lines. However, it can be determined from the loaded Q.

To determine the unloaded Q, it is easiest to make a circuit model of transmission through the cavity, as seen in Figure 1a. The circuit can be simplified, Figure 1b, by using the characteristic impedance of the input and output transmission lines, Z_1 and Z_z. The input and output coupling coefficients are given by

$$C_1 = \frac{(\omega M_1)^2}{R_s Z_1}$$

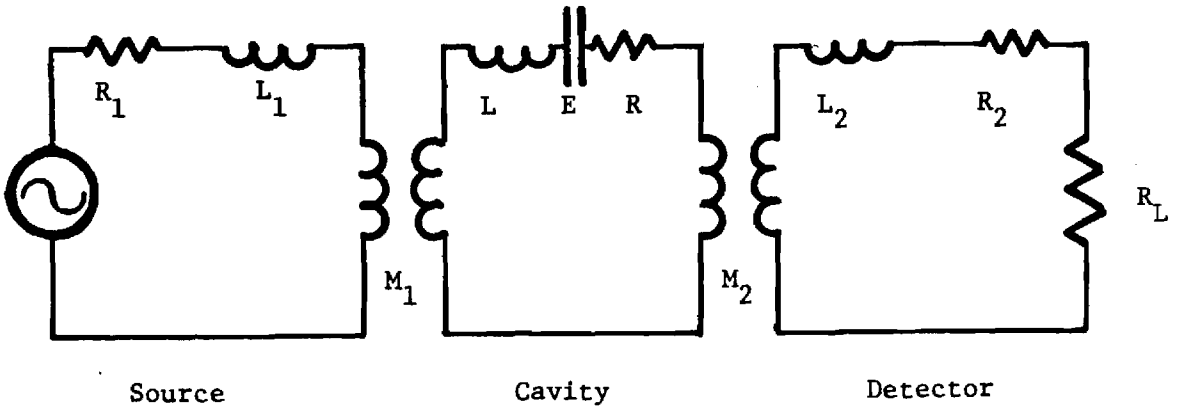

(a)

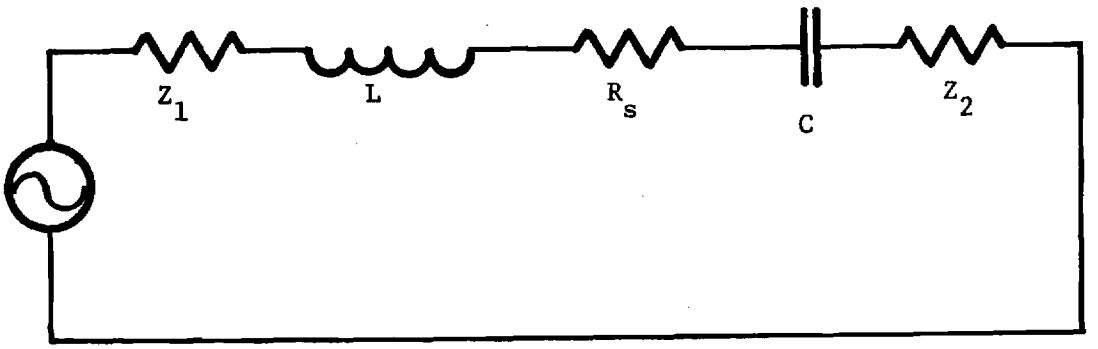

(b)

Figure 1. Circuit model of transmission through a resonant cavity.

$$C_2 = \frac{(\omega M_2)^2}{R_s Z_2}$$

The unloaded Q of the cavity, Q_o is then given by

$$Q_o = Q_L (1 + C_1 + C_2)$$

The loaded Q, Q_L, is given by

$$Q_L = \frac{\omega}{\omega^+ - \omega^-}$$

where ω^+ and ω^- represent the 3 dB points.

Therefore, if the coupling coefficients of the transmission lines going into and coming out of the cavity can be made to be small the unloaded Q will just be equal to the measured, loaded Q. By designing the transmission lines to weakly couple into the cavity, the unload Q can be easily determined.

III. The Effect of Measurement Error on Loss Tangent

Of the three measured quantities, the conductivity, (σ), the unload Q, and the resonant frequency, (f), small measurement errors in the conductivity produces the smallest variation in the loss tangent. This analysis was conducted by calculating the loss tangent for a known σ, Q, and f; and then varying each quantity by some percentage that represents a percent error in measurement. A 20% error in the conductivity produced a 2% error in the loss tangent, while a 20% error in the measurement of the Q or the resonant frequency produced approximately a 20% error in the loss tangent. It can be concluded then, that great care should be taken in designing the cavity so that a well defined, high Q resonance occurs. In Table 1, the loss tangent is calculated for an example sample that is placed in between two copper plates, where the conductivity of copper is taken to be $1.5 \times 10^6\ \Omega^{-1}\ in^{-1}$. As can be seen, to go beyond loss tangent of .001 the Q must be better than 500. For a loss tangent of .0001, the Q must be approximately 5000.

TABLE 1

Calculation of Loss Tangent for Example Sample

Diameter = 1.0 in.
Height = .5 in.
Resonant frequency = 10 GHz
Conductivity = $1.5 \times 10^6\ \Omega^{-1}\text{in}^{-1}$

Q	tan δ
500	.0016
1000	.0008
2000	.0004
5000	.0001

APPENDIX D

EVALUATION OF THE SIX-PORT NETWORK ANALYZER

Georgia Institute of Technology
ENGINEERING EXPERIMENT STATION
ATLANTA, GEORGIA 30332

10 March 1981

TECHNICAL MEMORANDUM

TO: A-1863-000

FROM: Thomas S. Taylor TST

SUBJECT: Analysis of a Six Port for Measuring Reflections from Shorts

The main advantage of a six port device is that four amplitude-only power detectors can be used to measure the complex reflection coefficient for any device. Also six ports are less expensive to build than network analyzers. They can be made to be as accurate as a network analyzer. In general, a small computer is necessary to calibrate a six port system; but the dc voltages from the four output ports are easily read by an automated system.

Theory

The scattering matrix of the six port shown in Figure 1 will be considered. Ports 3-6 are terminated with power detectors, port 1 is the input port and port 2 is terminated with the device under test. The scattering matrix has the form

$$\begin{bmatrix} b_i \\ b_k \end{bmatrix} = \begin{bmatrix} S_{ii} & S_{ik} \\ S_{ki} & S_{kk} \end{bmatrix} \begin{bmatrix} a_i \\ a_k \end{bmatrix} \qquad (1)$$

where $i = 1,2$
$k = 3,4,5,6$

The reflected scattering variables, b, at ports 3-6 can be written as a linear combination of the scattering variables of the test port, a_2 and b_2. The magnitude of the scattering variables at ports 3-6 is proportional to the power measured by the four power meters. Therefore, the power readings

can be written as a function of the test port scattering variables by

$$\begin{bmatrix} P_3 \\ P_4 \\ P_5 \\ P_6 \end{bmatrix} = \begin{bmatrix} \\ A^{-1} \\ \\ \end{bmatrix} \begin{bmatrix} b_2 b_2^* \\ b_2 a_2^* \\ b_2^* a_2 \\ a_2 a_2^* \end{bmatrix} \qquad (2)$$

where A^{-1} is the inverse of a 4x4 complex calibration matrix, A. Therefore, if the calibration matrix A is known, only four power readings are necessary to calculate the complex reflection coefficient for any device under test.

Design

A specific six port network is shown in Figure 2. The network can be easily made out of waveguide components. The wave amplitudes are shown at all of the inputs and outputs of each of the components, assuming that the components are ideal. The voltages at each of the four power meters would then be given by

$$\begin{aligned} V_3 &= -jd(\Gamma - j)\sqrt{2} \\ V_4 &= -d/\sqrt{2} \\ V_5 &= -d(\Gamma + 1 + j)/2 \\ V_6 &= jd(\Gamma - 1 + j)/2 \end{aligned} \qquad (3)$$

where $\Gamma = \Gamma_R + j\,\Gamma_I$

$\Gamma^* = \Gamma_R - j\,\Gamma_I$

The power levels at each of the four power meters would then be

$$\begin{aligned} P_3 &= V_3 V_3^* = \tfrac{1}{2}d^2\,(\Gamma_R^2 + \Gamma_I^2 - 2\Gamma_I + 1) \\ P_4 &= V_4 V_4^* = \tfrac{1}{2}d^2 \\ P_5 &= V_5 V_5^* = \tfrac{1}{4}d^2\,(\Gamma_R^2 + \Gamma_I^2 + 2\Gamma_R + 2\Gamma_I + 2) \\ P_6 &= V_6 V_6^* = \tfrac{1}{4}d^2\,(\Gamma_R^2 + \Gamma_I^2 - 2\Gamma_R + 2\Gamma_I + 2) \end{aligned} \qquad (4)$$

By combining the set of Equations given by (4), it can be easily shown that

$$\Gamma_R = \tfrac{1}{2}\,(P_5-P_6)/P_4$$

$$\Gamma_I = \tfrac{1}{4}(P_5 + P_6 - P_3 - P_4)/P_4 \qquad (5)$$

Therefore it can be seen that by measuring just the power levels at four ports the complex reflection coefficient of the device under test can be calculated. This obviously holds only for an ideal six port. For an actual six port some calibration method must be obtained. A calibration method will be discussed in the next section.

Calibration

A six port system can be calibrated with a repeatable two-position insertion device [1]. Using this method, no standards are needed; however, the insertion device must be highly repeatable. In this method, 32 different power readings are needed. An alternate method is to use four known standards [2]. In this method, Equation (2) can be written as

$$b = C \cdot p \qquad (6)$$

where C is a 4x4 real calibration matrix
p is a column matrix of power readings
b is a column matrix of a quadratic function of the test port scattering varaiables given by

$$[\,b\,] = |b|^2,\ \mathrm{Re}(ba^*),\ \mathrm{Im}(ba^*),\ |a|^2$$

To calibrate the six port system, one set of calibration standards is:

short: $\Gamma = 1$
open : $\Gamma = -1$
offset short: $\Gamma = 1(\cos\phi - j\sin\phi)$ where $\phi = \frac{2\pi L}{\lambda}$
-40 dB load: $\Gamma = .01(\cos\theta - j\sin\theta)$

To find all 16 elements of the calibration matrix, C, 4 sets of power readings must be taken using the 4 calibration standards. This will produce a 4x4 power reading matrix, P, and a 4x4 scattering variable matrix, B. The calibration matrix can then be calculated by

$$C = B\ P^{-1} \tag{7}$$

The scattering matrix, B, would then be given by:

	Short	Open	Offset Short	-40 dB Load
$\|b\|^2$	$\|a\|^2$	$\|a\|^2$	$\|a\|^2$	$.0001\ \|a\|^2$
$Re(ba^*)$	$\|a\|^2$	$\|a\|^2$	$\|a\|^2\cos\phi$	$.01\ \|a\|^2\cos\phi$
$Im(ba^*)$	0	0	$-\|a\|^2\sin\theta$	$-.01\ \|a\|^2\sin\theta$
$\|a\|^2$	$\|a\|^2$	$\|a\|^2$	$\|a\|^2$	$\|a\|^2$

The $|a|^2$ factor can be divided out to produce the matrix, B'

$$[B'] = \begin{bmatrix} 1 & 1 & 1 & .0001 \\ 1 & 1 & \cos\phi & .01\cos\phi \\ 0 & 0 & -\sin\theta & -.01\sin\theta \\ 1 & 1 & 1 & 1 \end{bmatrix}$$

where $B = |a|^2\ B'$

The calibration matrix C can be determined to within a scale factor, $|a|^2$ from Equation (7)

$$C = B\ P^{-1} = |a|^2\ B'P^{-1} = |a|^2\ C' \tag{8}$$

In the following section it will be shown that the unknown scale factor, $|a|^2$ can be calculated.

After calibration, the reflection coefficient, Γ_ℓ , for any unknown load can be calculated by noting the power levels at the 4 power detectors. The magnitude of the reflection coefficient $|\Gamma_\ell|^2$ is given by:

$$|\Gamma_\ell|^2 = \frac{|b|^2}{|a|^2} = \frac{b_1}{b_4} \qquad (9)$$

Using Equation (6)

$$b_1 = \sum_{i=1}^{4} C_{1i} P_i = |a|^2 = \sum_{i=1}^{4} C'_{1i} P_i = |a|^2 b'_1$$

and $$b_4 = \sum_{i=1}^{4} C_{4i} P_i = |a|^2 = \sum_{i=1}^{4} C'_{4i} P_i = |a|^2 b'_4$$

Therefore the unknown scale factor $|a|^2$ will divide out of the magnitude of the reflection coefficient. To find the exact value of the reflection coefficient one can use the fact that

$$\Gamma_\ell = |a|^2 b'_2 + j\ |a|^2 b'_3 \qquad (10)$$

and $$|\Gamma_\ell|^2 = |a|^4 (b_2'^2 + b_3'^2)$$

where $$b'_2 = \sum_{C=1}^{4} C'_{2i} P_{i+2}$$

$$b'_3 = \sum_{i=1}^{4} C'_{3i} P_{i+3}$$

Therefore the scale factor, $|a|$ can be calculated exactly from

$$|a|^4 = |\Gamma_\ell|^2 / (b_2'^2 + b_3'^2) \qquad (11)$$

Knowing the scale factor, the calibration matrix can be calculated exactly.

Accuracy

Cletus Hoer at the National Bureau of Standards has done some work on the imprecision of six ports [2,3] . The most important conclusion is that the accuracy is primarily determined by the linearity and resolution of the power detectors. The estimated accuracy of the reflection coefficient for diode detectors is .1 dB to .01 dB and for thermistor detectors .01 dB to .001 dB. By using NBS power meters with thermistor detectors housed in aluminum blocks held at constant temperature, the imprecision was established to be .0003 dB at 3 GHz. This certainly represents the upper limit of accuracy.

REFERENCES

1. C. A. Hoer, K. C. Rue, "Using an Arbitrary Six-Port Junction to Measure Complex Voltage Ratios," IEEE Trans. Microwave Theory Tech., Vol. MIT-23, p. 978-984, Dec. 1975.

2. C. A. Hoer, "Performance of a Dual Six-Port Automatic Network Analyzer," IEEE Trans. Microwave Theory Tech., Vol. MTT-27, pp. 993-998, Dec. 1979.

3. C.A. Hoer, "A Network Analyzer Incorporating Two Six-Port Reflectometers," IEEE Trans. Microwave Theory Tech., Vol. MTT-25, pp. 1070-1074, Dec. 1977.

TABLE I

Six-Port Parts List from MDL (10 GHz)

Qty	Part Description	Number	Cost/Unit	Total Cost
4	Sidewall coupler (3 dB, 90°)	90HS82	105	$ 420
1	H-Plane Tee(3 dB, 0°)	90TH62	237	237
8	Sidewall Panty Adapters	901532	41	328
1	Mixer with Adapter	90M146-1	260	260
2	Crystal Holders	90DH96-1	180	360
4	Elbows	90BH32	10.80	43.20
	Straight Sections/Aluminum	WR90	4.10/ft.	20
	Straight Section/Silver	WR90	N/A	
2	Precision Load	90LW56	176	352
				$ 2,020

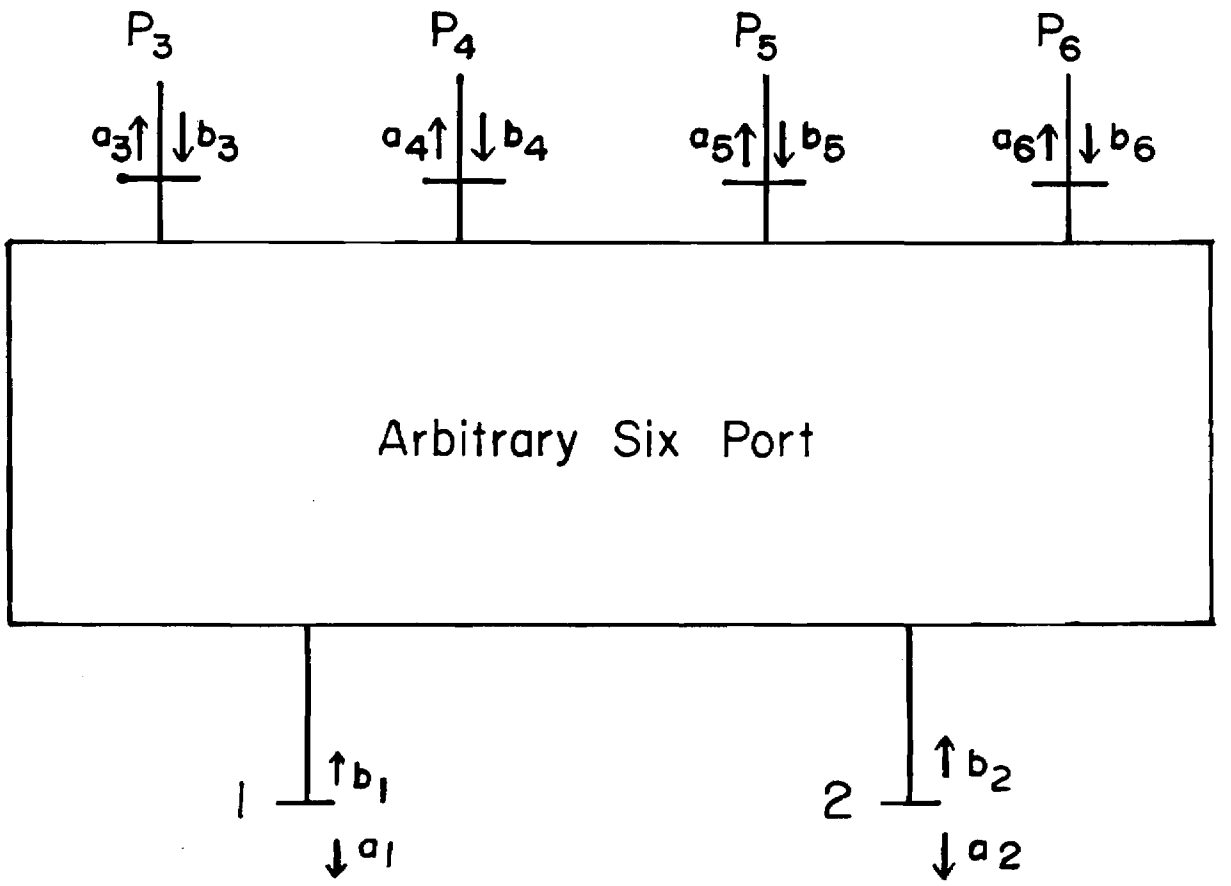

Figure 1. Arbitrary six port network.

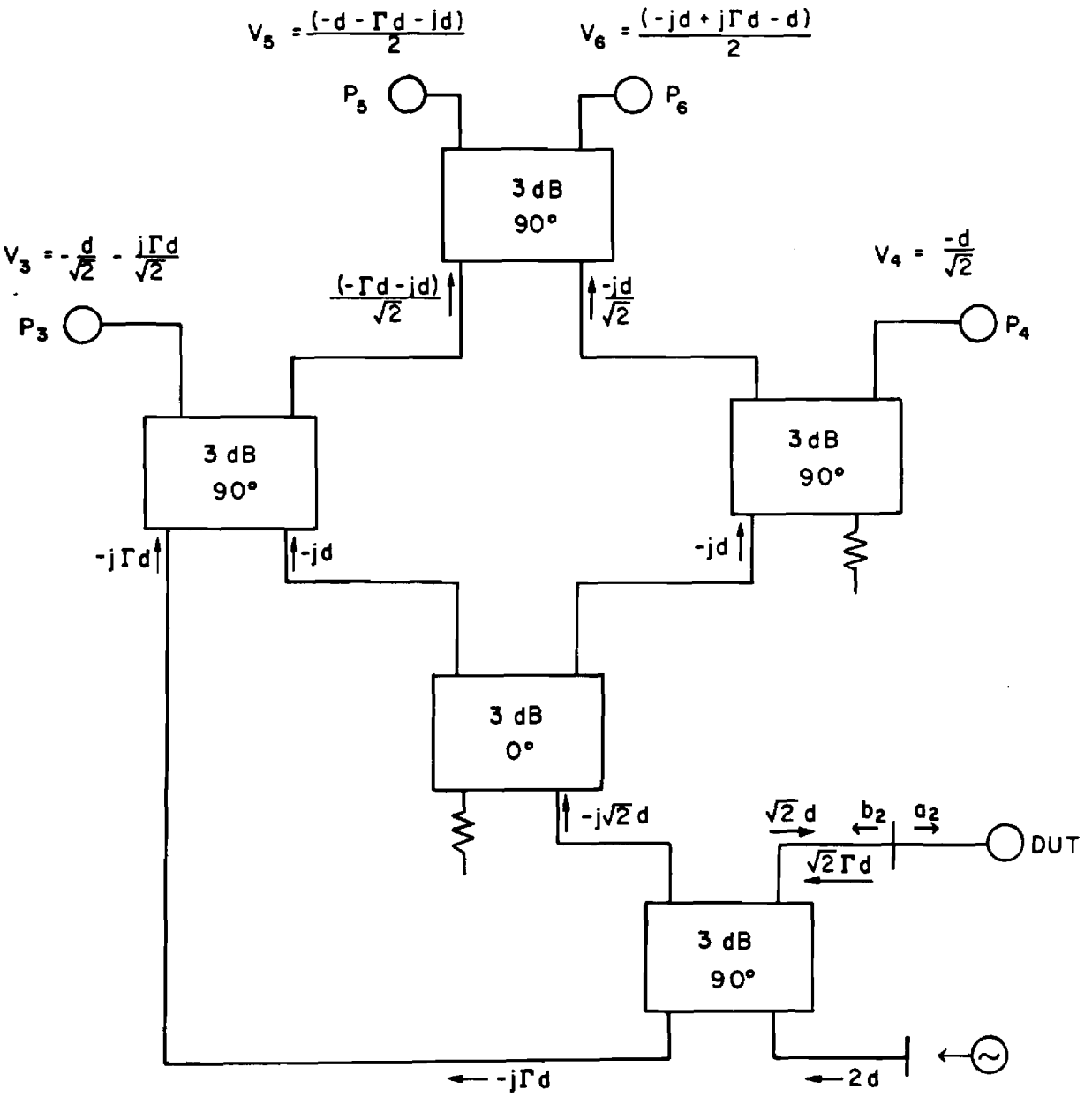

Figure 2. Six Port Network with Voltages.

APPENDIX E

IMPEDANCE DATA FOR SIMULATOR NO. 1

APPENDIX E

IMPEDANCE DATA FOR SIMULATOR NO. 1

This appendix presents the reduced data obtained from measurements on Simulator No. 1. This simulator contains five, probe-excited circular microstrip elements in the cross-section shown in Figure E-1. The subarray is etched on copper-clad, 1/16-inch Rexolite 1422, which has a dielectric constant K = 2.54. Probe feeds, formed by the extended center pin of an SMA flange-mount connector, are soldered to the top edge of each element, as indicated by the black dots.

Coupling between pairs of elements was measured from 6 to 9 GHz, in 0.1 GHz increments. Contributions to the coupling caused by reflections from the (imperfect) termination of the simulator waveguide were removed by processing measurements recorded for six positions of the sliding termination. The active element impedance of each of the allowed scan angles for this simulator was calculated from the error-corrected coupling data.

Figure E-2 shows the variation of scan angle (θ, ϕ) with frequency, for each of the eight propagating modes that can be excited and sampled with this simulator. At any one frequency, these eight modes correspond to eight scan angles for the equivalent infinite array.

Figures E-3 through E-10 present Smith Chart plots of the active impedance as a function of frequency. Each figure corresponds to one waveguide mode and, therefore, to a fixed scan plane ϕ and a small range of the angle θ from broadside. The four charts presented in each figure correspond to four thicknesses of the Rexolite 1422 cover layer, $T - t_s$ = 0, 1/16, 1/8, and 1/4 inch.

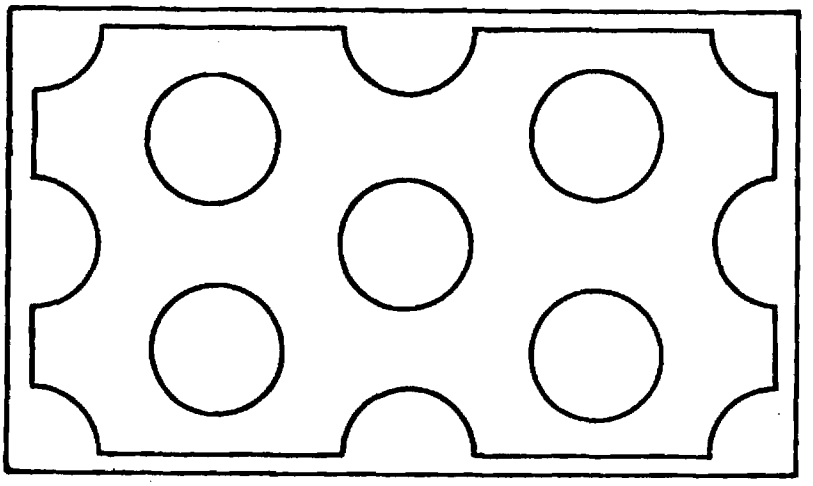

Figure E-1. Sketch of subarray for Simulator No. 1.
Nominal frequency: f_o = 6.373 GHz
Element diameter: d^o = 0.681 in.
Lattice size: ℓ = 1.136 in.
= 0.613 λ_o
Fill-factor: d/ℓ = 0.6

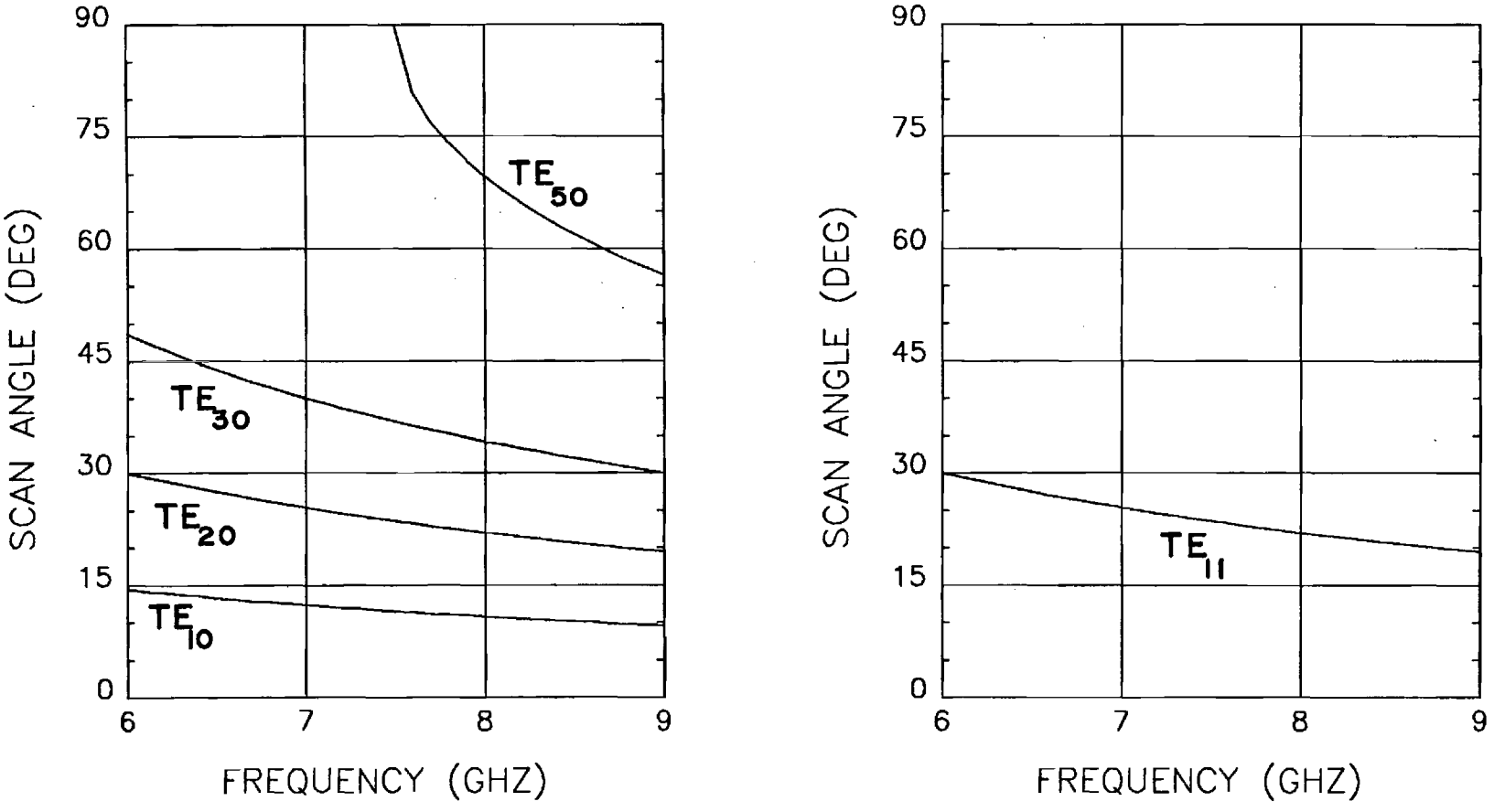

Figure E-2. Scan angles for waveguide modes excited in Simulator No. 1.

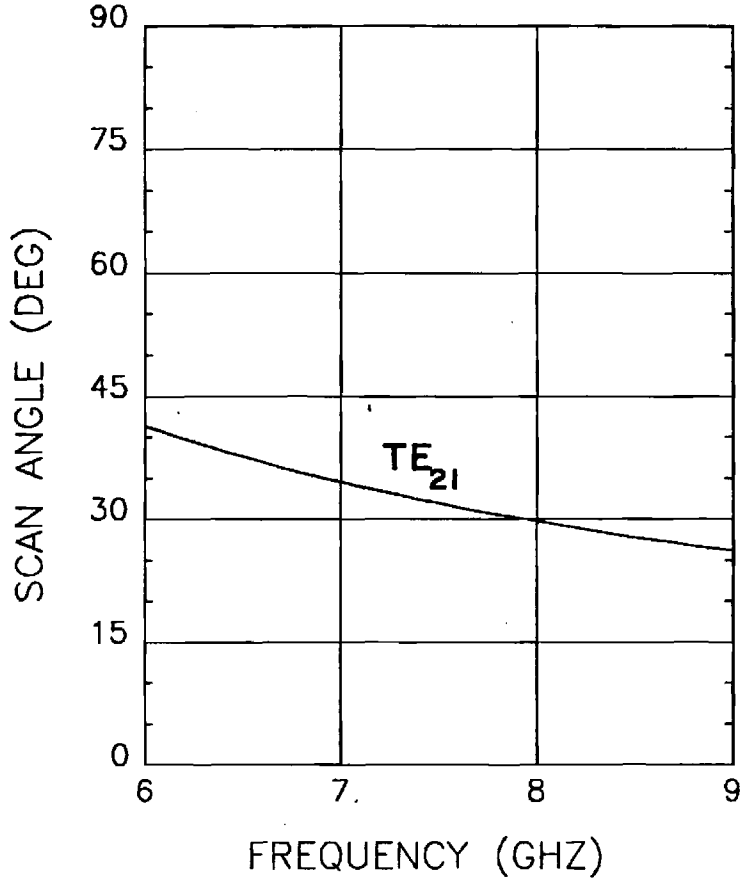

(c) ϕ = 40.9°

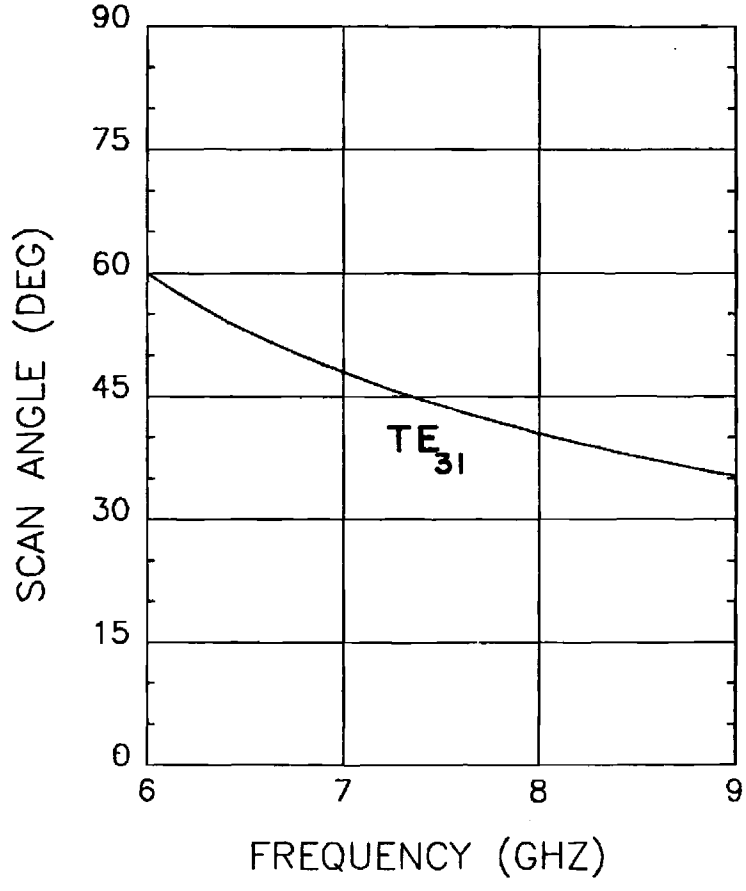

(d) ϕ = 30°

Figure E-2. Scan angles for waveguide modes excited in Simulator No. 1.

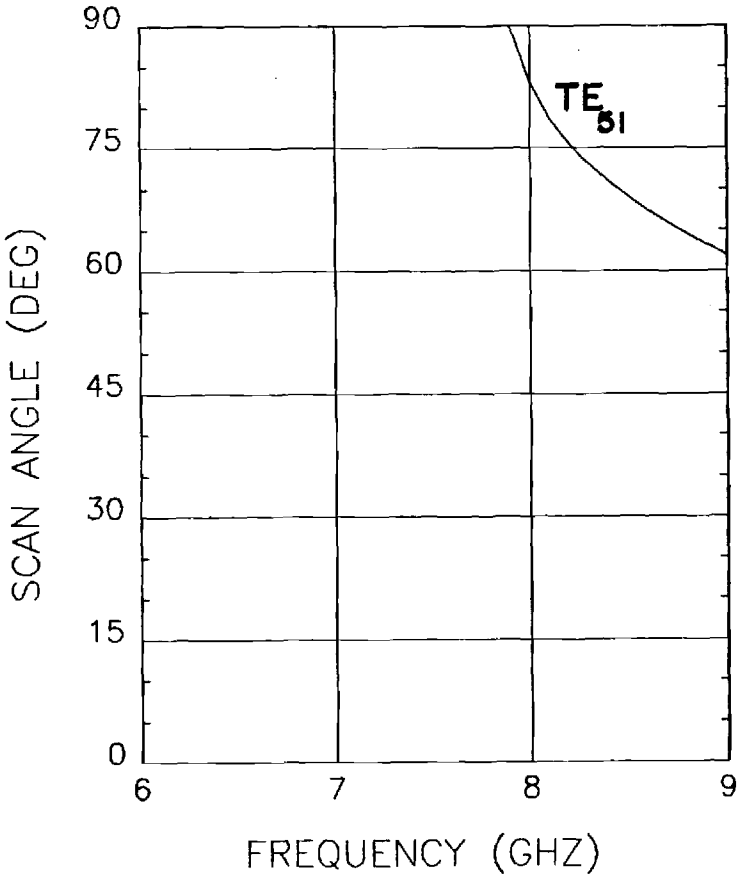

(e) 19.1°

Figure E-2. Scan angles for waveguide modes excited in Simulator No. 1.

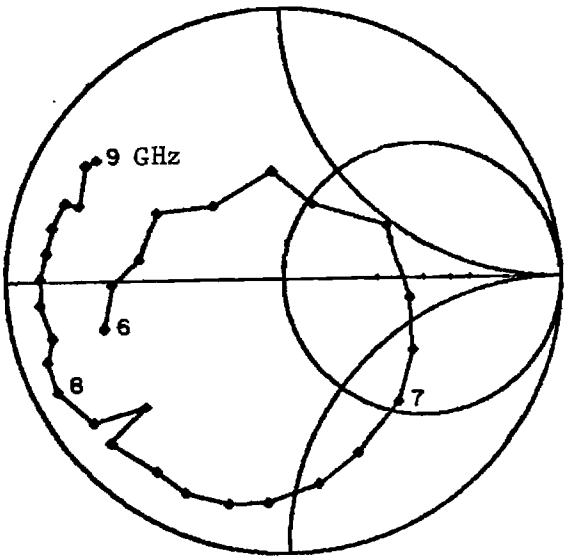

(a) No layer

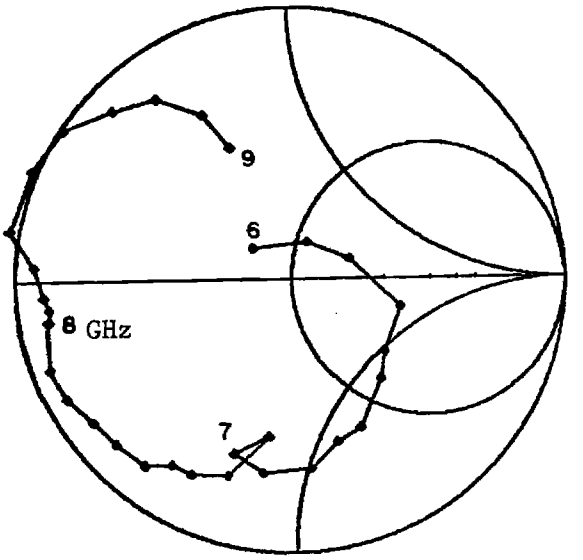

(c) 1/8" Rexolite layer

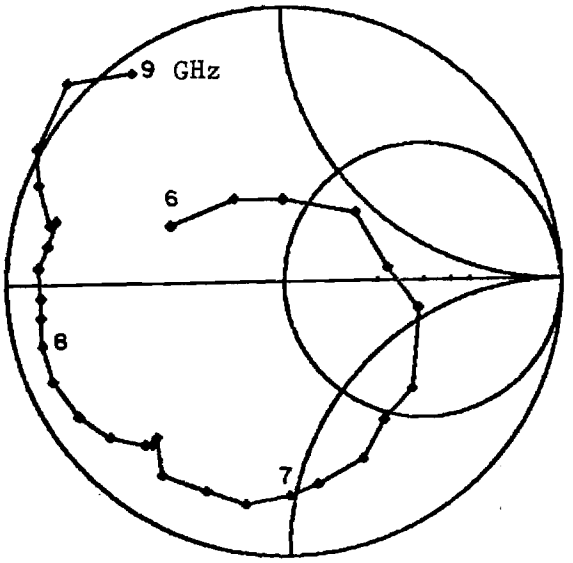

(b) 1/16" Rexolite layer

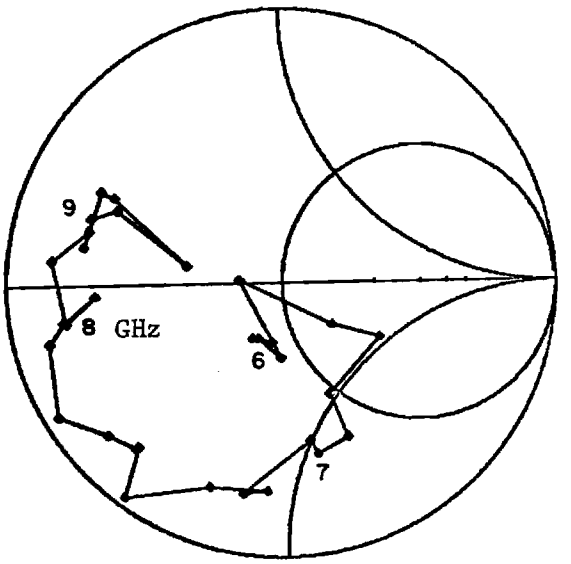

(d) 1/4" Rexolite layer

Figure E-3. Smith Chart impedance plots for the TE_{10}-mode in Simulator No. 1.

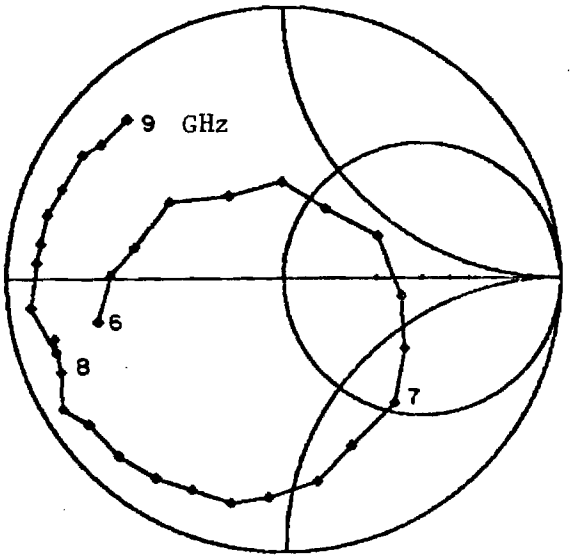

(a) No layer

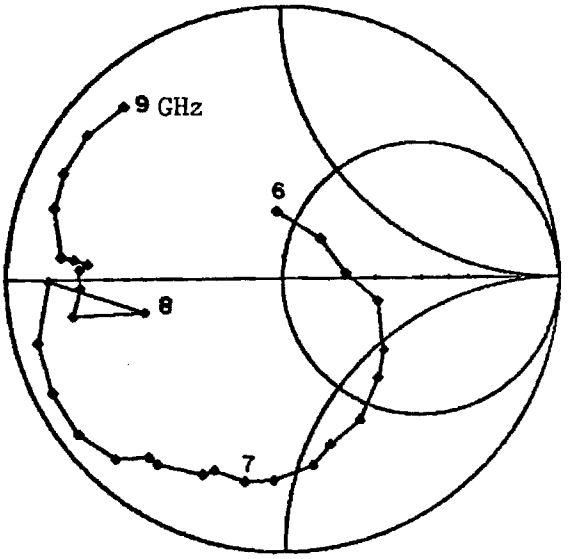

(c) 1/8" Rexolite layer

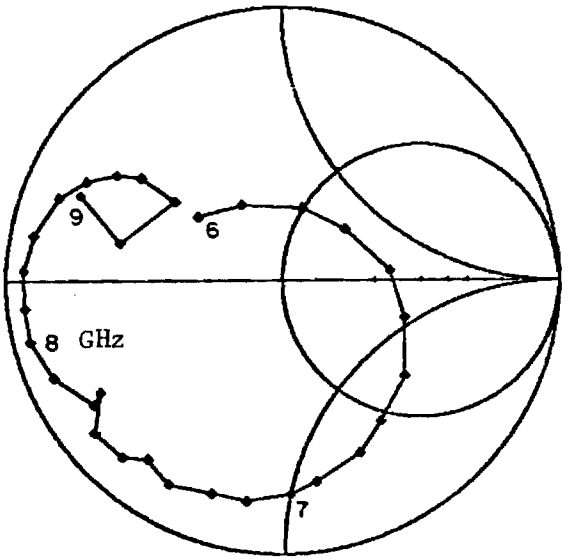

(b) 1/16" Rexolite layer

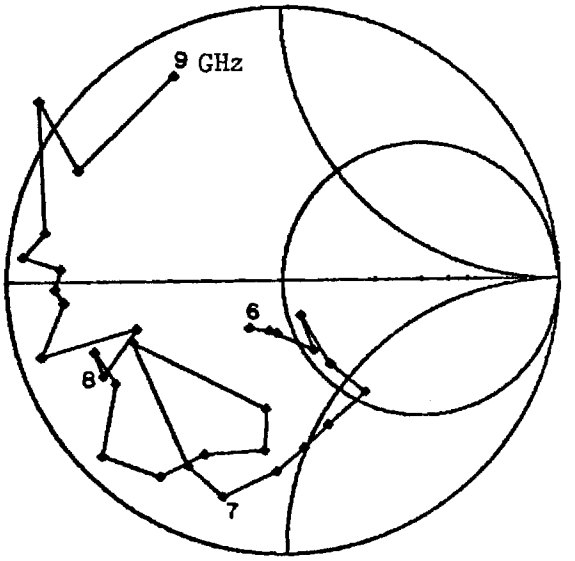

(d) 1/4" Rexolite layer

Figure E-4. Smith Chart impedance plots for the TE_{20}-mode in Simulator No. 1.

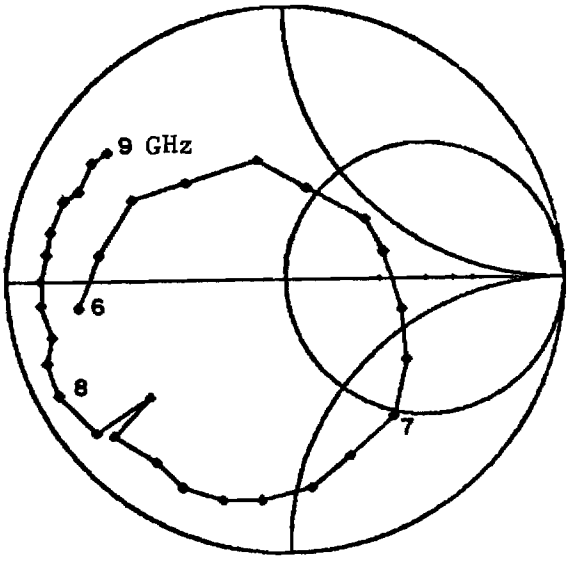

(a) No layer

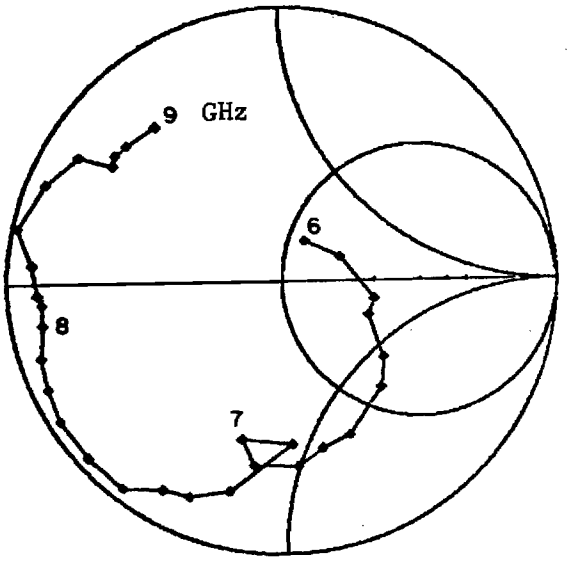

(c) 1/8" Rexolite layer

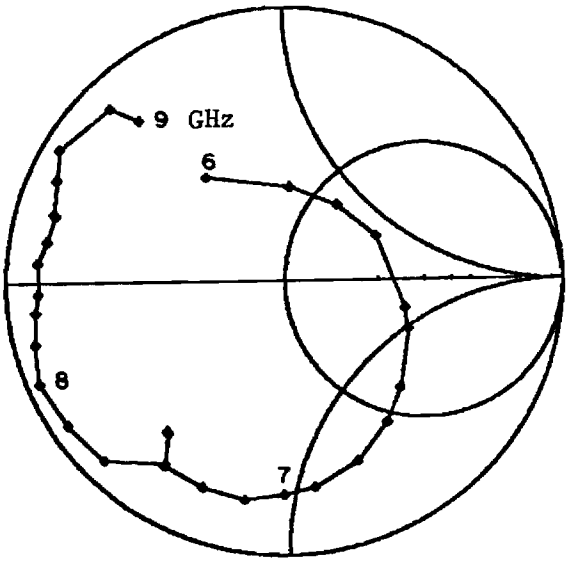

(b) 1/16" Rexolite layer

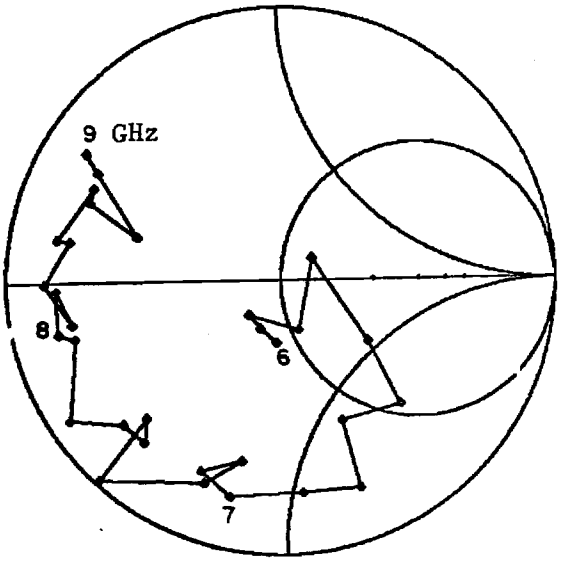

(d) 1/4" Rexolite layer

Figure E-5. Smith Chart impedance plots for the TE_{30}-mode in Simulator No. 1.

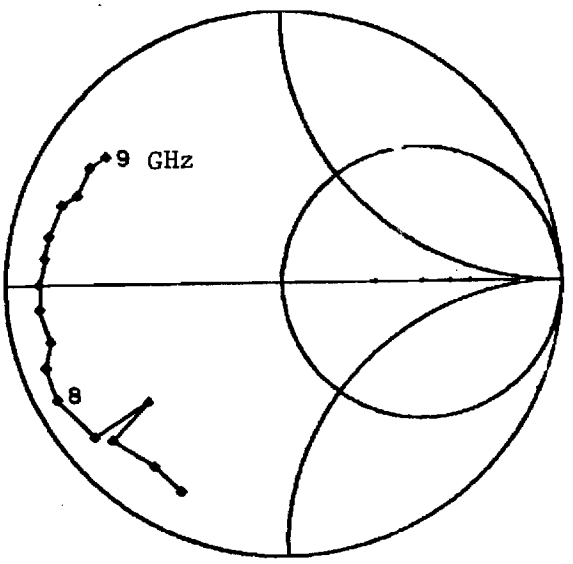

(a) No layer

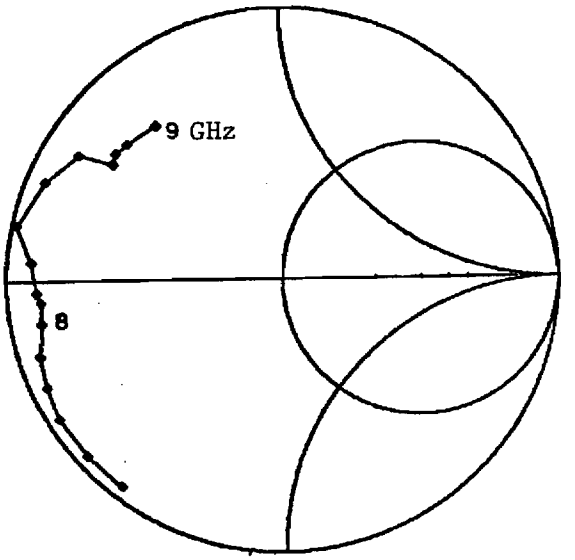

(c) 1/8" Rexolite layer

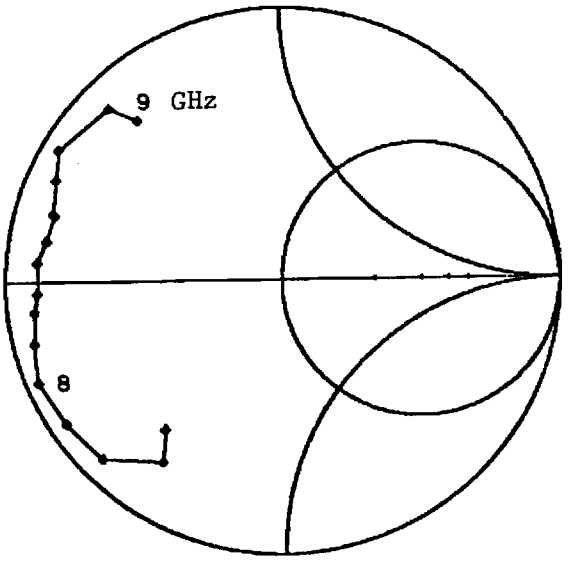

(b) 1/16" Rexolite layer

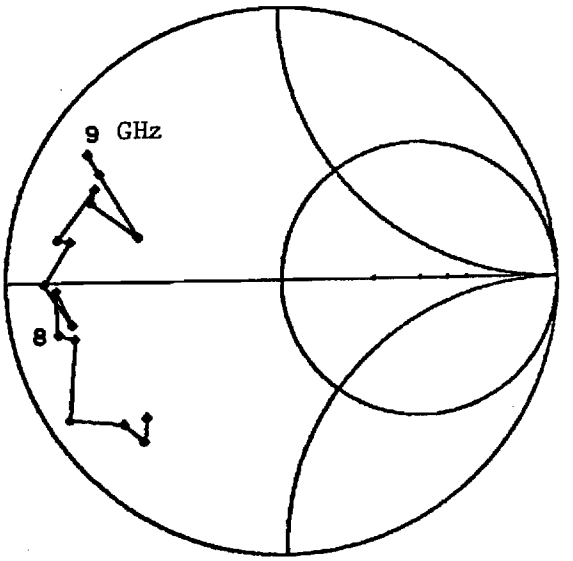

(d) 1/4" Rexolite layer

Figure E-6. Smith Chart impedance plots for the TE_{50}-mode in Simulator No. 1.

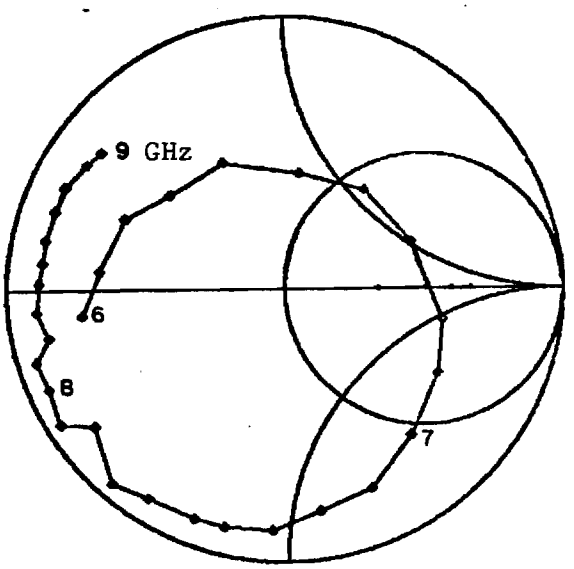

(a) No layer

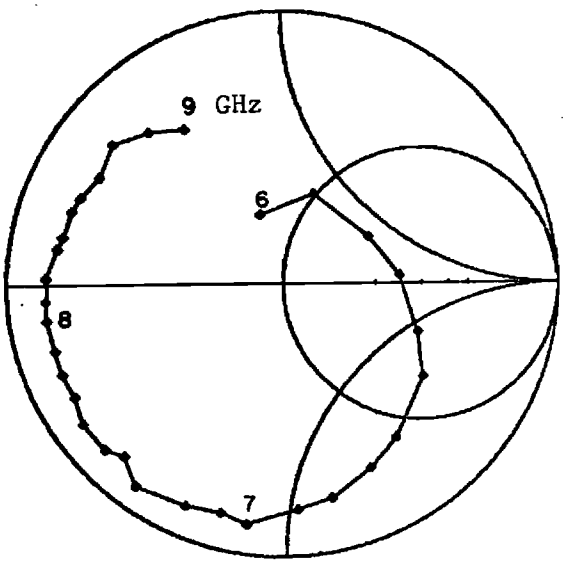

(c) 1/8" Rexolite layer

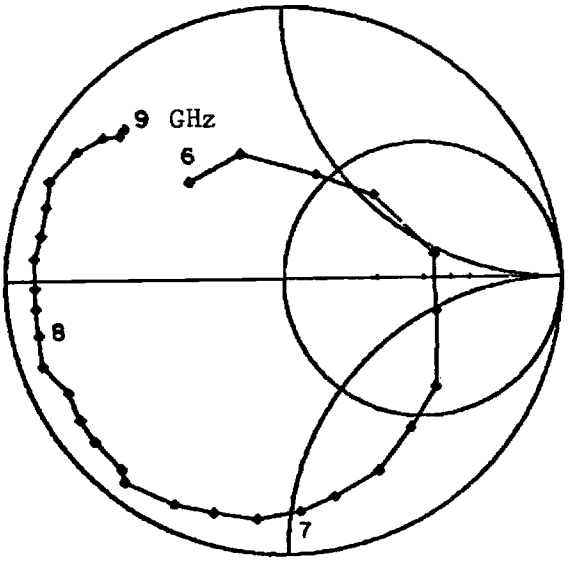

(b) 1/16" Rexolite layer

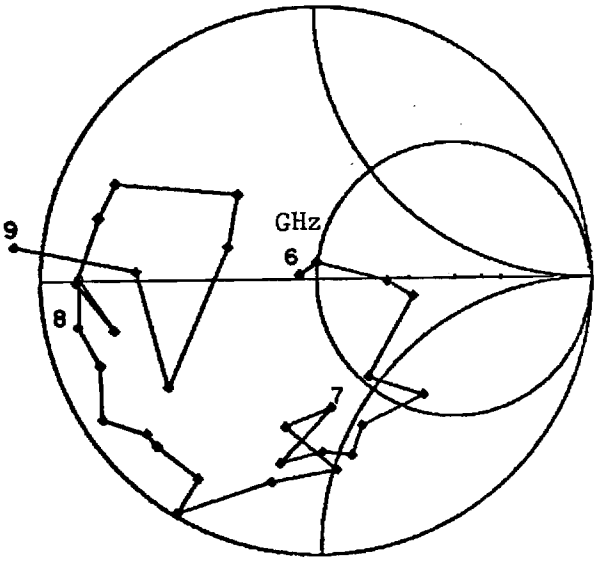

(d) 1/4" Rexolite layer

Figure E-7. Smith Chart impedance plots for the TE_{11}/TM_{11}-modes in Simulator No. 1.

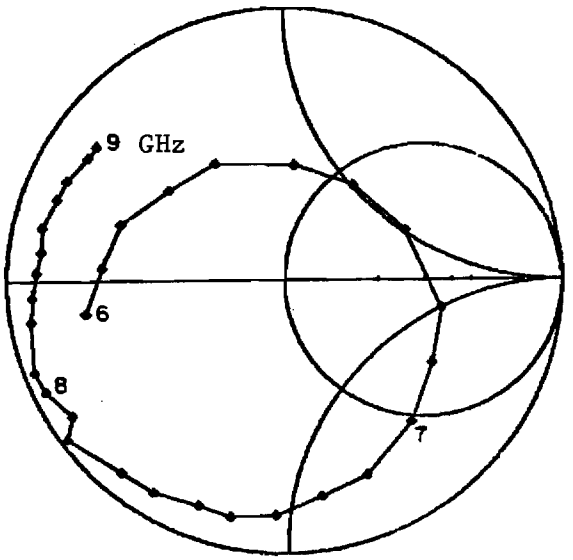

(a) No layer

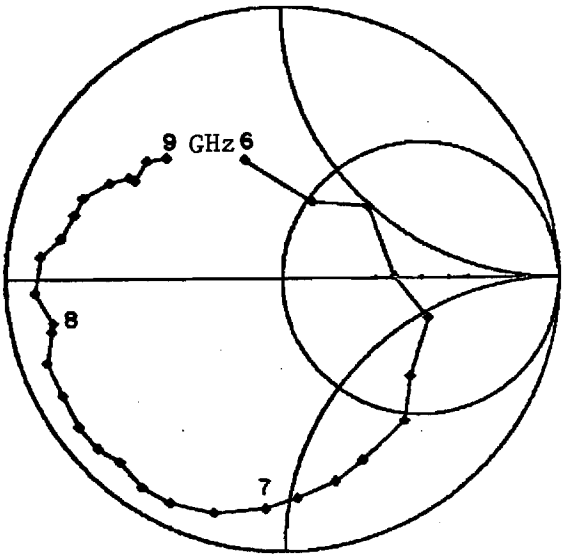

(c) 1/8" Rexolite layer

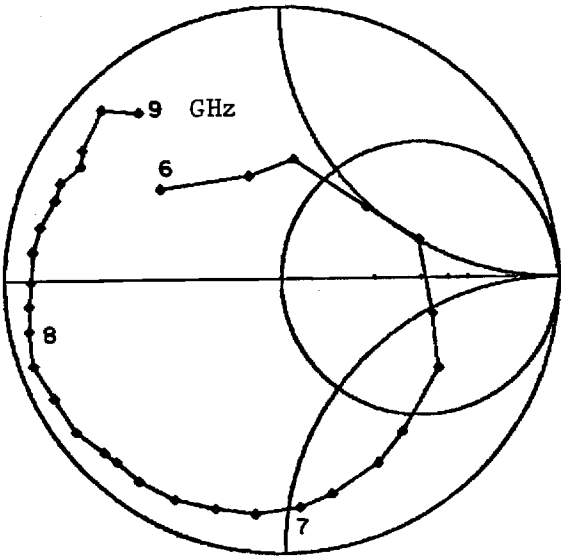

(b) 1/16" Rexolite layer

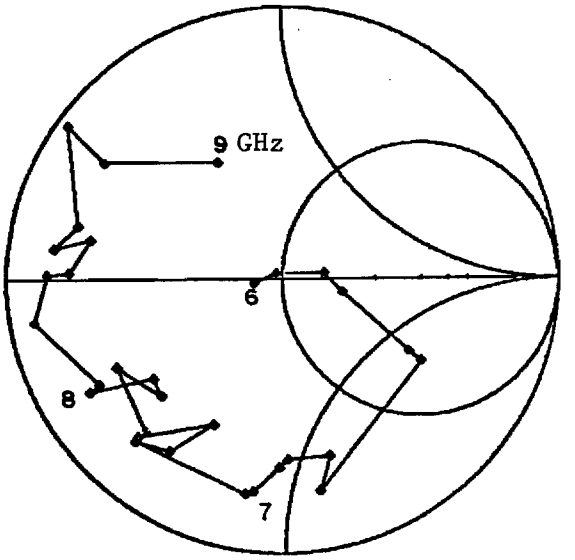

(d) 1/4" Rexolite layer

Figure E-8. Smith Chart impedance plots for the TE_{21}/TM_{21}-modes in Simulator No. 1.

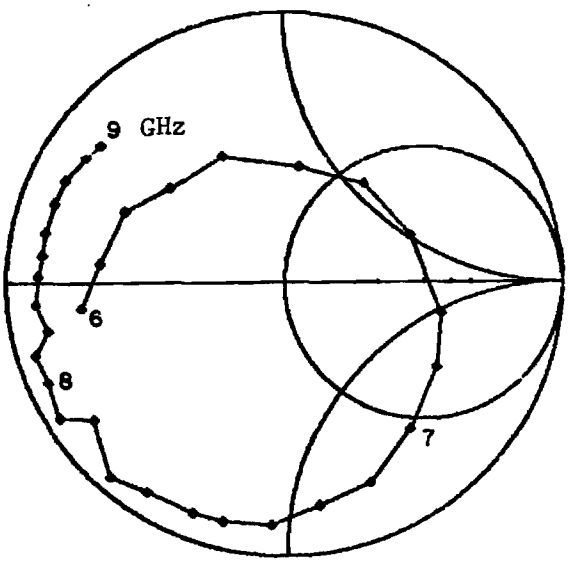

(a) No layer

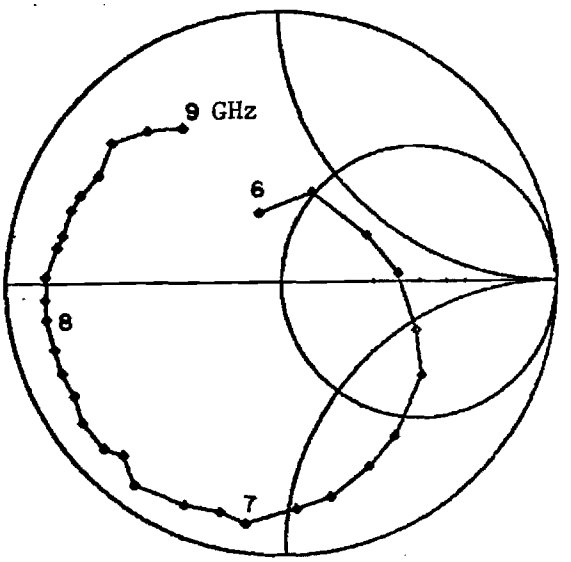

(c) 1/8" Rexolite layer

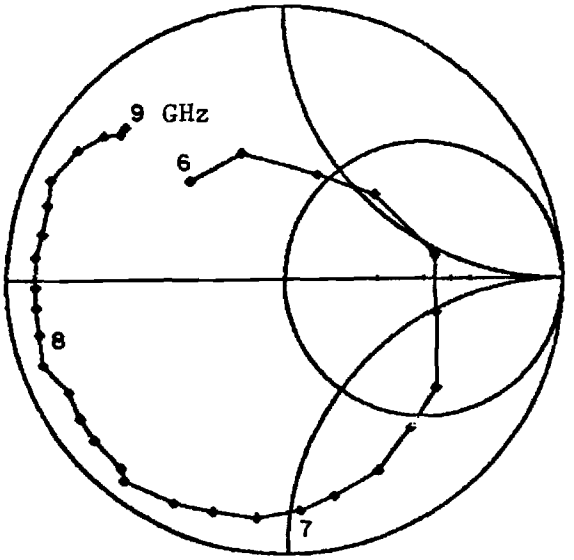

(b) 1/16" Rexolite layer

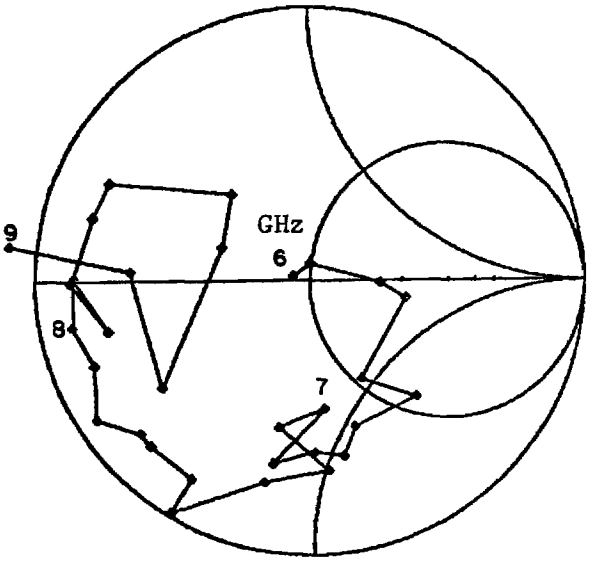

(d) 1/4" Rexolite layer

Figure E-9. Smith Chart impedance plots for the TE_{31}/TM_{31}-modes in Simulator No. 1.

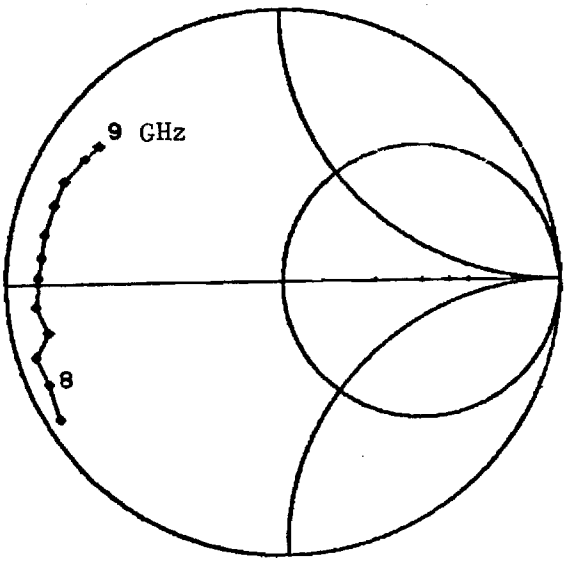

(a) No layer

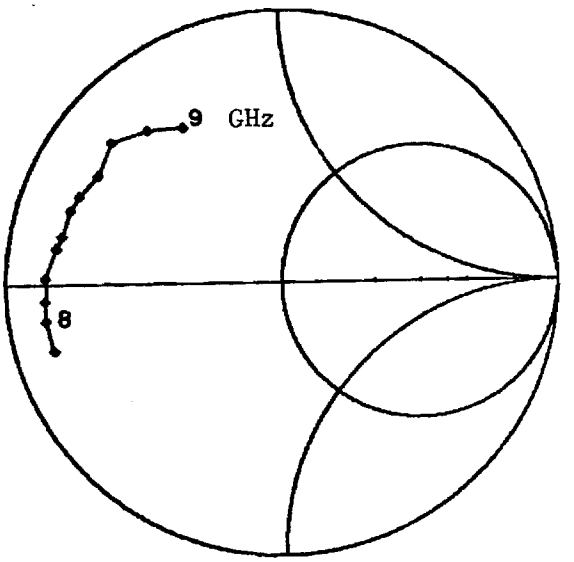

(c) 1/8" Rexolite layer

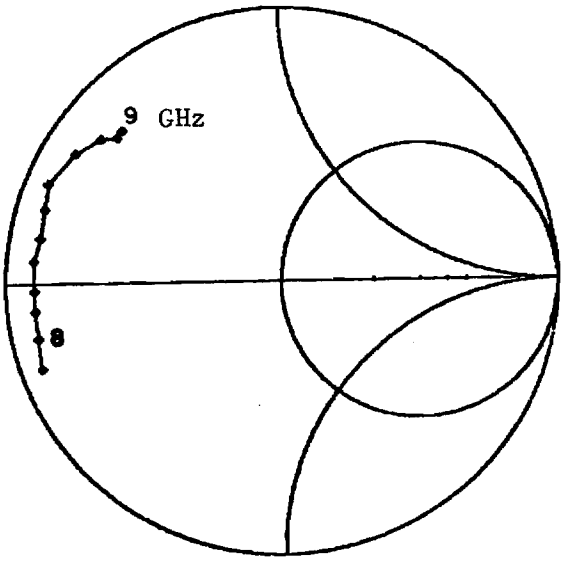

(b) 1/16" Rexolite layer

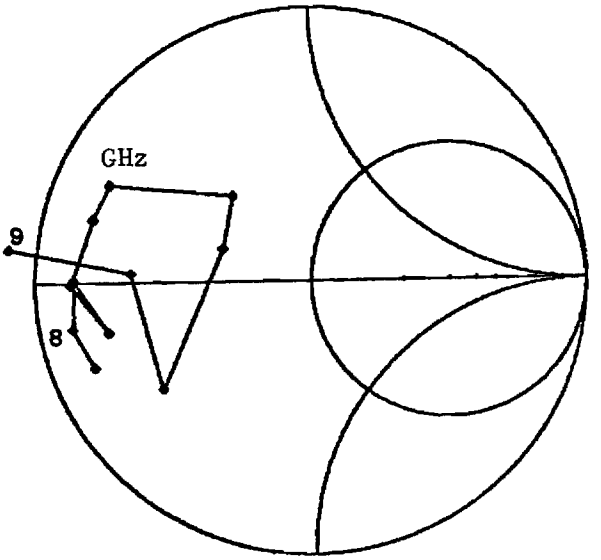

(d) 1/4" Rexolite layer

Figure E-10. Smith Chart impedance plots for the TE_{51}/TM_{51}-modes in Simulator No. 1.

APPENDIX F

IMPEDANCE DATA FOR SIMULATOR NO. 2

APPENDIX F

IMPEDANCE DATA FOR SIMULATOR NO. 2

This appendix presents the reduced data obtained from measurements on Simulator No. 2. This simulator contains thirteen, probe-excited circular microstrip elements in the cross-section shown in Figure F-1. The subarray is etched on copper-clad, 1/16-inch Rexolite 1422, which has a dielectric constant K = 2.54. Probe feeds, formed by the extended center pin of an SMA flange-mount connector, are soldered to the top edge of each element, as indicated by the black dots.

Coupling between pairs of elements was measured from 6 to 9 GHz, in 0.1 GHz increments. Contributions to the coupling caused by reflections from the (imperfect) termination of the simulator waveguide were removed by processing measurements recorded for six positions of the sliding termination. The active element impedance of each of the allowed scan angles for this simulator was calculated from the error-corrected coupling data.

Figure F-2 shows the variation of scan angle (θ ,ϕ) with frequency, for each of the fourteen propagating modes that can be excited and sampled with this simulator. At any one frequency, these fourteen modes correspond to fourteen scan angles for the equivalent infinite array.

Figures F-3 through F-16 present Smith Chart plots of the active impedance as a function of frequency. Each figure corresponds to one waveguide mode and, therefore, to a fixed scan plane ϕ and a small range of the angle θ from broadside. The two charts presented in each figure correspond to two thicknesses of the Rexolite 1422 cover layer, $T - t_s = 0$, and 1/16 inch.

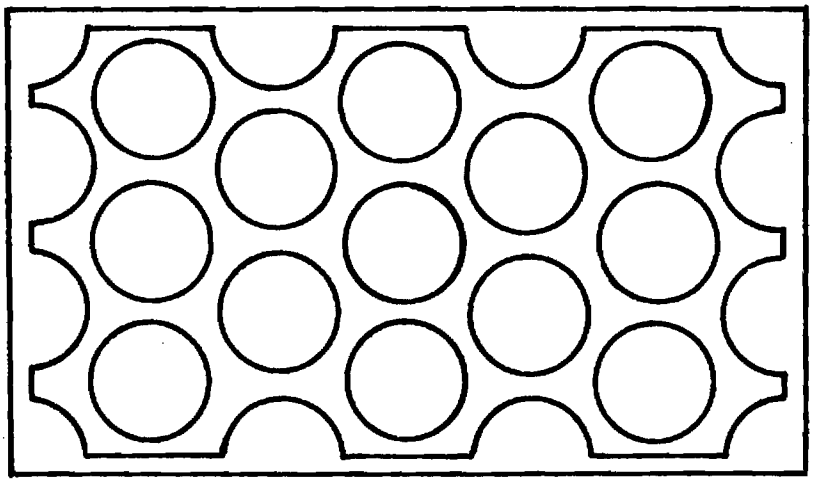

Figure F-1. Sketch of subarray for Simulator No. 2.
Nominal frequency f_o = 7.162 GHz
Element diameter: d^o = 0.606 in.
Lattice size: ℓ = 0.757 in.
= 0.459 λ_o
Fill-factor: d/ℓ = 0.8

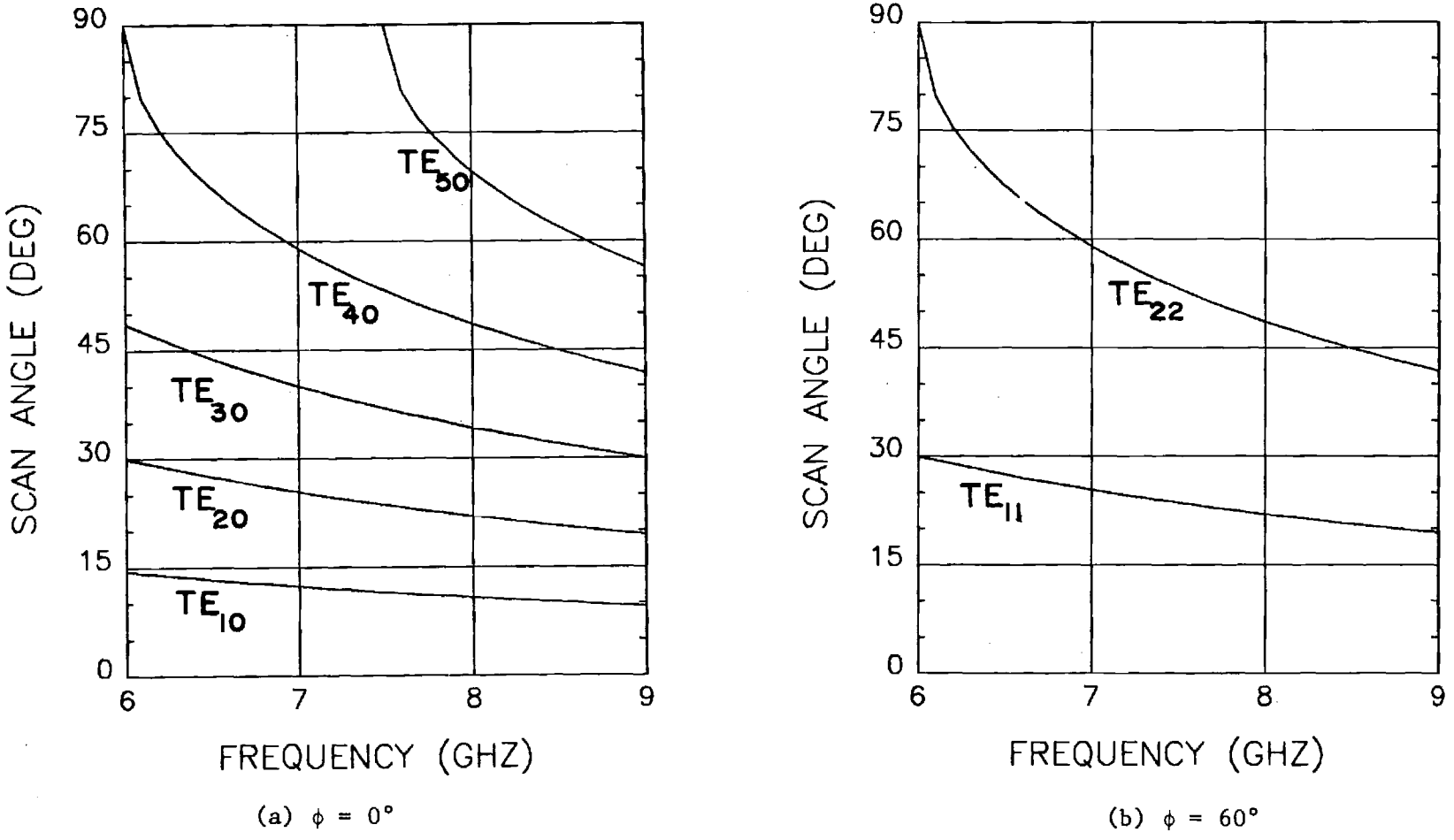

Figure F-2. Scan angles for waveguide modes excited in Simulator No. 2.

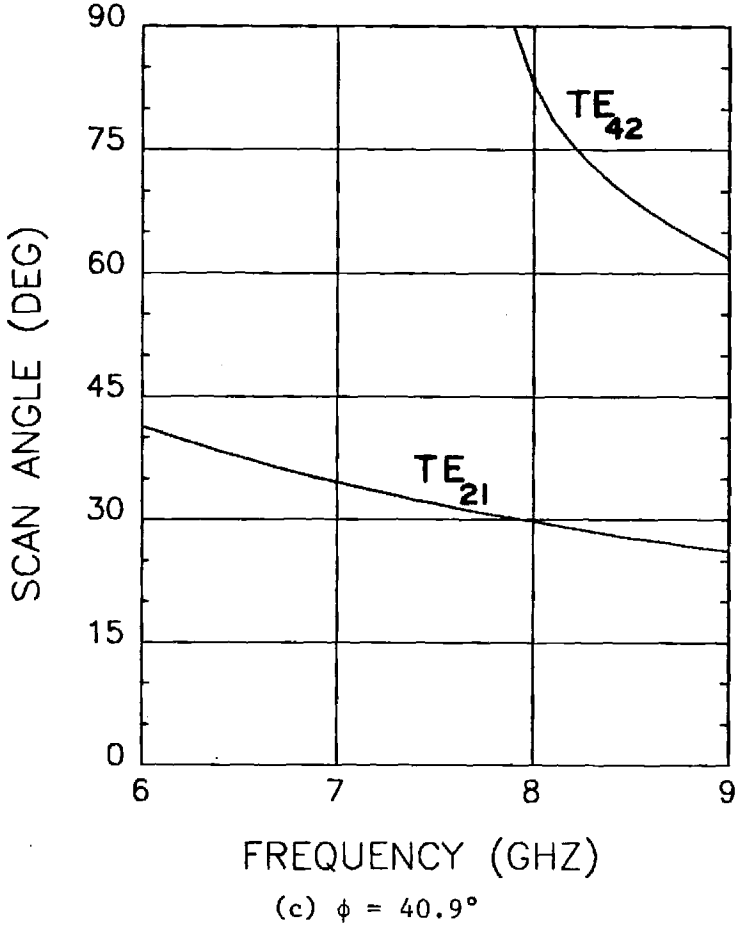

(c) ϕ = 40.9°

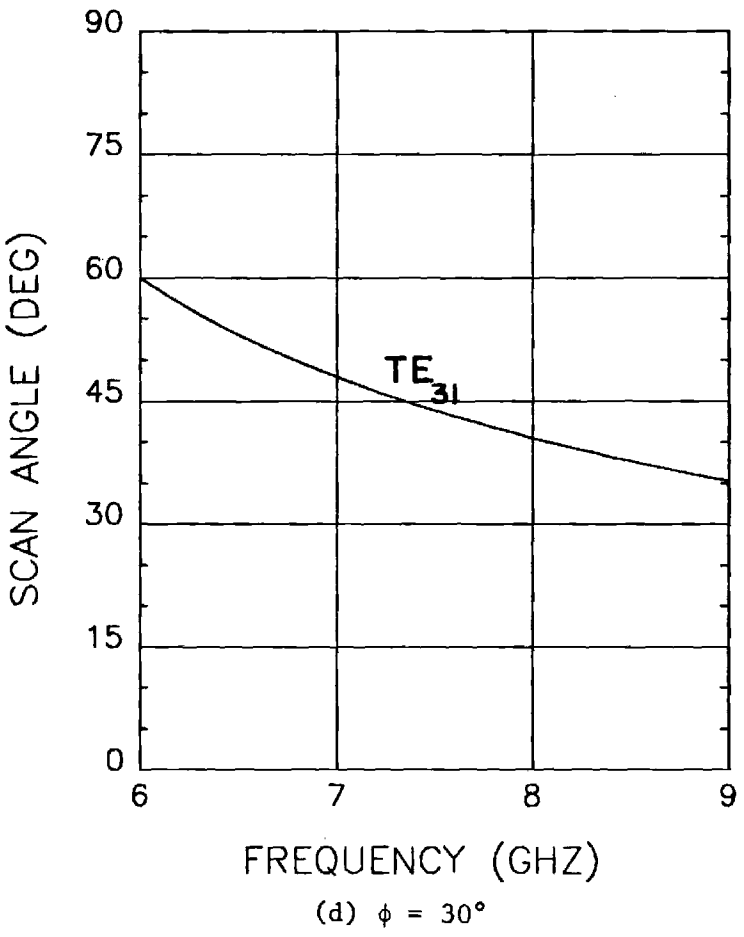

(d) ϕ = 30°

Figure F-2. Scan angles for waveguide modes excited in Simulator No. 2.

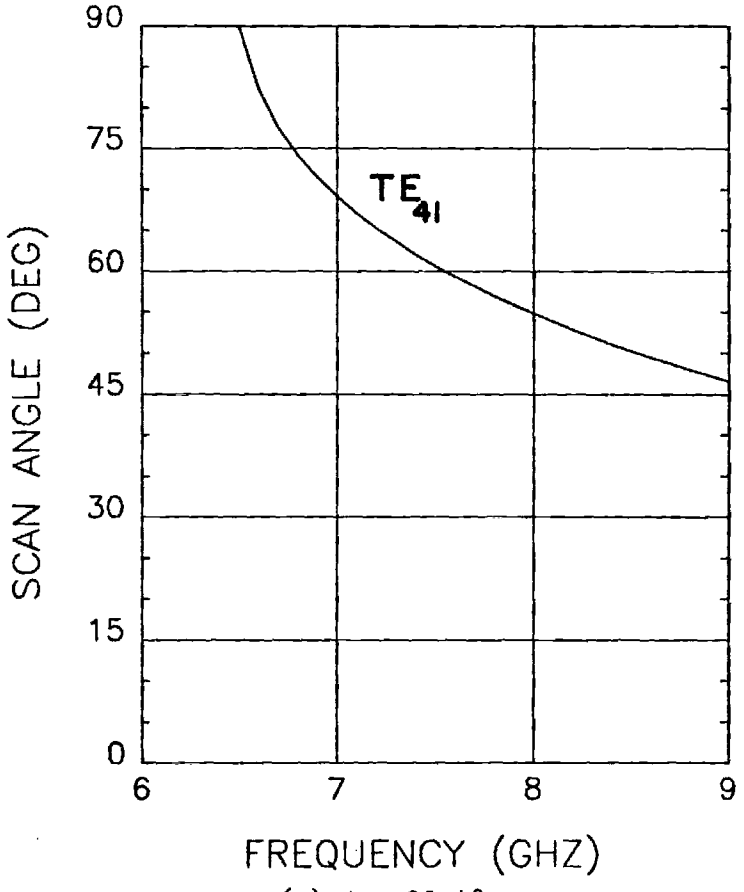

(e) ϕ = 23.4°

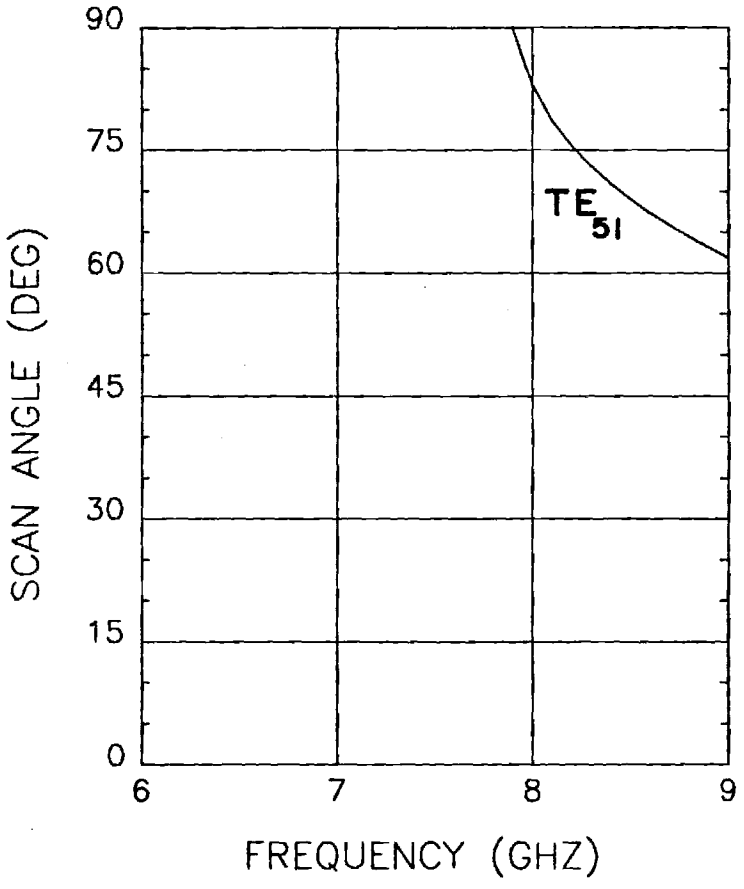

(f) ϕ = 19.1°

Figure F-2. Scan angles for waveguide modes excited in Simulator No. 2.

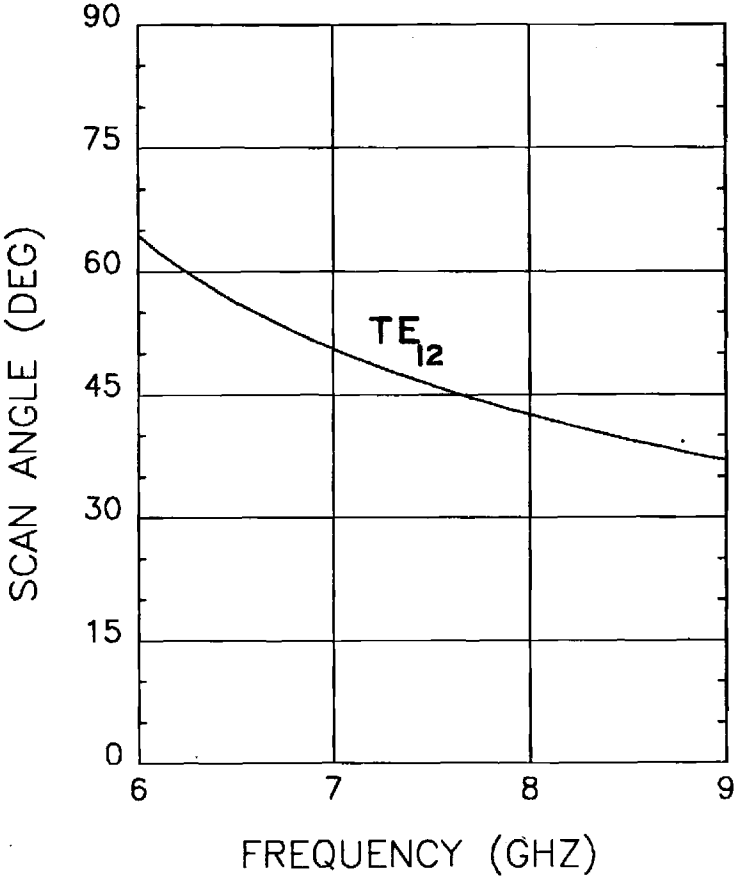

(g) ϕ = 73.9°

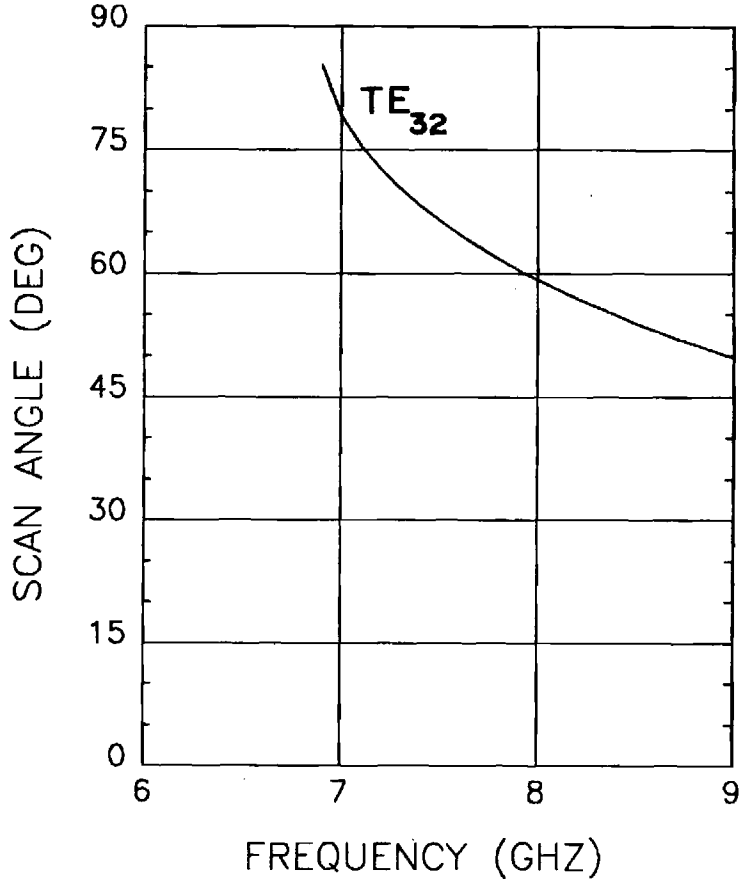

(h) ϕ = 49.1°

Figure F-2. Scan angles for waveguide modes excited in Simulator No. 2.

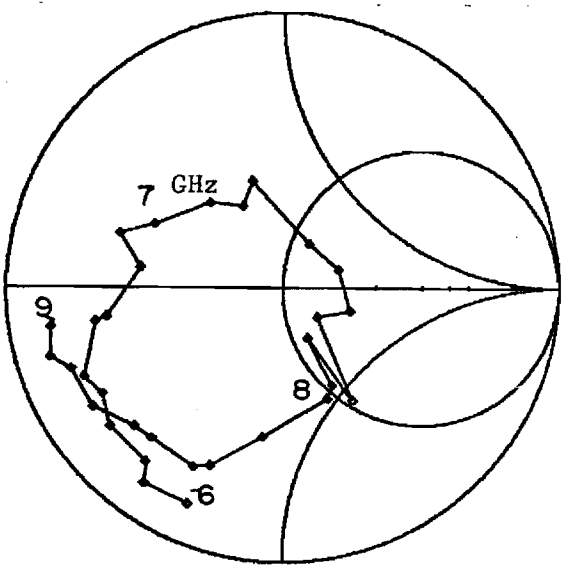

(a) No layer

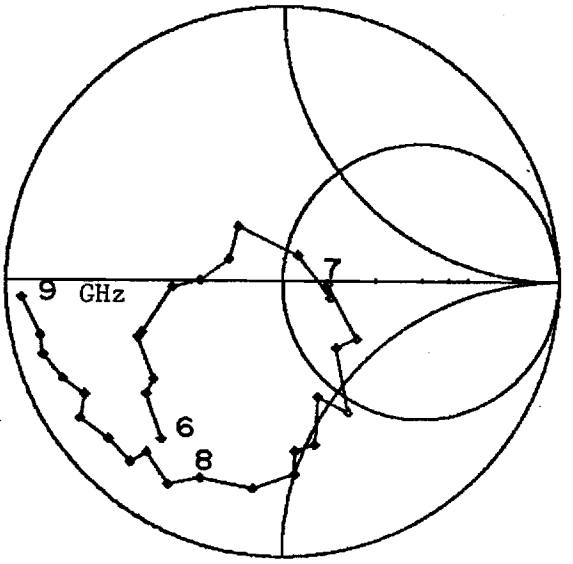

(b) 1/16" Rexolite layer

Figure F-3. Smith Chart impedance plots for the TE_{10}-mode in Simulator No. 2.

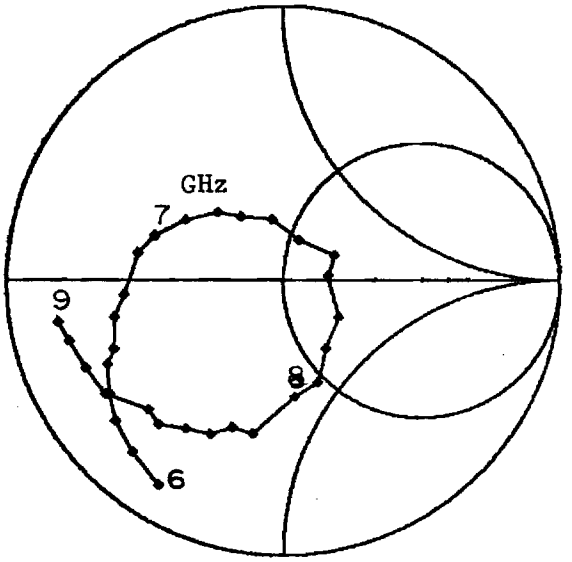

(a) No layer

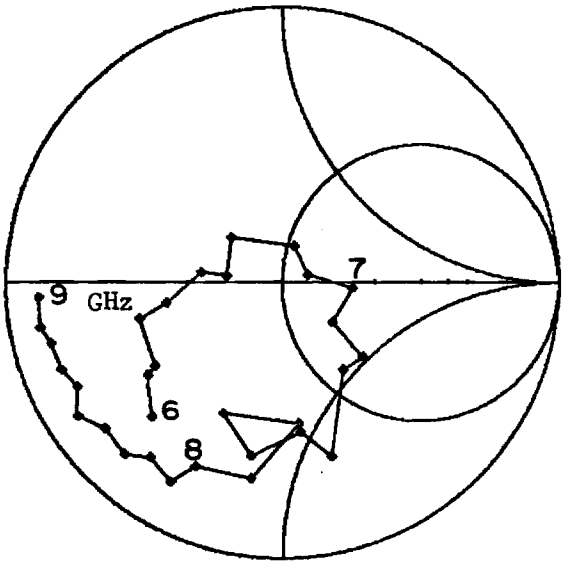

(b) 1/16" Rexolite layer

Figure F-4. Smith Chart impedance plots for the TE_{20}-mode in Simulator No. 2.

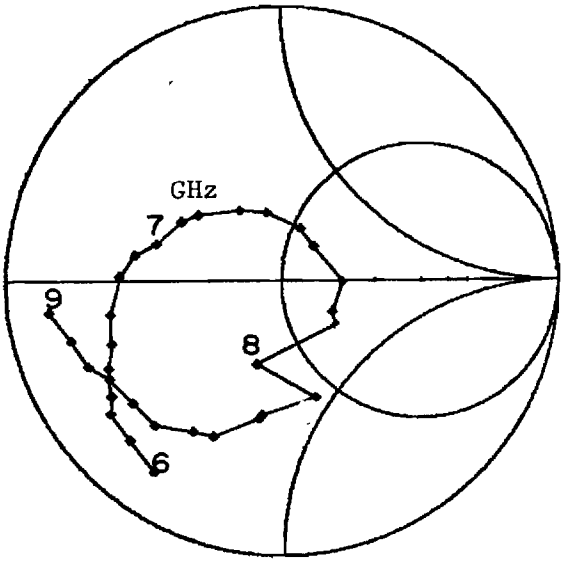

(a) No layer

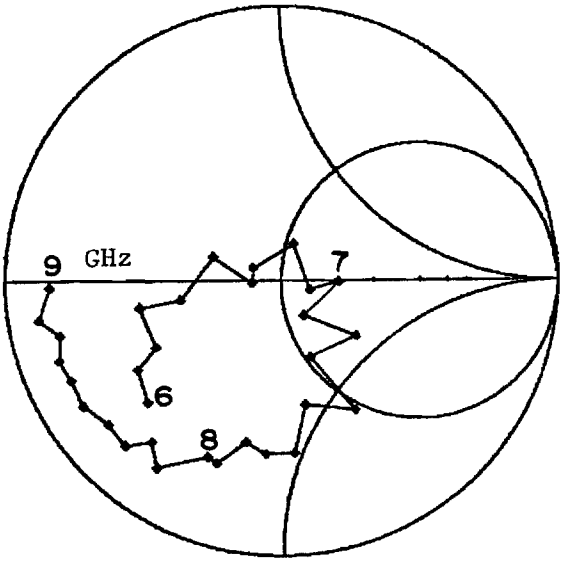

(b) 1/16" Rexolite layer

Figure F-5. Smith Chart impedance plots for the TE_{30}-mode in Simulator No. 2.

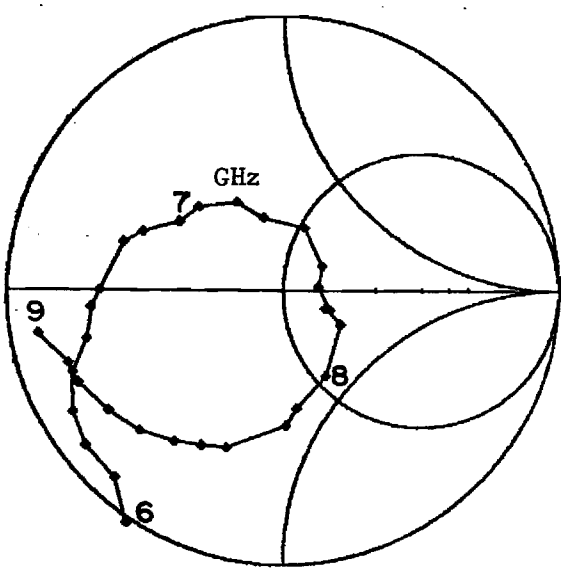

(a) No layer

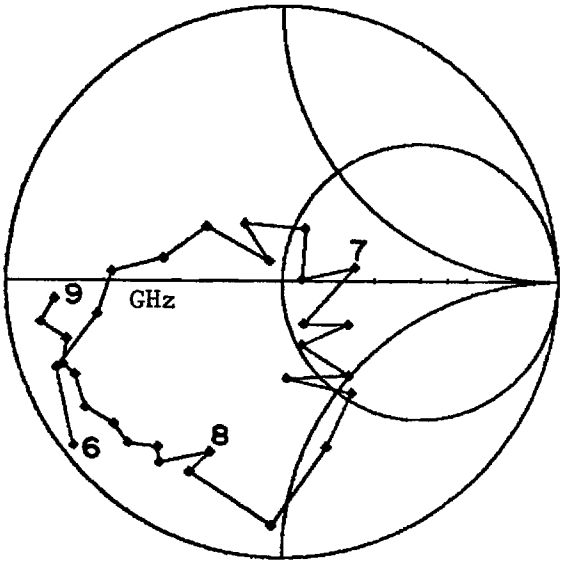

(b) 1/16" Rexolite layer

Figure F-6. Smith Chart impedance plots for the TE_{40}-mode in Simulator No. 2.

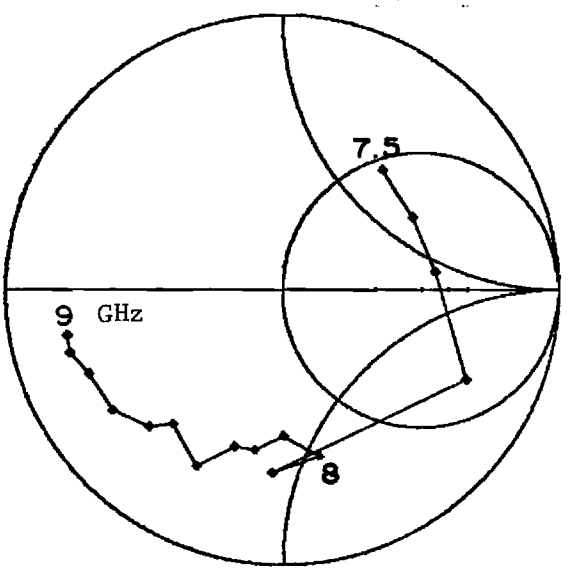

(a) No layer

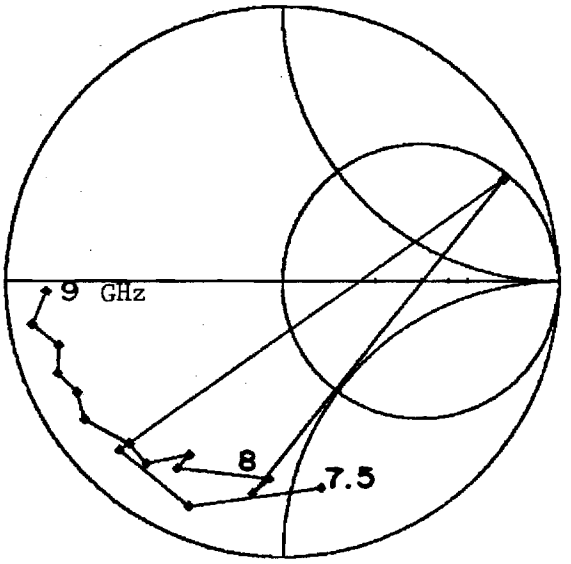

(b) 1/16" Rexolite layer

Figure F-7. Smith Chart impedance plots for the TE_{50}-mode in Simulator No. 2.

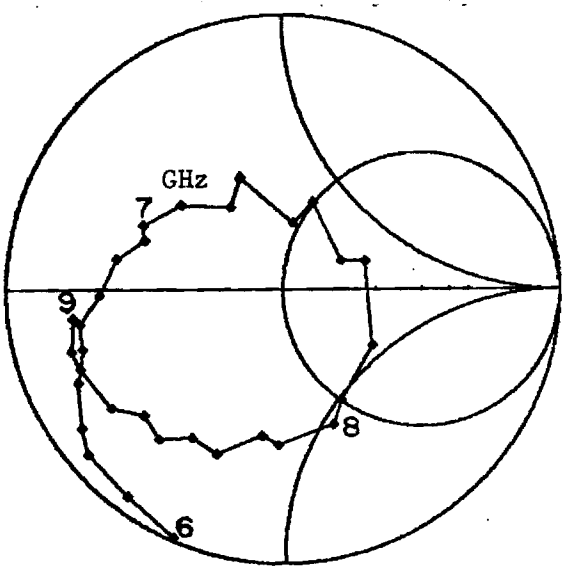

(a) No layer

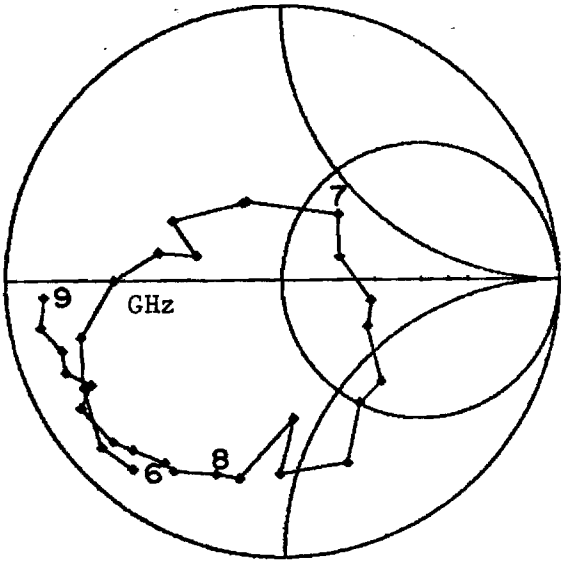

(b) 1/16" Rexolite layer

Figure F-8. Smith Chart impedance plots for the TE_{11}/TM_{11}-modes in Simulator No. 2.

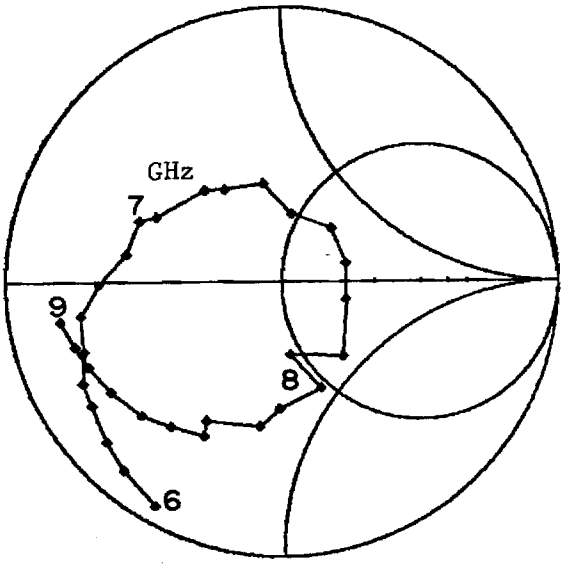

(a) No layer

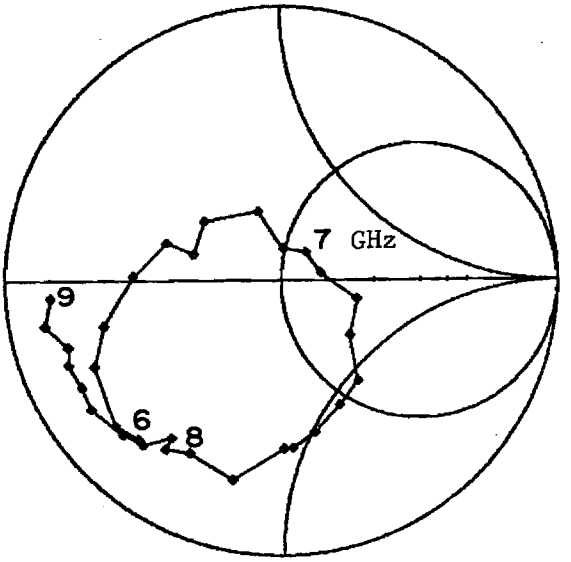

(b) 1/16" Rexolite layer

Figure F-9. Smith Chart impedance plots for the TE_{21}/TM_{21}-modes in Simulator No. 2.

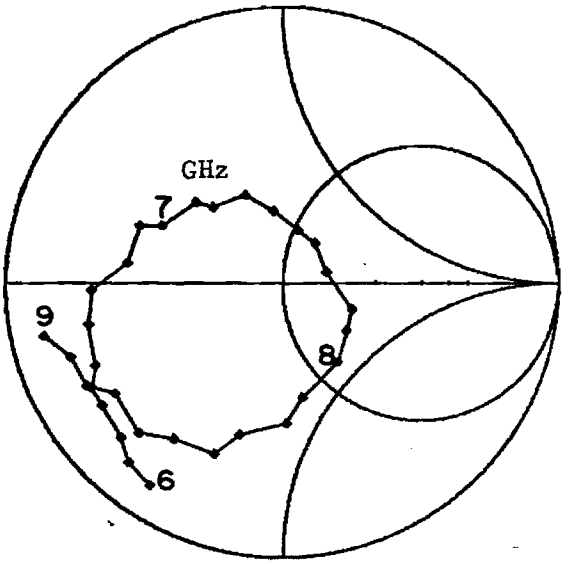

(a) No layer

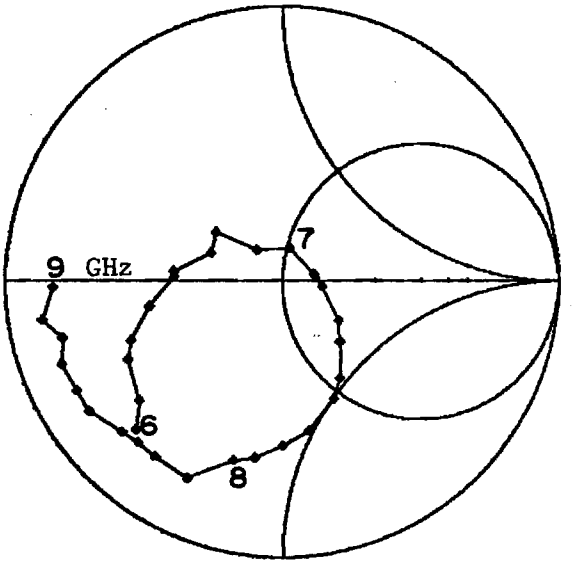

(b) 1/16" Rexolite layer

Figure F-10. Smith Chart impedance plots for the TE_{31}/TM_{31}-modes in Simulator No. 2.

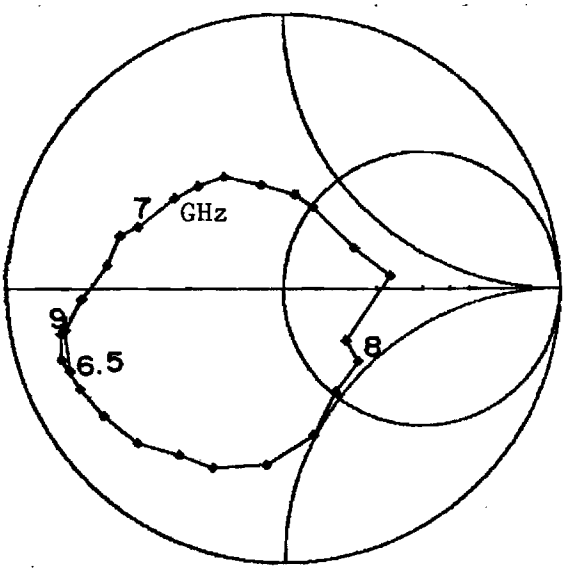

(a) No layer

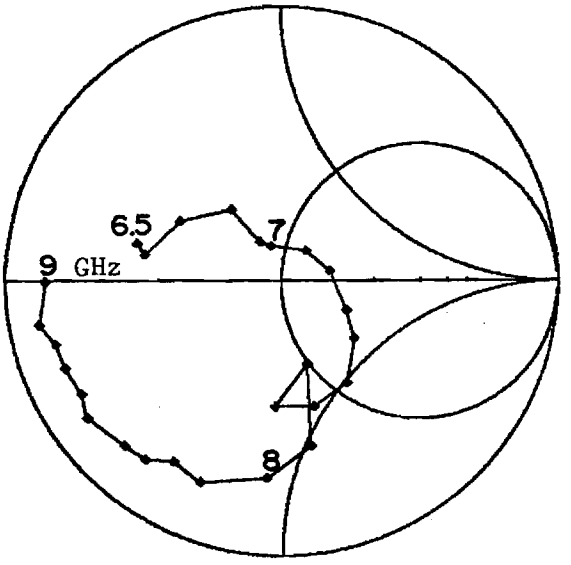

(b) 1/16" Rexolite layer

Figure F-11. Smith Chart impedance plots for the TE_{41}/TM_{41}-modes in Simulator No. 2.

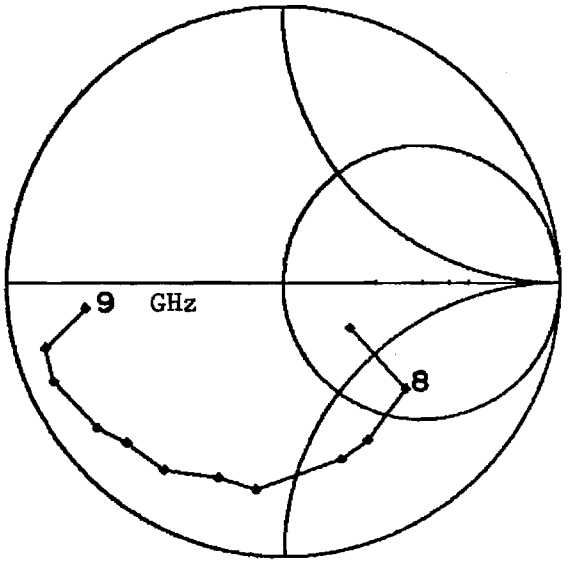

(a) No layer

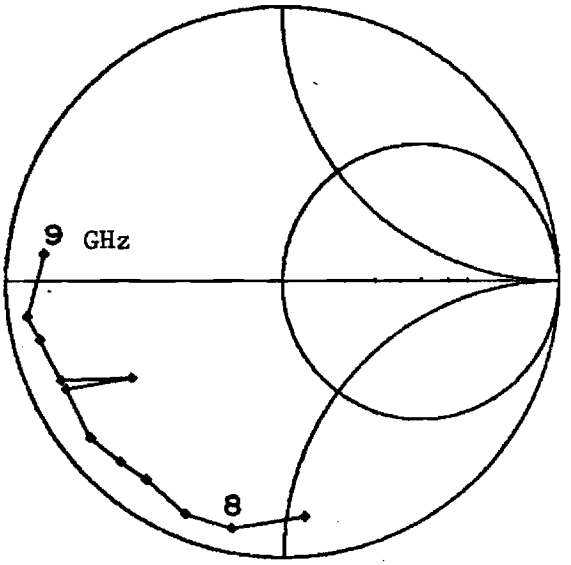

(b) 1/16" Rexolite layer

Figure F-12. Smith Chart impedance plots for the TE_{51}/TM_{51}-modes in Simulator No. 2.

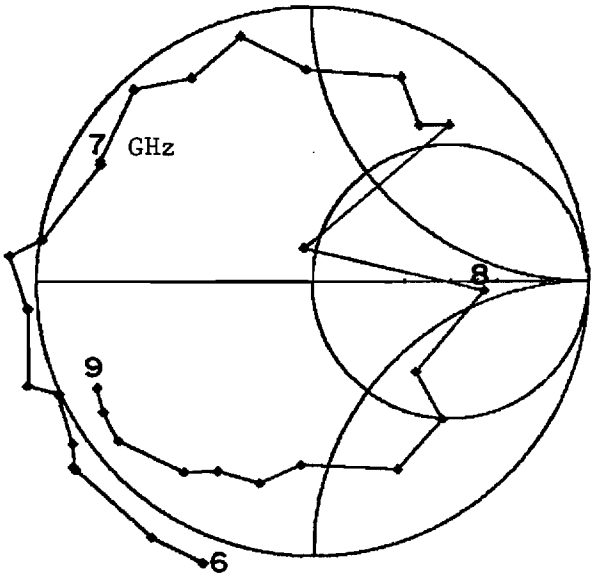

(a) No layer

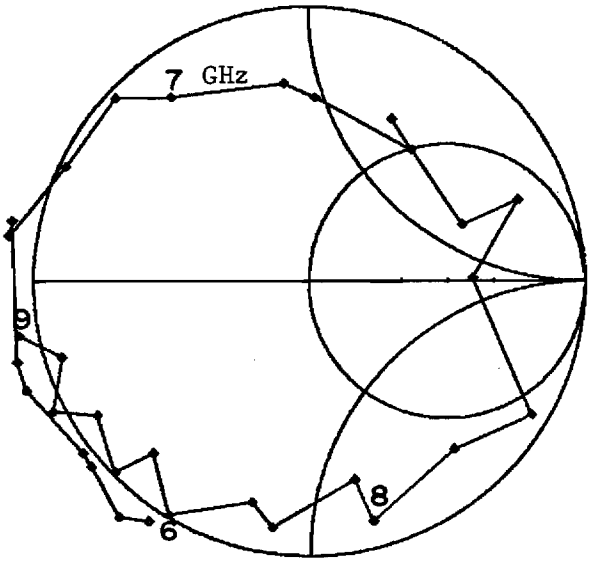

(b) 1/16" Rexolite layer

Figure F-13. Smith Chart impedance plots for the TE_{12}/TM_{12}-modes in Simulator No. 2.

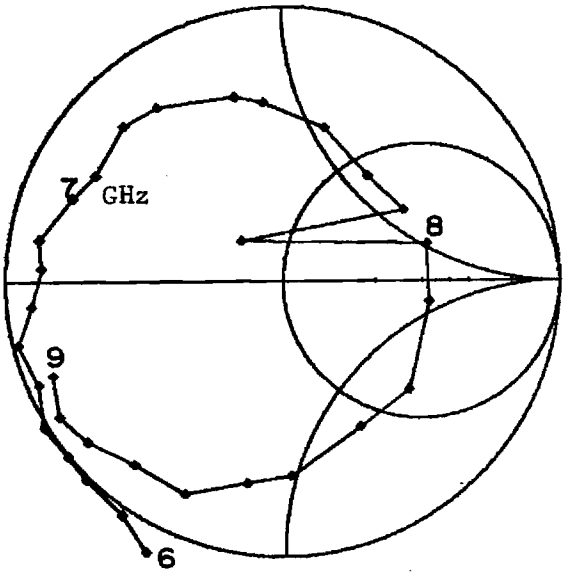

(a) No layer

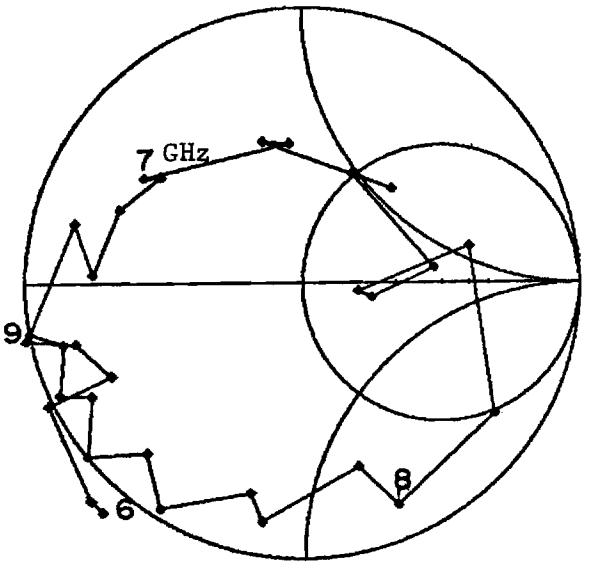

(b) 1/16" Rexolite layer

Figure F-14. Smith Chart impedance plots for the TE_{22}/TM_{22}-modes in Simulator No. 2.

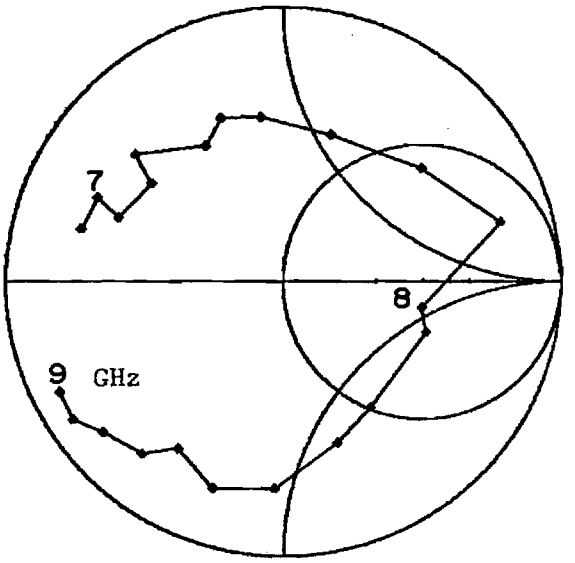

(a) No layer

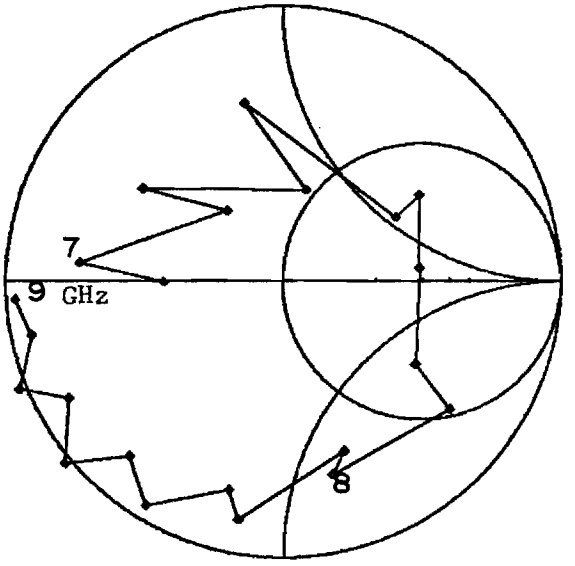

(b) 1/16" Rexolite layer

Figure F-15. Smith Chart impedance plots for the TE_{32}/TM_{32}-modes in Simulator No. 2.

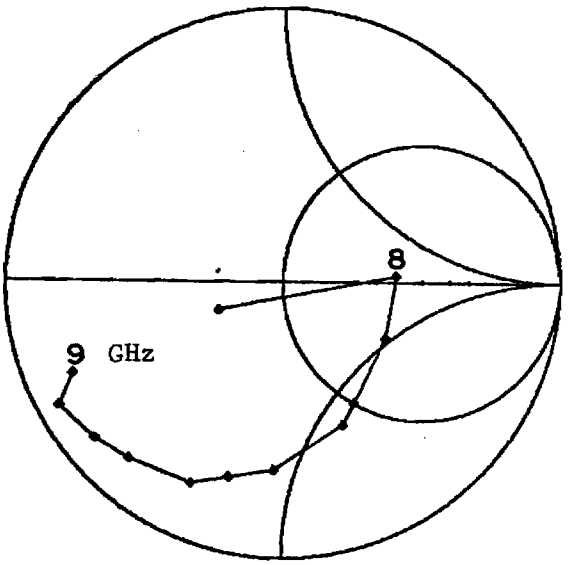

(a) No layer

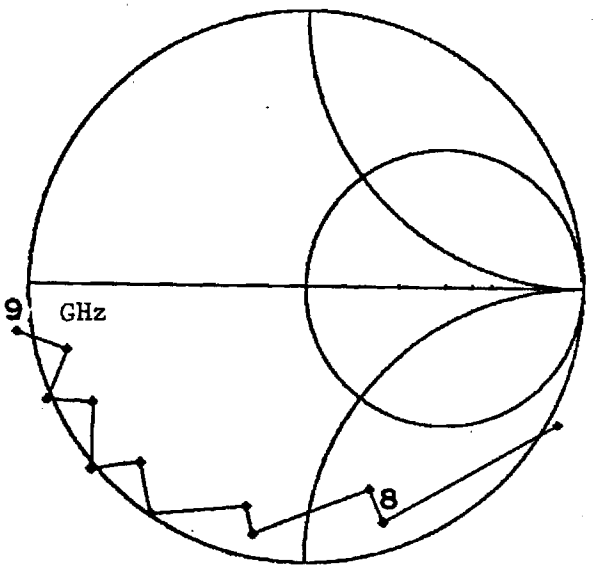

(b) 1/16" Rexolite layer

Figure F-16. Smith Chart impedance plots for the TE_{42}/TM_{42}-modes in Simulator No. 2.

APPENDIX G

IMPEDANCE DATA FOR SIMULATOR NO. 3

APPENDIX G

IMPEDANCE DATA FOR SIMULATOR NO. 3

This appendix presents the reduced data obtained from measurements on Simulator No. 3. This simulator contains thirteen, probe-excited circular microstrip elements in the cross-section shown in Figure G-1. The subarray is etched on copper-clad, 1/16-inch Rexolite 1422, which has a dielectric constant K = 2.54. Probe feeds, formed by the extended center pin of an SMA flange-mount connector, are soldered to the top edge of each element, as indicated by the black dots.

Coupling between pairs of elements was measured from 6 to 9 GHz, in 0.1 GHz increments. Contributions to the coupling caused by reflections from the (imperfect) termination of the simulator waveguide were removed by processing measurements recorded for six positions of the sliding termination. The active element impedance of each of the allowed scan angles for this simulator was calculated from the error-corrected coupling data.

Figure G-2 shows the variation of scan angle (θ , ϕ) with frequency, for each of the fourteen propagating modes that can be excited and sampled with this simulator. At any one frequency, these fourteen modes correspond to fourteen scan angles for the equivalent infinite array.

Figures G-3 through G-16 present Smith Chart plots of the active impedance as a function of frequency. Each figure corresponds to one waveguide mode and, therefore, to a fixed scan plane ϕ and a small range of the angle θ from broadside. The two charts presented in each figure correspond to two thicknesses of the Rexolite 1422 cover layer, $T - t_s = 0$, and 1/16 inch.

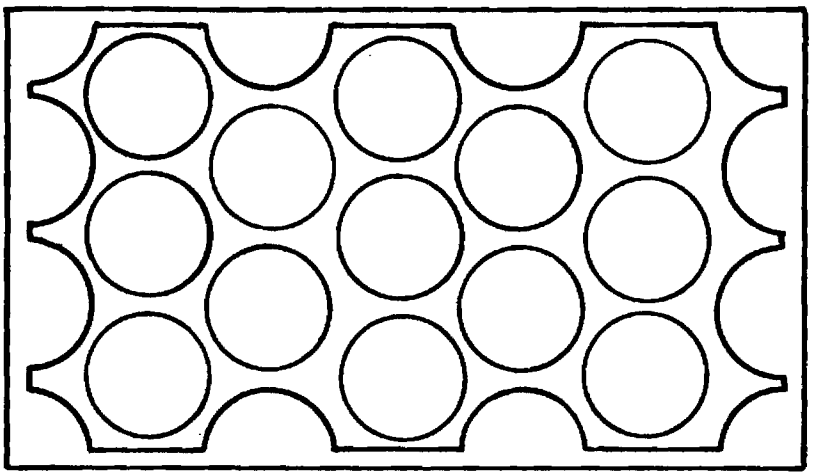

Figure G-1. Sketch of subarray for Simulator No. 3.
Nominal frequency: f_o = 6.373 GHz
Element diameter: d^o = 0.681 in.
Lattice size: ℓ = 0.757 in.
= 0.409 λ_o
Fill-factor: d/ℓ = 0.9

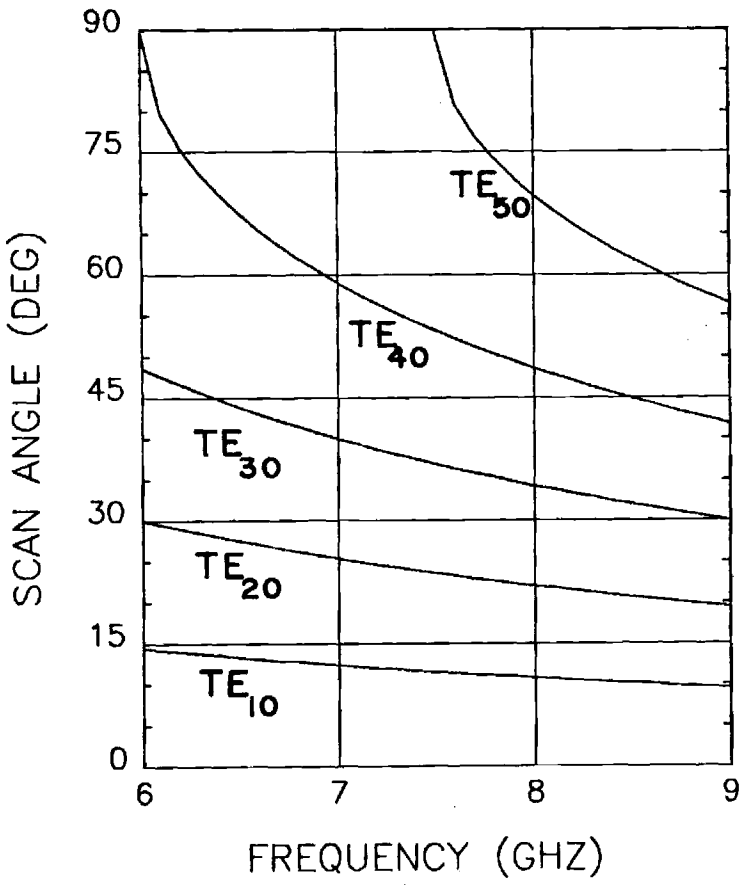

(a) $\phi = 0°$

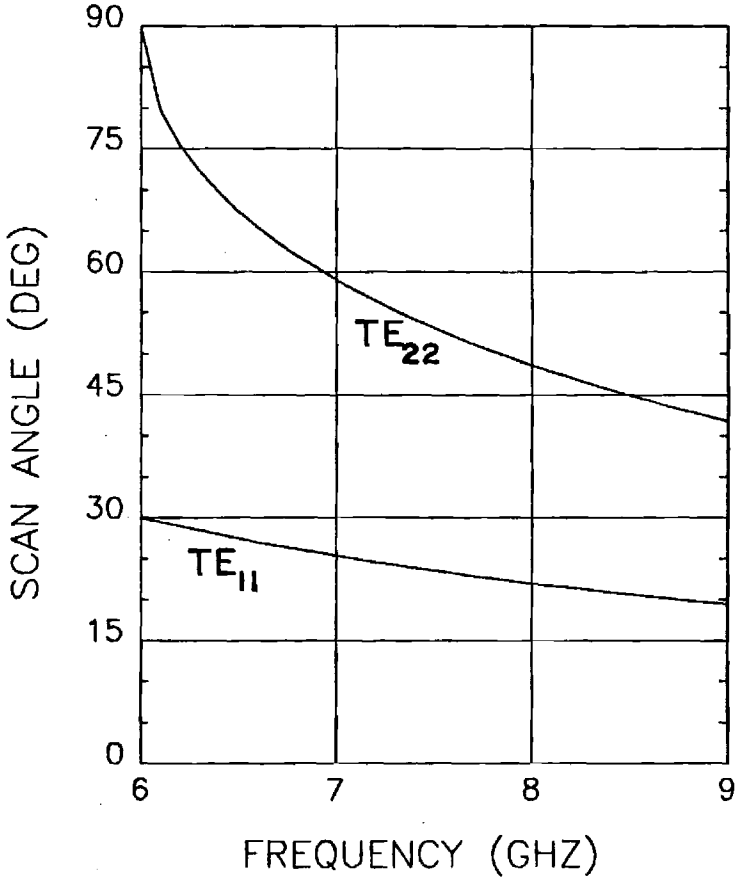

(b) $\phi = 60°$

Figure G-2. Scan angles for waveguide modes excited in Simulator No. 3.

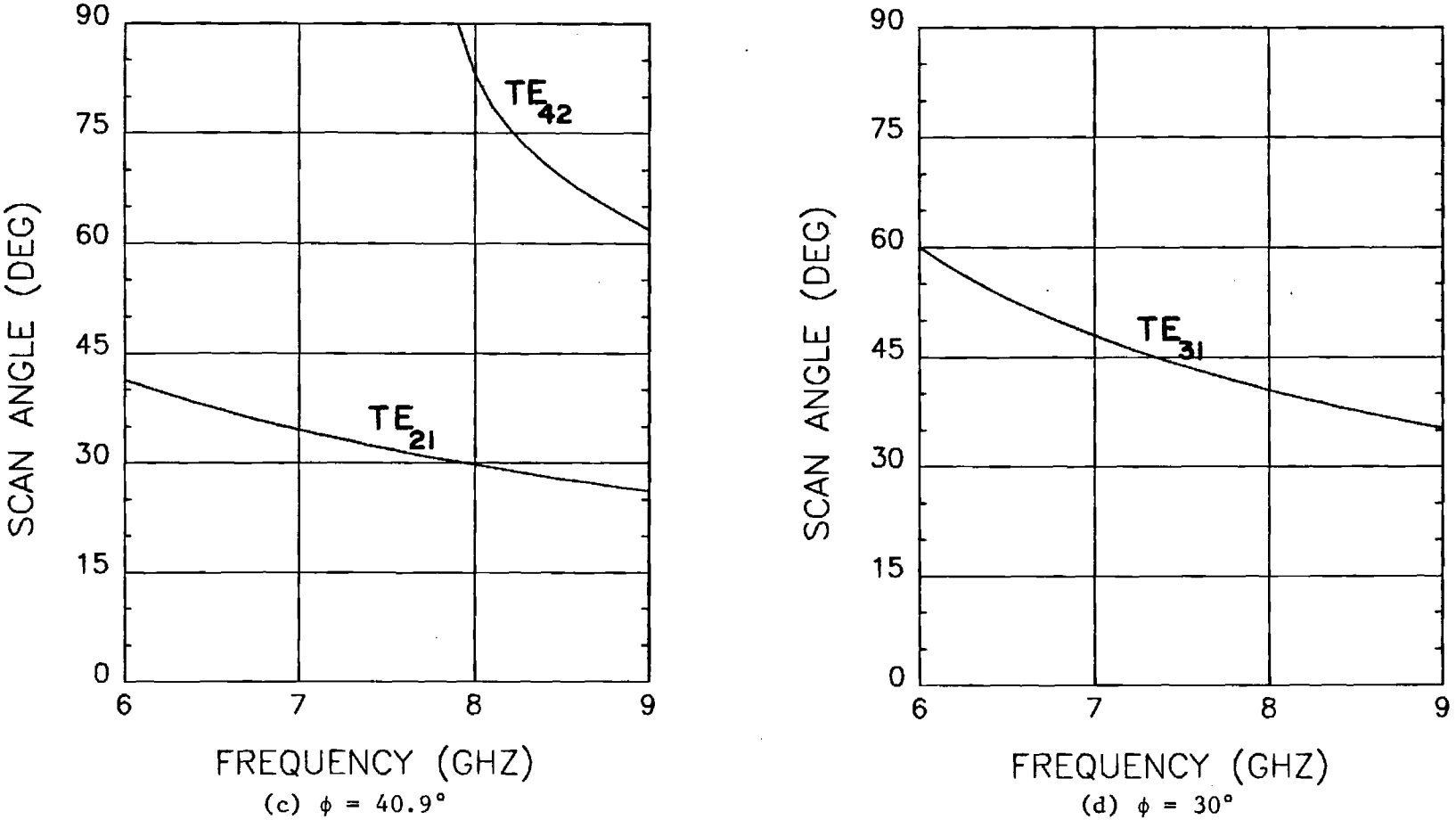

Figure G-2. Scan angles for waveguide modes excited in Simulator No. 3.

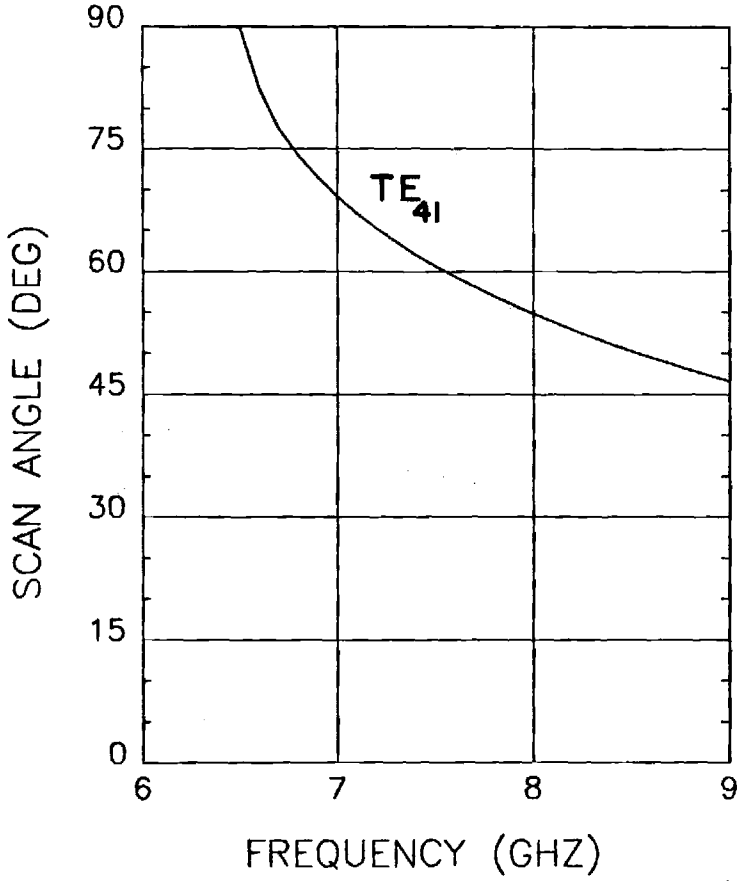

(e) ϕ = 23.4°

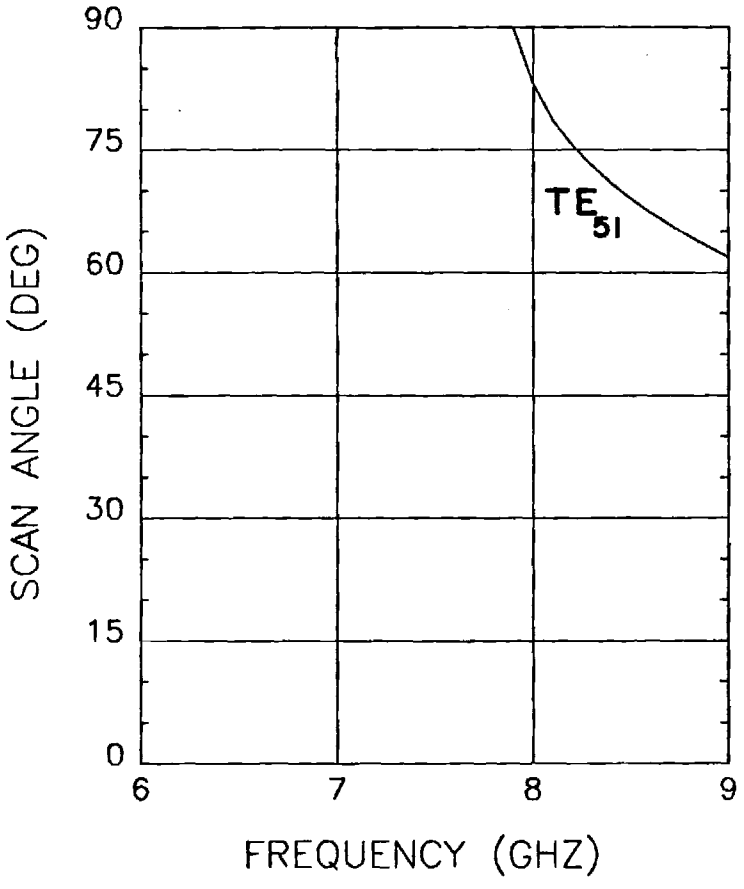

(f) ϕ = 19.1°

Figure G-2. Scan angles for waveguide modes excited in Simulator No. 3.

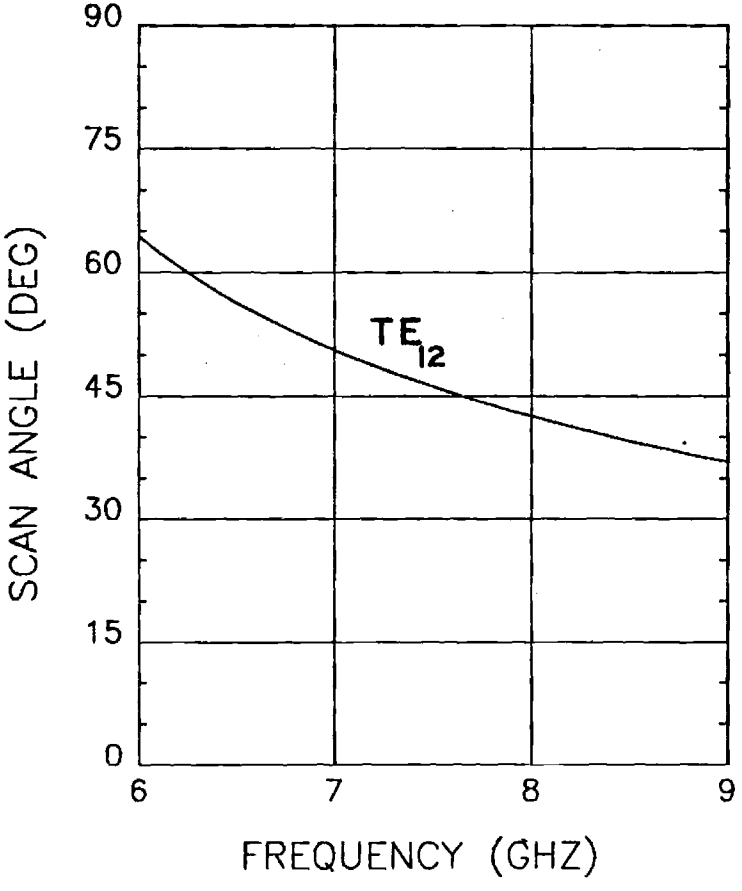

(g) ϕ = 73.9°

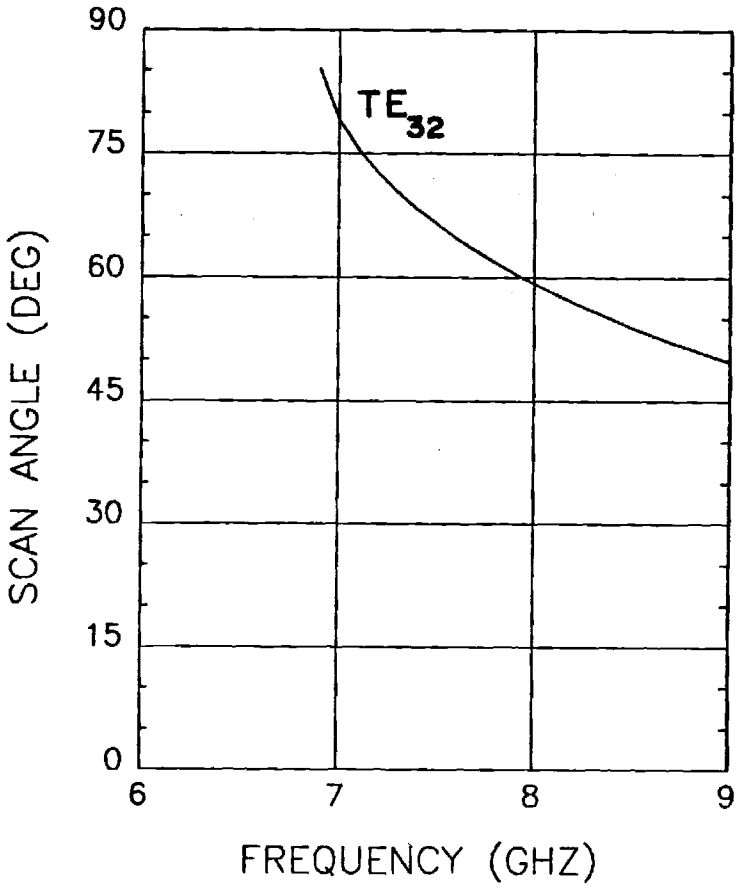

(h) ϕ = 49.1°

Figure G-2. Scan angles for waveguide modes excited in Simulator No. 3.

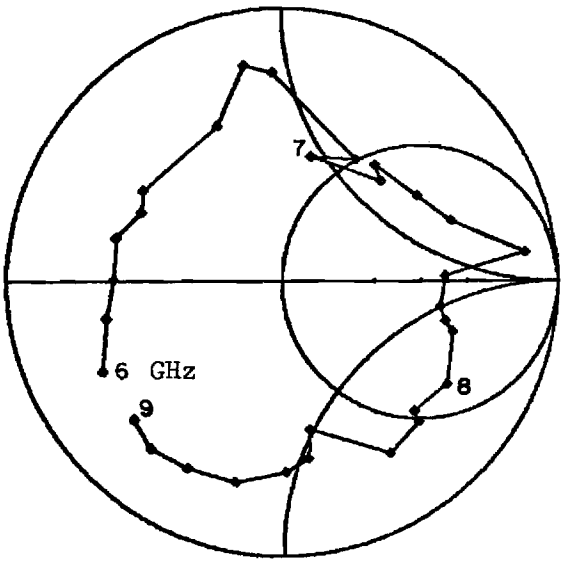

(a) No layer

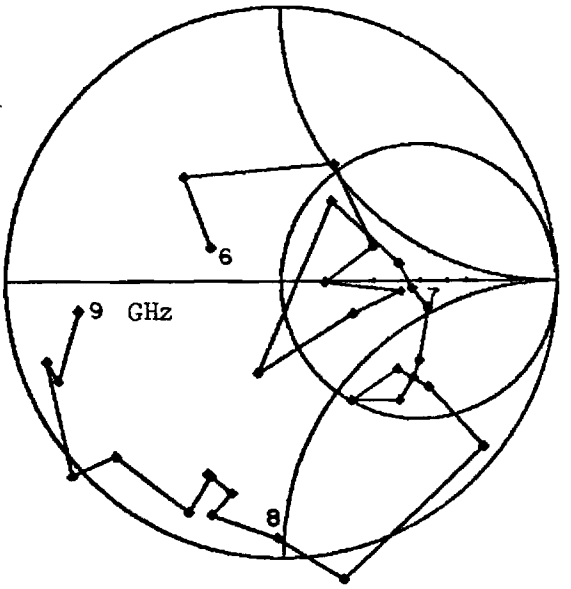

(b) 1/16" Rexolite layer

Figure G-3. Smith Chart impedance plots for the TE_{10}-mode in Simulator No. 3.

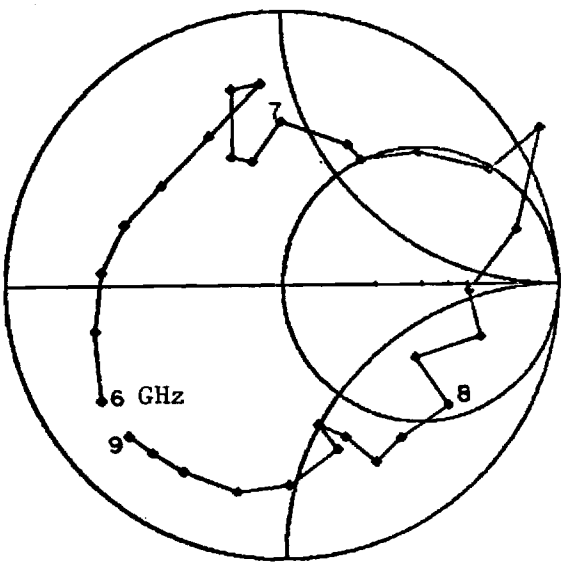

(a) No layer

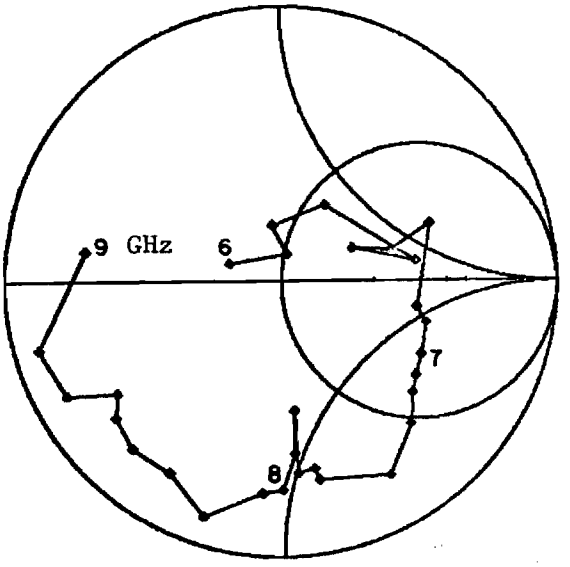

(b) 1/16" Rexolite layer

Figure G-4. Smith Chart impedance plots for the TE_{20}-mode in Simulator No. 3.

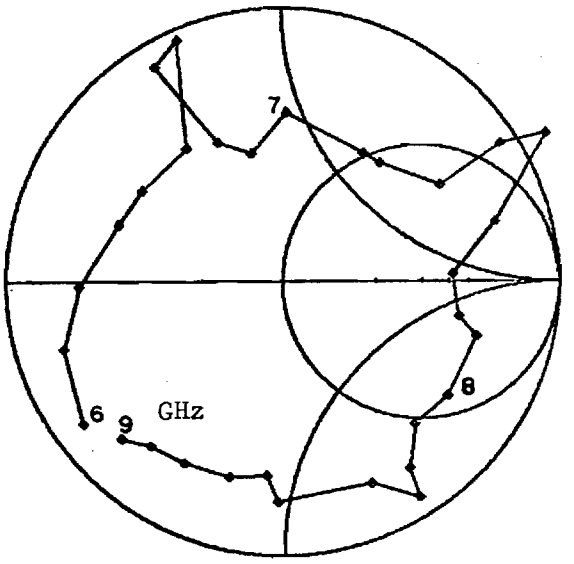

(a) No layer

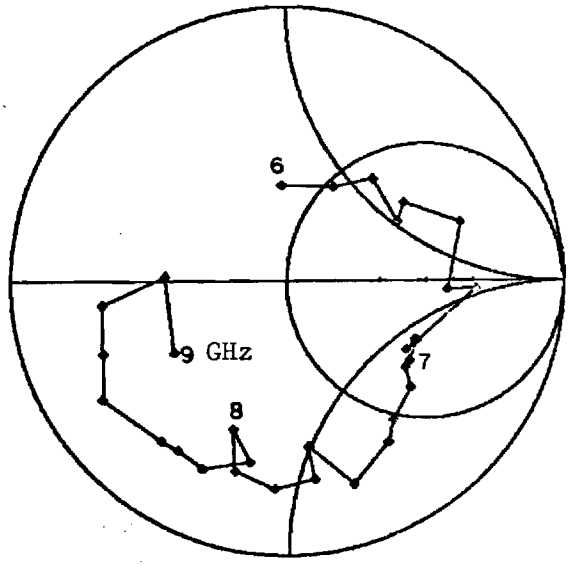

(b) 1/16" Rexolite layer

Figure G-5. Smith Chart impedance plots for the TE_{30}-mode in Simulator No. 3.

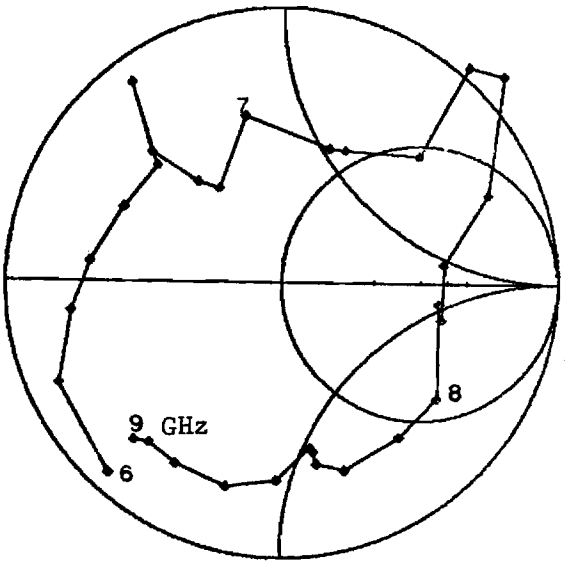

(a) No layer

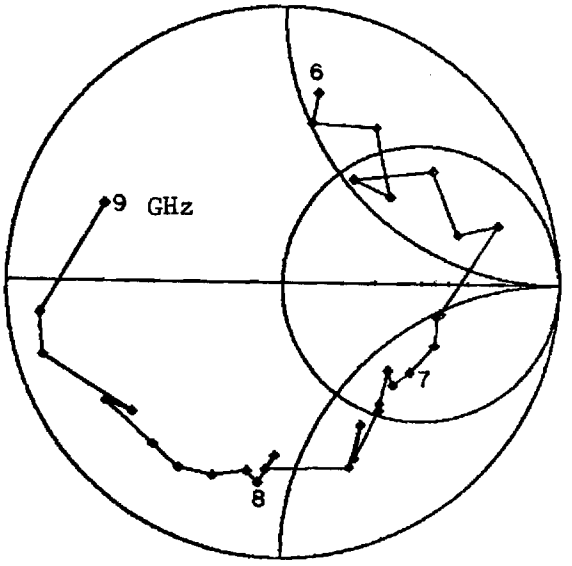

(b) 1/16" Rexolite layer

Figure G-6. Smith Chart impedance plots for the TE_{40}-mode in Simulator No. 3.

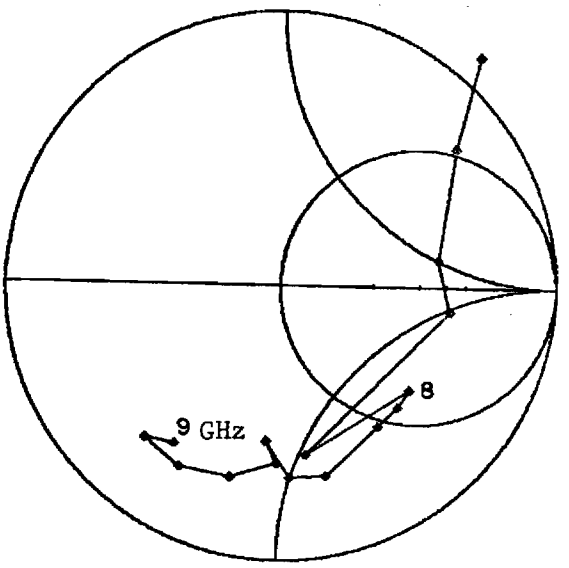

(a) No layer

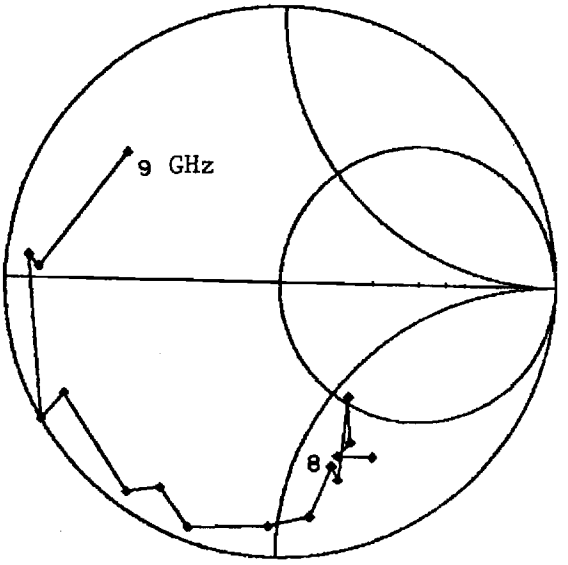

(b) 1/16" Rexolite layer

Figure G-7. Smith Chart impedance plots for the TE_{50}-mode in Simulator No. 3.

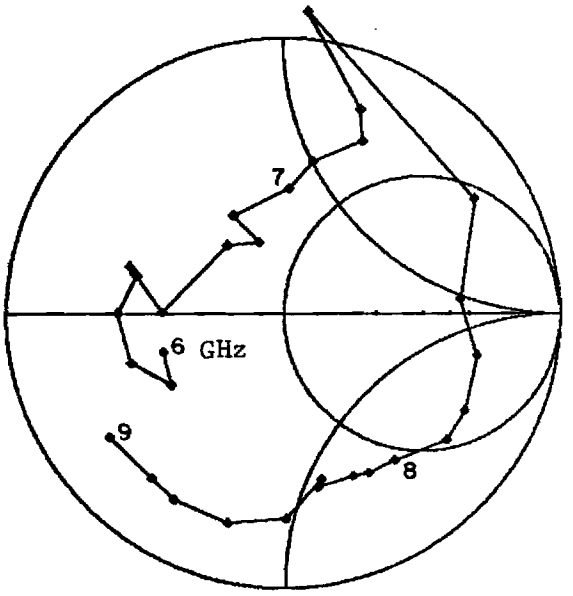

(a) No layer

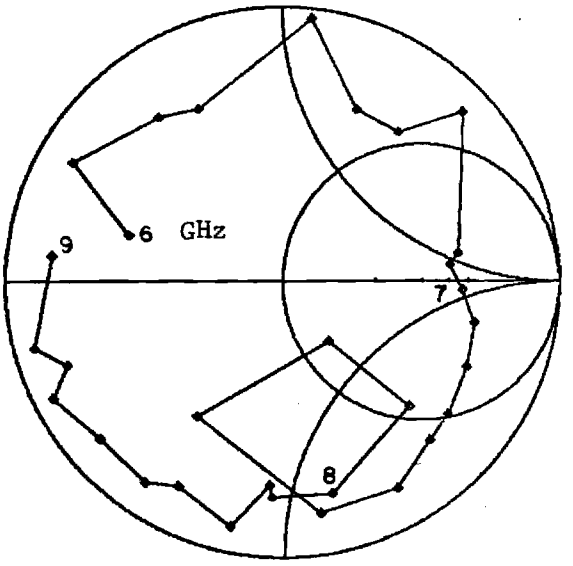

(b) 1/16" Rexolite layer

Figure G-8. Smith Chart impedance plots for the TE_{11}/TM_{11}-modes in Simulator No. 3.

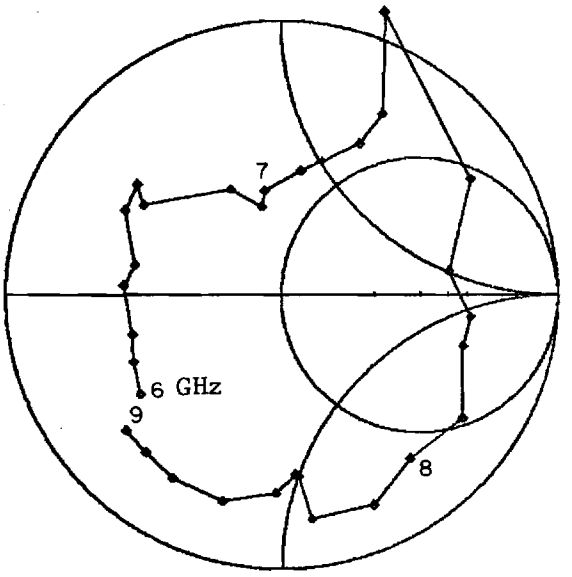

(a) No layer

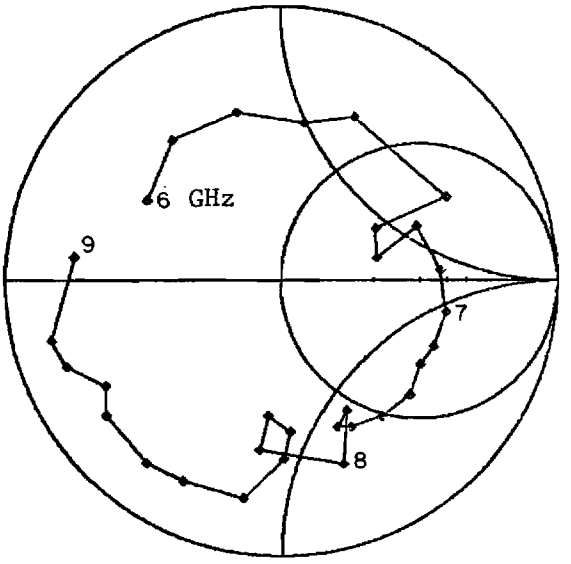

(b) 1/16" Rexolite layer

Figure G-9. Smith Chart impedance plots for the TE_{21}/TM_{21}-modes in Simulator No. 3.

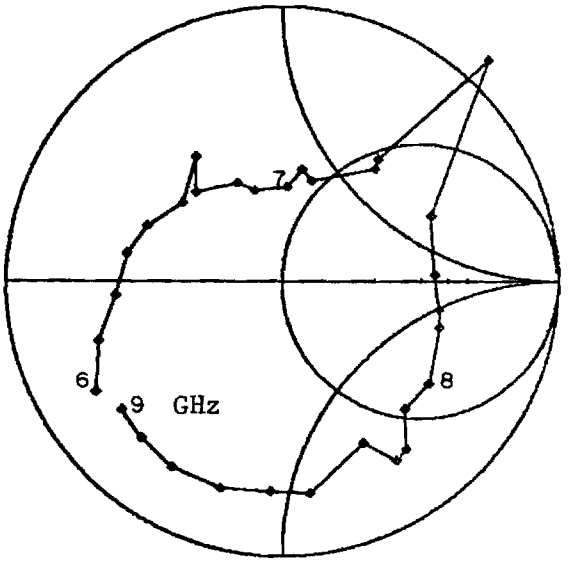

(a) No layer

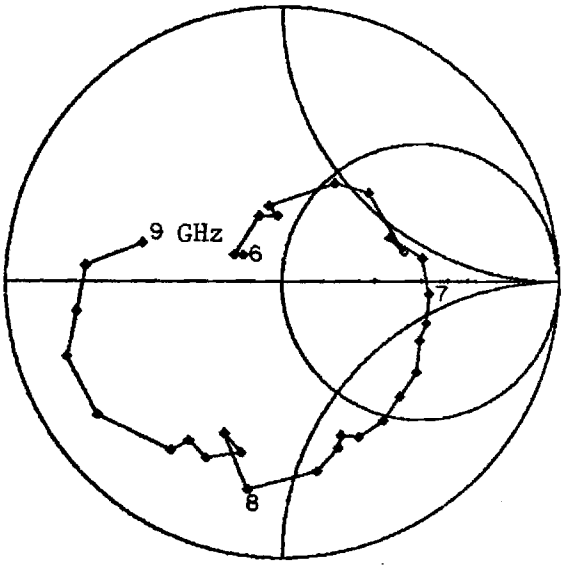

(b) 1/16" Rexolite layer

Figure G-10. Smith Chart impedance plots for the TE_{31}/TM_{31}-modes in Simulator No. 3.

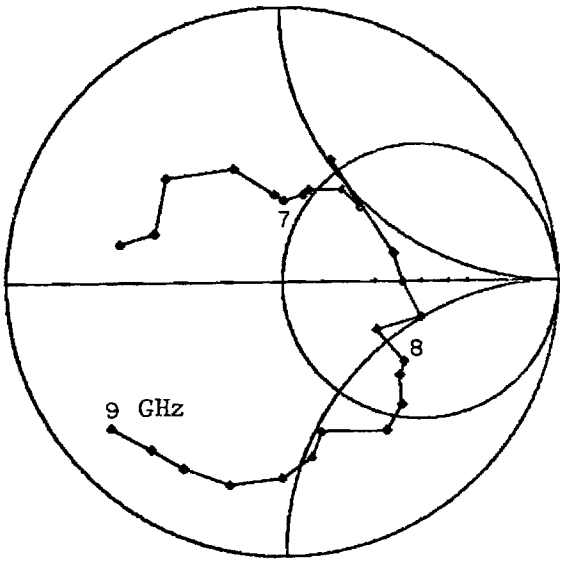

(a) No layer

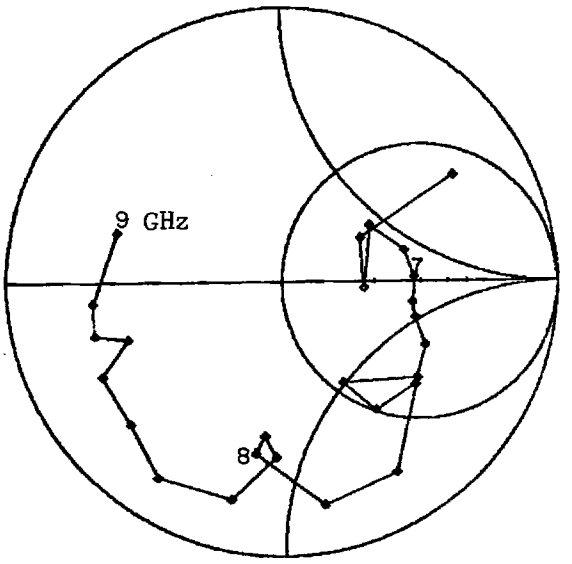

(b) 1/16" Rexolitelayer

Figure G-11. Smith Chart impedance for the TE_{41}/TM_{41}-modes in Simulator No. 3.

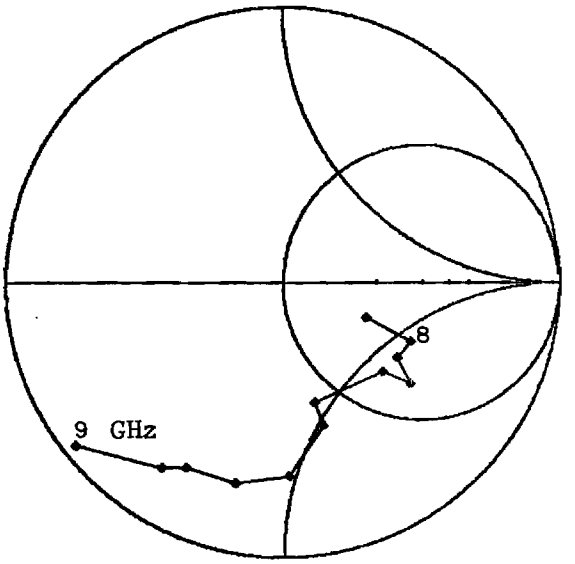

(a) No layer

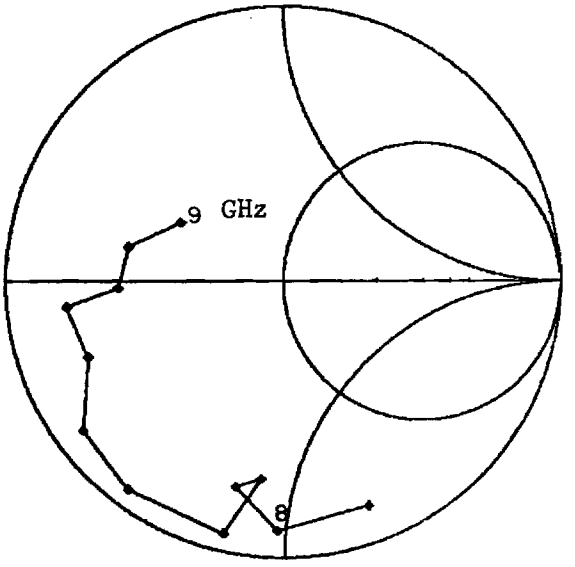

(b) 1/16" Rexolite layer

Figure G-12. Smith Chart impedance plots for the TE_{51}/TM_{51}-modes in Simulator No. 3.

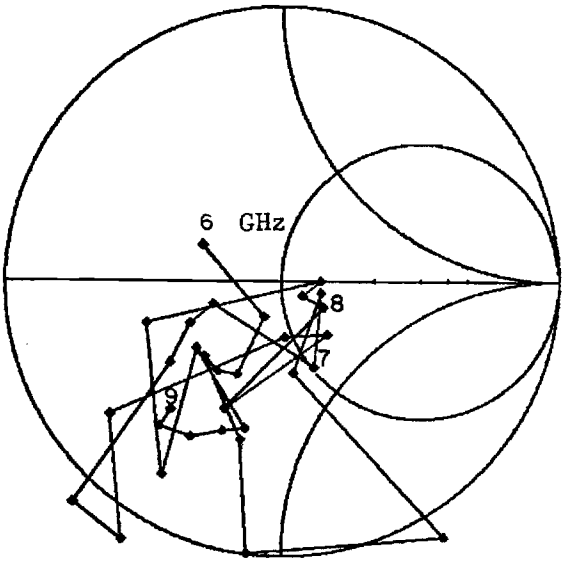

(a) No layer

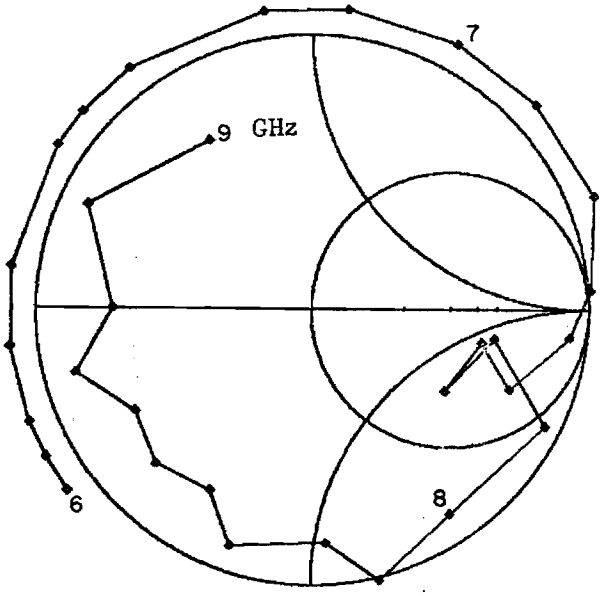

(b) 1/16" Rexolite layer

Figure G-13. Smith Chart impedance plots for the TE_{12}/TM_{12}-modes in Simulator No. 3.

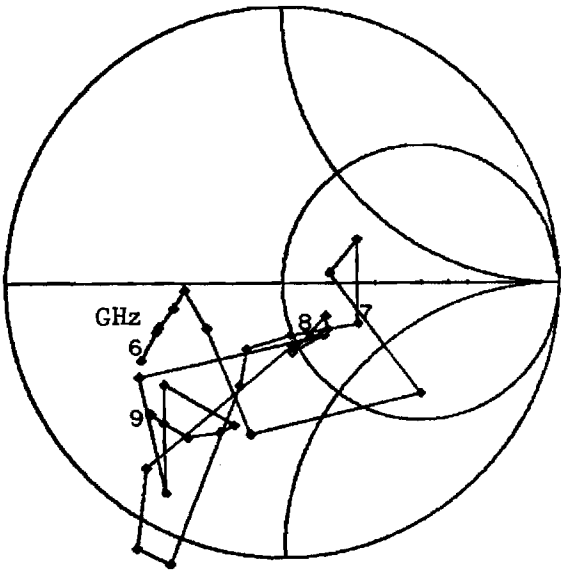

(a) No layer

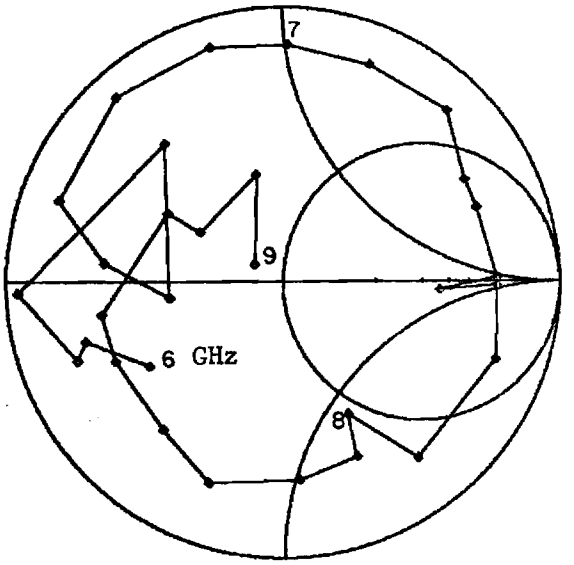

(b) 1/16" Rexolite layer

Figure G-14. Smith Chart impedance plots for the TE_{22}/TM_{22}-modes in Simulator No. 3.

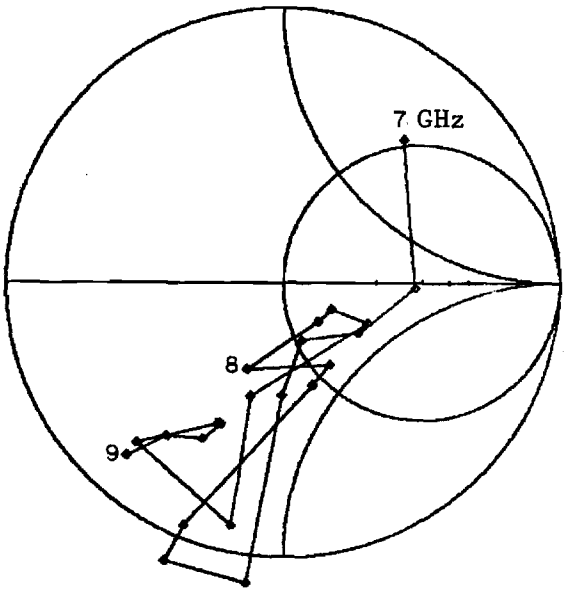

(a) No layer

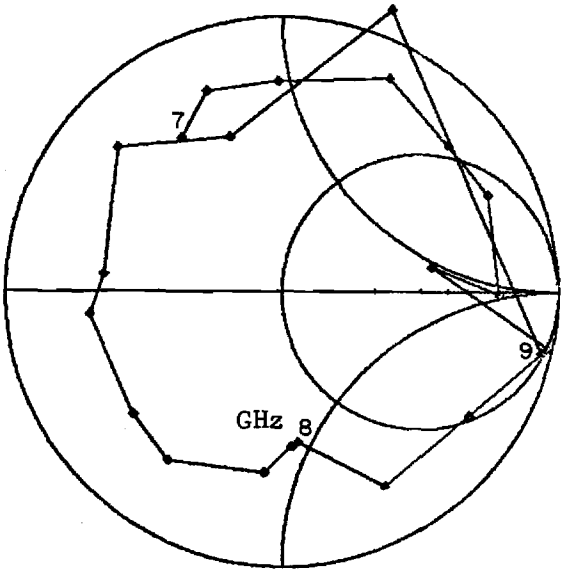

(b) 1/16" Rexolite layer

Figure G-15. Smith Chart impedance plots for the TE_{32}/TM_{32}-modes in Simulator No. 3.

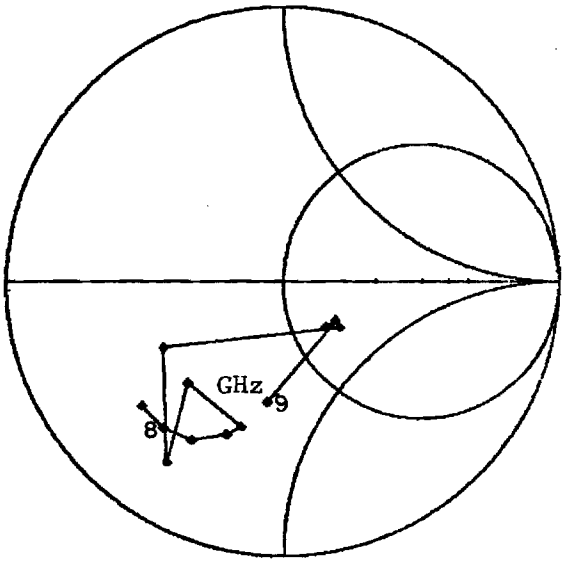

(a) No layer

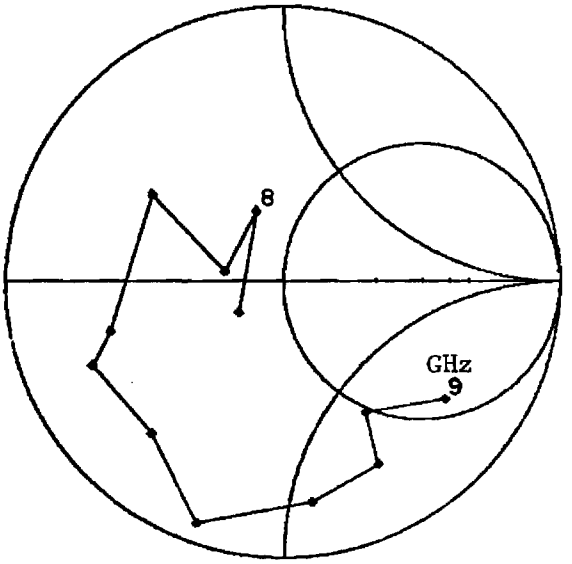

(b) 1/16" Rexolite layer

Figure G-16. Smith Chart impedance plots for the TE_{42}/TM_{42}-modes in Simulator No. 3.

APPENDIX H

IMPEDANCE DATA FOR SIMULATOR NO. 4

APPENDIX H

IMPEDANCE DATA FOR SIMULATOR NO. 4

This appendix presents the reduced data obtained from measurements on Simulator No. 4. This simulator contains five, probe-excited circular microstrip elements in the cross-section shown in Figure H-1. The subarray is etched on copper-clad, 1/16-inch Rexolite 1422, which has a dielectric constant K = 2.54. Probe feeds, formed by the extended center pin of an SMA flange-mount connector, are soldered to the top edge of each element, as indicated by the black dots.

Coupling between pairs of elements was measured from 3.5 to 6.5 GHz, in 0.1 GHz increments. Contributions to the coupling caused by reflections from the (imperfect) termination of the simulator waveguide were removed by processing measurements recorded for six positions of the sliding termination. The active element impedance of each of the allowed scan angles for this simulator was calculated from the error-corrected coupling data.

Figure H-2 shows the variation of scan angle (θ,ϕ) with frequency, for each of the six propagating modes that can be excited and sampled with this simulator. At any one frequency, these six modes correspond to six scan angles for the equivalent infinite array.

Figures H-3 through H-8 present Smith Chart plots of the active impedance as a function of frequency. Each figure corresponds to one waveguide mode and, therefore, to a fixed scan plane ϕ and a small range of the angle θ from broadside. The two charts presented in each figure correspond to two thicknesses of the Rexolite 1422 cover layer, $T - t_s = 0$, and 1/16 inch.

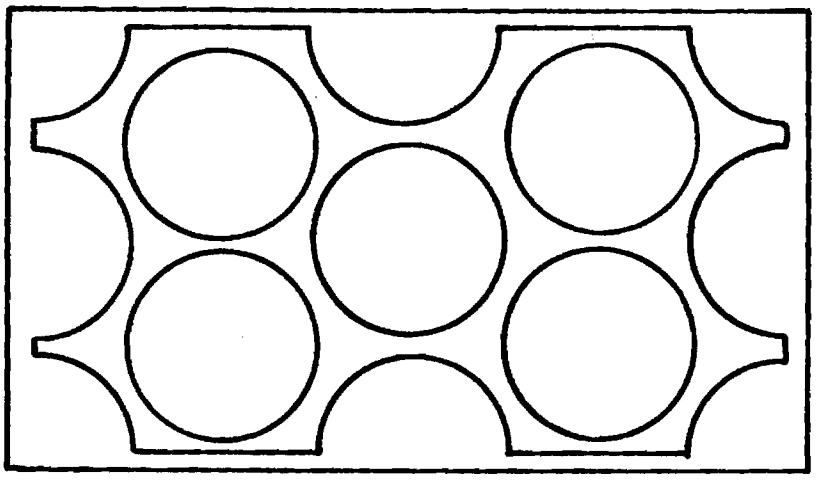

Figure H-1. Sketch of subarray for Simulator No. 4.
Nominal frequency: f_o = 4.246 GHz
Element diameter: d^o = 1.022 in.
Lattice size: ℓ = 1.136 in.
= 0.409 λ_o
Fill-factor: d/ℓ = 0.9

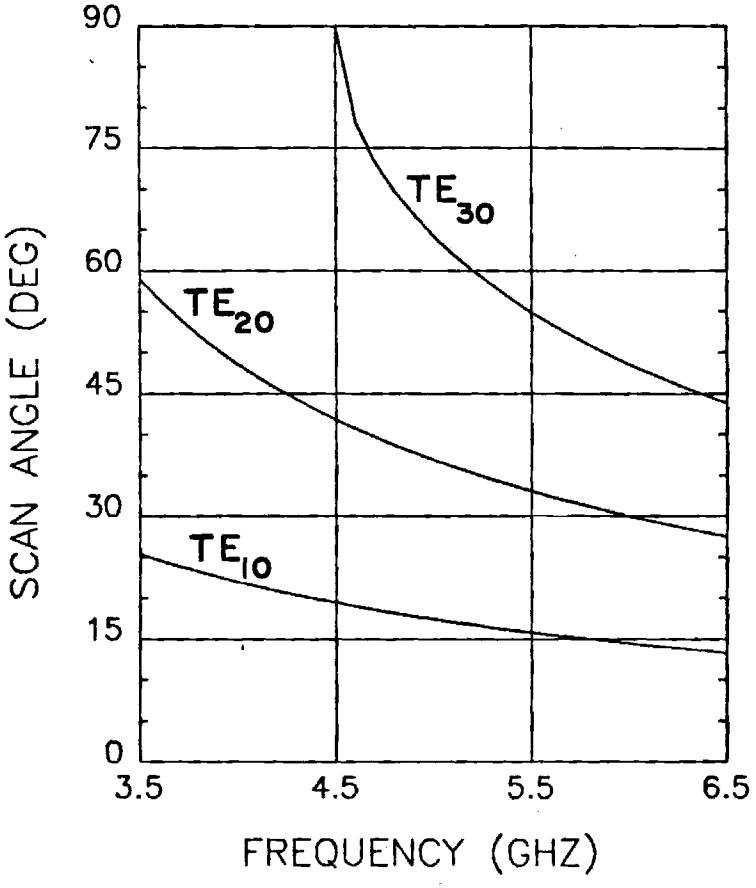

(a) $\phi = 0°$

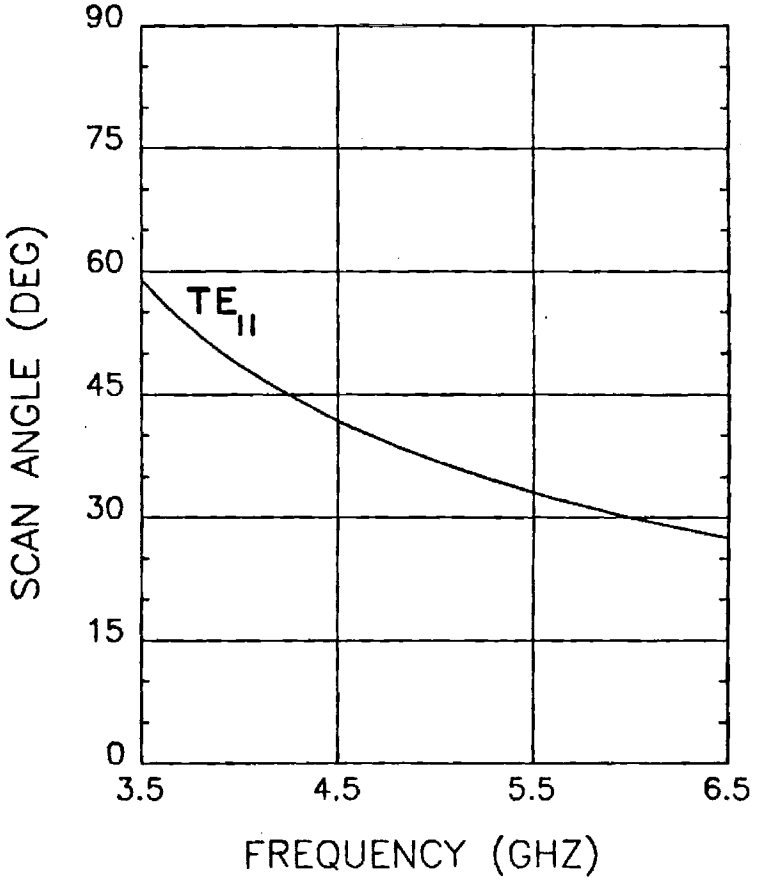

(b) $\phi = 60°$

Figure H-2. Scan angles for waveguide modes excited in Simulator No. 4.

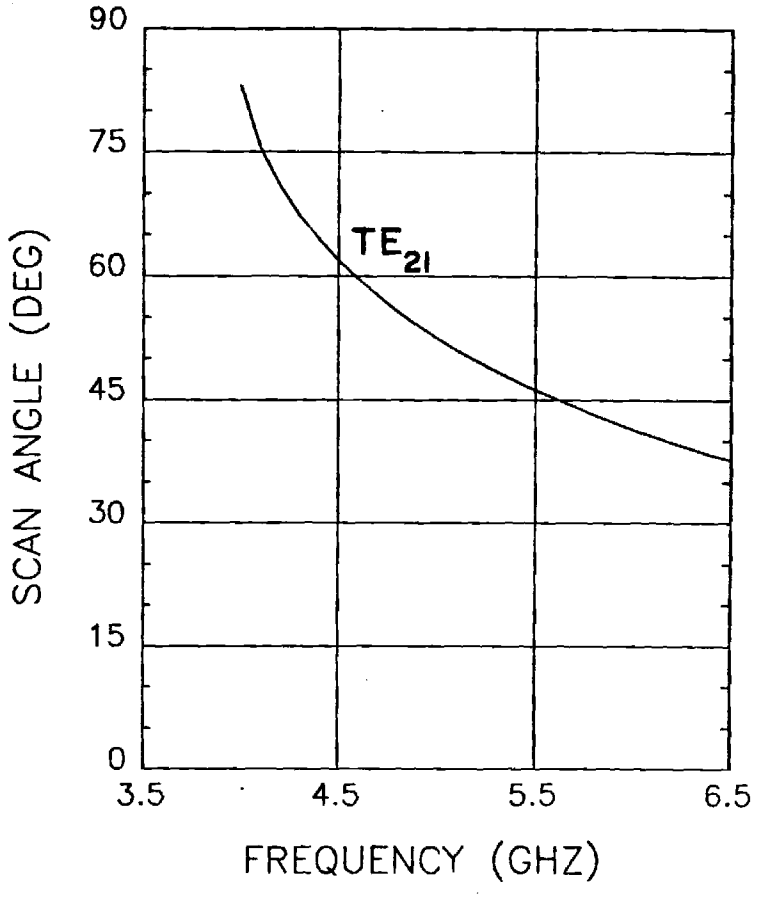

(c) ϕ = 40.9°

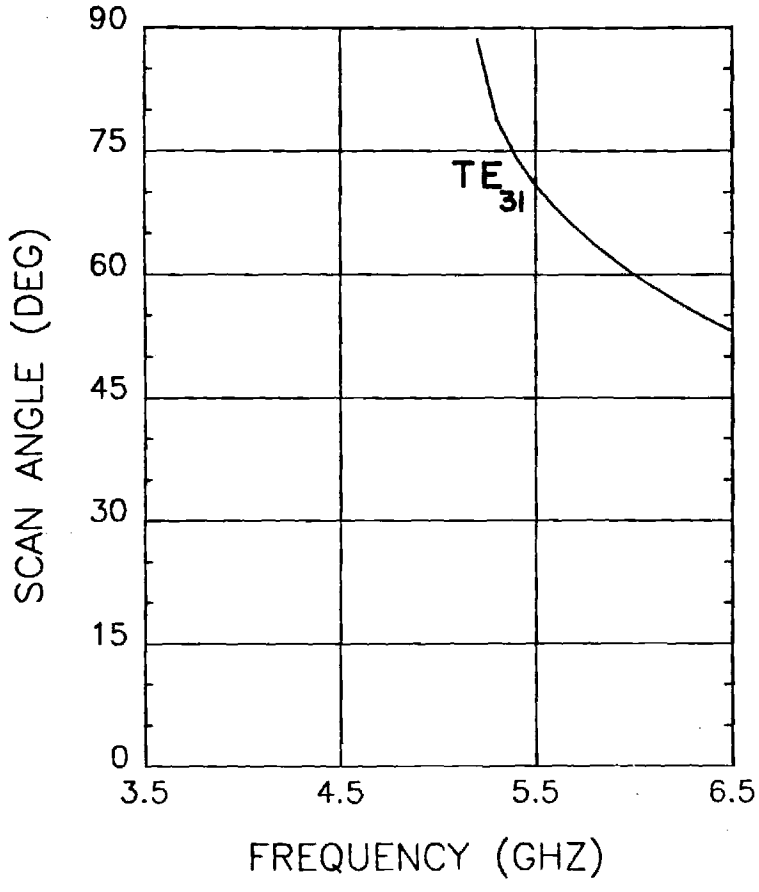

(d) ϕ = 30°

Figure H-2. Scan angles for waveguide modes excited in Simulator No. 4.

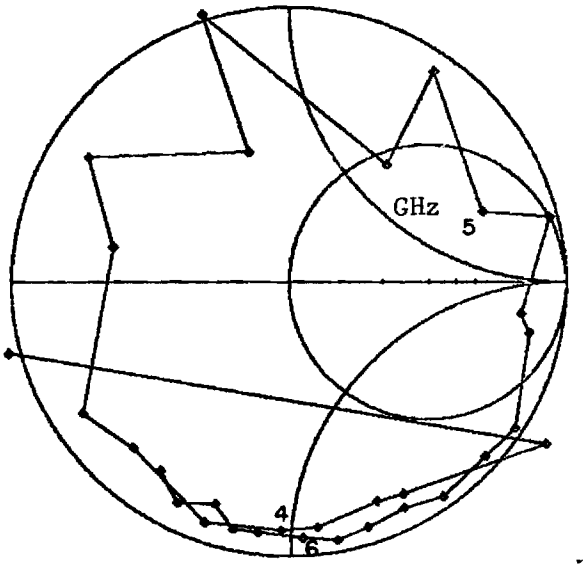

(a) No layer

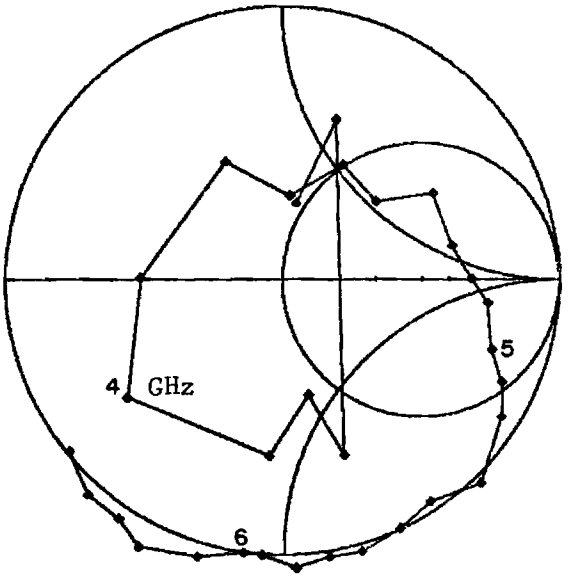

(b) 1/16" Rexolite layer

Figure H-3. Smith Chart impedance plots for the TE_{10}-mode in Simulator No. 4.

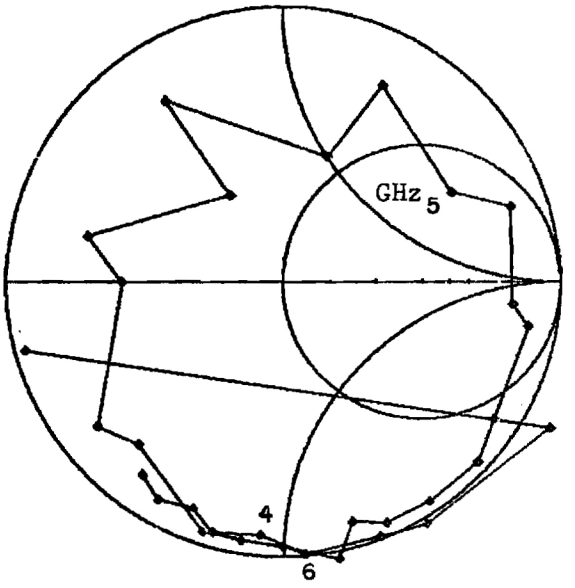

(a) No layer

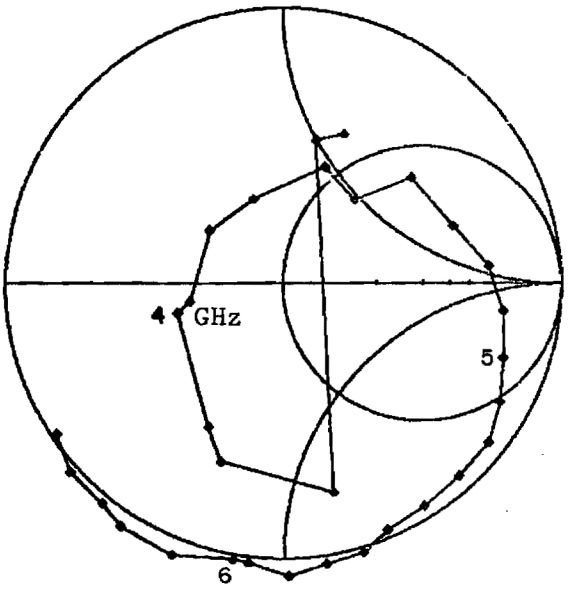

(b) 1/16" Rexolite layer

Figure H-4. Smith Chart impedance plots for the TE_{20}-mode in Simulator No. 4.

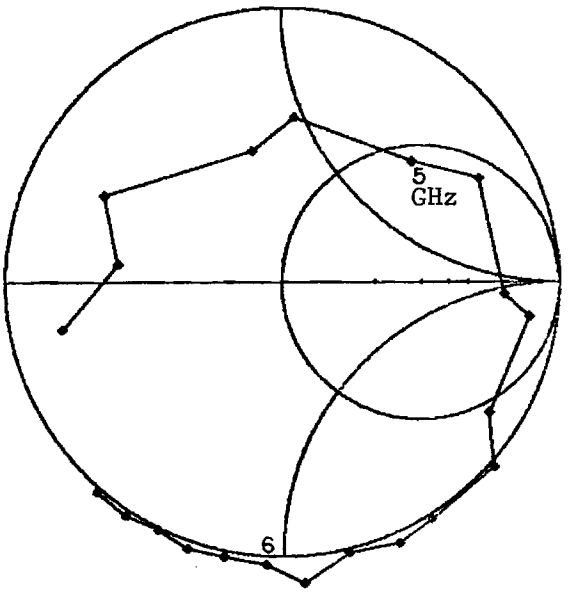

(a) No layer

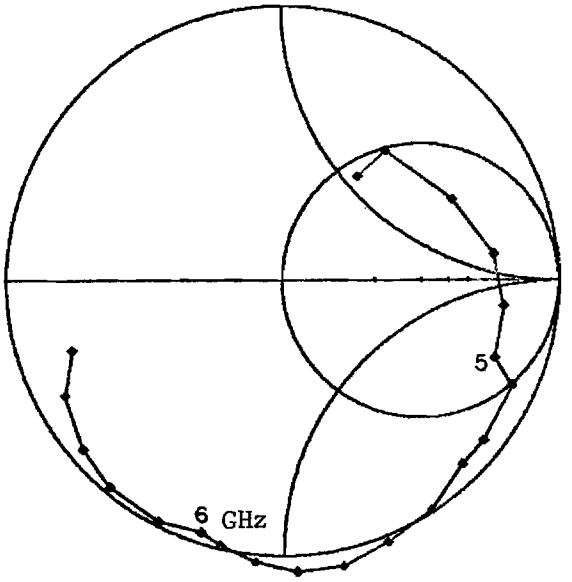

(b) 1/16" Rexolite layer

Figure H-5. Smith Chart impedance plots for the TE_{30}-mode in Simulator No. 4.

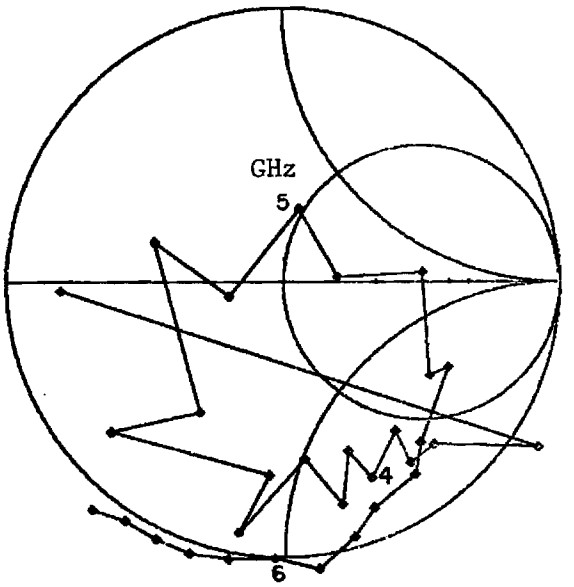

(a) No layer

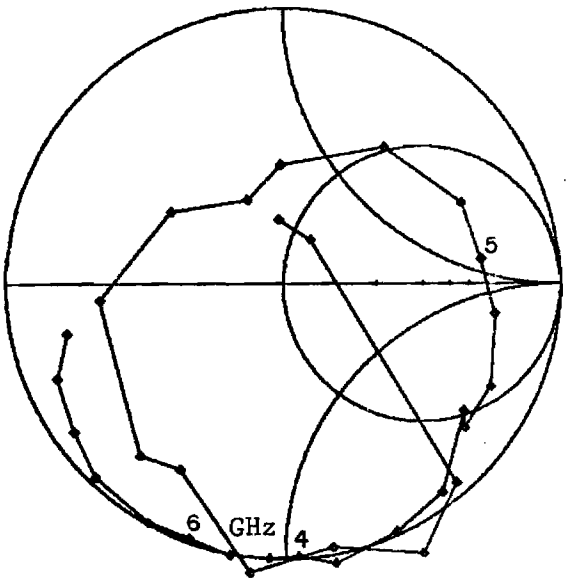

(b) 1/16" Rexolite layer

Figure H-6. Smith Chart impedance plots for the TE_{11}/TM_{11}-modes in Simulator No. 4.

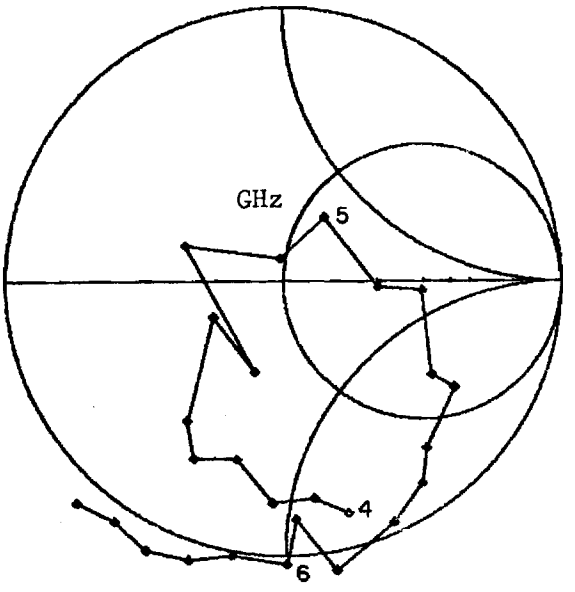

(a) No layer

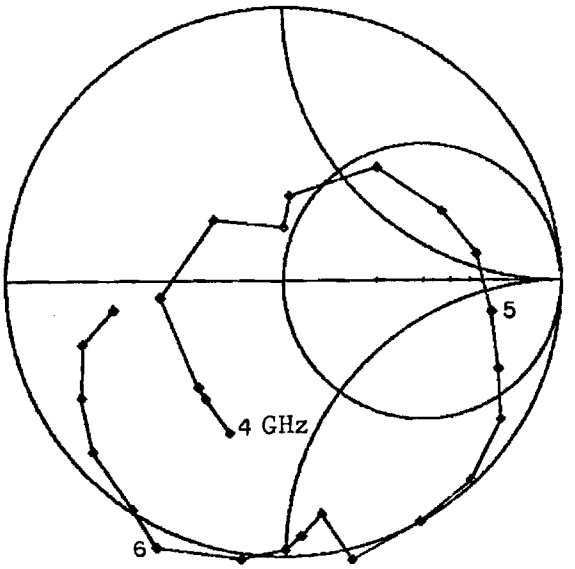

(b) 1/16" Rexolite layer

Figure H-7. Smith Chart impedance plots for the TE_{21}/TM_{21}-modes in Simulator No. 4.

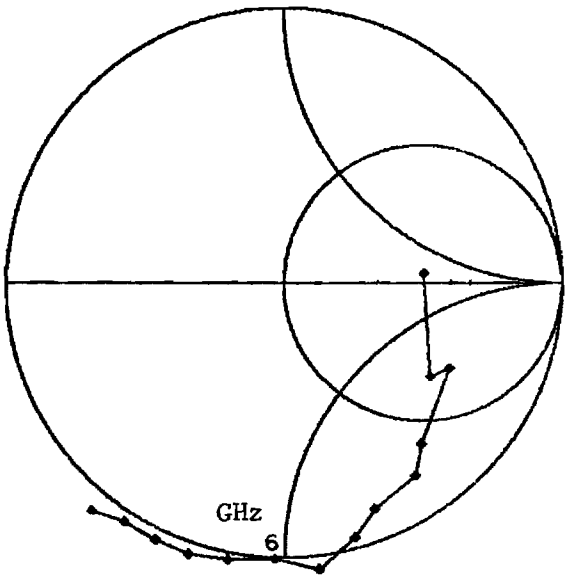

(a) No layer

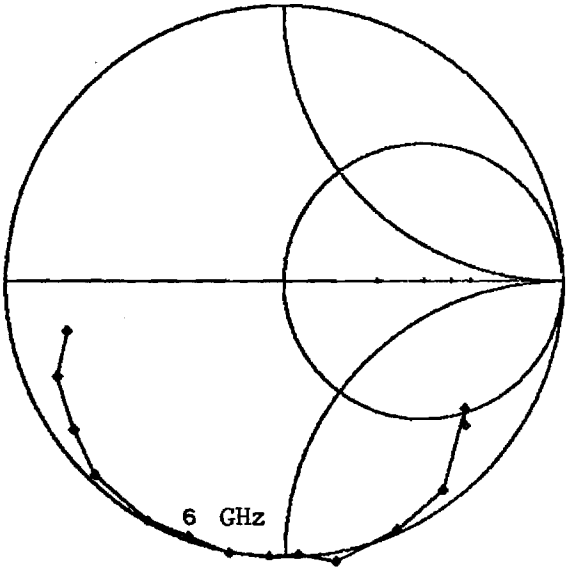

(b) 1/16" Rexolite layer

Figure H-8. Smith Chart impedance plots for the TE_{31}/TM_{31}-modes in Simulator No. 4.